The most exciting phrase to hear in science, the one that heralds new discoveries, is not ‘Eureka!’ (I found it!) but ‘That’s funny ...’

Isaac Asimov

University of Alberta

Nanometer Scale Connections to Semiconductor Surfaces

by

Janik Zikovsky

A thesis submitted to the Faculty of Graduate Studies and Research
in partial fulfillment of the requirements for the degree of

Doctor of Philosophy

Department of Physics

Fall 2009
Edmonton, Alberta

Examining Committee

Robert Wolkow, Physiscs

Frank Hegmann, Physics

Mark Freeman, Physics

Christopher Backhouse, Electrical and Computer Engineering

Miquel Salmeron, Materials Sciences Division, Lawrence Berkeley National Laboratory

To

My wife Vanessa

Abstract

Extending electronic devices beyond the limitations of current micro-electronics manufacturing will require detailed knowledge of how to make contacts to semiconductor surfaces. In this work, we investigated several methods by which such connections to silicon surfaces could be achieved. Scanning tunneling microscopy (STM) was our main experimental tool, allowing direct imaging of the surfaces at the atomic level.

First, the growth of self-forming linear nanostructures of organic molecules on silicon surfaces offers a possibility of creating devices with hybrid organic-silicon functionality. We have studied the growth of many different molecules on a variety of hydrogen-terminated silicon surfaces: H-Si(100)-2×1, H-Si(100)-3×1, and H-Si(111)-1×1. We found molecular growth patterns affected by steric crowding, by sample doping level, or by exposure to ion-pump created radicals. We formed the first contiguous "L-shaped" molecular lines, and used an external electric field to direct molecular growth. We attempted to study a novel method for nanoscale information transfer along molecular lines based on excitation energy transfer.

The second part of the work focuses on the development and use of a new multiple-probe STM instrument. The design and the custom STM control software written for it are described. Connections to Si surfaces were achieved with a combination of lithographically defined metal contacts and STM tips. Two-dimensional surface conductivity of the Si(111)-7×7 surface was measured, and the effect of modifying the surface with organic molecules was investigated. A novel method, scanning tunneling fractional current imaging (STFCI), was developed to further study surface conductance. This method allowed us to determine, for the first time, that the resistance of steps on the Si(111)-7×7 surface is significantly higher than that of the surface alone.

Acknowledgements

I would like to acknowledge everyone in Dr. Wolkow's group - no one could find a nicer, smarter, and more helpful and friendly group than these. In particular, I thank:

Dr. Stas Dogel, with whom I have worked on many projects: in particular, most of the line growth experiments and e-beam lithography for contacts on Si.

Mark Salomons, for designing and building the multiple probe STM, and for fixing it when I broke it.

Gino DiLabio, for chemistry calculations, insight, and very helpful discussions.

And to all the other members of the group: Josh Mutus, Jason Pitters, Baseer Haider, Mohammed Rezeq, Paul Piva, Martin Cloutier, Shoma Sinha, Manuel Smeu, Radovan Urban, Mustafa Muhammad, Lucian Livadaru, Cristian Vesa; all of whom have helped me many times over the years.

Lars Holm and others at the Physics Electronics Shop.

All the staff at the Physics machine shops.

Last but not least, I would like to thank Dr. Wolkow, for his support, help, and insights.

Table of Contents

List of Tables

List of Figures

Chapter 1

Introduction

1.1 The Importance of Silicon

Silicon dominates the electronics world, and forms the basis of the vast majority of integrated circuits being manufactured. Because of the huge technological importance of silicon, the goal of this work was to study the chemistry and physics of silicon surfaces, with an eye for reducing device size and extending the functionality of silicon-based devices into domains where conventional silicon technology is weak — in particular, interactions with organic molecules.

The scanning tunneling microscope (STM) was our main investigative tool. In an effort to perform patterning of silicon at length scales smaller than conventional lithography, molecular nanostructures on silicon surfaces were made via a self-forming process; the chemistry of the process was studied and we improved the control on the patterns written. Nanometer-scale connections to silicon surfaces were realized in support of the goal of extending silicon functionality, using a combination of multiple-probe STM and lithography.

1.2 Scanning Tunneling Microscopy

The scanning tunneling microscope (STM) is the ultimate tool for studying surfaces when an atom-level view is desired. While there are many techniques that can characterize surfaces over large areas, only STM and related scanning probe methods such as atomic-force microscopy (AFM) are able to image a single atom or molecule on a surface. A wealth of information can be had from scanning probe experiments.

The STM was developed in 1982 by Binnig and Rohrer [1] and won the 1986 Nobel prize for its inventors. It uses a sharp metal tip biased at a moderate voltage and placed within a few angstroms of the surface under investigation. Despite the lack of a direct contact between the two materials that would allow current to conduct, the distance between the tip and sample is small enough to allow electrons to tunnel through the vacuum gap, as seen in Figure 1.1.

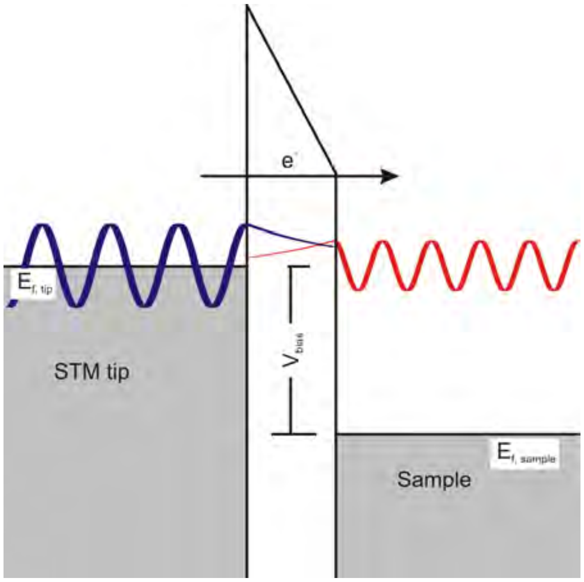

Figure 1.1: Band diagram showing electrons tunneling from a negatively biased tip through a vacuum gap to a metal sample.

The tunneling current depends exponentially on the tunneling gap distance: $I \propto e^{-\kappa d}$, where κ is a characteristic length scale of the order of Å^{-1}; d is the tunneling gap width; I is the tunneling current. This exponential dependence gives the STM its extremely good height resolution.

The typical way to obtain an image of a surface is to scan a tip in a raster pattern while a feedback loop maintains a constant tunneling current — this is known as *constant-current imaging*. The height of the tip required to maintain this current is recorded, providing a 3-dimensional image of the surface topography.

The height of the surface is only part of the information that can be obtained through STM — the tunneling current between two materials also depends on the density of electronic states available for tunneling. Therefore, by varying the sample bias used, the STM can also be used as a sensitive probe of the electronic structure of a surface.

In Chapter 2, we present finite element method (FEM) calculations which help us understand the electronic state of Si surfaces during STM imaging.

1.3 Electronics Miniaturization

Today's microchips have gone a long way since the very first integrated circuit was built in 1958 by Jack Kilby [2]. The number of transistors built into a single circuit has continually increased, closely following the empirical rule of doubling in density every 18 months first predicted by Gordon Moore in 1965 [3].

The size of transistors has of course gone down in step with the increase in their density. The Intel 4004 processor (1971) used 10 μm technology; by 1978, the 8086 processor used 3 μm process; the first Pentium processor (1993) used 0.8 μm; and current dual-core Pentium processors now use a 65 nm process [4]. The International Technology Roadmap for Semiconductors lays out a plan to reach 32 nm by 2013 [5]. The physics occurring when these devices reach nanometer scales make further miniaturization difficult, but molecular electronics and nanotechnology research aims to find a solution by moving to alternative electronics architectures.

Chapter 3 presents a method by which features of organic molecules can be made on a silicon surface with sub-nm precision: self-assembled molecular lines. The control on the way the molecular lines grow was extended by careful study of their chemical properties; additional control was achieved with the use of an external electric field, as described in Chapter 8. These lines were proposed to be used for a novel method of information transfer at molecular scales, described in Chapter 4.

1.4 Making Nanometer-Scale Contacts

Studying the properties of nanoscale objects requires the ability to image and contact extremely small objects. To do this, we designed and built a multiple-probe STM, capable of bringing 3 sharp metal tips within a few tens of nanometers of each other. The instrument hardware is described in Chapter 5, and its control software is described in Chapter 6.

To make reproducible and well-defined metallic contact pads on the surface, we used titanium silicide island formation and electron-beam lithography (EBL). The methods used are described in Chapter 7.

1.5 Electrical Properties of Silicon Surfaces

Using the multiple-probe STM, we were able to study the properties of silicon surfaces; we measured the surface conductivity of the Si(111)-7×7 surface, and found it to be extremely sensitive to doses of organic molecules in the vacuum chamber - these results are described in Chapter 9. The sub-micron spacing of the metal contacts, which we were able to achieve thanks to our multiple-probe STM and EBL, enhances our sensitivity to the surface conductance, because it dominates at shorter length scales. The resistance between two point contacts on a semi-infinite 3D conductor of σ_b conductivity is given by:

$$R_{3D}^{2pp} = \frac{1}{\pi\sigma_b}\left(\frac{1}{r} - \frac{1}{s-r}\right) \tag{1.1}$$

and for an infinite 2D sheet conductor of σ_s conductivity by:

$$R_{2D}^{2pp} = \frac{1}{\pi\sigma_s}\ln\left(\frac{s-r}{r}\right) \tag{1.2}$$

s is the spacing, r is the contact radius [6]. These two equations are plotted in Figure 1.2, showing the dominance of the surface conductivity at smaller s.

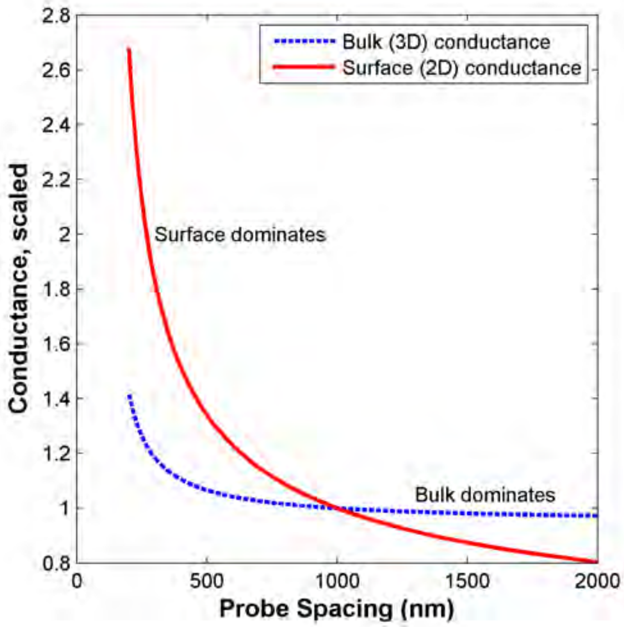

Figure 1.2: Figure showing the general trend of surface vs. bulk conductance between two contacts (of 50 nm radius; based on Equations 1.1 and 1.2). Their conductances are scaled to be equal at 1 micron spacing; the surface dominates at closer distances, and becomes harder to measure as the spacing increases.

We also developed a method for imaging the conductance of the surface of a semiconductor — scanning tunneling fractional current imaging (STFCI), which is analogous to scanning tunneling potentiometry. The method, detailed in Chapter 10, shows good qualitative agreement with FEM simulations. We used STFCI to directly observe how a patch of Si(111)-7×7 is more conductive than surrounding H-Si(111)-1×1. Also, the resistance of steps on the Si(111)-7×7 surface was found for the first time to be significantly higher than that of the surface alone.

Chapter 2

Electrostatic Modeling of a STM Tip

2.1 Introduction

Scanning tunneling microscopy probes a surface to obtain information such as topography and electronic states, however it is important to remember that the presence of a biased, metallic object a few angstroms from any surface will disturb it significantly. In the case of tunneling to a metallic substrate, it is a reasonable approximation that the substrate is at a constant potential, and that the entire potential drop of the tunneling bias occurs in the vacuum gap. However, when the substrate is a semiconductor such as silicon, a significant portion of the potential will drop in the substrate itself.

To have a clear understanding of a STM image we obtain of a semiconductor surface, it is necessary to model the complex interaction between the tip, the bulk semiconductor, and its surface. In our specific case, we wanted to be able to predict the charge of dangling bonds (DBs) on the surface during imaging (see Section 2.3.4). For silicon in the absence of a tip, it is fairly straightforward to calculate the average charge of DBs on the surface at a given dopant concentration. However, in the presence of a disturbance like a STM tip with a voltage applied, the situation can be greatly different. While simple and often solvable analytically, a one-dimensional model representing parallel plates would be quite inadequate to represent the field from a very sharp tip. A three-dimensional model is thus required.

Feenstra [7] developed an appropriate model to solve this problem, taking into account the way charge develops in a semiconductor when it is under a potential. His algorithm used a finite element method to solve Poisson's equation in a convenient geometry (prolate spheroidal in vacuum and cartesian in the semiconductor). We chose to develop a more generalized model, using the commercial finite element software FEMLAB (later renamed Comsol Multiphysics). This allowed us to define more complex problems — for instance, by accounting for a surface with DBs able to hold charge. Feenstra later refined his model to include surface states as well [8].

2.2 One-Dimensional Models

Early research on metal-insulator-semiconductor structures [9, 10] can provide a useful starting point on which to base further developments. These devices consist of an insulator sandwiched between a doped Si substrate and a metallic contact, and are used in voltage-variable capacitors as well as charge-coupled devices (CCD). A one-dimensional model can describe these devices to a good approximation. Sze [11, ch. 7] offers a good overview of the theory of an ideal MIS diode, and gives us the general features of the effect of a biased tip near a semiconductor surface. In a STM experiment, of course, the insulator is replaced by vacuum; also, the fact that a STM tip is a sharp point rather than a flat plate can significantly change the degree of band-bending that occurs.

Figure 2.1 shows the energy-band diagram of a MIS diode with no bias applied. In this case, the metal and semiconductor are connected together, making their Fermi levels E_F align, resulting in flat bands. Recall that energy-band diagrams show the potential energy of an *electron*, therefore a negative voltage is shown as a *higher* line.

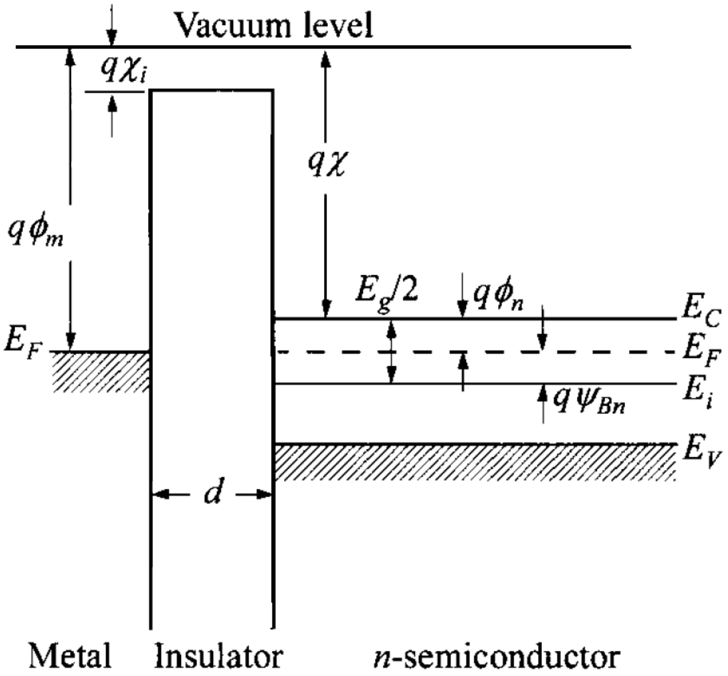

Figure 2.1: Energy-band diagram for an ideal MIS diode on n-type semiconductor at 0 bias. [11, fig. 7.2] E_g: semiconductor band gap; d: insulator thickness; E_F: Fermi Level; E_i: intrinsic Fermi level; ψ_{Bn}: potential difference between E_F and E_i; ϕ_n: Fermi potential with respect to the conduction band edge; χ: semiconductor electron affinity; χ_i: insulator electron affinity; ϕ_m: metal work function.

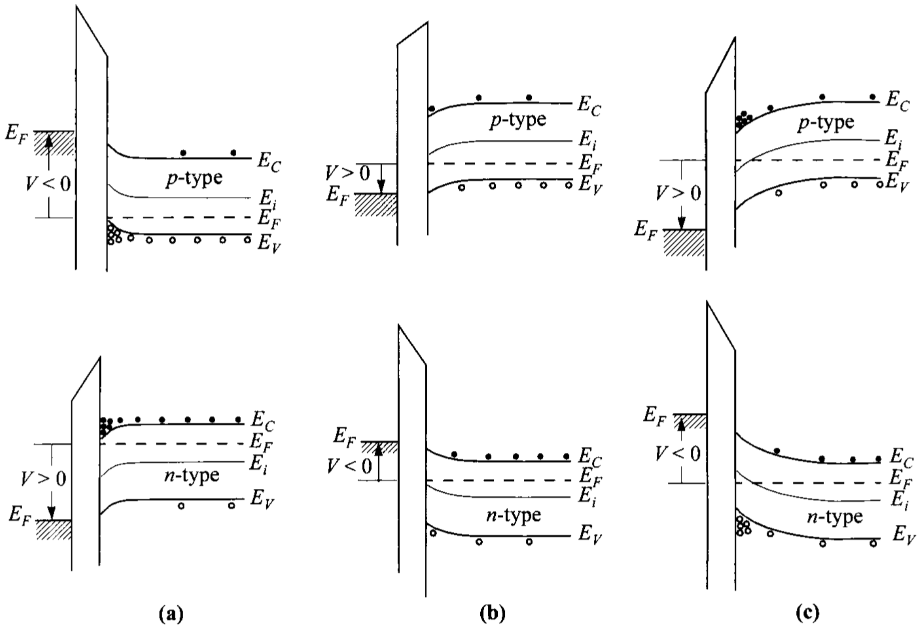

Figure 2.2: Energy-band diagram for ideal MIS diodes, n-type and p-type, with $V \neq 0$ [11, fig. 7.3]. (a) accumulation; (b) depletion; (c) inversion.

Figure 2.2 shows the influence of a biasing voltage V applied between the metal and the semiconductor. In the case of a n-type semiconductor, a positive voltage applied to the metal pulls the bands down, resulting in an accumulation of negative charge in a small volume below the surface. Similarly, a negative voltage applied to the metal in the case of a p-type semiconductor accumulates positive charge (Figure 2.2(a)). If the voltage polarity is reversed, the band bending changes direction, resulting in depletion at moderate voltages (Figure 2.2(b)), and inversion at higher bias (Figure 2.2(c)). In the inversion case, the density of minority carriers in the semiconductor becomes larger than the majority carriers, inverting the charge in the semiconductor in the region just below the surface.

The potential ψ inside the semiconductor can be obtained using the Poisson equation

$$\frac{d^2\psi}{dx^2} = \frac{-\rho(x)}{\epsilon_S} \tag{2.1}$$

where ϵ_S is the permittivity in the semiconductor, as long as the charge density ρ is known throughout the semiconductor.

2.3 Charges in a semiconductor

Several charge density contributions add up in the volume of a semiconductor. In the absence of interfaces or applied voltages, the sum of these will be 0 everywhere in the semiconductor. The position of the Fermi level E_F adjusts itself so as to satisfy this charge neutrality condition.

2.3.1 Density of ionized donors and acceptors

A semiconductor is doped with atoms that have the ability to become ionized — for n-type dopants, the atoms donate an electron, whereas p-type dopants accept an electron. Not all dopants become ionized however, so it is necessary to determine the proportion that will contribute to charge in the semiconductor. For instance, a typical electron donor will have an energy level E_D near the conduction band edge. The density of ionized donors N_D^+ is then given by the Fermi-Dirac probability of the level being occupied. In the case of silicon,

$$N_D^+ = \frac{N_D}{1 + 2\exp\left(\frac{E_F - E_D}{kT}\right)} \tag{2.2}$$

where N_D is the dopant density. The factor of 2 is due to spin degeneracy — the donor can accept an electron of spin up or down. Similarly, the density of ionized acceptors N_A^- is given by

$$N_A^- = \frac{N_A}{1 + 4\exp\left(\frac{E_A - E_F}{kT}\right)} \tag{2.3}$$

where N_A is the p-type dopant density, and E_A is that dopant's acceptor level, typically located near the valence band edge. The factor of 4 is due to the spin degeneracy and the valence band degeneracy in Si (at $\vec{k} = 0$).

2.3.2 Occupied states in the conduction band, unoccupied states in the valence band

Electrons are thermally activated around the Fermi level position in a distribution given by the Fermi-Dirac equation:

$$F(E) = \frac{1}{1 + \exp\left(\frac{E - E_F}{kT}\right)} \tag{2.4}$$

where E is the level of the state. The integral of this distribution for parabolic bands is given by:

$$F_{1/2}(\eta_f) \equiv \int_0^\infty \frac{\eta^{1/2} d\eta}{1 + \exp(\eta - \eta_f)} \tag{2.5}$$

where $\eta_f \equiv (E_F - E_C)/kT$. Finally, to obtain the density of occupied states, this integral is multiplied by the effective density of states in the conduction band N_C:

$$n = N_C \frac{2}{\sqrt{\pi}} F_{1/2}\left(\frac{E_F - E_C}{kT}\right) \tag{2.6}$$

where E_C is the position of the conduction band edge. Similarly, the density of holes at the top of the valence band is given by:

$$p = N_V \frac{2}{\sqrt{\pi}} F_{1/2}\left(\frac{E_V - E_F}{kT}\right) \tag{2.7}$$

where N_V is the effective density of states of the valence band, and E_V is the position of the valence band edge.

2.3.3 Total space charge in a semiconductor

The sum of these contributions to charge density in the semiconductor is thus:

$$\begin{aligned} \rho(x) = & \quad q\left(-n + p + N_D^+ - N_A^-\right) && (2.8)\\ \frac{\rho(x)}{q} = & \quad -N_C \frac{2}{\sqrt{\pi}} F_{1/2}\left(\frac{E_F - E_C}{kT}\right) + N_V \frac{2}{\sqrt{\pi}} F_{1/2}\left(\frac{E_V - E_F}{kT}\right) && (2.9)\\ & \quad + \frac{N_D}{1 + 2\exp\left(\frac{E_F - E_D}{kT}\right)} - \frac{N_A}{1 + 4\exp\left(\frac{E_A - E_F}{kT}\right)} \end{aligned}$$

in which it can be seen that the charge density in the semiconductor is entirely determined by the position of the Fermi level E_F. Note that these equations assume a small or no current flow — at higher currents, the speed of diffusion of carriers can become a limiting factor. In these situations, the Fermi level is no longer valid to describe charges in the semiconductor; it is sometimes replaced by two quasi-Fermi levels (for electrons and holes).

We define the potential in the semiconductor ψ as the difference between the actual Fermi level position and what its position would be in a flat-band condition. We therefore have, in theory, all the necessary parts to solve the one-dimensional Poisson equation $\frac{d^2\psi}{dx^2} = \frac{-\rho(x)}{\epsilon_S}$. These derivations are detailed in Sze [11] and will not be reproduced here.

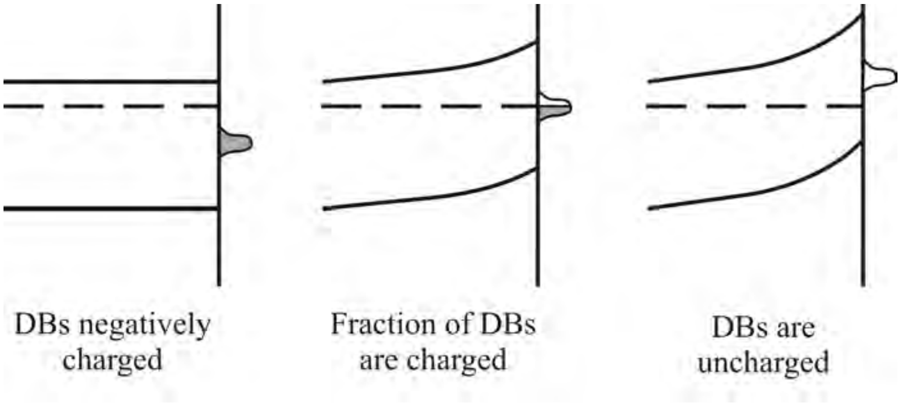

Figure 2.3: Energy-band diagram showing the charge state of dangling bonds on a n-type semiconductor for different band-bending situations. The fraction of DBs that are charged depends on the position of the Fermi level at the surface relative to the DB acceptor level, and the temperature.

2.3.4 Dangling Bonds on Si Surface

In the previous discussion we considered the surface of the semiconductor to be a passive interface which would simply follow the potential through vacuum and the semiconductor. Our typical surface of study, H-Si(100)-2×1, would indeed be passive if hydrogen termination were complete. However, this is never the case – termination of the surface is normally incomplete, and the missing H atoms leave *dangling bonds* (DBs) on the underlying Si atoms.

Dangling bonds act as charge traps on the Si surface. Normally, a DB holds a single electron and is electrically neutral. However, they are able to accept an electron, with an acceptor level located roughly in the middle of the Si band gap [12, 13]. For instance, if the surface is neutral and the substrate is n-type, the Fermi level will be located above the DB acceptor level. This means that the DB will be able to accept an electron, and will become doubly occupied, with a net negative charge. The DB is also able to lose an electron – it has a donor level located a few tenths of an eV above the valence band edge.

As more and more DBs become charged, the surface will become charged negatively. This will bend the bands upward, moving the Fermi level closer to the DB level, as shown schematically in Figure 2.3. This tends to reduce the occupancy of DBs, therefore the potential will reach an equilibrium. Depending on the doping level, a larger or smaller fraction of the DBs on the surface acquire a charge. The surface charge σ is given by the Fermi-Dirac occupancy of both the donor and acceptor levels:

$$\sigma = \sigma_{DB}\left[\frac{1}{1+\exp\left(\frac{E_F-E_{D,DB}}{kT}\right)}-\frac{1}{1+\exp\left(\frac{E_{A,DB}-E_F}{kT}\right)}\right] \tag{2.10}$$

where σ_{DB} is the surface density of DBs, E_F is the Fermi level at the surface, $E_{D,DB}$ is the position of the DB donor level, and $E_{A,DB}$ is the position of the DB acceptor level.

2.4 Two-Dimensional Model

Our discussion so far used a simple, one-dimensional model consisting of a semi-infinite metal surface close to a semi-infinite semiconductor surface. This model is appropriate when dealing with semiconductor devices of relatively large dimensions; however we want to apply this theory to the case of a STM tip at tunneling distances to the silicon surface. A typical tungsten STM tip has a radius of curvature in the 10 nm range, small enough that it is comparable to the Debye length of the semiconductor. We therefore need to use a model that takes this size into account.

A full 3-dimensional treatment is not necessary, because we can take advantage of the fact that both the STM tip and sample have rotational symmetry. Using a 2D model greatly reduces the computation time. We define a simple geometry consisting of a spherical tip of radius r, forming the apex of the wire which has a shank angle θ. The end of the tip is at a distance d from the Si surface.

Our work expands on modeling performed by Feenstra [7]. In that work, the tip shape was assumed to be hyperbolic, allowing the use of a prolate spheroidal coordinate system to simplify calculations. We use a cylindrical coordinate system, allowing the construction of most any shape of tip if desired. Also, in our model, the dopant concentration and type can be made non-uniform within the bulk of the semiconductor. Finally, the Si surface is allowed to develop a non-uniform charge, the value of which depends on an arbitrary function of the Fermi-level at each r position. This makes it possible to model the presence of DBs on the surface by using equation 2.10. We model the surface charge density to be a smooth function representative of the average density of charged DBs, rather than model DBs as individual point charges.

This flexibility is obtained by using finite element methods to solve the Poisson equation:

$$\nabla^2\psi\left(z,\theta\right) = -\frac{\rho\left(z,\theta\right)}{\varepsilon} \tag{2.11}$$

in a two-dimensional model with cylindrical symmetry.

2.5 Finite Element Method

The finite element method (FEM) is a proven and flexible way to numerically solve partial differential equations (PDEs) such as the Poisson equation (2.11). PDEs are, in general, unsolvable analytically except for simple geometries. In FEM, the space of interest is divided in small, discrete areas called *finite elements*, and various mathematical techniques are used to attempt to satisfy the PDE in each of these elements.

In our work, we used the commercial software package COMSOL Multiphysics 3.0 [14], formerly called FEMLAB, to define our problem and solve Poisson's equation in it. For efficiency and reproducibility, we used Matlab to call FEMLAB routines. A Matlab program was written that would perform all of the necessary steps for defining and solving the problem, as well as analyzing the resulting data.

2.5.1 Defining Geometry

The first step in modeling is to define the geometry of the system. FEMLAB provides a graphical user interface for this purpose; however, we used Matlab functions to define it programmatically. As mentioned, the model will be two-dimensional with rotational symmetry. The tip is drawn as a hemispherical tip with a straight shank. The apex of the tip is a small distance from the flat surface of the semiconductor. The parameters defined and used to draw the geometry are listed in Table 2.1. The resulting geometry is drawn schematically in Figure 2.4.

Parameter	**Symbol**	**Typical Value**
Tip radius	a	20 nm
Shank half-angle of the tip	θ	45 degrees
Tip distance to semiconductor	d	5 Å
Height of modeled area above surface	H	300 nm
Semiconductor thickness	t_{semi}	500 nm
Width of modeled semiconductor area	w	500 nm

Table 2.1: Typical parameters used for FEM geometry.

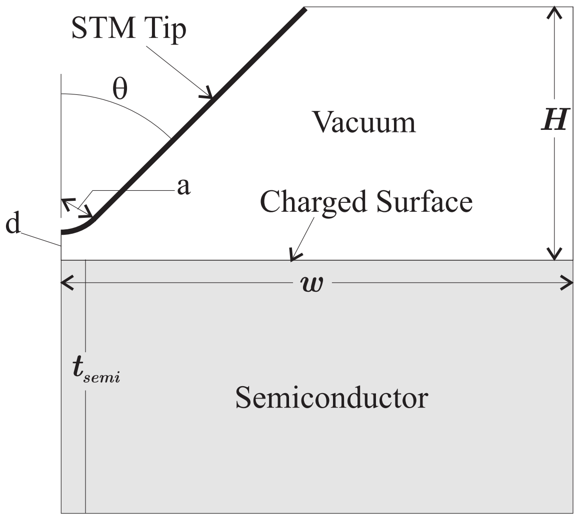

Figure 2.4: Geometry of the FEMLAB model.

2.5.2 Specifying Physics

We use FEMLAB's Electrostatics module in 2D-Axial Symmetry mode to define our problem. This model does not include the effect of currents flowing through the semiconductor. For large currents, the spreading resistance and corresponding voltage drop in the semiconductor could be significant. Modeling a transistor or diode, for example, would be inaccurate without taking into account the effect of current. However, it is easily ignored in the case of a tip in tunneling, where the current is usually below 1 nA.

2.5.3 Defining Subdomains

Subdomains are distinct volumes in the model — given our use of rotational symmetry, those volumes are represented as surfaces. There are two subdomains in this model: vacuum and the semiconductor (the metal tip is not treated as a volume, as we will see in Section 2.5.4). The Poisson equation modeled in the subdomain is given in slightly different form than previously:

$$-\nabla \cdot \epsilon_0 \epsilon_r \nabla V = \rho \tag{2.12}$$

where V is the electrostatic potential at each point in space. A grounded plane (in this case, the back of the semiconductor) will be at $V = 0$.

ϵ_r is the relative permittivity (or dielectric constant) of the material — we used a value of 1 for the vacuum subdomain and 12 for the silicon subdomain. These are constants throughout each subdomain.

The value of ρ corresponds to the charge density in the semiconductor. This is set to identically 0 in the vacuum subdomain. In the semiconductor, we instruct FEMLAB to call a Matlab function (f_ChargeDensity.m) to calculate numerically what the charge density in the semiconductor should be. This function uses Equation 2.9 to calculate the charge. At this point it is important to define V clearly. Equation 2.9 uses the Fermi level E_f; in the semiconductor relative to the vacuum level, V is defined so that the *difference* between the E_f at that point versus E_{f0}, which is the Fermi level at the back contact of the semiconductor. Therefore, $E_f = E_{f0} + V$. This value of E_{f0} is solely calculated from the doping value of the silicon. In a zero-current situation, we normally draw the Fermi level as being flat, and the semiconductor bands bend as determined by the value of V. When $V(z) > 0$ the bends are bent *down*, and for $V(z) < 0$ the bends are bent *up*.

Our model also allows for variations in doping concentration along the depth profile of the semiconductor. For example, a surface layer of silicon might have seen its dopants passivated by the hydrogen termination process, resulting in an effectively lower doped surface layer on a high-doped substrate. The calculated charge in the semiconductor will reflect the change in the Fermi level caused by this dopant profile. For simplicity, in the calculations presented here, we kept a uniform dopant concentration.

2.5.4 Defining Boundaries

Boundaries are the edges of the subdomains; they are 1-dimensional in our 2-D model, but represent surfaces in the real world. There are several distinct boundaries in the problem geometry, and each one has its own relevant boundary condition that must be set in order for Poisson's equation to be solved correctly:

The STM tip surface is a Dirichlet boundary condition — a fixed potential $V = V_{bias}$ corresponding to the STM tip bias.

The back of the semiconductor is also a Dirichlet boundary condition, here set to ground, or $V = 0$. Note that since the potentials are relative, it is equivalent to biasing the sample at $V = -V_{bias}$ with the tip at ground, which is frequently the configuration in STM. In reality, it is commonly the far edges of the semiconductor that are biased — however given the large distance (several millimeters) between the tip and the sample bias contact, it is a good approximation to model the back of the semiconductor as the biased surface. The thickness of the semiconductor was chosen to be several times larger than the Debye length for the lowest-doped material to be modeled.

The edges of defined space, such as the exterior edge of defined Si and the vacuum edges, are defined as electric insulators, where $\vec{n} \cdot \vec{D} = 0$, i.e. no electric field component perpendicular to the surface. This approximates an infinite extent of the material, which is a reasonable approximation as long as the modeled volume is large enough that the semiconductor is approximately neutral at the edges.

The surface of the semiconductor uses the surface charge boundary condition. This is given by Equation 2.10, using $E_f = E_{f0} + V$. During solving, a matlab callback function is used to numerically calculate the charge at any point of the surface.

2.5.5 Defining Points

Points are zero-dimensional objects that occur at the intersection of vertices; they can also be added manually. In FEMLAB's electrostatics modeling, points can hold a charge Q. In our model, we do not explicitly set the charge at any point, therefore the value was set to $Q = 0$ for every point.

2.5.6 Meshing

The division of continuous space into discrete elements is called *meshing*. There are numerous ways to mesh space, with the best choice depending on the problem to be solved. A simply geometry could use square mesh elements, for example, whereas some cases might require curvilinear shapes; FEMLAB uses triangular mesh elements, which is the most common way to divide space.

The size of each mesh element is a critical factor in obtaining a reliable result from FEM. The goal is that each element approximates the potential to as high an accuracy as possible. The potential in one element is not normally assumed to be constant — a linear or polynomial interpolation between neighboring elements is used to provide a more accurate description. For slowly-varying fields it will be sufficient to use large elements, but high gradients or areas with a sharp radius of curvature will require much smaller mesh elements.

Reducing the mesh size leads to significant increases in performance — solving time increases polynomially with the number of mesh elements. One major way to reduce the mesh size is to use symmetry. As mentioned previously, we are using axial symmetry, which greatly reduces the number of mesh elements required. A full 3D model of the same problem would quickly run into memory limitations if run on a single computer.

FEMLAB performs excellent meshing automatically, with more elements being generated in regions with small dimensions — for instance, the gap between the STM tip and the Si surface in our simulations. The number of mesh elements increases greatly if there is a large disparity between the size of the whole system and its smallest dimension; this can make the calculation time unmanageable.

FEMLAB offers many settings to set constraints on automatic meshing — for instance, one can specify the maximum or minimum mesh element size near a boundary or point; or specify the rate of increase of mesh size when moving away from a small dimension. In our case, the default FEMLAB options were found to be sufficient. In most cases, the mesh was made more precise by using the *Refine Mesh* command once. This subdivides each element into approximately 4 smaller mesh elements. Since further mesh refinement was not found to change the results significantly, we opted for these meshing parameters.

2.5.7 Solving

FEMLAB can solve problems in a variety of manners. The simplest solver that can be used is the *stationary linear solver*. Only simple problems can be solved using the linear solver — for example, field lines between two plates of a capacitor. Such problems, where the material properties are assumed to not depend on field, potential or charge, can be solved readily with a linear solver.

Our model, however, is not linear. This can be seen in the relevant equations such as Equation 2.9 for the charge density in the semiconductor and Equation 2.10 for the surface charge: both of these charges depend on the position of the Fermi level, i.e. the electrostatic potential. Since the potential calculated by the solver depends on the charge in the semiconductor and on its surface, the two values are coupled and must be solved in a non-linear way. Therefore, we used the *stationary non-linear solver* option in FEMLAB to solve our model.

Given the exponential dependence of charge density on the potential, our problem is highly non-linear. This can cause problems in getting the solver to converge. We selected the *highly non-linear problem* option, which makes the solver use smaller steps to avoid problems when solving. By trial and error, the damping parameters (such as the maximum step change and minimum step size) were tuned to allow the solution to converge successfully. The details of the algorithms used by the FEMLAB solver are beyond the scope of this work.

2.6 Results of Modeling

The main goal of this model was to answer questions posed while writing Piva et al. [15], wherein we describe a proof of concept of a single-molecule transistor, gated by a single charge on a dangling bond. The samples used were highly doped n-type silicon, and we expected DBs on their surface to be negatively charged. The STM images confirming the transistor-like effect were taken with a negatively biased tip, which might have repelled the electron charging the DBs in some conditions. It was thus important to ensure that the expected charge of the DBs were not altered by the imaging process.

2.6.1 Test Cases in the Absence of a Tip

A useful test case is the surface in the absence of a tip. To model this situation, we used the same code and geometry used to model the case with a tip — however, the tip-sample distance was increased (e.g. to 250 nm) so as to keep the mesh size convenient. Additionally, the boundary condition for the tip surface was changed from a fixed voltage to electric insulation. To increase the speed of calculations, the area modeled was made narrower. For improved accuracy near the surface, FEMLAB was instructed to use a maximum mesh element size of 1 nm at the Si-vacuum interface.

High-doped n-type

The first sample studied was high n-type Si, doped with arsenic to a resistivity of 3-4 mΩ-cm. This corresponds to a dopant concentration of 2×10^{19} cm^{-3}.

If we specify that the surface does not have any DBs, then the calculation is trivial: the semiconductor is simply at ground throughout. If there are some DBs, however, those sites are able to accept charge and will induce band-bending near the surface. Figure 2.5(a) shows the band-bending that occurs in a high-doped, n-type semiconductor with a typical DB concentration of 8×10^{11} DBs/cm^2 — which corresponds to 50 DBs in one 80x80 nm scan window. The Fermi level is above the acceptor level, therefore 100 % of the DBs are quickly charged. The resulting charge density is small, giving a very modest band-bending of only 18 mV. Figure 2.5(b) shows the same situation with a fully clean, hydrogen-free surface. In this case, the very large number of acceptors requires significant band-bending of 0.62 V.

We see that the potential drops in the semiconductor over a short distance of a little more than 5 nm. We can compare this to analytical calculations of the

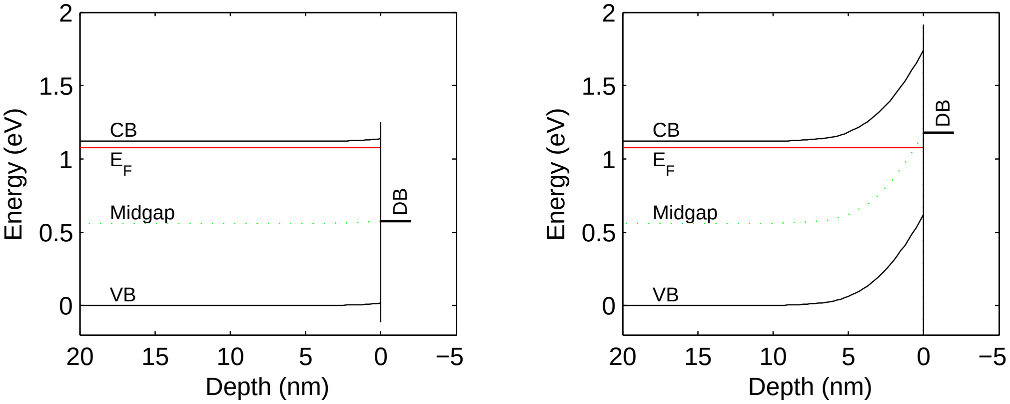

(a) A moderate DB concentration (8×10^{11} DBs/cm^2) results in band bending of 18 mV. 100% of DBs are charged.

(b) A clean surface (7×10^{14} DBs/cm^2) results in band bending of 0.62 V. 1.8% of DBs are charged.

Figure 2.5: Band bending diagrams for high-doped n-type (2×10^{19} cm^{-3}) Si, in the absence of a STM tip, with varying surface DB density.

depletion-layer width of an abrupt junction [11]. First we calculate the Debye length analytically as shown in Equation 2.13:

$$L_D = \sqrt{\frac{\epsilon_s}{q N_B \beta}} \tag{2.13}$$

where $\beta = q/kT$ and L_D is the Debye length. The relationship between the Debye length and the depletion-layer width W at a junction is as follows:

$$W = L_D \sqrt{2\left(\beta V_{bi} - 2\right)} \tag{2.14}$$

where V_{bi} is the built-in voltage at the junction — in our case, the amount of band-bending at the surface. β is approximately 39.6 V^{-1} at room temperature. In the case of the clean, high-doped surface, we obtain a Debye length of $L_D = 0.9$ nm; for our band-bending of 0.62 V, we obtain a depletion-layer width $W = 6.1$ nm, which is in excellent agreement with the results of the simulation as seen in Figure 2.5(b).

Low-doped n-type

The same calculations were performed in the case of a low-doped n-type crystal, with a dopant concentration of 1×10^{16} cm^{-3}. Figure 2.6(a) shows the result with a low concentration of DBs, and Figure 2.6(b) shows a clean surface.

Using the measured band-bending, we can again calculate the expected depletion

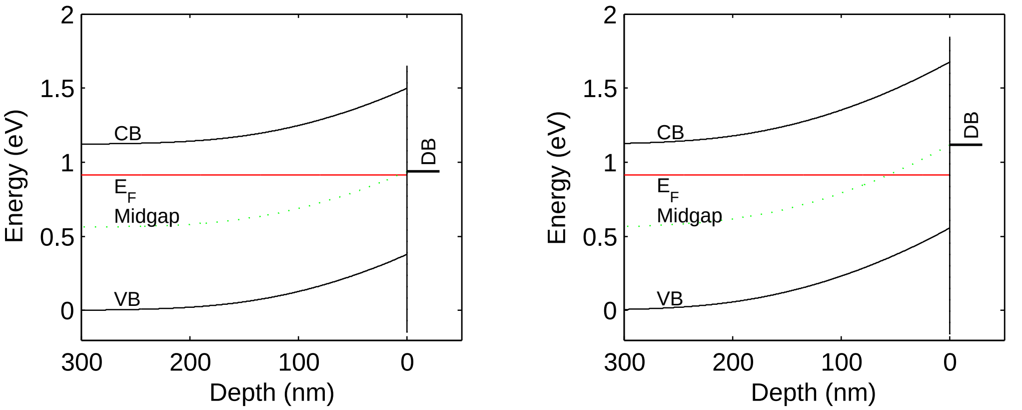

(a) A moderate DB concentration (8×10^{11} DBs/cm^2) results in band bending of 0.38 V. 27.1% of DBs are charged.

(b) A clean surface (7×10^{14} DBs/cm^2) results in band bending of 0.56 V. 0.04% of DBs are charged.

Figure 2.6: Band bending diagrams for low-doped n-type (1×10^{16} cm^{-3}) Si, in the absence of a STM tip, with varying surface DB density.

layer widths using Equation 2.14: for Figure 2.6(a) we get $W = 209$ nm; for Figure 2.6(b) we get $W = 259$ nm. The correspondence between the analytical result and our calculation is again quite good.

Conclusions

We can conclude from this set of calculations that the dopant concentration will have a significant impact on the charging of surface dangling bonds. The key difference between high and low-doped crystals is that a semiconductor with a high dopant density is much more effective at screening the electric field from a surface charge. If the dopant concentration is low, the field from the surface charge will require many hundreds of nm to be screened. In the absence of any other charge, the field from a uniformly charged surface is constant throughout space. Therefore, if it is screened over a long distance, the potential built up by this field ($V \approx W \times E$) is very high. As the bands bend up, this equilibrates with the Fermi-Dirac occupation probability of the dangling bond acceptor site. For a low-doped crystal, it only takes a very small percentage of charge on dangling bonds to build up this potential. A high-doped crystal sees the surface charge field screened over a very short distance, and so if there are only a few DBs on the surface, they will become charged easily and only slightly bend the bands.

2.6.2 Effect of the STM Tip

Next, we introduce a biased STM tip so as to model the imaging conditions described in Piva et al. [15]. The first situation described in that work is scanning a high-doped, n-type crystal, at positive and negative sample bias, with a moderate concentration of surface DBs. We need to confirm that on sufficiently high-doped Si, DBs will remain negatively charged at all the imaging conditions used.

First is the case of imaging with a positive tip (or negative sample bias, occupied state imaging), as shown in Figure 2.7(a). This potential attracts electrons to the surface, and the bands are bent down. Since DBs were already fully charged in the absence of a tip, this potential does not affect their charge level further.

With a negative tip (unoccupied state imaging), the situation is less clear before calculations. The negative tip will repel electrons, and so could reduce the charge in DBs. Figure 2.7(b) shows the result for a tip at -2 V, with a DB concentration of 8×10^{11} cm^{-2}. The bands are bent up, but not sufficiently to affect the charge. The Fermi level is still well above the DB level, and so 100% of DBs remain charged. In this experiment, we used very highly doped n-type, and so the excess negative charge in the crystal is so great that under normal imaging conditions, it is not possible to discharge the DBs. A lower-doped sample would respond differently; alternatively, using voltages much lower than -2.0 V could discharge DBs, though it is usually not possible to STM silicon at such harsh voltages.

This model is entirely static: there is no allowance for the effects of current flowing in the semiconductor, which may have an effect in some situations.

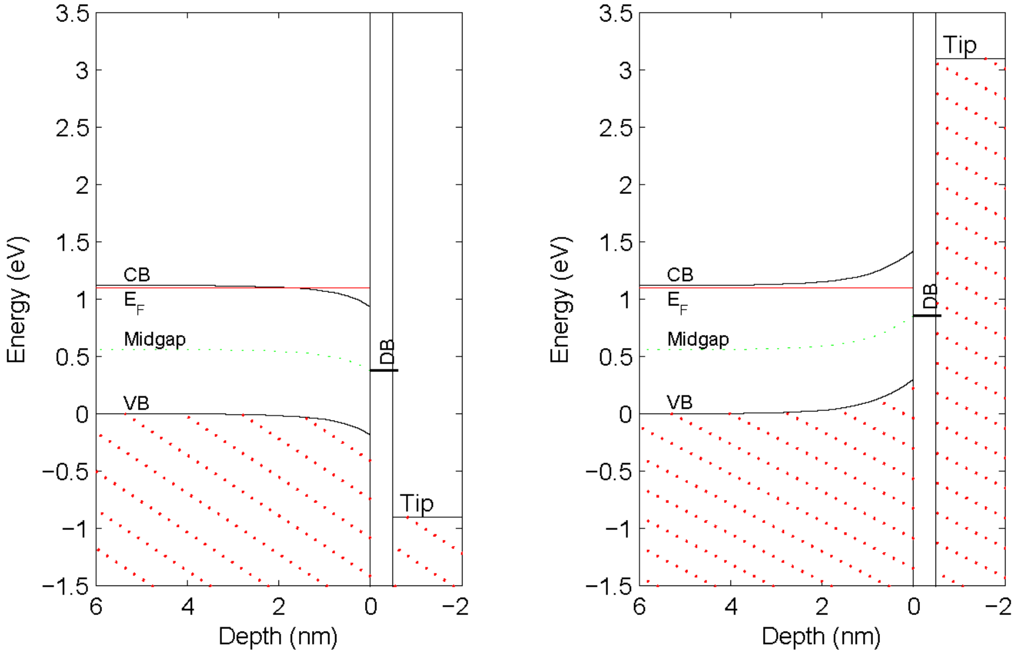

(a) With the tip biased at +2.0 volts, band bending is 0.19 V down, and 100% of DBs are charged.

(b) With the tip biased at −2.0 volts, band bending is 0.30 V up, while DBs remain 100% charged.

Figure 2.7: Band bending diagrams along the tip axis for high-doped n-type (9.6×10^{16} cm^{-3}) Si, with a STM tip 5 Å away from the surface; DB density is 8×10^{11} cm^{-2}; tip potential varies.

2.6.3 Lateral Extent of Tip-Induced Band-Bending

Also of interest is how far laterally band-bending extends near the tip apex. While tunneling occurs from a single atom, the electrostatic field has an effect over a much larger area, and this is something to take into account when investigating charging on surfaces.

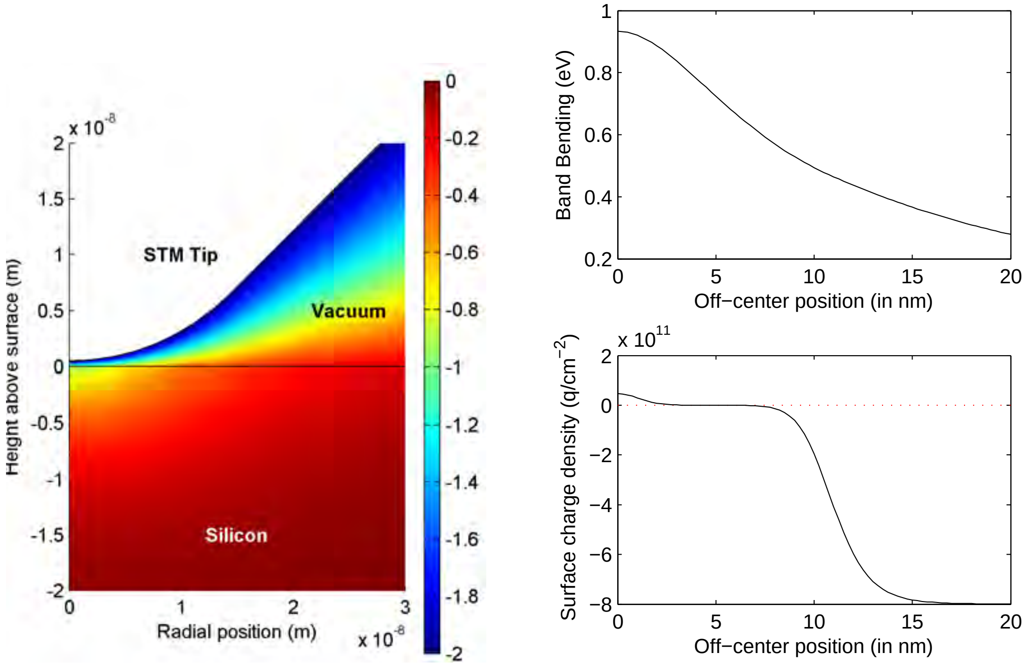

(a) Potential plot of a radial cross-section of the Si surface and vacuum above. Band bending in eV is equal to negative the potential, as indicated by the color bar.

(b) Top: Lateral band bending at the Si surface, going away from the tip apex. Bottom: Corresponding surface charge density.

Figure 2.8: Lateral extent of tip-induced band bending for medium-doped (10^{-18} cm^{-3}) n-type silicon. STM tip radius is 20 nm, biased at −2.0 V, 5 Å from the surface. DB density is 8×10^{11} cm^{-2}.

Figure 2.8(a) shows a color map of the potential in the semiconductor and nearby vacuum. The electric field from the biased tip penetrates in the material as it does in all dielectrics — however, charge redistribution shields some of this field penetration. It is clearly seen that the tip-induced band-bending is at a maximum just below the apex of the tip, where the field is maximum. As one moves away from the apex, the surface band-bending diminishes, as shown in Figure 2.8(b) (top). The lower plot shows the charge density due to charged DBs under the tip. Far from the tip, all available DBs are charged, resulting in a charge of 8×10^{11} $e^{-}\mathrm{cm}^{-2}$. As we move closer to the tip apex, the surface bands are bent past the DB acceptor level, discharging them. A neutral surface charge is observed until the bands are bent so much that the DB donor level reaches the Fermi level, removing the remaining electron and thereby charging the DBs positively.

The same calculations were repeated for tip radii of 3, 10, 20 and 100 nm; the lateral distribution of band-bending induced by these different tips is shown in Figure 2.9. The results show that a broad tip not only broadens the lateral extent of tip-induced band-bending, but also deepens it — maximum band bending for a 100 nm-radius tip is 1.1 eV, versus 0.6 eV for a 3 nm-radius tip. This shows that the shape of the tip is very relevant to the real imaging conditions while acquiring a STM image, since the broadness of the tip determines how efficiently potential can penetrate within the semiconductor. The radius of the tip can be determined using, for example, field ion microscopy (FIM) — see Section 5.7.

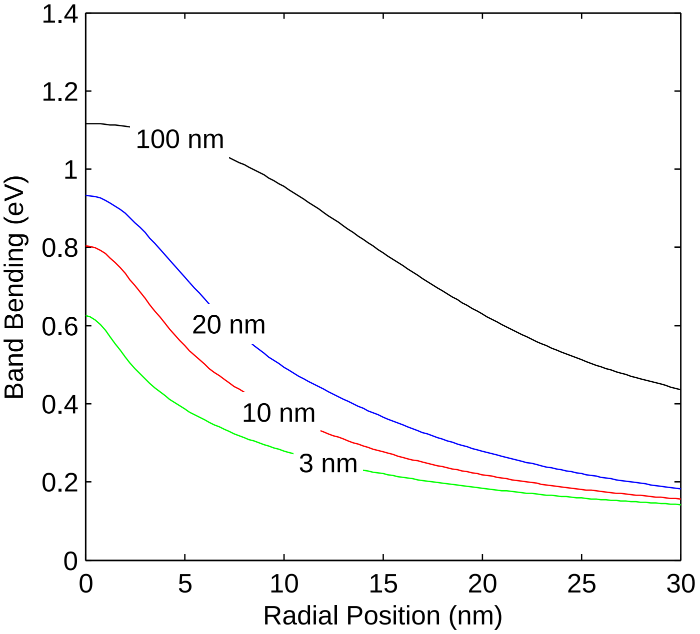

Figure 2.9: Comparison of lateral band bending for 4 different tip radii. Tip is biased at −2.0 V and is 5 Å from the surface.

2.7 Conclusion

We have presented the characteristics of a finite element method model that can be used to simulate the effect of a biased metallic tip near a semiconductor surface. Our model is quite flexible, allowing for different tip radii, spacings and geometry; non-uniform dopant concentration and type; and charge acceptor and donor levels on the surface. The main limitation of the model is the assumption of no current flow, but this is reasonable in most STM experiments, where less than a nA of current is normally used. The results of this work were used in Piva et al. [15] to confirm that the dangling bond charge level did not change during the STM experiments described therein.

Chapter 3

Molecular Line Growth

In this chapter, we describe the process of molecular line growth on hydrogen-terminated Si(100) surfaces. We review the various molecules that are known to grow lines. We then describe our experimental results of molecular line growth for a wide variety of compounds that we attempted, some which did grow lines (Section 3.2), and many which did not (Section 3.3). We go into more detail in describe the growth of trimethylene sulfide (Section 3.4), which shows different chemistry on silicon with different doping type. In Section 3.5, we show the first molecular lines forming contiguous "L-shapes". We describe in Section 3.6 how the growth of molecules in the butadiene family differs due to steric interactions. Finally, we present a cautionary note on the use of ion pumps with H-terminated surfaces in Section 3.7.

3.1 Introduction

Several years ago, Lopinski et al. [16] described a promising process in which a chain reaction allowed the formation of self-directed, linear structures of organic molecules on a hydrogen-terminated silicon surface. This process requires a single silicon dangling bond (DB) as a starting point. The molecule bonds to this DB, leaving an unpaired electron on an atom in the molecule, which becomes passivated by abstracting a nearby hydrogen atom. The new DB thus created acts as a point for the next molecule to react, allowing the reaction to proceed in a chain and form ordered linear structures. We will examine this growth process in more detail in Section 3.1.2.

This method of building molecular nanostructures is of interest for several reasons: first, it is self-directed, and many dozens of molecules can be built into a structure from a single starting point. Other methods of building such well defined structures using STM, for example work by Eigler et al. [17], require painstaking movement of individual atoms — a process much too slow for practical mass fabrication.

Second, since this growth process occurs on silicon, it is a gateway to introduce molecular functionality into very well known and heavily used silicon semiconductor fabrication processes. Such hybrid silicon-molecular devices could form an important technology.

Also, these self-directed structures are not limited to just one or a few candidate materials. In fact, a wide variety of organic molecules undergo this growth process — we will summarize these molecules in Section 3.1.3. The fact that many different compounds will show the same growth opens up the possibility of customizing functionality of lines — perhaps using some as active electronic devices, or chemical sensors, while others might be interconnects to form molecular-scale integrated circuits. Our own experiments, described in Section 3.2 and the following sections, have shown molecular nanostructure growth for many new molecules.

3.1.1 Hydrogen Termination of Si(100)

The self-directed growth of molecules on silicon starts with a hydrogen-terminated surface. The typical procedure to obtain H-Si(100)-2×1 is as follows [13]: a new crystal of Si (any doping level) is degassed for a few hours at a low temperature of around 600 C through direct current heating. This temperature preserves the protective natural oxide coating of the Si, yet still desorbs water and other contaminants from the sample holder. The sample is then flashed to 1200 C for 5 seconds to remove the oxide; several flashes are typically performed. Hydrogen gas, flowing through a tube with a liquid nitrogen cold trap, is introduced into the chamber through a variable leak valve at a pressure of 10^{-6} Torr. A tungsten filament, previously degassed, is heated to approximately 1800 C. The H_2 gas is cracked into atomic hydrogen by the heat of the filament. The sample is exposed to the atomic hydrogen for 2 minutes, then flashed to 1200 C, and then lowered to approximately 320 C. The exposure continues for 2 minutes, at which point both the filament and the heating are stopped simultaneously, and the H_2 gas flow is stopped.

Figure 3.1(a) shows a STM image of a typical H-Si(100)-2×1 surface obtained by the procedure described above. The dimer rows are visible as the bright rows; a schematic of a dimer row is shown in Figure 3.1(b). Three terraces are visible in this image; each terrace is one layer of Si atoms higher than the next (corresponding to a height difference of 1.4 Å). The direction of the dimer rows changes on each

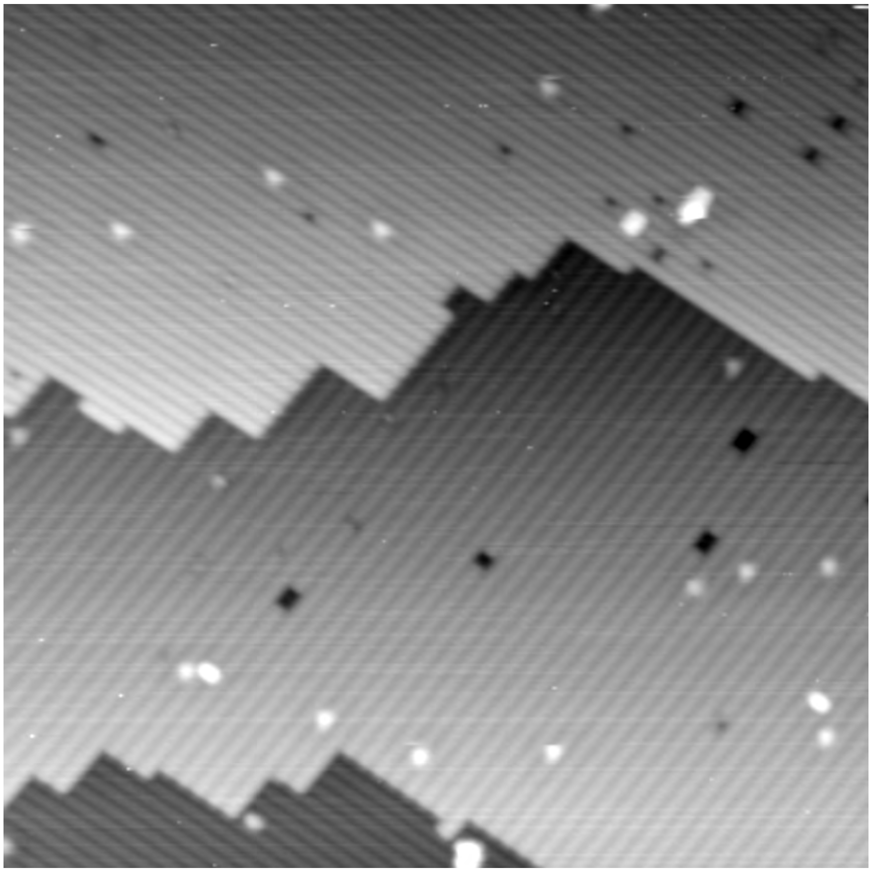

(a) STM image of a typical H-Si(100)-2×1 surface (30 nm wide, low-doped n-type, −3 V, 60 pA).

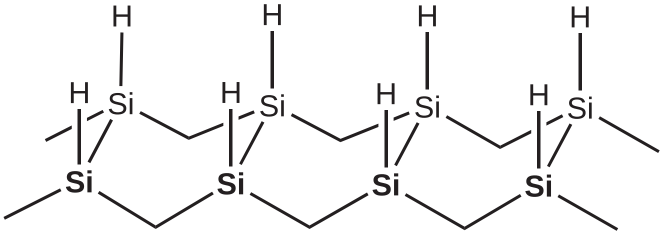

(b) Schematic of the H-Si(100)-2×1 surface.

Figure 3.1: The H-Si(100)-2×1 surface: STM image and schematic.

subsequent terrace of the 2×1 reconstruction. The bright white features correspond to silicon atoms where the hydrogen is missing, leaving a dangling bond (DB). The DB has electronic levels in the semiconductor band gap, giving more states to which electrons can tunnel. This increases the tunneling current flowing through it, making the DB appear higher than the surrounding hydrogen, despite being physically smaller. The dark spots are typically missing Si atoms on the surface or other defects.

3.1.2 Line Growth Process

A normal H-Si(100)-2×1 surface is almost entirely passivated with one H atom per surface Si atom. However, the termination process is never perfect, and a certain concentration of naturally occurring dangling bonds (DBs) remains. The DB is highly reactive — an alkene easily reacts with it, forming a Si-C single bond (see Figure 3.2). An intermediate species, with a carbon-centered radical on the second carbon, is formed. This radical is able to abstract hydrogen from a nearby site, leaving a new DB in its place. The remaining DB is able to react with another molecule, hence resulting in a chain reaction. This type of chain reaction of H-terminated Si was first described in 1994, in the case of liquid-phase chemistry on H-Si(111) [18].

Dosing of molecules is done in the gas phase, in the UHV chamber. The chemical is typically a liquid at room temperature. To purify it, we subject it to many freeze-thaw cycles: the liquid is frozen, then the gas above it is pumped out with a turbo pump. The frozen chemical is thawed, releasing dissolved gases and impurities in small bubbles. It is then frozen again, and the cycle repeats. If the vapor pressure of the liquid is sufficiently low, the chemical can be pumped as it thaws, for a more effective cleaning. This process pumps out any impurities with a higher vapor pressure than the chemical of interest. Any impurities with a *lower* vapor pressure will remain in liquid form when the desired chemical vaporizes; therefore, the vapor should be of a high purity.

Once the chemical is known to be clean, it is introduced into the UHV chamber through a variable leak valve. Dosing is typically done at a pressure of 10^{-6} Torr, as measured by the ion gauge. The dose is measured in Langmuirs (L), with 1 L equivalent to a dose of 10^{-6} Torr for 1 second. Note that the sensitivity of an ion gauge depends on the molecule dosed; in this work, we have not corrected the ion gauge reading to account for this effect.

Molecules known to grow rapidly can be dosed at lower pressures, e.g. 10^{-7} Torr for 10 seconds, simply to make the dose time more manageable. A typical dose for

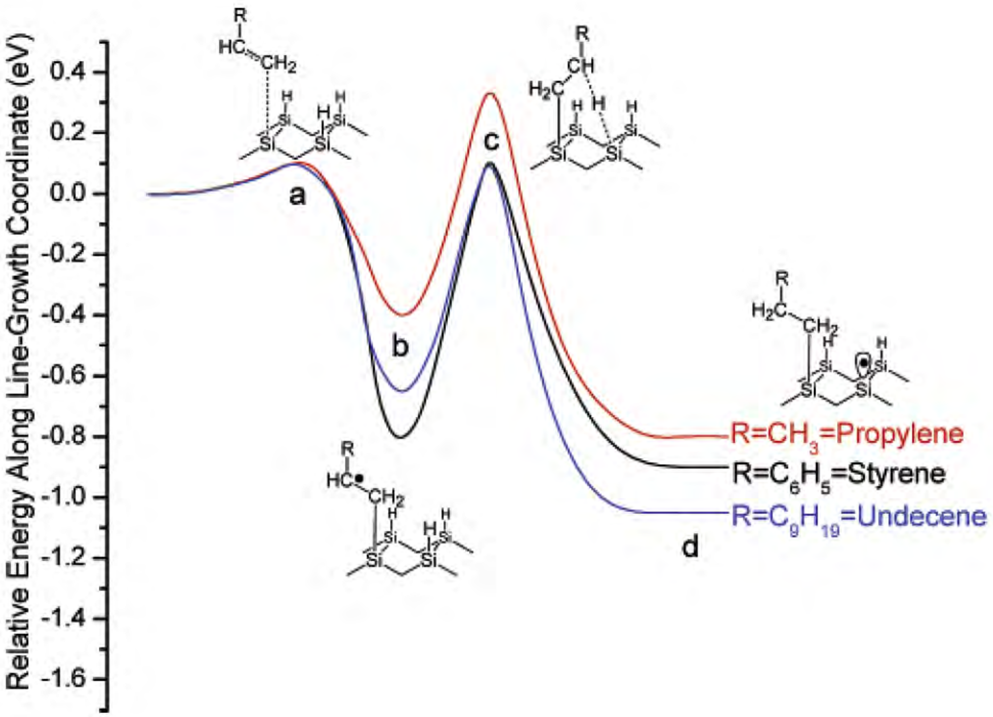

Figure 3.2: Schematic of the energy change in the line growth process. a) Transition state of the molecule addition and formation of a Si-C bond with the dangling bond. b) Addition product: formation of a carbon-centered radical. c) Barrier to the abstraction of a hydrogen atom from the neighboring dimer row. d) Final product: the molecule is stable and a new dangling bond can act as a site for the next reaction. From Ref. [19].

styrene is 10 Langmuirs, however compounds may require more or less of a dose to generate acceptable growth.

Dosing can be performed with the sample in any chamber, or in scanning position in the STM. If obtaining before and after STM images of dosing, we typically retract the tip by at least the full fine scanning range so as to avoid “shading” the surface with the tip. This may not be required, as line growth has been observed during scanning, when the tip was in tunneling to the surface.

3.1.3 Molecules Known to Grow Lines

Styrene was the first molecule to be shown to grow self-directed structures [16]. On H-Si(100)-2×1, growth is exclusively along dimer rows. On the H-Si(111)-1×1 surface, styrene was found to grow in a random-walk pattern [20]. On this surface, unlike 2×1, there is no energetic preference to growing in any particular direction. Finally, styrene on the H-Si(100)-3×1 surface has been shown [21] to grow exclusively *across* dimer rows.

Several styrene derivatives, such as **methyl styrene** [22], and **CF_3 or OCH_3 subsituted styrene** [23] also grow lines in the same manner as styrene. **2,4-dimethylstyrene** was also shown to grow lines [24].

Benzaldehyde and **acetaldehyde** were both found to grow lines on H-Si(100)-2×1 [25]. For these aldehydes, bonding to the silicon occurs through an oxygen atom rather than a carbon. Also, these molecules usually grow in double-width lines, with the molecule bonding to both silicons on each dimer.

Cyclopropyl methyl ketone (CPMK) was also shown to grow on silicon [26]. This molecule’s radical has a sufficiently long reach that allows abstraction of hydrogen from several sites. Thus, the growth of CPMK on H-Si(100)-2×1 follows a meandering path.

Vinylferrocene was shown to grow along dimer rows on H-Si(100)-2×1 [27]. Because of the large size of the ferrocene moiety, the molecules arrange themselves in a zig-zag pattern so as to reduce steric crowding. Ferrocene is of interest in several reactions (e.g. in redox reactions), therefore having a ferrocene unit attached to silicon could provide interesting chemistry on Si surfaces.

Linear alkanes were also found to grow lines on H-Si(100)-2×1 [19]. At room temperature, molecules smaller than 1-heptene (7 carbons) were found to not grow lines — but **1-octene** (8 carbons), **1-undecene** (11 carbons), and **1-tetradecene** (14 carbons) were all found to grow lines. The longer alkenes are able to grow lines thanks to an intermediate that is stabilized by dispersion interaction with the surface. More recent work showed that by dosing at low temperature (180 K), line growth of the smaller alkanes **1-hexene** and **1-heptene** was indeed possible [24].

Allyl mercaptan was found to grow exclusively across dimer rows on H-Si(100)-2×1 [28]. We were able to reproduce this result; however we found that random line growth was even more likely than perpendicular growth. Additionally, registered images did not normally show a starting DB where allyl mercaptan lines were found. This might indicate that line growth is affected by radicals created by the ion pump; similar effects were observed in the growth of butadiene (see Section 3.7).

Benzonitrile has been predicted theoretically to be able to grow lines on H-Si(100)-2×1 [29]. This molecule would bond through the carbon-nitrogen triple bond, and line growth would proceed in much the same way as with styrene; to our knowledge, this growth has not been confirmed experimentally.

Lines of **trimethylene sulfide** [30] will be discussed in Section 3.4; **butadiene** lines will be discussed in Section 3.6.

3.1.4 Molecules Reported Not To Grow Lines

Based on barrier height calculations [19], styrene's intermediate radical remains on the surface for ∼5 seconds before desorbing. This residence time is comparable to the time for hydrogen abstraction — therefore line growth can occur. By contrast, **Propylene** was found to adsorb but not grow lines [16], due to a very short residence time of the radical intermediate ($\sim 1\ \mu s$ at room temperature). This molecule will desorb before abstracting a H to contrinue line growth.

Vinyl cyclohexane was found to not grow lines on H-Si(100)-2×1 [19], due to the lack of radical delocalization that is present in the phenyl ring of styrene.

Hossain et al. [31] have reported that **allyl methyl sulfide** and **4-vinyl pyridine** do not show line growth. We have confirmed the lack of growth of 4-vinyl pyridine.

3.2 Line Growth Experiments

Motivated by the observation of cross-dimer row growth of allyl mercaptan [28], but its inability to form contiguous shapes with styrene for example, we set out to explore the growth of several other candidate molecules. We looked for molecules which, when in their radical state, were long enough to be able to abstract hydrogen from the next dimer row, but which were less likely to be able to abstract from the next dimer on the same row because of a lack of flexibility. The STM experiments were performed by the author and Dr. Stas Dogel; supporting calculations were performed by Dr. Gino DiLabio. This section describes molecules which showed some positive results; the following sections will detail interesting cases we found.

3.2.1 2-Allylphenol Line Growth

We expect that 2-allylphenol (Figure 3.3(a)) will grow lines in the same way as styrene. STM images of a typical H-Si(100)-2×1 surface dosed with 20 L of 2-allylphenol (Figure 3.3(b)) shows that the molecule grows in a random-walk pattern. The molecule appears to be able to abstract hydrogen from any number of neighboring sites, and growth is able to continue to form patterns similar to that of styrene dosed on H-Si(111)-1×1 [20].

Similar random-walk patterns were observed on high-doped n-type Si (Figure 3.3(c)). The only observable difference with this surface was that a much higher dose of 240 L was necessary to obtain similar line length. Finally, we attempted to grow lines of allylphenol on H-Si(100)-3×1, but without clear success. The STM image in Figure 3.3(d) shows some evidence of cross-row growth (like that of styrene on 3×1), but those examples were fairly rare.

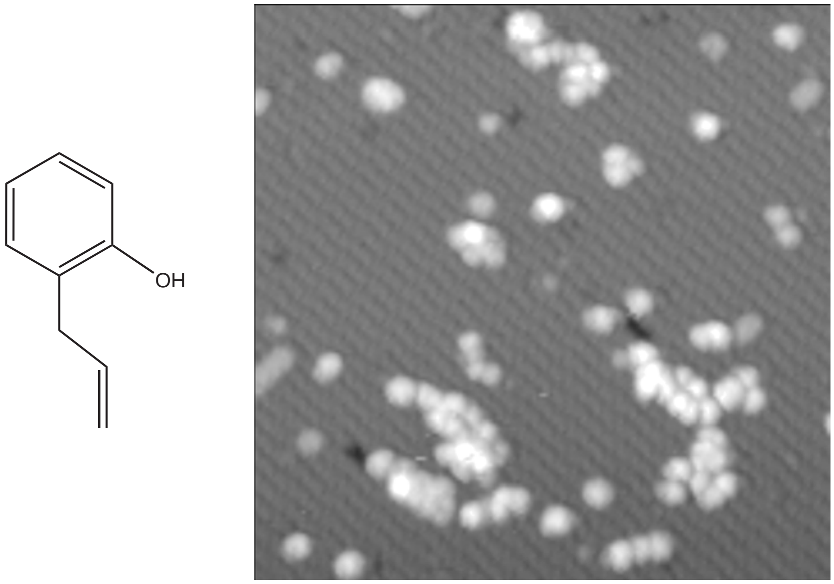

(a) 2-Allylphenol

(b) STM image (20×20 nm, −3.0 V, 0.06 nA) of 20 L of allylphenol dosed on medium p-type H-Si(100)-2×1.

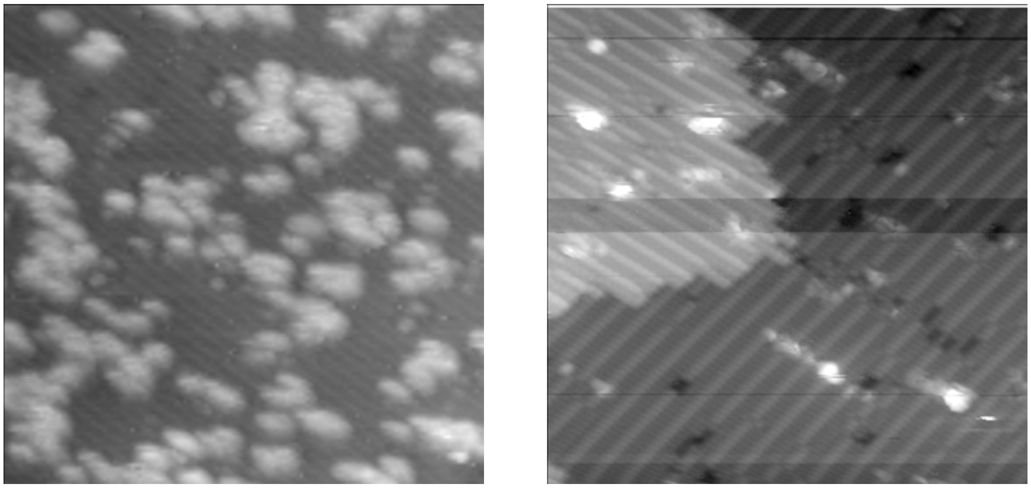

(c) STM image (20×20 nm, −2.0 V, 0.08 nA) of 240 L of allylphenol dosed on high n-type H-Si(100)-2×1.

(d) STM image (20×20 nm, −2.5 V, 0.08 nA) of 40 L of allylphenol dosed on medium n-type H-Si(100)-3×1.

Figure 3.3: Line growth of 2-allylphenol on 3 different surfaces.

3.2.2 2-Vinylnaphthalene Line Growth

The molecule 2-vinylnaphthalene (Figure 3.4(a)) is closely related to styrene, but contains a naphthalene unit (two fused benzene rings) rather than a single benzene. Given its similarity to styrene, we expect that it will grow lines in the same way.

Since 2-vinylnaphthalene is a solid at room temperature, dosing it requires special handling. Some molecules that are solid at room temperature, such as naphthalene or TEMPO, have a sufficiently high vapor pressure to allow dosing in the usual method. 2-vinylnaphthalene, however has a vapor pressure below 10^{-4} Torr at room temperature. We used a hot air gun to melt the solid (melting point of 63-67 C). Once liquid, 2-vinylnaphthalene has a vapor pressure of a few Torr, and can be dosed normally. To avoid condensation of the gaseous molecule on the inner walls of tubing, valves and gauges, the entire dosing line was wrapped in heating tape and heated to 120-150 C. Growth of 2-vinylnaphthalene was quite facile, with the molecule forming very long lines (see Figure 3.4) with good order.

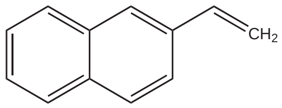

(a) 2-Vinylnaphthalene

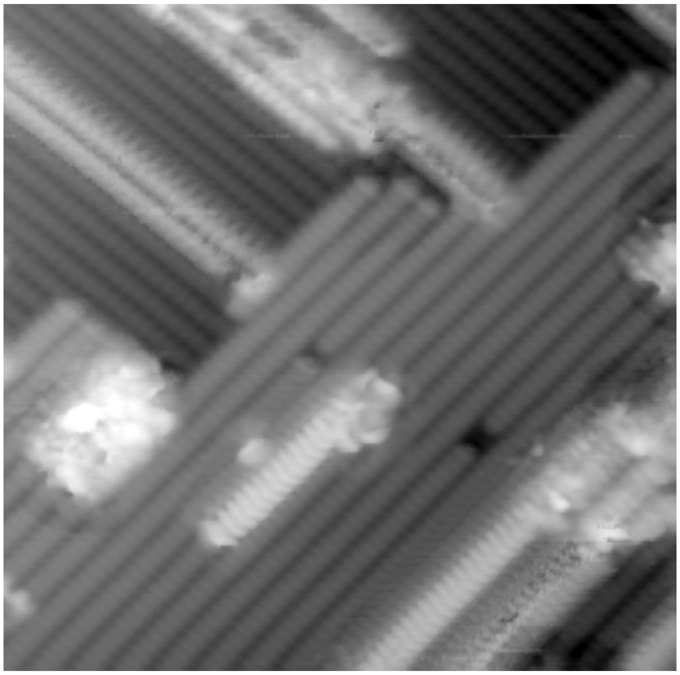

(b) STM image of lines of 2-Vinylnaphthalene (80 L dose on medium-doped n-type H-Si(100)-2×1, 15 nm wide, −2.5 V, 60 pA).

Figure 3.4: Growth of 2-vinylnaphthalene lines on H-Si(100)-2×1.

3.2.3 9-Vinylanthracene Line Growth

9-vinylanthracene (Figure 3.5(a)) is similar to vinylnaphthalene, except that the vinyl moiety is on a anthracene molecule (consisting of 3 fused benzene rings). Like 2-vinylnaphthalene, it is a solid at room temperature, with a melting point near 62 C. The molecule has to be dosed in the same way — by warming up the solid 9-vinylanthracene to its melting point, and keeping the molecular dosing line at a hotter temperature to avoid condensation. In addition, we found that keeping the sample at an elevated temperature (of approximately 100 C) through direct current heating (usually only 20-30 mA) seemed to help the deposition and line growth process, possibly by facilitating diffusion of molecules along the surface.

As can be seen in Figure 3.5(b), the molecule does form lines, however they are not as high-quality as in the case of 2-vinylnaphthalene. Only a few lines were found, with most growth occurring as more random clumps of molecules.

The molecules 9-vinylanthracene and 2-vinylnaphthalene were of interest for our project of light detection from the STM, described in Chapter 4. See Section 4.6 for a discussion of their use in that experiment.

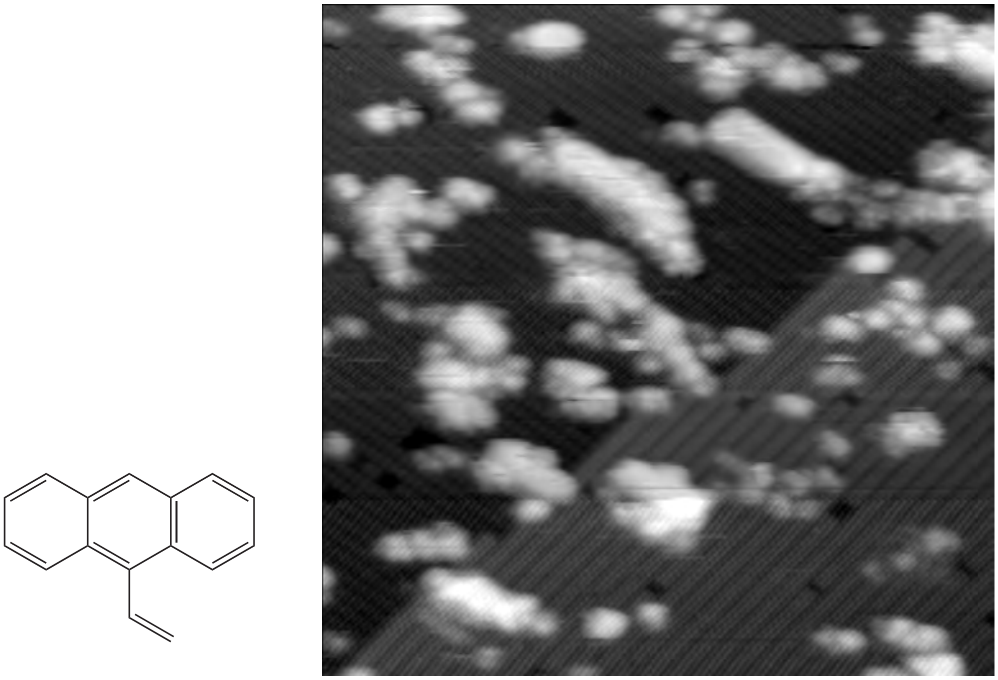

(a) 9-Vinylanthracene

(b) STM image of 9-Vinylanthracene lines (4 L dose on medium-doped n-type H-Si(100)-2×1, 25 nm wide image, −3 V, 100 pA).

Figure 3.5: Growth of 9-vinylanthracene lines on H-Si(100)-2×1.

3.2.4 1,3-cyclohexadiene Line Growth

Figure 3.6(b) shows the result of a 60 L dose of 1,3-cyclohexadiene (Figure 3.6(a)) on medium-doped n-type H-Si(100)-2×1. The molecular lines are quite short, and they appear unusual in that the molecules are not on adjacent dimer rows, but are separated by one (or sometimes two) dimers. We do not have an explanation as to what is the process by which this occurs — the position we would expect for the radical on the cyclohexadiene intermediate is far too short to be able to abstract a hydrogen two dimer rows away.

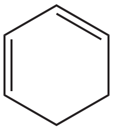

(a) 1,3-cyclohexadiene

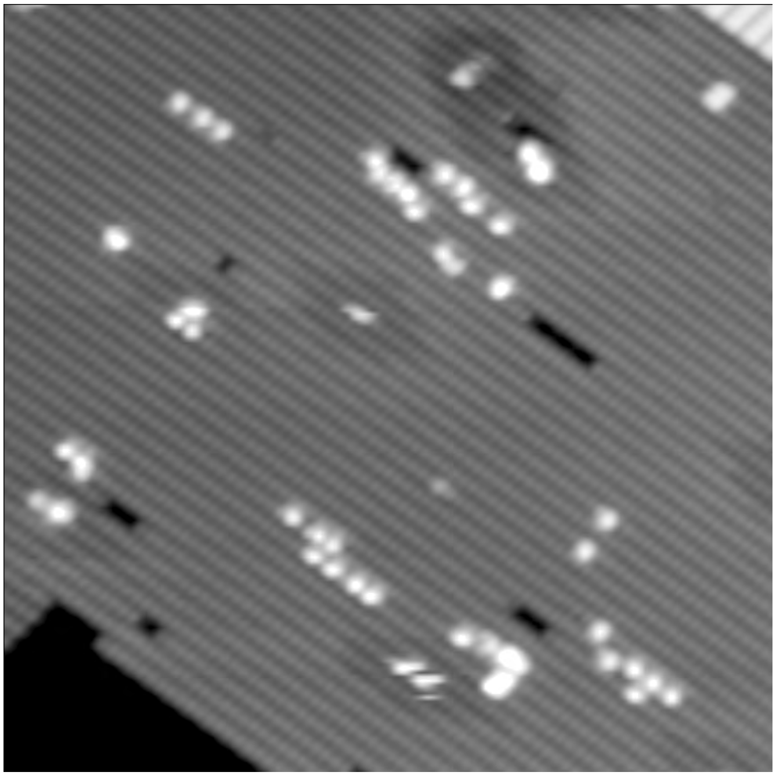

(b) STM image of 1,3-cyclohexadiene lines (60 L dose on medium-doped n-type H-Si(100)-2×1, 20 nm wide image, −2.7 V, 50 pA).

Figure 3.6: Growth of 1,3-cyclohexadiene lines on H-Si(100)-2×1.

3.3 Molecules Where Line Growth Did Not Occur

In addition, we attempted the growth of numerous molecules where the result was negative and no clear lines or structures were formed on the surface. Figure 3.7 summarizes those results by showing the structure of the molecule under test and describing the surface used as well as the dose performed. Because no growth features could be observed, STM images were omitted. Note that it cannot be excluded that some of these molecules will grow lines in different conditions.

The growth of 1,4-cyclohexadiene (Figure 3.7(a)) and cyclooctatetraene (Figure 3.7(b)) were attempted after we observed successful growth of 1,3-cyclohexadiene. The lack of radical delocalization in 1,4-cyclohexadiene is the likely explanation for the lack of growth of this molecule.

The following molecules also failed to show any growth: 4-vinyl-1-cyclohexene (Figure 3.7(c)), p-formotoluidide (Figure 3.7(d)). Again, the lack of radical delocalization in the cyclohexene moiety of 4-vinyl-1-cyclohexene is likely the cause of the failure of that molecule.

4-Vinylpyridine (Figure 3.7(e)) and 4-Pyridinecarboxaldehyde (Figure 3.7(f)) were attempted because a successful line of either of these molecules would have a nitrogen atom in the top position of the ring. It would then have been conceivable to perform post-line-growth modification of the lines using the nitrogen atom as a site for H-bonding. We speculate that these molecules bond to DBs preferentially through their nitrogen atom, making line growth impossible.

Allyl methyl sulfide (Figure 3.7(g)) showed evidence of bonding but not of line growth, despite a large dose of 600 L. This negative result supports the support growth model of allyl mercaptan, where an internal hydrogen transfer occurs from the SH group. The methyl in allyl methyl sulfide is too large to undergo this transfer, preventing line growth.

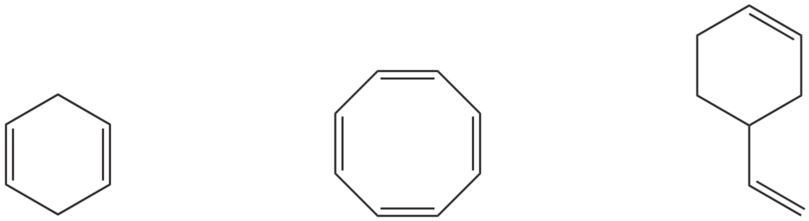

(a) 1,4-cyclohexadiene was dosed at 60 and 200 L on medium doped n-type H-Si(100)-2×1.

(b) Cyclooctatetraene was dosed at 60 L on medium doped n-type H-Si(100)-2×1.

(c) 4-vinyl-1-cyclohexene was dosed at 40 L on medium doped n-type H-Si(100)-2×1.

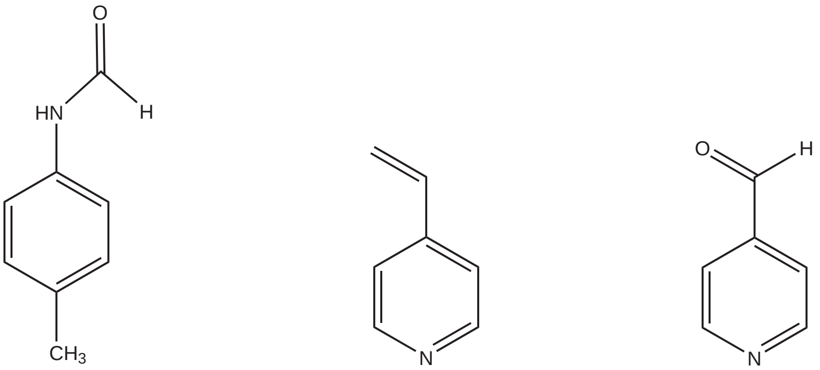

(d) p-formotoluidide was dosed at 30 to 40 L on medium doped n-type H-Si(100)-2×1.

(e) 4-Vinylpyridine was dosed at 80 L on high doped n-type, 500 L on low doped n-type, and 100 L on high-doped p-type H-Si(100)-2×1.

(f) 4-pyridinecarboxaldehyde was dosed at 300 L on medium doped n-type H-Si(100)-2×1.

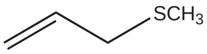

(g) Allyl methyl sulfide was dosed at 600 L on medium doped p-type H-Si(100)-2×1.

Figure 3.7: Molecules for which line growth was found to be unsuccessful.

3.4 Line Growth of Trimethylene Sulfide

Trimethylene sulfide (TMS) is a cyclical molecule of 3 carbons and one sulfur atom. It is able to grow lines through a ring-opening reaction similar to the case of the growth of CPMK [26]. A particularly unusual feature of this molecule is that it reacts differently to a dangling bond depending on the dopant of the Si crystal, as we will see in the following sections. The work in this section was published in Dogel et al. [30].

3.4.1 TMS on p-type medium doped H-Si(100)-2×1

Figure 3.8A shows a STM image of the result of a 200 L dose of TMS on medium-doped p-type H-Si(100)-2×1. Growth of TMS lines occurs at most DBs on the surface. Figure 3.8B highlights the double-line character of growth. It can be clearly seen from the STM images that TMS grows on two adjacent dimer rows, and not on both sites of a single dimer.

Growth Process

To help determine the likely growth process, calculations were performed by Gino DiLabio, using the Gaussian-03 suite of programs [32]. For details on the model settings, refer to [30]. Our proposed growth mechanism is shown in Figure 3.8C. Since the crystal was medium-doped p-type, we expect that dangling bonds on the surface should be uncharged. The first step in the reaction is a weakly stabilizing dative interaction between the neutral DB and a sulfur lone-pair of electrons from TMS. A Si-S covalent bond forms concurrently with the breaking of the S-C bond, which opens the ring of TMS. The linear structure obtained has a carbon-centered radical at the end of the chain. The overall reaction is exoergic by 18 kcal/mol.

Another possible reaction path for TMS would be the formation of a Si-C covalent bond — however calculations indicate that the barrier to this process would be of 16.1 kcal/mol. Therefore, on p-type the growth of TMS is strongly favored to occur via Si-S bonding.

Once the TMS has attached to the surface, it can in theory abstract hydrogen from several nearby sites. Given the maximum length of the radical of 4.2 Å, the possible abstraction sites are shown in Figure 3.9A. Calculations were performed to determine the barrier to abstraction from these sites. The most likely site, with a barrier of 2.6 kcal/mol, is the H on the next dimer row (site a). The next dimer in the same row (site n) offers an abstraction barrier of 2.9 kcal/mol and is the next most likely site. Abstraction from the same dimer (site s) has a barrier of 3.5

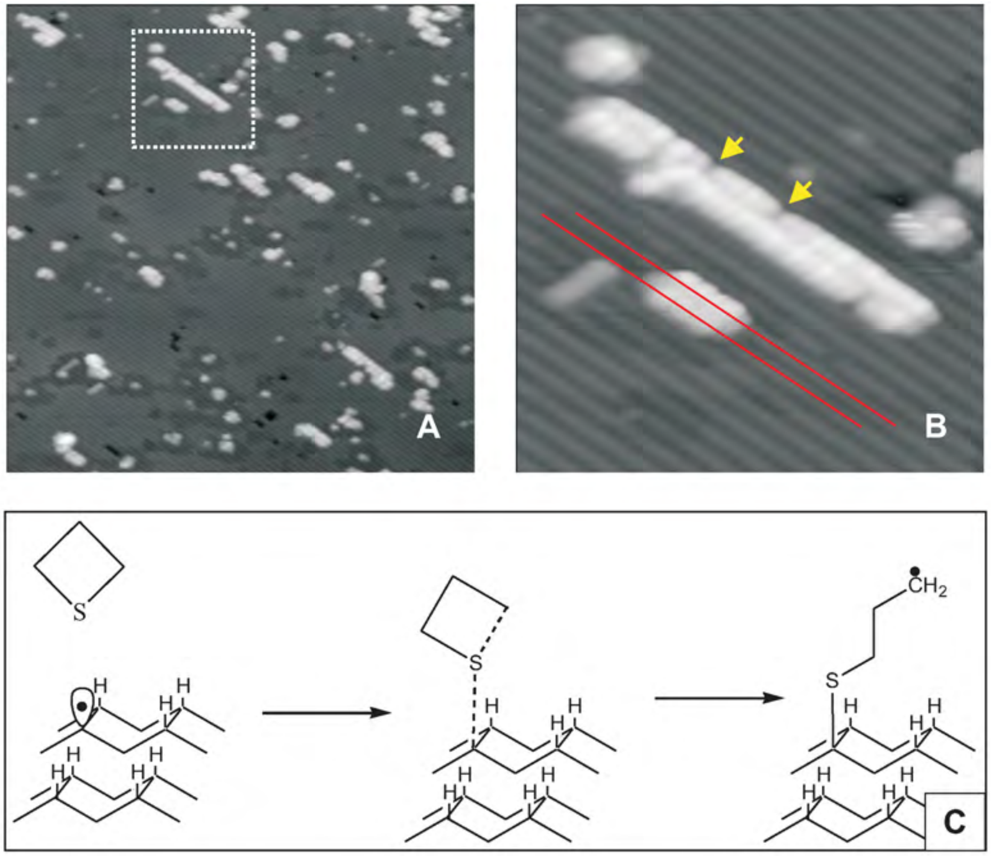

Figure 3.8: Growth of 200 L of TMS on medium doped p-type H-Si(100)-2×1. A) 50×50 nm STM image (−3.0 V, 0.06 nA). B) Close-up of one line, with lines indicating the center of 2 dimer rows. C) Reaction mechanism for the addition of TMS on p-type H-Si(100)-2×1. Taken from Figure 1 of [30].

kcal/mol but also requires overcoming a barrier to rotation and so is less likely to occur. Diagonal sites ds and dn have abstraction barriers of 8.4 and 8.9 kcal/mol respectively, making them much less likely to ever occur.

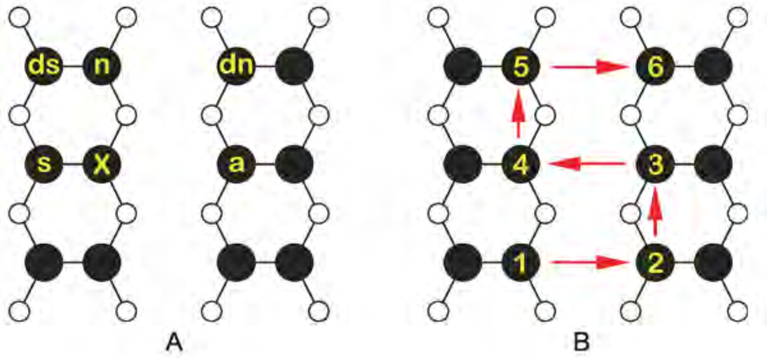

Figure 3.9: A) Possible abstraction sites of TMS. The molecule is placed in the spot labeled X, and the adjacent sites are labeled as shown. B) Schematic of growth process of TMS resulting in double lines on adjacent dimers. Taken from Figure 2 of [30].

Given these expected barriers, the double-line growth of TMS we observe in STM is consistent. The “square-wave” growth process we expect is shown in Figure 3.9B. In this process, the first abstraction occurs on the next dimer row. This new radical cannot abstract across the next dimer row since it is already occupied, and abstraction from the same dimer or the diagonal sites is much less likely. Therefore, it is left with only the possibility to abstract from the next dimer in the same row. That new radical is then most likely to abstract from the next dimer row, continuing the growth in a double-wide line. However, since the barriers between same-row and neighboring-row abstraction are very similar, it is possible for growth to continue along one row for a few molecules. This is observed experimentally in STM: Figure 3.8B highlights with arrows two gaps in the double line where this occurred.

High-resolution electron energy loss spectroscopy (HREELS) measurements on the TMS-covered surface of p-type H-Si(100)-2×1 were performed by Stas Dogel, and the results are shown in Figure 3.10. Two observations in the spectrum support our model of Si-S bonding. First, a Si-S stretching peak is expected at 500 cm^{-1}(labeled 7 in the figure). The 20% broadening of peak 6 (Si-H bending peak) is consistent with the presence of a real Si-S stretching peak. Additionally, if addition of TMS occurred in the alternative way of Si-C bonding, we would expect to see a S-H stretching peak near 2500 cm^{-1}. This peak is absent in the spectrum, also supporting our model of addition.

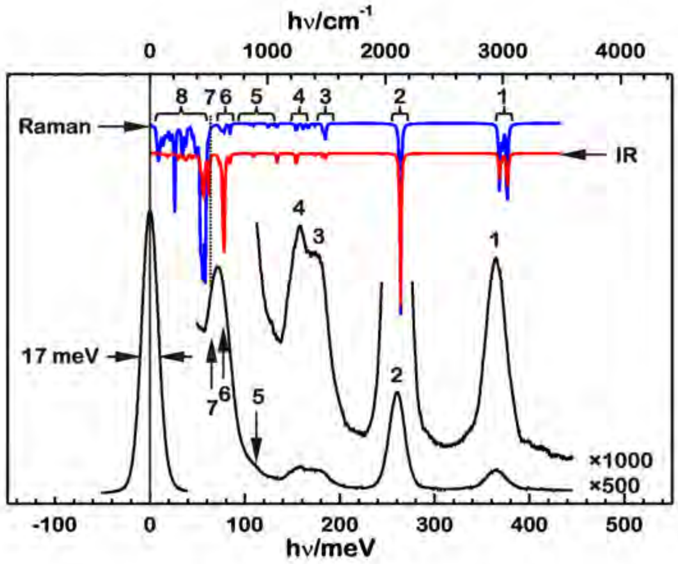

Figure 3.10: HREELS spectrum of 200 L of TMS on medium doped p-type H-Si(100)-2×1 taken at 110 K. Taken from Figure 3 of [30].

3.4.2 TMS on n-type medium doped H-Si(100)-2×1

We performed the same set of STM and HREELS measurements on a medium-doped n-type H-Si(100)-2×1 sample. The STM results, shown in Figure 3.11A and B, are very similar to those obtained on p-type. Growth of TMS also occurs in double lines on adjacent dimers.

There is however a significant difference in the DBs of the surface: for a normal, reasonably low DB concentration on medium-doped n-type H-Si(100)-2×1, we expect that most DBs will be negatively charged. This has a significant effect on the addition of TMS on the surface. Anion-lone-pair repulsion prevents addition of TMS through the S atom — calculations show that the approach of the S atom to the negatively charged DB is completely repulsive, and so the reaction cannot occur in this way. It is however possible for addition to occur through a carbon atom, forming a Si-C bond, as shown schematically in Figure 3.11C. Calculations indicate a barrier of 14.9 kcal/mol and an end product stable by 11.6 kcal/mol. We believe that the charge of the DB is pushed back into the bulk Si when addition occurs, and the radical molecule has one unpaired electron on the terminal S atom.

We can again calculate the barriers to abstraction for the neighboring sites shown in Figure 3.9A. As in the case of p-type H-Si(100)-2×1, we find that the dimer

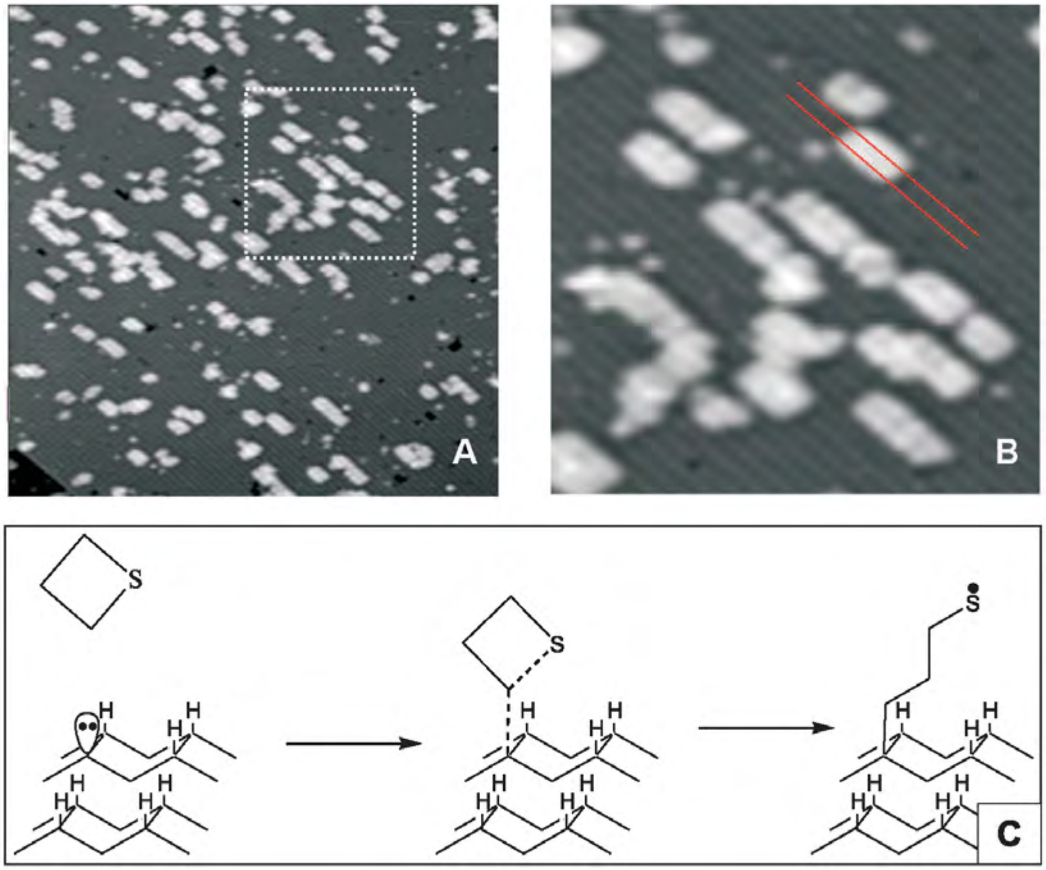

Figure 3.11: Growth of 80 L of TMS on n-type medium doped H-Si(100)-2×1. A) 50×50 nm STM image (−3.0 V, 0.05 nA). B) Close-up of a few lines, with lines indicating the center of 2 dimer rows. C) Reaction mechanism for the addition of TMS on n-type H-Si(100)-2×1. Taken from Figure 4 of [30].

immediately across the point of attachment (site a) is most likely to occur, with a barrier of 2.9 kcal/mol. The next most likely site is again the next dimer on the same row (site n), with a higher barrier of 4.1 kcal/mol. Abstraction from the same dimer (site s) is even less likely with a 5.6 kcal/mol barrier. Abstraction from the diagonal sites ds and dn have barriers of 7.5 and 13.4 kcal/mol respectively, therefore we do not expect them to occur. These barrier heights indicate that the same type of square-wave growth (shown in Figure 3.9B) that occurs on p-type H-Si(100)-2×1 should occur on n-type H-Si(100)-2×1.

Next we consider the results of HREELS measurements on this surface, shown in Figure 3.12. The relevant peaks are labeled 2 and 3. Peak 3, at 2523 cm^{-1}, is assigned to S-H stretching, which was calculated to be 2580 cm^{-1}. This stretching mode is expected in the final, reacted molecule, since the S radical reacts with H. Peak 2, near 2750 cm^{-1}, was observed only in presence of the TMS molecular lines and only on n-type Si, but we were not able to identify the molecular vibration that would explain it.

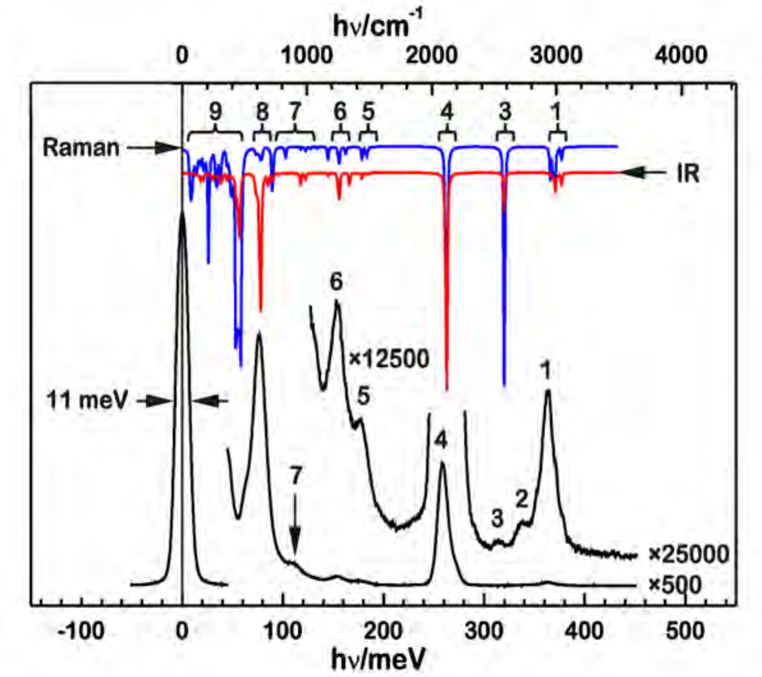

Figure 3.12: HREELS spectrum of 180 L of TMS on medium doped n-type H-Si(100)-2×1 taken at 130 K. Taken from Figure 5 of [30].

3.4.3 Dopant-Mediated Chemistry

The combined picture obtained from STM, HREELS and calculations of TMS growth on both p- and n-type H-Si(100)-2×1 shows us a situation where the dopant in Si is the determining factor differentiating between two possible reactions. The negative charge that DBs receive in the case of n-type H-Si(100)-2×1 prevents addition of TMS through its S atom. Thus, it might be possible to use other means to direct a particular reaction on the surface. For example, a biased contact on the surface of a n-type Si might locally empty the charge from DBs, and allow S addition to occur preferentially — providing a means to locally change the chemistry of the surface. While this experiment would be feasible in our instrumentation, STM would not be sufficient to distinguish between the two types of bonding since the lines appear too similar on n- and p-type; HREELS does not have the spatial resolution required to resolve a nm-scale spot of differently-bonded molecules.

3.4.4 Conclusions

In conclusion, we contrasted the molecular nanostructures of TMS formed on n- and p-type H-Si(100)-2×1 using STM, HREELS, and calculations. The molecule grows in a "square-wave" pattern, forming two adjacent lines of molecules on two dimer rows of the surface. The STM does not show a significant difference in the growth on these two substrates; however HREELS measurement combined with modeled vibration spectra showed that on p-type H-Si(100)-2×1, attachment of TMS occurred through the formation of a Si-S bond; for n-type, attachment was made through a Si-C bond. This is an example where the dopant of the crystal (an impurity in the ppm range) alters the chemistry occurring at the surface dangling bond.

3.5 Contiguous Perpendicular Molecular Lines

Hossain et al. reported the exclusive cross-dimer row growth of allyl mercaptan [28] on H-Si(100)-2×1; however, they found that it was not possible to follow or precede growth of allyl mercaptan with styrene, which will grow along the dimer rows, to form a molecular "L-shape". To form such shapes, they required an intermediate lithography step where a new DB was formed using the tip [31]. For a practical application parallel processing is desired, requiring the ability to change the direction of growth of one or more molecular species *without* time-consuming intermediate lithography steps.

After studying the growth of TMS on H-Si(100)-2×1, we attempted line growth of TMS on H-Si(100)-3×1, which as we will see, grows in the dimer row direction as on 2×1. Given that styrene is known to grow across dimer rows on H-Si(100)-3×1 [21] (see Figure 3.13 for the growth process), this gave us the tools to attempt the growth of contiguous molecular L-shapes using these two molecules in sequence. This work was published in Ref. [33].

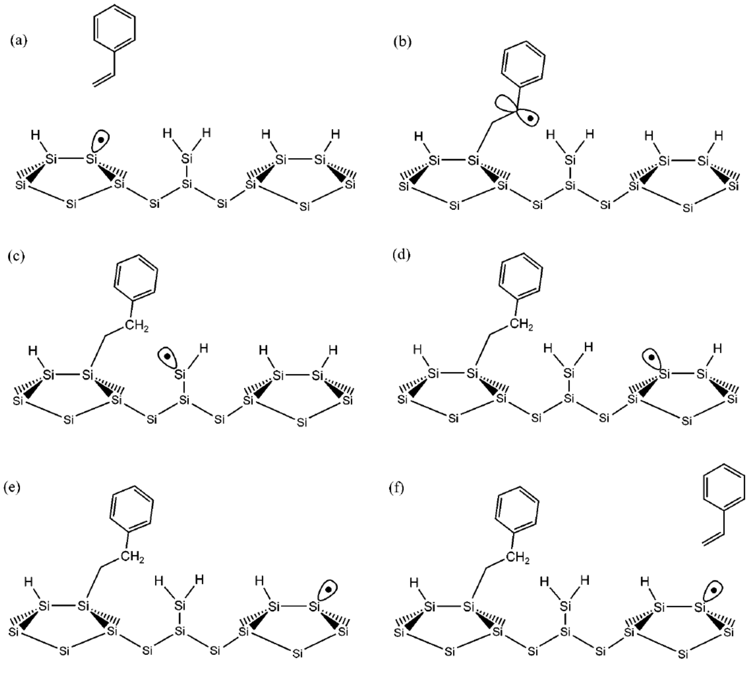

Figure 3.13: Schematic of the cross-dimer-row growth process of styrene on H-Si(100)-3×1 proposed by Tong et al. [21]

3.5.1 H-Si(100)-3×1 Surface Preparation

The preparation of the H-Si(100)-3×1 surface is very similar to that of H-Si(100)-2×1 (see Section 3.1.2). The difference is in the temperature during atomic H exposure: whereas 2×1 requires a temperature near 320 C, a lower temperature near 100 C is used to obtain 3×1 [34]. In our experimental set-up we would achieve such a temperature either by using direct current heating with some small current, or by adjusting the proximity of the sample holder to the hydrogen cracking filament. Because the needed temperature is lower than the measurement threshold of the pyrometer used, we used a thermocouple placed on the holder, near the sample, to obtain an estimate. The holder would get heated to approximately 100 C through the normal degassing and flashing procedure of H-termination, and would stay near this temperature during the 2- to 4-minute atomic hydrogen exposure.

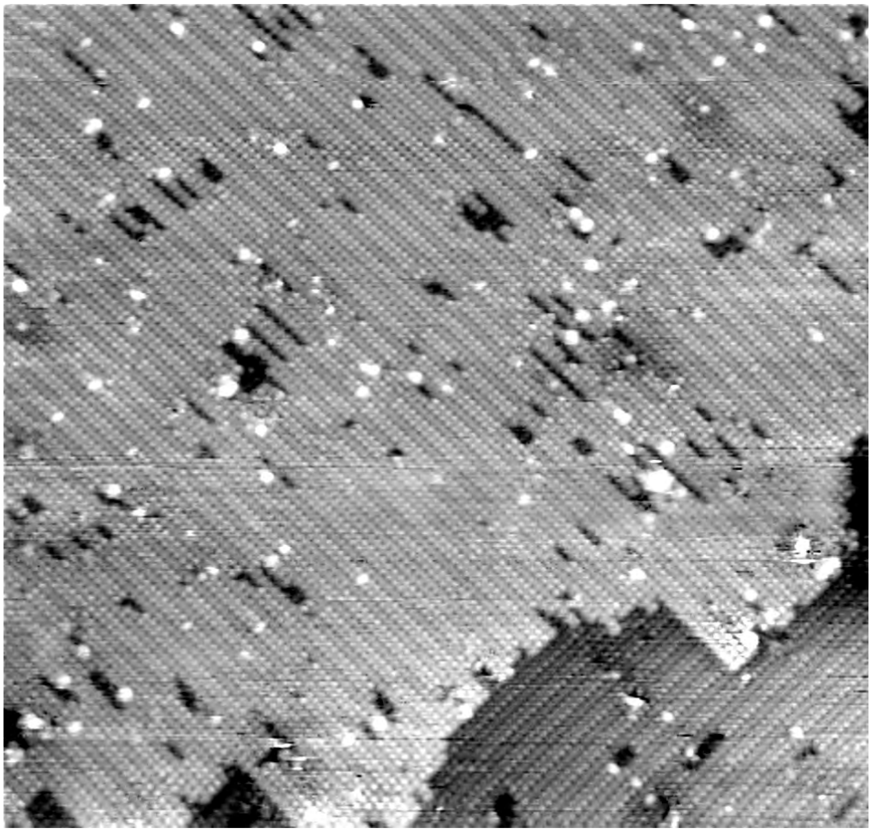

Figure 3.14: A typical H-Si(100)-3×1 surface (35 nm wide, 1.6 V, 80 pA) showing the alternating rows of monohydride dimers (bright rows) and single dihydrides (dark rows).

The H-Si(100)-3×1 surface consists of alternating rows of two Si monohydrides (one H per Si formed in dimers like 2×1), and rows of a single Si dihydride (two H atoms per Si). When imaged in STM the monohydride rows appear light, whereas the dihydride rows appear darker [34]. A typical H-Si(100)-3×1 surface like the one shown in Figure 3.14 does not have perfect surface reconstruction — small areas of 2×1 can cause the dimer rows to misalign. At intermediate H exposure temperatures, patches of 2×1 will coexist with 3×1.

3.5.2 Growth of TMS on H-Si(100)-3×1

We prepared H-Si(100)-3×1 surfaces on several substrates: highly doped n-type, medium-doped n-type, and medium-doped p-type. We then dosed trimethylene sulfide on these surfaces, and we found along-dimer-row growth in all of these cases; an example is shown in Figure 3.15.

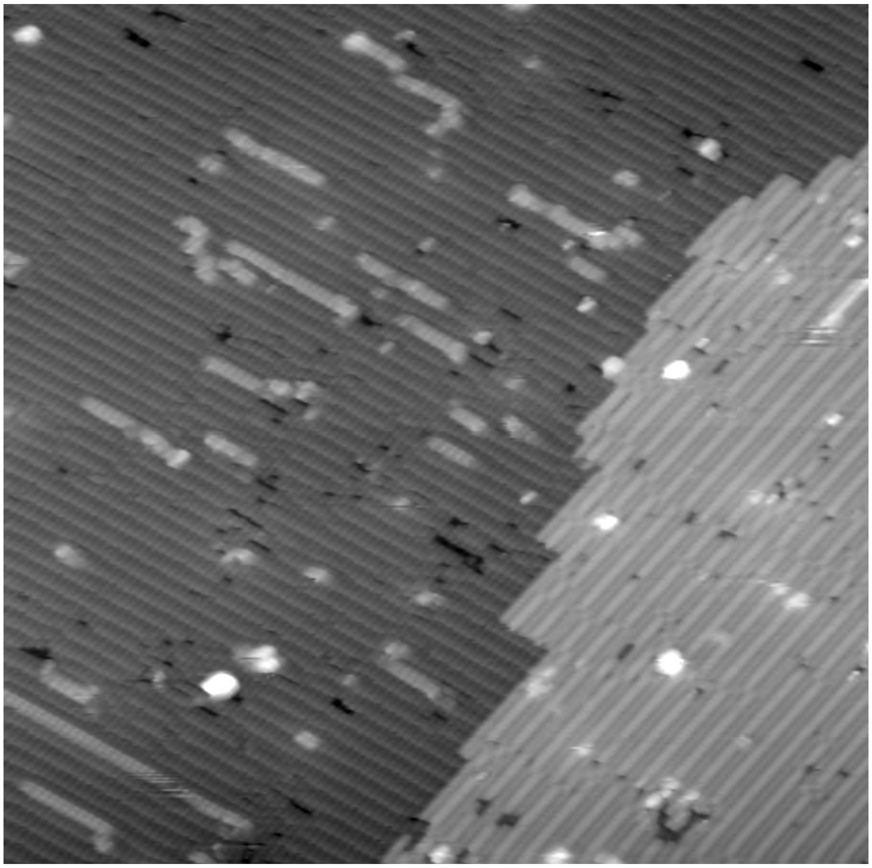

Figure 3.15: STM image (40×40 nm, −2.2 V, 0.06 nA) of 100 L of trimethylene sulfide dosed on medium doped n-type H-Si(100)-3×1.

We found no significant difference in the appearance of the TMS lines between growth on different substrates; we did however note that on medium-doped p-type a larger dose of 300 L resulted in shorter lines than smaller doses on n-type, indicating a perhaps reduced reactivity on that substrate. We expect that the same differences in bonding will occur as observed on H-Si(100)-2×1 — for the medium-n crystals studied here, the growth process of TMS on 3×1 should be the same as shown previously in Figure 3.11C.

3.5.3 Perpendicular Nanostructures

After we observed the along-dimer-row growth of TMS of H-Si(100)-3×1, we first attempted to form L-Shapes by following a 60 L TMS dose with a 40 L styrene dose. While we observed growth of both molecules (along and across rows), in several images we did not find a clear contiguous L-shape of TMS followed by styrene. In a subsequent experiment, we reversed the dosing order, starting with 50 L of styrene and adding 80 L of trimethylene sulfide. The STM images we acquired (Figure 3.16) showed many instances of what appeared to be contiguous L-shapes.

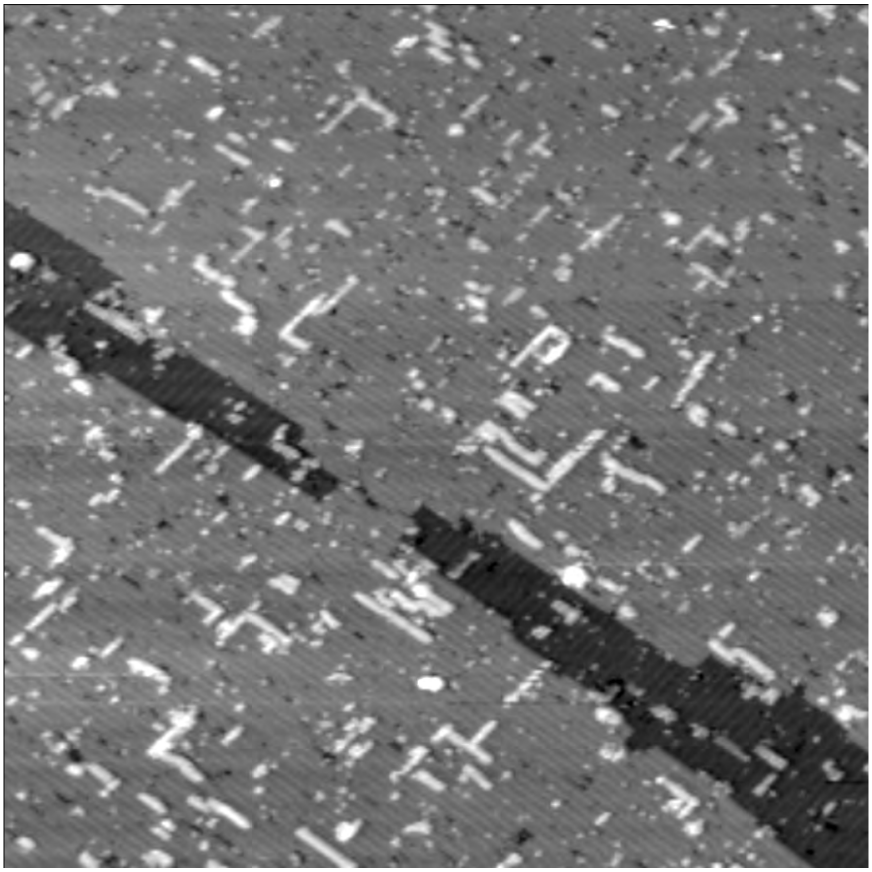

Figure 3.16: STM Image (80×80 nm, −3.0 V, 0.08 nA) of a H-Si(100)-3×1 surface dosed with 50 L of styrene followed by 80 L of TMS.

For the experiment shown in Figure 3.16, we did not acquire images of the *same* areas before dosing of each molecule. Therefore, we cannot conclude for certain on the basis of the resulting structures that the molecular L-shapes are indeed contiguous — they could result from one TMS line growing from a second DB toward a styrene line, and its growth would have to stop when the lines met. Indeed, we observe a few T-shapes that can only be explained in this way. However, since a large proportion of the touching TMS and styrene lines were joined at the end, it would seem statistically likely that contiguous growth from a single DB was indeed occurring.

To confirm that the observed L-shapes grew from a single dangling bond and formed a contiguous nanostructure, we first imaged a large area of the surface before dosing. To have high-resolution data over a large are, we took STM images of many overlapping windows of 80×80 nm in size. These images were aligned using software, and combined into the large scan area shown in Figure 3.17(a). We then dosed the first molecule, 50 L of styrene, without moving the tip laterally (although the tip was taken out of tunneling to avoid shading the surface). Drift and piezo creep however required us to take several STM images before recognizing an area that had been imaged before. The same area was imaged in several scans (Figure 3.17(b)). An additional dose of 140 L of TMS was then performed in the same manner, and part of the same area was imaged (Figure 3.17(c)). The presence of molecules on the tip degraded the overall scanning quality.

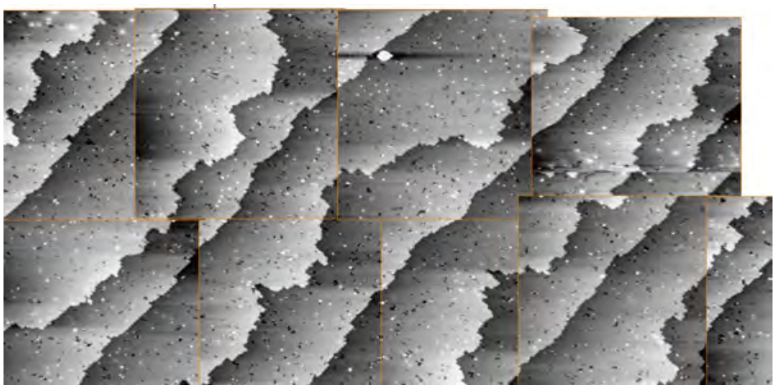

(a) H-Si(100)-3×1 surface before dosing.

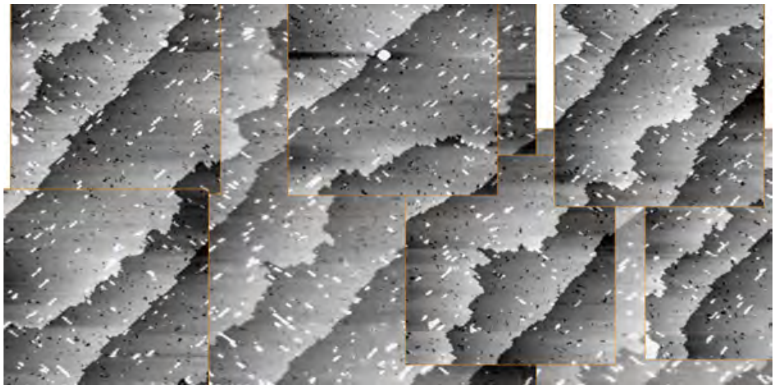

(b) After a 50 L dose of styrene.

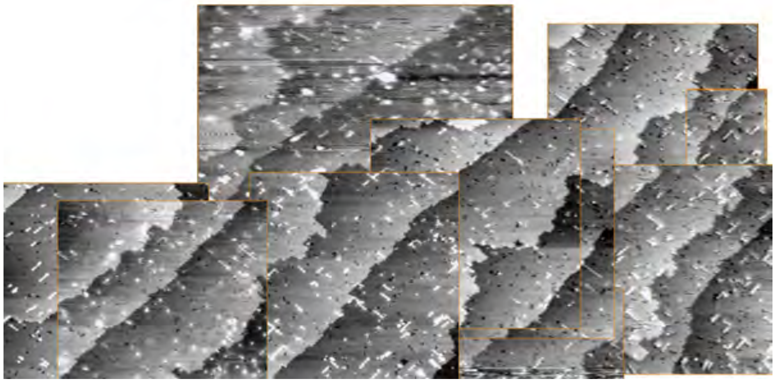

(c) After an additional 140 L dose of TMS.

Figure 3.17: Combined registered images (approx 250×150 nm) of dosing styrene and TMS on medium n-type H-Si(100)-3×1.

Figure 3.18 shows a close-up of a part of the crystal where 4 l-shaped molecular structures grew in close proximity. Images from a) to c) follow the same area on the surface after the consecutive doses of styrene and trimethylene sulfide. It is made clear by the yellow arrows that a single dangling bond was the originating point from which each structure grew; no intermediate lithography was necessary to obtain these shapes.

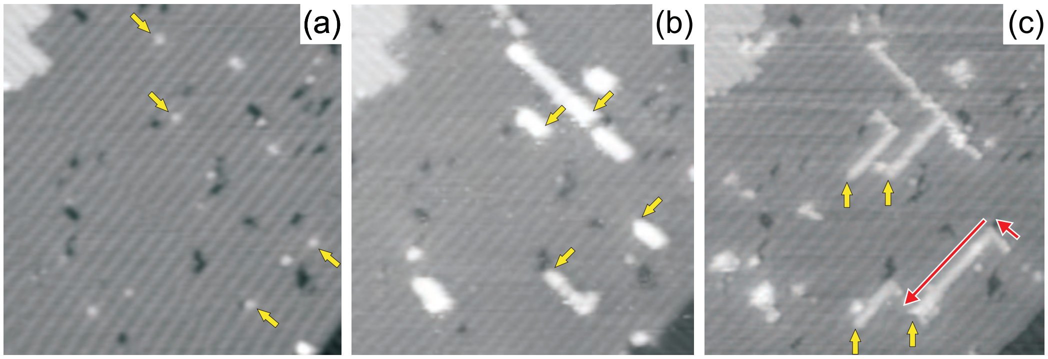

Figure 3.18: Sequence of STM images (30×30 nm) showing growth of several contiguous, L-shaped molecular lines. Images a) to c) are of the same area of the surface. a) Initial 31 H-terminated surface (0.08 nA, −2.8 V), showing the DBs of which several will react. b) Following a 50 L dose of styrene (0.08 nA, −2.8 V), several styrene lines have grown perpendicular to dimer rows. c) Following a 140 L dose of TMS (0.12 nA, −3.4 V), a few contiguous L-shaped molecular lines of styrene followed by TMS formed. The yellow arrows indicate the DB positions and the direction of subsequent line growth; the red arrows trace the growth of one structure. From Ref. [33].

3.5.4 Conclusions

These experiments demonstrate that we can obtain molecular lines that turn a corner in a “hands-off”, massively parallel process. Indeed, since no lithography is required for those shapes to grow, a large number of these L-shapes were grown simultaneously on an entire macroscopic Si crystal. Our control of the resulting shapes was not complete. First, the final yield was fairly low: perhaps as few as 10% of DBs were starting points for full L-shapes. Second, their shapes varied in size. However, the length of each segment could, in theory, be controlled by carefully dosing a fixed amount of each molecule, yielding more identical structures. These experiments show the first steps towards a higher level of control of the nanostructure growth.

3.6 Butadiene Line Growth

Butadiene (Figure 3.19(a)) is a 4-carbon alkene with a double C-C bond between its carbons 1 and 2. DiLabio et al.[19] have shown that only long alkenes of more than 7 carbons can grow lines, so it might be expected that butadiene would not grow lines. However, butadiene has 2 C-C double bonds; the second double bond, between carbons 3 and 4, stabilizes the radical intermediate and allows line growth to occur at room temperature. The results described in this section were published in Ref. [35].

Butadiene was chosen as a candidate molecule for line growth that would be perpendicular to the dimer row direction on H-Si(100)-2×1. We initially found that seeing plain butadiene growth required very large doses, and speculated that its small size reduced the residence time of the molecule on the surface (for a discussion of diffusion of molecules on surfaces, see e.g. Ref. [36, 37]). A larger molecule would show more physisorption, so we experimented with isoprene and 2,3-dimethyl-1,3-butadiene (Figure 3.19). These two molecules did indeed seem to require a smaller dose to obtain similar growth coverage — a 5000 L dose of 1,3-butadiene resulted in less growth than a 2400 L dose of 2,3-dimethyl-butadiene.

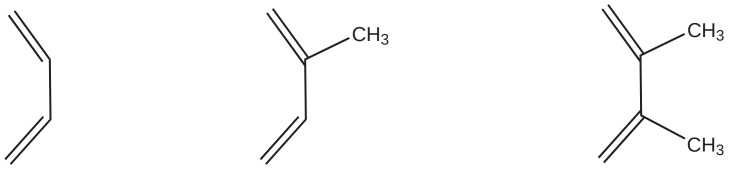

(a) 1,3-butadiene (b) 2-methyl-1,3-butadiene, also called isoprene (c) 2,3-dimethyl-1,3-butadiene

Figure 3.19: Three molecules in the butadiene family.

None of these 3 molecules in the butadiene family were found to grow exclusively across dimer rows, in the way that allylmercaptan does [28]. Instead, it became apparent that abstraction of H was possible from either the next dimer along the row, or the closest H across the dimer row — much like the double line growth of benzaldehyde [25]. The two possible reaction pathways are shown in Figure 3.20.

Dr. Gino DiLabio performed reaction modeling of the two possible reaction pathways in for both 1,3-butadiene and 2,3-dimethyl-1,3-butadiene using density functional theory. The details of the calculations are described in Ref. [35] and references therein. The results of those calculations are shown in Table 3.1. The barrier height calculations are crucial for determining which type of growth will occur more readily: across-row or along-row. The barriers for H abstraction from

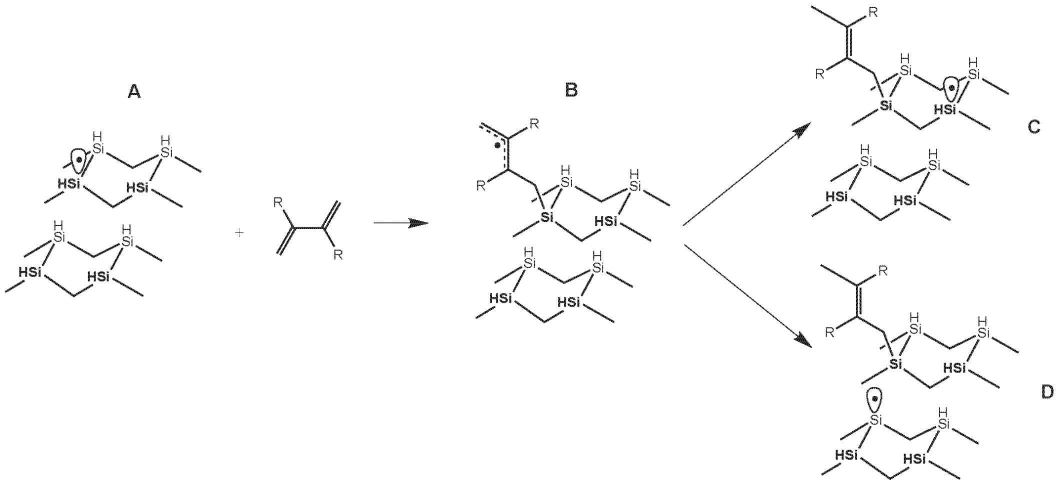

Figure 3.20: The two possible reactions for 1,3-butadiene (R=H) and 2,3-dimethyl-1,3-butadiene (R=CH_3). In (A), a dangling bond on the Si surface reacts with the molecule to form a radical intermediate in (B). The unpaired electron is delocalized into the remaining double bond, which stabilizes the intermediate. From there, two possible reactions can occur: in (C), abstraction of the H on the next dimer row continues line growth along the dimer row direction. This is the preferred reaction pathway when R=CH_3. In (D), abstraction occurs on the next row. For R=H, both the C and D pathways occur. Figure from Ref. [35].

the next row (Figure 3.20 D) are lower than the barrier for abstraction of H from the next dimer in the same row (Figure 3.20 C). The difference is 2.4 kcal/mol for 1,3-butadiene and 3.7 kcal/mol for 2,3-dimethyl-1,3-butadiene, which implies that square-wave growth should occur: the first abstraction will preferentially be from the next row. The next butadiene molecule in the line will no longer be able to abstract from the next row and will therefore abstract from the next dimer in the same row. The process continues, forming two parallel lines on two neighboring dimer rows.

Reaction	Energy (kcal/mol)	
	1,3-Butadiene	2,3-Dimethyl-1,3-Butadiene
Addition: Butadiene + Si	−23.8	−20.5
H Abstraction barrier: next dimer	−12.1 (+11.7)	−7.2 (+13.3)
H Abstraction barrier: next row	−14.5 (+9.3)	−11.0 (+9.6)
Final product	−32.3	−26.9

Table 3.1: Calculated energies in kcal/mol for the molecule addition and barrier height for H atom abstraction for 1,3-butadiene and 2,3-dimethyl-1,3-butadiene on H-Si(100)-2×1. From Ref. [35].

The results of the calculations shown in Table 3.1 indicate that the growth pattern of both 1,3-butadiene and 2,3-dimethyl-1,3-butadiene should be a square wave. However, our STM experiments have shown that this is not the case. Figure 3.21 shows the results of two molecular dosing experiments using each molecule. These dosing experiments were performed with only a turbomolecular pump maintaining vacuum, with the normally-used ion pumps turned off (the reason for this will be made clear in Section 3.7). The 5000 L dose of 1,3-butadiene performed between Figure 3.21 A and Figure 3.21 B resulted in growth of small molecular nano-structures at DB sites all over the surface. A close-up view in Figure 3.21 C reveals that the molecular lines grown are quite short but span two dimer rows, consistent with the square-wave growth model. The size of the structures appears limited to 20×20 Å.

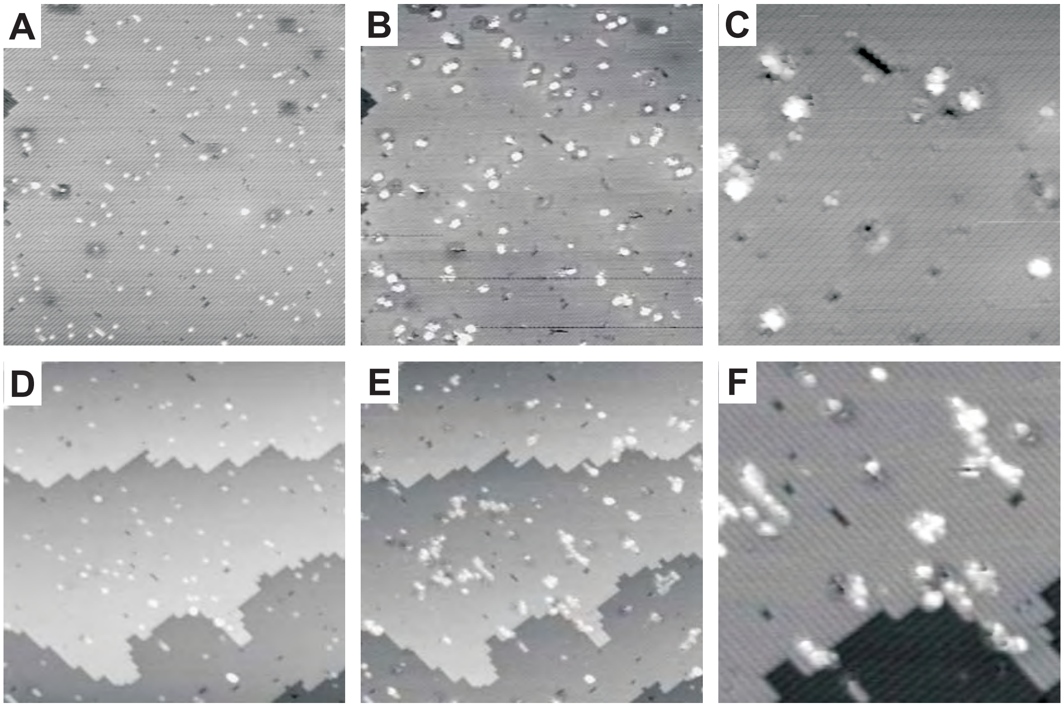

Figure 3.21: STM images of the growth character of butadiene on H-Si(100)-2×1. A: Pre-dose image. B: Same area shown in A following a 5000 L dose of 1,3-butadiene. C: Higher resolution view of a central portion of B showing the growth of 1,3-butadiene.

Second measurement: D: Pre-dose image. E: Same area shown in D following a 2400 L dose of 2,3-dimethyl-1,3-butadiene. F: Higher resolution view of a central portion of E showing the growth of 2,3-dimethyl-1,3-butadiene.

Images A,B,D and E are 80×80 nm^2; C and F are 30×30 nm^2. STM sample biases and currents are A: −2.84 V, 70 pA; B and C: −2.7 V, 55 pA; D, E and F: −2.3 V, 80 pA. From Ref. [35].

A second dosing experiment was performed in the same way for 2,3-dimethyl-1,3-butadiene. Figure 3.21 E and F show the result of dosing 2400 L of the molecule on the same area shown in Figure 3.21 D. By comparing Figures 3.21 C and F we can see that the growth patterns of the two molecules are quite different. 2,3-dimethyl-1,3-butadiene shows a tendency to grow mostly along a single dimer row, with only occasional crossings onto the next dimer row. The resulting structures also appear longer.

The results of the density functional calculations shown in Table 3.1 would not enable us to conclude that growth of the two molecules should be different. To resolve the discrepancy in growth pattern, Dr. DiLabio performed additional calculations to determine the barrier to rotation about the achoring Si-C bonds for the two molecules. His calculations evaluated the barrier to rotation between the most energetically stable configuration to the configuration allowing H abstraction from the next row. In the case of 1,3-butadiene, the barrier is approximately 2.5 kcal/mol. The same rotation of in the 2,3-dimethyl-1,3-butadiene case has a barrier of 6.8 kcal/mol. These barriers show that the rotation of the 2,3-dimethyl-1,3-butadiene is strongly hindered by the steric interactions between the two methyl groups and the surface of hydrogen atoms, causing a different growth pattern to emerge.

We expect that isoprene, an intermediate molecule between 1,3-butadiene (no methyl group) and 2,3-dimethyl-1,3-butadiene (two methyl groups) containing only one methyl group, would exhibit an intermediate character in its growth pattern. STM experiments confirm this intuition, as shown in Figure 3.22. A mixture of growth is observed, being sometimes on a single dimer row and sometimes on two (or more) adjacent rows.

This set of STM experimental evidence and supporting density functional theory calculations have shown that the steric interactions between the butadiene molecule and the surface can have a significant effect on the way the growth occurs. In theory, it would be possible through calculations to predict how steric interactions would affect line growth and design and synthesize custom molecules according to the desired result.

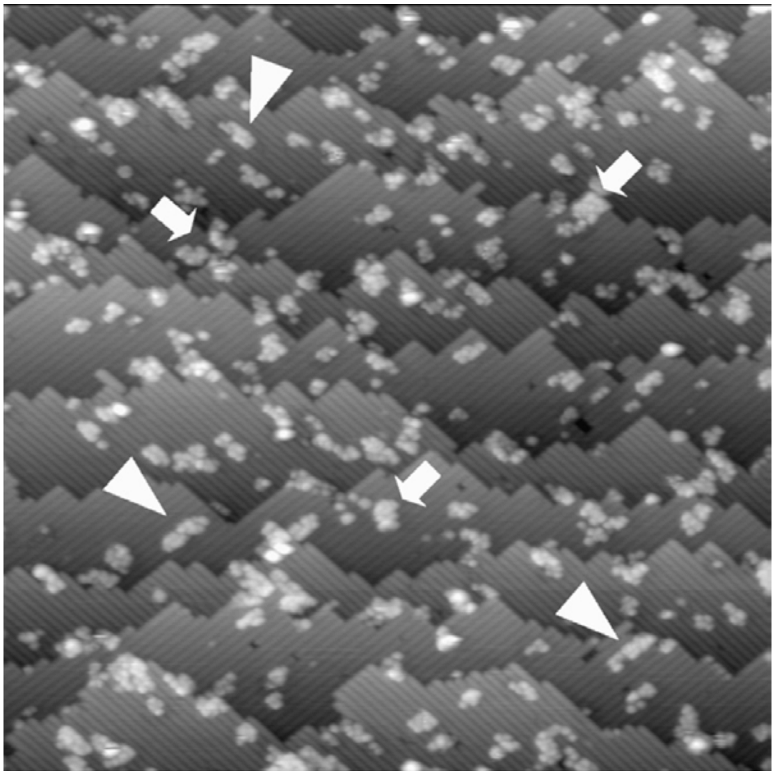

Figure 3.22: STM image of the molecular growth of isoprene lines on H-Si(100)-2×1, following a 3600 L dose (60×60 nm^2, 50 pA, −2.5 V). Examples of growth along dimer rows are indicated by wedges; examples of random growth are indicated by arrows. From Ref. [35].

3.7 Effect of Ion Pump on Molecular Dosing

3.7.1 Introduction

We have seen in all our previous discussions on molecular line growth that the starting point of the self-directed growth process is a hydrogen terminated Si(100)-2×1 or 3×1 surface with a low density of naturally occurring dangling bonds. The quality of the H-Si(100)-2×1 surface is crucial to obtaining good, reproducible results, which is why the surface is prepared and the experiment performed in ultra-high vacuum (pressure below 10^{-9} Torr).

In this section, we present experimental evidence of the harmful effect of ion pump-generated radicals on H-terminated surfaces. These results were published in Ref. [38].

3.7.2 Ion Pump Operation

To maintain the extremely low pressure requirements of UHV, sputter-ion pumps are typically used. They are ideal for use in UHV-STM systems because they are completely vibration free and therefore do not adversely affect STM images, even while operating.

Sputter-ion pumps generate electrons using a high electric field (a voltage of 7 kV is applied in the pumps used). These high-energy electrons collide with gas molecules, ionizing them. A magnetic field is normally used to increase the gas ionization rate. Under the influence of the electric field, the ions are accelerated into a titanium electrode — see Figure 3.23. Pumping occurs in two ways — first, the accelerated ions sputter titanium from the cathodes, which deposits as a thin layer on the anode. This fresh titanium is extremely reactive and chemically fixes some of the gases in the pump. Some of the ions hitting the cathode end up embedded in it, and are therefore removed from the gas phase — this is the second way ion pumps operate.

We have found that the sputtering effect of ions on the electrode material releases fragments of molecules which were previously pumped by the cathode — either by getting embedded or when physisorbed on the cathode surface. These molecular fragments can then escape the ion pump and react with our hydrogen-terminated Si surfaces.

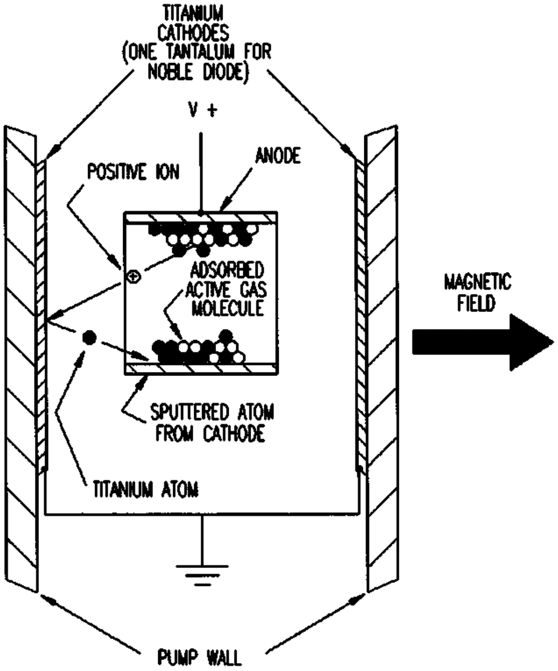

Figure 3.23: Diagram of how a diode sputter-ion pump operates. Ions are created by electron bombardment, and are accelerated from the anode to the cathode. The ions sputter away titanium, which redeposits on the anode to chemically pump gases (gettering action). Some accelerated ions embed themselves in the cathode material. From [39].

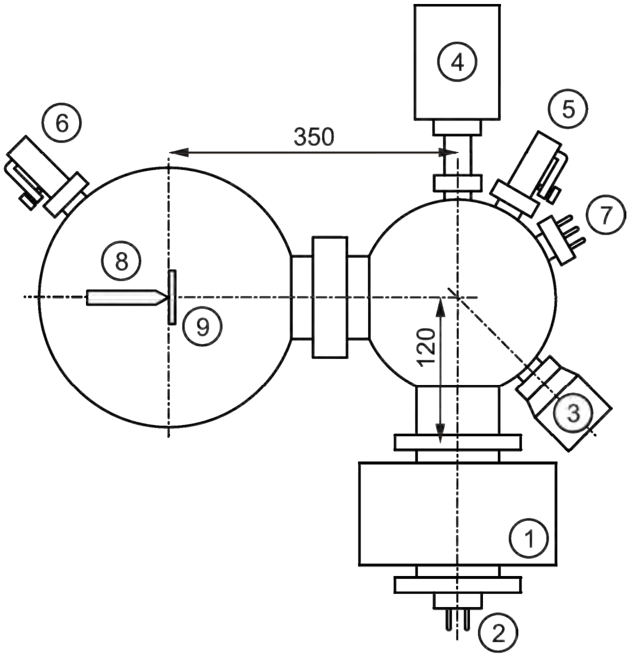

Figure 3.24: Schematic of the experimental setup used. 1: ion pump, 2: TSP filaments, 3: turbomolecular pump, 4: residual gas analyzer, 5: leak valve (used to dose He), 6: leak valve (used to dose molecules), 7: ion gauge, 8: STM tip, 9: sample (viewed from the side). Drawing not to scale, distances shown are in millimeters. Figure and caption from Ref. [38].

3.7.3 STM Results

We noticed this effect from ion pumps when performing our first butadiene dosing experiments as described in Section 3.6. In order to see any reaction on the surface, this experiment required much larger doses than typical line-growth experiments, such as those using styrene. After performing dosing experiments with registered before-and-after images, we noticed growth of molecular features where no DBs were visible in the "before" images.

To investigate this effect further, we performed comparative dosing experiments with and without an ion pump in operation. These experiments were performed in the HREELS-Omicron STM 1 system, a schematic of which is shown in Figure 3.24. The results of these dosing experiments are shown in Figure 3.25. Figures 3.25 A and C show the initial H-Si(100)-2×1 surfaces prepared with the normal method describe in Section 3.1.1. The surface is almost entirely covered with H atoms, with the exception of a few rare dangling bonds. In both images, a white circle highlights a small section of the surface and white arrows point out the DBs that were present on the surface before the dosing experiment. DB densities and surface quality are similar in both cases. The sample used was a 0.1 Ω·cm resistivity n-type Si crystal in both cases.

Figure 3.25 B shows the result of dosing 250 L of 2,3-dimethyl-1,3- butadiene with the ion pump operating. This is the normal procedure for molecular dosing in UHV STM systems. The image shows numerous growth patterns over the entire surface. We do not expect the molecule to be able to grow a molecular nanostructure absent of a DB acting as the starting point. However, Figure 3.25 B shows many growth patterns where no DB was present in the previous images — these are highlighted by the white circle. Excluding molecular growth that could have started from an original DB, 175 new features were counted in the frame shown. This number of new features yields a density of at least 1.25×10^{13} cm^{-2} new reaction sites created during the dosing procedure, equivalent to 1.8% of the surface Si atoms.

To test whether the ion pump was indeed responsible for these unexplained growth features, we performed the same dosing experiment without an ion pump operating. H-Si(100)-2×1 surface preparation was done normally with an ion pump running, but a gate valve to a running turbomolecular pump was opened and the ion pump was turned off (though not gated off) immediately following H-termination. From that point on, vacuum was maintained using exclusively the turbomolecular pump. The vibration from the turbomolecular pump had only a slight influence of the quality of the STM images and did not cause a problem.

Figure 3.25 D shows the result of a 2400 L dose of 2,3-dimethyl-1,3-butadiene

(2×10^{-6} Torr for 1200 s) on the surface shown Figure 3.25 C. Molecular growth is observed at the pre-existing DB sites, as highlighted by the arrows. Comparing the two images yields no new molecular growth initiation sites, despite a total dose that is nearly ten times larger than performed with the ion pump running.

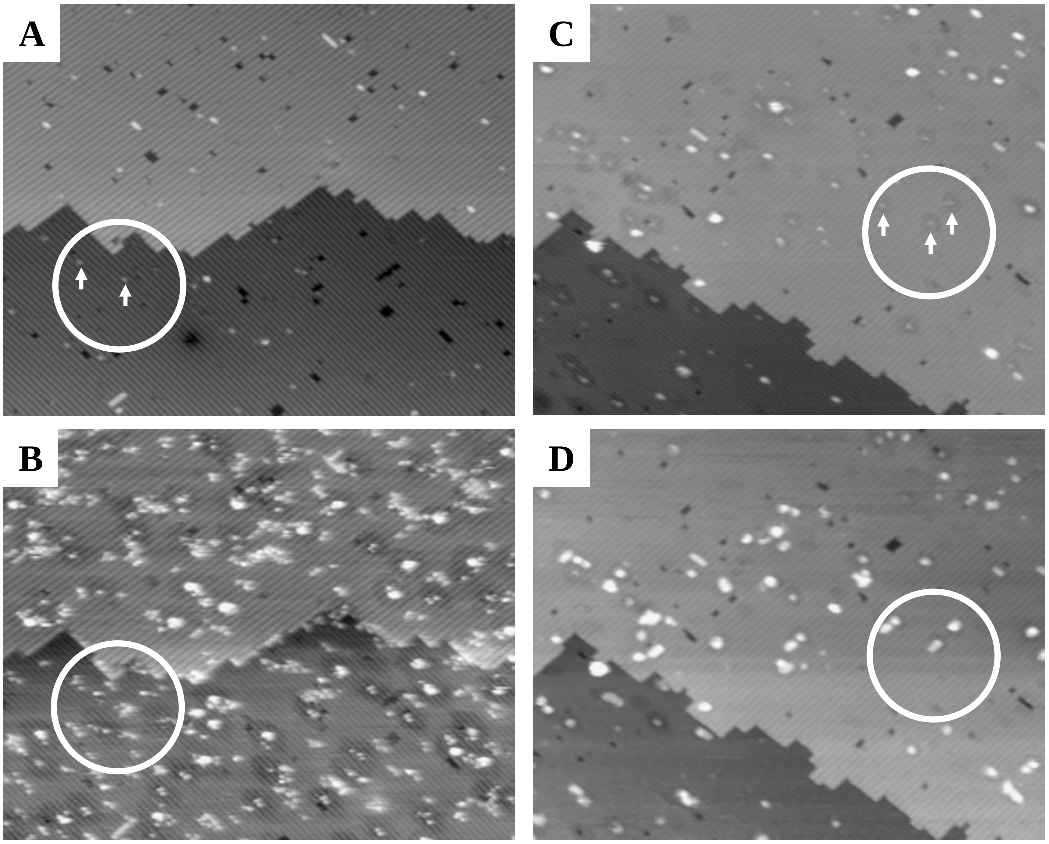

Figure 3.25: STM images ($\sim 40 \times 35$ nm) of two 2,3-dimethyl-1,3-butadiene dosing experiments. Images A (0.08 nA, −1.8 V) and C (0.065 nA, −3.0 V) were taken before dosing. Image B (0.05 nA, −2.2 V) shows the result of a 250 L dose of 2,3-dimethyl-1,3-butadiene with the ion pump turned on. Image D (0.065 nA, −3.0 V) shows the result of dosing 2400 L of the same molecule, using only a turbomolecular pump (see text for details). White circles highlights the same area in A and B, and in C and D. White arrows point out initial dangling bonds. Figure and caption from Ref. [38].

3.7.4 Residual Gas Analysis Results

From Zikovsky et al. [38]:

> To investigate more directly the quality of the vacuum during a dosing experiment, we acquired mass spectra with a RGA (Figure 3.26 A) while taking care to leave the RGA filament off so as to only detect existing ions in the chamber. Multiple mass spectra were obtained while no molecules were being dosed and the ion pump alone was operating (Figure 3.26 A, line 1), which show that no peaks are present in the chamber beyond the noise level of $\sim 10^{-14}$ Torr. Similarly, line 2 in Figure 3.26 A shows the average of many mass spectra taken while dosing 10^{-5} Torr of 2,3-dimethyl-1,3-butadiene with only the turbomolecular pump maintaining vacuum. No peaks are visible beyond our noise level of $\sim 10^{-13}$ Torr (the noise level in line 1 is lower because we were able to average 25x more spectra). Finally, line 3 in Figure 3.26 A shows the result of dosing 2,3-dimethyl-1,3-butadiene at 10^{-5} Torr with only the ion pump maintaining vacuum. In addition to a large peak near 1 amu, three small peaks are visible above the noise, at masses of 28, 67.3 and 82.6 10. We note that the two largest peaks in the expected mass spectrum (Figure 3.26 B, data from NIST [40]) at 82 and 67 are observed in our experimental spectra. The mass peak near 82 corresponds to the mass of the whole 2,3-dimethyl-1,3-butadiene molecule; the peak near 67 can be attributed to the molecule losing a CH_3 group. These mass spectra show clearly that at high dosing pressures, the ion pump ionizes the 2,3-dimethyl-1,3-butadiene molecule, which then breaks into smaller, reactive fragments. We note that only ions generated near the inlet of the ion pump will be able to escape the electric field within; however, neutral radicals produced by the breakup of ionized molecules will be unaffected and may escape the ion pump if they are not ionized and pumped themselves. Therefore, we expect that the concentration of neutral molecular fragments will be much higher than those of the ions measured in this way. It is also noted that because of molecular fragmentation, multiple neutral fragments can result from a single ionized molecule. Unfortunately, in a normal RGA measurement with the ionizing filament on, the signal from the ionizer-induced fragmentation of the parent molecule is large and overlaps the small signal from the neutral molecular fragments produced in the pump. In many experiments, both

the neutral and ionized molecular fragments that escape the ion pump could cause undesired reactions to occur.

When the ion pump is operating, Figure 3.26 A shows a very large peak near 1 atomic mass unit, which we attribute to H atoms (the maximum value of the peak is actually at 1.5 amu, but this is due to a cutoff in RGA response near 1 amu, and the units inability to record data below 1 amu). H_2 can be excluded as the source of that peak, since when dosed in the chamber with the RGA filament on it appears as a peak centered at 2.0 amu. The ionized atomic hydrogen is being released from the ion pump while it is pumping a modest gas pressure. It is a known effect that after extended use, ion pumps become saturated, and reach an equilibrium condition where ion bombardment on the cathode causes gas re-emission [41]. This saturation point can be reached in as little as an hour at pressures near 10^{-6} Torr for reactive gases. Sputtering of the cathode when exposed to a large gas flux also releases molecules that were previously pumped and a measurable amount of hydrogen and other gases previously adsorbed is released from the cathode. The mass spectrum in Figure 3.26 A shows that at least part of those released gases will ionize and fragment to generate atomic hydrogen ions. Although we cannot measure them directly in the RGA, it is likely that neutral hydrogen atoms are also released by this process. Similarly, the mass peak at 28 likely corresponds to carbon monoxide (CO), a gas commonly present in background UHV pressure, being remitted from the ion pump. Our STM experiments show that these reactive H atoms/ions are able to abstract H from the H-Si(100)-2×1 surface, creating a new DB site for line growth [42]. In our chamber geometry there is no line of sight between the ion pump and the sample in the STM, however we have found that with substantial probability atomic H can survive chamber wall collisions to reach a sample. This was confirmed by performing hydrogen termination with no line of sight between the hot filament producing atomic hydrogen and the sample. We found that the surface would still become H-terminated surface despite atomic hydrogen needing to bounce off the chamber walls to reach the sample.

From the mass spectra presented above, we conclude that hydrogen atoms/ions and reactive molecular fragments escaping from the ion pump created the surface DBs that resulted in the additional molecular growth features seen in Fig. 2 B. Based on the number of created DB sites, and

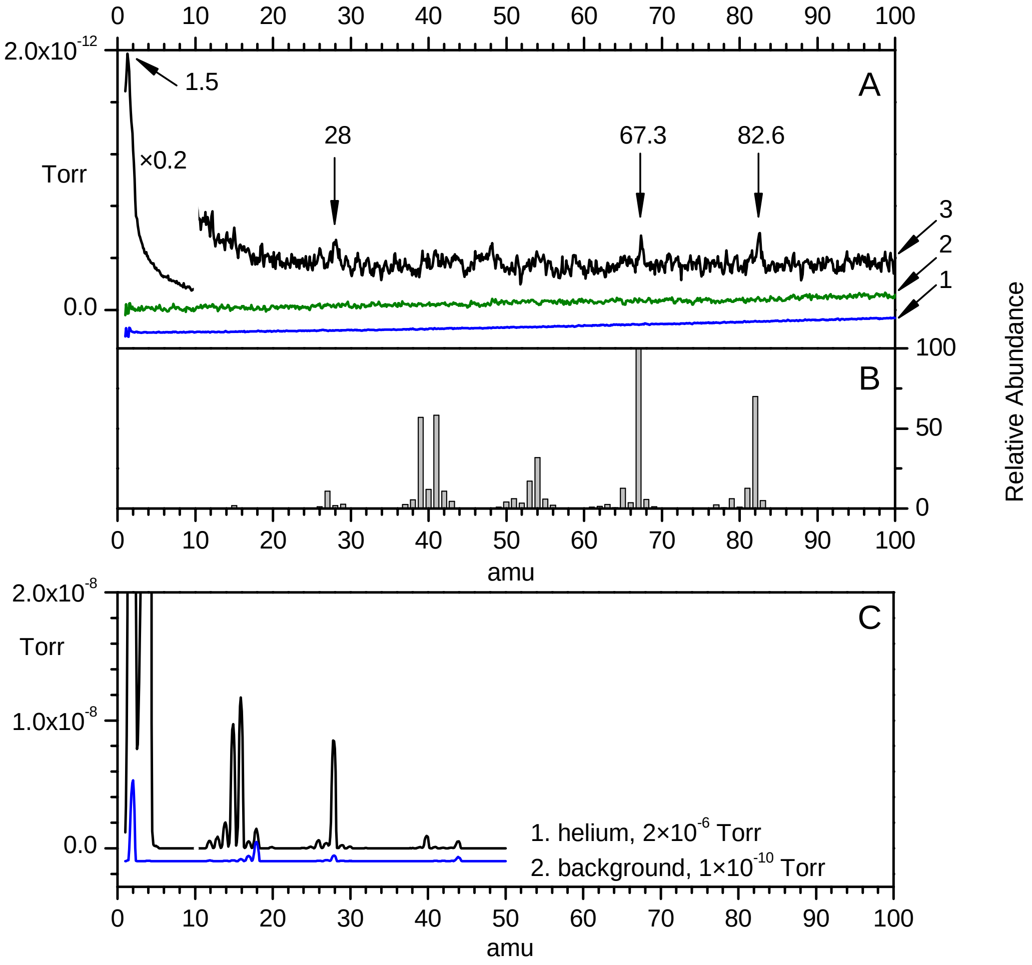

Figure 3.26: (A): averaged mass spectra obtained with a RGA with its filament turned off, in 3 different conditions: Line 1, in blue, the background signal with the ion pump turned on and no molecules being dosed (average of 1000 spectra); Line 2, in green, the mass spectra while dosing 10^{-5} Torr of 2,3-dimethyl-1,3-butadiene with only the turbomolecular pump operating (average of 26 spectra); Line 3, in black, the mass spectra from the same pressure (10^{-5} Torr of 2,3-dimethyl-1,3-butadiene) with the ion pump operating (average of 31 spectra). The curves have been offset for clarity; below 10 amu, line 3 has been reduced in height by a factor of 5; the scales for the 3 lines are identical otherwise. (B): expected fragmentation pattern for 2,3-dimethyl-1,3-butadiene as measured in a mass spectrometer (data from NIST [40]). (C): mass spectra obtained with a RGA with its filament turned on and the chamber pumped by the ion pump: Line 1, in black, helium at the pressure 2×10^{-6} Torr; Line 2, in blue, the background signal, arbitrarily offset for clarity (pressure 10^{-10} Torr). Figure and caption from Ref. [38].

> assuming an impingement rate of 1 molecule$\cdot s^{-1}$ for each surface atom in the STM image, 0.007% of molecules hitting the surface during exposure are impurities. Such a result is consistent with a minute fraction of reactive species escaping the ion pump.

3.7.5 He Dosing Results

From Zikovsky et al. [38]:

> Subsequently, we performed an experiment where a normal H-terminated Si(100) surface was exposed to a pressure of 2×10^{-6} Torr of ultra-pure He for 20 minutes (a 2400 L dose) while pumped with the ion pump. Figure 3.26 C, line 1, shows a normal mass spectrum acquired with the ionizing filament on during this dose. A large amount of H_2 (amu 2) is seen to be released from the ion pump. Numerous other peaks far exceeding background levels (Figure 3.26 C, line 2) are visible in this spectrum notably peaks at amu 15 and 16, which we assign to CH3 and CH4 respectively. The height of these peaks, $\sim 10^{-8}$ Torr, is far above the concentration of impurities present in the ultra-pure helium used (99.999% minimum purity, giving a total partial pressure of impurities below 2×10^{-11} Torr). These peaks are likely due to the release of methane from the ion pump. We suspect that some carbon and hydrogen were released by sputtering action inside the ion pump, forming CH_4 and CH_3 and releasing these into the UHV chamber [41].
>
> Registered STM images of the surface taken before and after dosing He are shown in Figure 3.27. These images show that the He dose created a range of new features on the surface first, several DBs were created by atomic hydrogen ions or other reactive species released by the ion pump. The concentration of new surface DBs, $\sim 1.7 \times 10^{12}$ cm^{-2}, is within an order of magnitude of what was observed in Figure 3.25 B. Second, a smaller number of DBs were found to have been capped by an incoming H atom. Finally, some DBs were seen to have reacted with unknown molecular fragments, imaged as bright features. These results show that fragments of molecules previously pumped by an ion pump (in our case, H_2 during hydrogen termination and organic molecules during dosing) can be released and modify reactive surfaces even when a non-reactive, noble gas such as He is dosed.

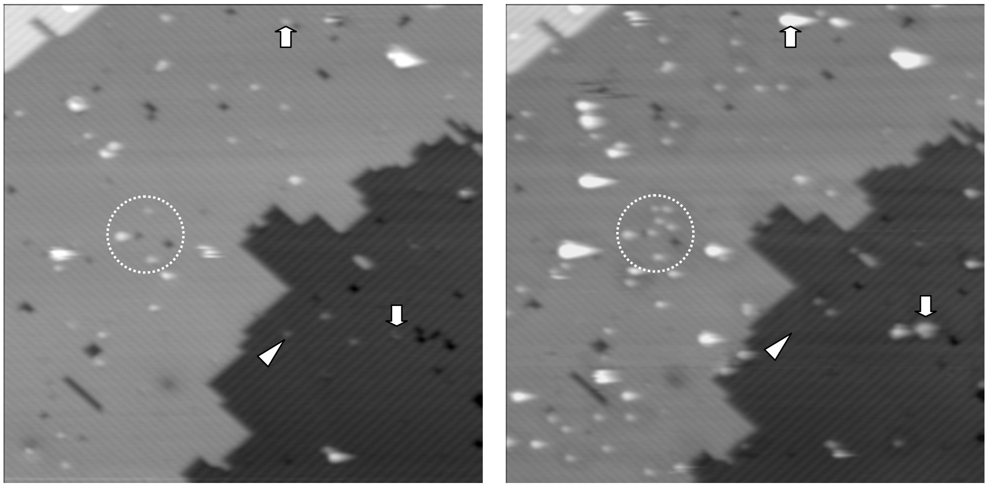

Figure 3.27: STM images (∼ 40 × 40 nm) of n-type medium doped H-Si(100)-2×1 surface before (left; 0.07 nA, −2.5 V) and after (right; 0.07 nA, −2.5 V) helium was leaked into the chamber pumped with the ion pump at the pressure of 2×10^{-6} Torr for 20 minutes (2400 L exposure). Some changes on the surface are highlighted as follows: the dashed circle indicates an area where four new DBs appeared, the arrows mark DBs which are present on the left image but look much brighter and larger than a usual DB on the right image, and the wedge shows an example of a DB that disappeared. Overall we counted 27 new DBs, 6 modified DBs and 2 capped DBs in the displayed area. This yields a density of $\sim 1.7 \times 10^{12}$ cm^{-2} new DBs/cm^2. Figure and caption from Ref. [38].

3.7.6 Conclusions

We have presented evidence that dosing organic molecules in a UHV chamber pumped by an ion pump causes the release of reactive molecular radicals. These radicals modify the H-Si(100)-2×1 surface by bonding to it or by taking one of the surface hydrogens, leaving a new dangling bond. This has been shown by STM experiments of 2,3-dimethyl-1,3-butadiene molecular line growth, and by RGA measurements. Even dosing He, an inert gas, causes the re-release of molecules that had been previous adsorbed or embedded in the ion pump walls.

We do not believe that our group's previously published line growth results were significantly affected by this problem — the molecules used in these papers were more reactive, requiring doses of typically 10 L or less, at pressures at or below 10^{-6} Torr. Therefore, ion-pump generated radicals were likely kept to a minimum in these cases. This effect should be taken into consideration for any future molecular line growth experiments, since it can cause unexplained molecular line growth. Pumping with a turbomolecular pump instead of an ion pump for the duration of the molecule dose should prevent any such problems.

3.8 Conclusions

While much of the motivation in studying self-assembled organic molecular lines on Si surfaces is in their possible applications, the interesting surface chemistry features we discovered are perhaps of a more fundamental importance. With a large set of experimental and theoretical data on different line-growth reactions on H-Si(100)-2×1, we are finding parameters for picking and choosing the particular way the molecules will self-assemble. We have found reactions that depend on the silicon dopant type, as in the case of trimethylene sulfide (Section 3.4); using steric interactions to affect the way line growth occurs, as in the case of the butadiene family of molecules (Section 3.6); creating L-shapes by using two different molecules (Section 3.5).

To envisage self-directed line growth as a viable commercial process, much more control would be needed. A perfectly H-terminated surface would have to be realized (the use of TEMPO to cap DBs [43] can get one closer). Dangling bonds would need to be reliably created on a large scale — perhaps using multiple tip arrays [44] and feedback-controlled lithography [45], also Section 6.3.10. The direction and extent of growth would need to be controlled to a high degree, perhaps by using electric field as described in Chapter 8. Finally, growth of chosen functional molecules would need to be achieved (perhaps using the molecular lines as templates post-line growth modification). All these challenges are quite significant, but the insight on surface science and chemistry learned from their pursuit will be valuable in innumerable other ways.

Chapter 4

Photon Emission from the STM

In this chapter, we review the theory of excitation energy transfer (EET) and some of the systems where it occurs. We suggest that EET could be used as a novel way to transfer information on the nanoscale, and we propose an experiment to demonstrate it by detecting photon emission from the STM. We review results from other instruments capable of collecting light during STM scanning, and we describe our experimental attempts to observe excitation energy transfer (EET) along a molecular line on H-Si(100)-2×1.

4.1 Excitation Energy Transfer

Excitation energy transfer is a process by which the energy of an electron excited above its ground state in one molecule is transferred to an electron in a nearby molecule. This effect was first observed in 1922 by Cario and Franck during fluorescence experiments on a mixture of thallium and mercury vapor [46]. When the mixture was exposed to the light of the mercury resonance line, it showed the emission spectra of both the thallium and the mercury. Since the thallium could not absorb the light directly, some kind of indirect excitation energy transfer had to occur.

The theory behind this energy transfer was developed by Forster [47, 48]. He describes an electrostatic dipole-dipole interaction between the two molecules, the rate of which has a distance dependence $\propto 1/r^6$ where r is the intermolecular distance; this mode of EET is often described as Forster energy transfer. Intermolecular distances between 2 and 5 nm are typically small enough for Forster energy transfer to occur.

A second process can occur if the molecules are sufficiently close to each other, and this was described by Dexter [49]. In the so-called Dexter energy transfer process, electron exchange occurs when an electrostatic perturbation mixes the electronic wavefunctions. This has an exponentially decreasing distance dependence, because it depends on the wavefunction overlap of the molecules. However, while Forster transfer is limited to singlet excitations because of selection rules, Dexter transfer can also occur between triplet excitations. The distinction between the two EET processes is made clear by the diagram in Figure 4.1.

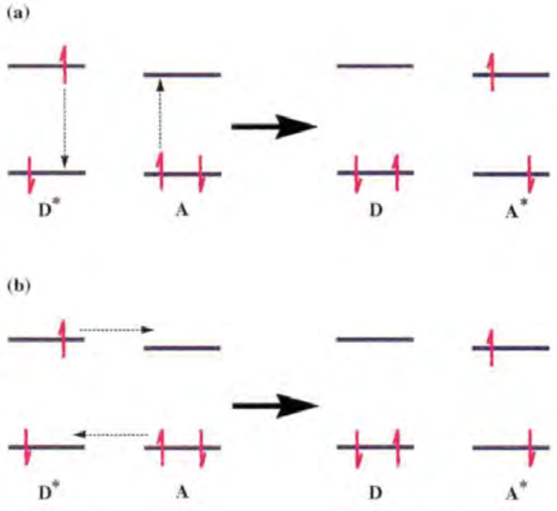

Figure 4.1: Schematic representation of the two possible excitation energy transfer mechanisms. D labels the donor molecule, A is the acceptor molecule. In a), the Forster process, a dipole-dipole transfer occurs. In b), the Dexter process, electron exchange occurs. The net effect is the same in both cases. [50]

4.2 EET in photosynthesis

The goal of photosynthesis is the conversion of light energy from the sun into chemical energy that is usable by a biological organism. For that purpose, a light absorbing pigment is used — Chlorophyll. Chlorophyll-a (Chl-a) absorbs in two major peaks, at 670 and 430 nm (1.9 and 2.9 eV). A complex photosystem uses the energy absorbed to drive an uphill chemical reaction. However, in order to increase efficiency, several Chl-a are present in a single photosystem. They are assembled in a light-harvesting antenna, which makes very effective use of excitation energy transfer. It consists of connected rings of Chl molecules, arranged in a precise geometry (see Figure 4.2). Incoming light can send any single Chl molecule into an excited electronic state. Once this happens, the energy is transferred along in the ring by excitation energy transfer. Energy transfer also occurs between rings in a directed way because of decreasing excitation energies: the 850nm excitation (B850 in LH-II in Figure 4.2) transfers to the slightly lower energy 875nm excitation of LH-I. It then is transferred to a reaction center RC, where the excitation energy is utilized for chemical purposes. The light-harvesting antenna system increases the efficiency of the overall photosynthetic system by about two orders of magnitude, in addition to allowing the absorption of a broader range of wavelengths of incoming light [51].

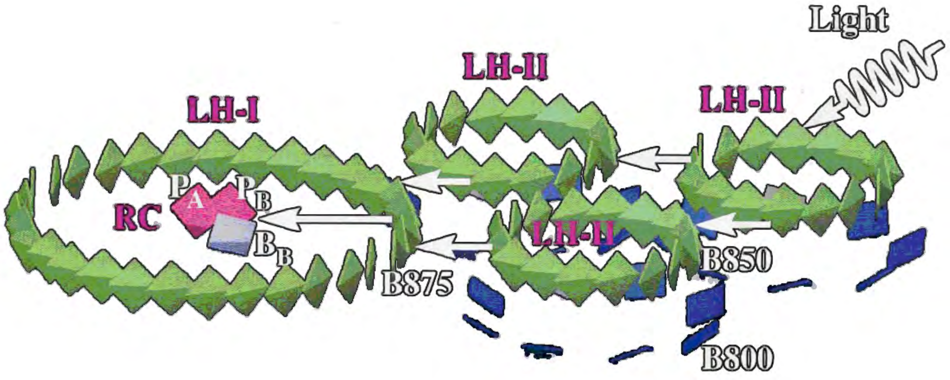

Figure 4.2: Schematic of the excitation energy transfer pathways in the light-harvesting antenna in purple bacteria. [50]

The natural light-harvesting antenna systems have inspired researchers and chemists to create their own molecular macrostructures capable of EET. Giant porphyrin wheels have been synthesized as photosynthetic antenna analogs [52]. Photon-harvesting polymers of several kinds have been realized [53] — these were reviewed by Webber [54]. EET has been used to increase organic solar cell efficiency [55]. Researchers attempting to produce artificial photosynthesis [56, 57, 58] have also used artificial light-harvesting antennae [59, 60] in an attempt to mimic nature.

4.3 EET for Information Transfer

Excitation energy transfer has several properties that make it attractive as a possible method for transmitting information on a nanometer scale. The transfer is spontaneous; it requires no driving potential difference, such as what is needed to move an electron from point A to point B. The timescale for the energy transfer, even over fairly long distances, is of the order of tens to hundreds of picoseconds [51]. For instance, in the light-harvesting antennae of purple bacteria, excitation energy is transferred a distance of several nm in less than 100 picoseconds.

Several researchers have taken steps in the direction of using EET as a tool for information transfer and possibly logic. For example, Salman et al. [61] have been able to design bichromophoric molecules that perform full addition (a logic function) in a molecular system. EET can also occur between quantum dots, and Crooker et al. [62] used layered assemblies of quantum dots to engineer the flow of energy between the dots. This principle was further used by Klar et al. [63] to funnel excitons to a particular layer in a multi-layered nanocrystal system, increasing the overall luminescence yield.

The molecular line structures described in Section 3.1.2 have some characteristics that are analogous to the light-harvesting antennae of photosynthetic systems: both are well-defined molecular superstructures where relatively large molecules are aligned in a fixed orientation. It occured to us that a line composed of the right molecule might show EET on a Si surface, and could be a prototype for a novel way to transfer information on a surface.

Our experimental goal was to use STM to demonstrate excitation energy transfer along a molecular line on a surface. In photosynthesis and in bulk luminescence studies, molecules are normally excited using light. These methods provide high signal-to-noise, thanks to the ability to probe a large number of molecules simultaneously. In our experiment, we wished to have highly localized excitation, so that we may excite individual molecules with high lateral precision. Therefore, in our case the current from the STM tip will be the source of the excitation, which will give us sub-Angstrom precision. We will also be able to acquire STM topography images in the same experiments. A schematic of the proposed experiment is shown in Figure 4.3.

In order for this experiment to be realized, a STM capable of collecting light emission data is needed. The following section contains a review of instruments with this capability and a description of the instrument we designed.

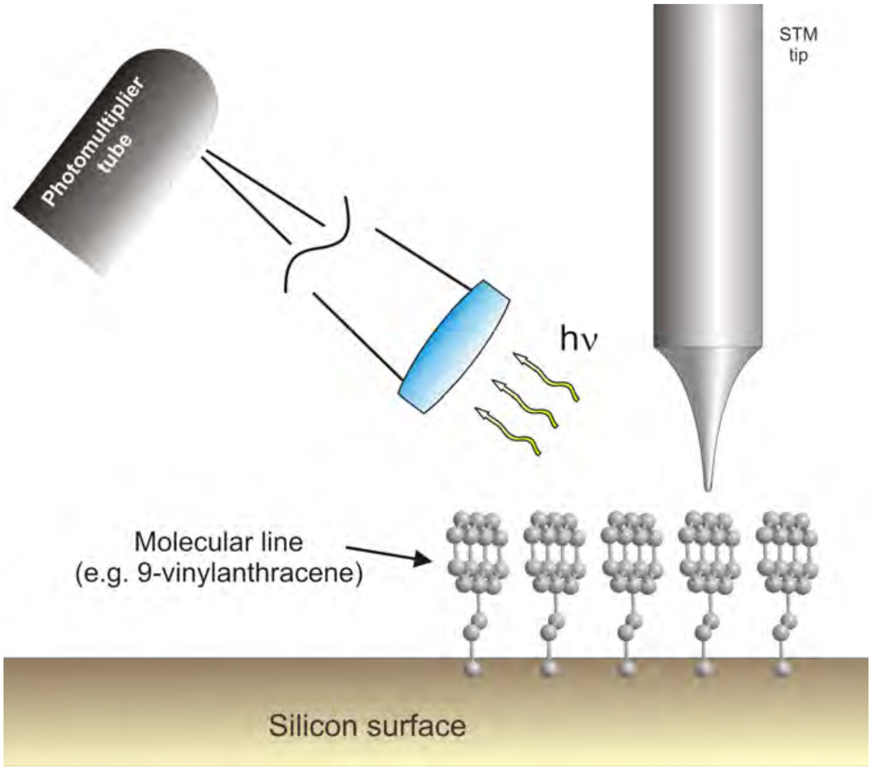

Figure 4.3: Schematic of the experiment for STM detection of EET.

4.4 Instruments for Detecting Photon Emission from the STM

The first detection of light emission from a STM tip was performed by Gimzewski et al. [64] in 1988. To detect the photons emitted from the sample under STM, they simply placed a photomultiplier tube on a viewport facing the vacuum gap. The small solid angle of acceptance resulted in low counts (50 cps/μA being typical), but the authors were able to see photon emission from Si(111)-7×7 at tip-sample biases above 10 V. Later contributors were able to use the technique to observe a III-V heterostructure junction with nm resolution [65]. A more capable instrument was build by Berndt et al. circa 1991 [66]. Berndt's instrument significantly improved the photon collection efficiency by placing an ellipsoidal reflector in the UHV chamber, with the tip-sample contact point being at the focus of the reflector. The photons emitted at the STM tip were collected by a photomultiplier or spectrometer situated outside of UHV. With this improved instrument, Berndt et al. were able to detect photon emission from a single molecule of C_{60} [67]. Typical count rates were of 400 photons/second at a 4 nA tunneling current, at a temperature of 5 K. These early STM-induced luminescence experiments were reviewed by Samuelson et al. [68] and Berndt et al. [69].

We modified our multiprobe STM instrument (see chapter 5) to collect photons from the tip-sample interface. Because of space limitations, we opted to use lenses rather than mirrors to concentrate the light emitted from our STM. A ray-tracing diagram of the lenses used is shown in Figure 4.4. All lenses and viewports used were made of high-quality UV fused silica, which transmit a greater range of wavelengths in the UV region of the spectrum. A small biconvex lens (10 mm diameter, 12 mm focal distance) is mounted in UHV. Light from the tip-sample region is focused by the lens and made nearly parallel to travel about 25 cm to reach the flat UHV viewport, leaving the UHV chamber. A planoconvex lens refocuses the beam onto a Hamamatsu cooled photomultiplier tube. Ray-tracing calculations show that the spot size at the PMT for all wavelengths of interest will be sufficiently small to be fully captured by the PMT. This arrangement collects light in a solid angle spanning 0.45 sr — or about 3.6% of the total light emitted, assuming uniform angular distribution.

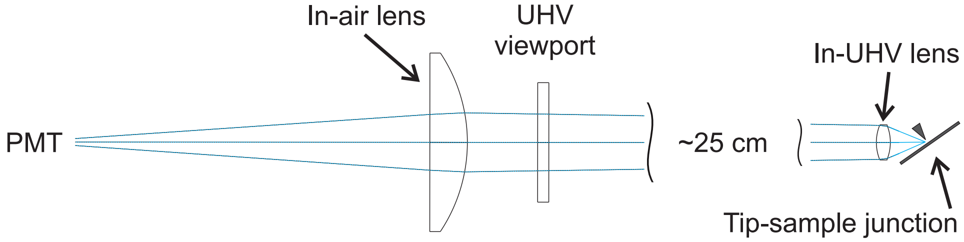

Figure 4.4: Scale ray-tracing diagram of the lenses used in the STM photo-emission setup.

The in-vacuum lens is mounted on the arm of the left probe of our multiprobe STM — see Figure 4.5. This probe is mounted on a custom-made 3-dimensional UHV stick-slip coarse mover (see Section 5.4). This arrangement allows us to move the lens in the X, Y and Z directions so as to adjust its focus optimally. Rotation of the lens is not possible; it is not necessary since a slight lateral offset can correct for small errors in the angular alignment of the lenses. The left probe arm was modified so as to allow the use of either the lens or the usual STM tip in the left probe — but if a tip is present it is not possible to move the lens into focus without hitting the sample with it.

To hold the out-of-vacuum lens and the PMT onto the vacuum chamber, a focusing assembly was designed (see Figure 4.6). It consisted of an outer cylinder clamped down on the exterior of a UHV window flange, holding the plano-convex lens fixed. A second inner cylinder was mounted to the PMT, and its position inside the outer cylinder could be adjusted for focusing. The assembly was made light-tight. The PMT was mounted in a water cooled thermoelectric chiller which maintains a temperature below -25 C, reducing the dark count of the PMT.

4.5 Photon Emission from Organic Molecules

As mentioned in Section 4.3, the goal of our experiment was to observe excitation energy transfer along a line of organic molecules on Si. A wide variety of materials have been reported to show STM-induced light emission: semiconductors such as InP [70]; GaAs/AlGaAs quantum wire structures [71]; and small metal clusters [72]. Thirstrup et al. [73] were able to observe light emission from a pattern of dangling bonds on a H-Si(100)-3×1 surface.

Light emission from organic molecules has also been reported in several instances in the literature. Cavar et al. [74] performed fluorescence spectroscopy on single C_{60} molecule. Fluorescence spectra were obtained from films of porphyrin molecules

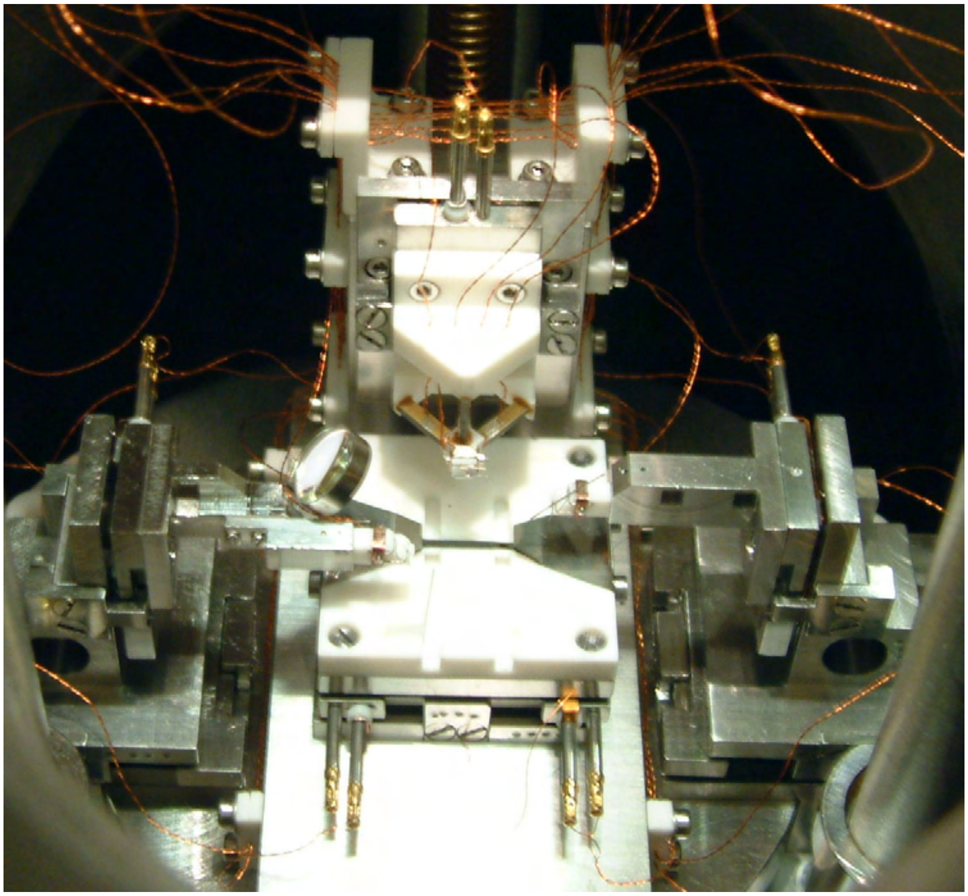

Figure 4.5: Photograph of the multiprobe STM instrument equipped with an in-vacuum lens on the left probe. The right probe is equipped with only a tip holder. The STM tripod scanner can be seen in the center, above a movable 2-D sample stage.

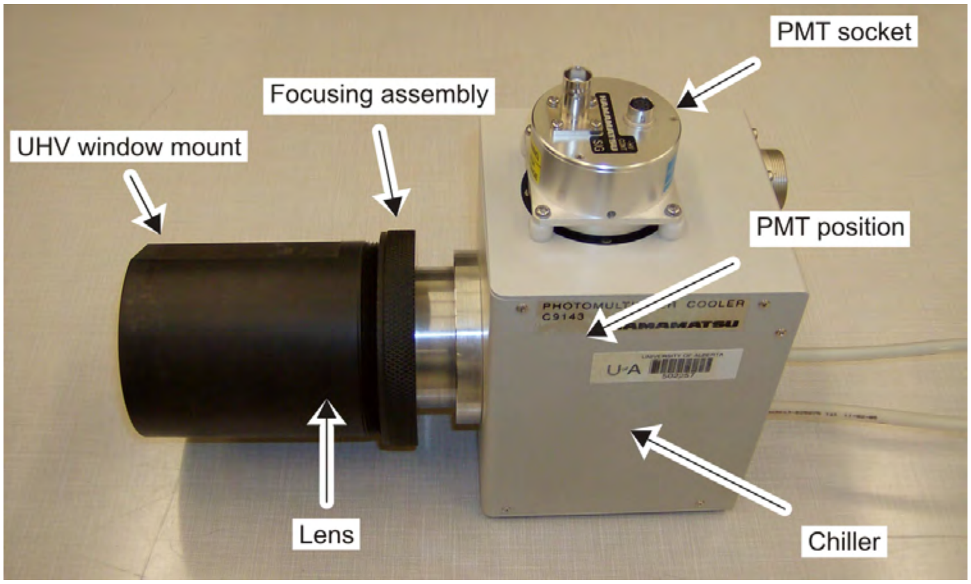

Figure 4.6: Photograph of the photomultiplier tube chiller, UHV window mount, lens and focusing assembly.

on Au(100) [75, 76], Ag [77], and Cu(100) [78] substrates. Qiu et al. [79] were even able to locally excite different parts of a single large porphyrin molecule.

If an organic molecule excited by the STM tip is too close to a metal, its fluorescence is "quenched" — the electron energy is transferred to the metal at a much faster rate than it can re-radiate as fluorescence [80, 81]. In the cases where light emission from organic molecules was observed, the experimenters took steps to avoid coupling the molecule to the metal surface. Some used multiple monolayers of the same molecule [75, 76, 78, 77], others used a thin insulator layer such as an oxide [79] or a NaCl film [74].

One significant issue with our attempted experiment was the possible quenching of the organic molecule fluorescence with the bulk Si. The excited moiety of the molecule is normally only a few Å from the surface — the exact length depending on the molecule: an allylbenzene would be spaced further out than a vinylbenzene, for instance. This very close proximity increases quenching. Some experiments on metal surfaces required more than 3 monolayers of molecular coverage to observe fluorescence [75]. On the other hand, Qiu et al. [79] observed fluorescence of a molecule separated from a metal surface by an insulator less than 5 Å thick.

One factor working in our favor is that our organic molecules are above a semiconductor rather than a metal [82]. In a metal, the absence of a band gap means that even the lowest energy photon can create an electron-hole pair. Si has a band gap of 1.12 eV, so any photons below that energy could not be absorbed in that way. In addition, the band gap of Si is *indirect*, giving a much smaller rate of photon absorption since it requires the simultaneous absorption or emission of a phonon. The direct band gap of Si is above 3 eV. These factors point in the direction that organic molecules on Si may fluoresce even at close distances, whereas the same spacing on a metal might fully quench fluorescence.

If excitation energy transfer does occur along molecular lines, we hoped to observe it in a variation in photon emission intensity along a line. For example, one might expect to get less light emission near the ends of a line, since fewer acceptor molecules are nearby that might accept the excitation energy. The presence of a nearby molecule with different electronic character could have resulted in light emission of a different color, which would be revealed by spectroscopy.

4.6 Experimental Methods

To keep out stray light, all the viewports of the UHV chamber were covered with two layers of light-blocking black fabric. The STM tip was then brought within tunneling range of the surface. The in-vacuum lens was positioned by observing by eye the image of the tip-sample junction and attempting to center it in view. This was likely the most error-prone part of the experiment — a better procedure would use a known light source at the tip-sample junction, which could then be aligned by maximizing the photon count as the in-vacuum lens was aligned. Unfortunately, such a device was not readily available.

The Hamamatsu PMT was connected to a Ortec 9302 Amplifier Discriminator unit, which takes in the pulses from the PMT and amplifies the ones exceeding a certain discriminator threshold to produce clean pulses. The discriminator level was set to the lowest level that would not generate spurious pulses due to noise. This output could then be connected to a pulse counter which simply counts all the photons received within a set period of time. The output of the discriminator could also be connected to an Ortec 449 Log-Lin Ratemeter, which counts the rate of incoming photons and outputs a DC voltage proportional to that rate. The ratemeter has many range settings, from as low as 10 cps up to 10^6 cps; and can also output a DC voltage proportional to the logarithm of the rate. A time constant setting (from 0.03 to 30 seconds) smooths out the signal.

The ratemeter was equipped with a 0 to +10 V analog output which scales to the displayed value (e.g. on a 1000 cps scale, a value of 500 cps outputs +5 V). This analog output was fed into the STM electronics' additional ADC input. During

STM imaging, this value could be recorded digitally at the same time as the usual signals of topography and tunneling current, giving a map of light emission intensity.

For use as samples, surfaces of H-Si(100)-2×1 were prepared in the usual method. The prototypical molecule used to grow line is styrene, containing a single benzene ring. Larger molecules typically have smaller HOMO-LUMO gaps, which would make electron excitation achievable at smaller energies. Therefore, we also considered the growth of lines of 2-vinylnaphthalene and 9-vinylanthracene (Sections 3.2.2 and 3.2.3), since these molecules contain two and three benzene rings respectively. Unfortunately, 9-vinylanthracene did not reliably form well-ordered lines and was not usable for this purpose.

4.7 Experimental Results

The first test of the light-collecting apparatus involved counting the number of incoming photons with the tip out of tunneling, and comparing to the count while in tunneling. The sample used was a medium-doped (0.01 Ω·cm) n-type clean Si(100). With no discriminator used, a dark rate of 9.5 cps was obtained. With the lens aligned, and the tip in tunneling with a sample bias of +5 V and a tunneling current of 10 nA, a rate of 1520 cps was measured. With the sample bias lowered to +4 V, the rate dropped to 168.8 cps, still significantly higher than the dark rate.

Next, we attempted to take simultaneous STM images while imaging a H-terminated Si(100) surface which was dosed with 15 L of styrene. Figure 4.7 shows side-by-side topography and photon map images taken at −2 V and 3 nA — an unusually high current. The horizontal streaks in the photon map image correspond to single photon detection events, primarily dark current, smoothed out by the ratemeter electronics. There are some indications of higher photon emission in areas with higher density of styrene lines (near the center of the image), but the rate is so low that it could simply be coincidental. A significant increase in photon count can be observed by going to higher energy conditions, e.g. −3.5 V and 5 nA, however these tunneling parameters are so intense as to completely destroy the styrene lines on the surface as the tip scans.

Similar results were obtained on a surface covered with vinylnaphthalene lines — significant photon emission was only observed at imaging conditions so harsh as to damage the lines. Figure 4.8 shows an example where a very high sample bias of +6.5 V was used. The topography image shows several features which appear during scanning (lines were scanned from the top down), and there is frequently a corresponding bright point of photon emission in the photon map. Photon counts

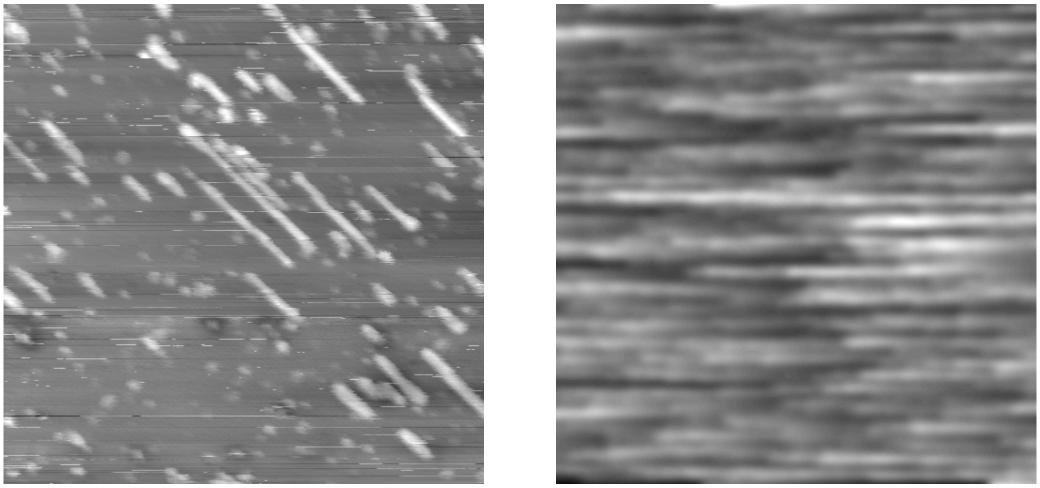

(a) Topography view, 85 nm width.

(b) Photon map (white = 15 cps) with 5 pixel radius blurring for clarity. Ratemeter time constant of 0.1 sec.

Figure 4.7: STM images and photon map of H-Si(100)-2×1 with styrene lines (-2 V, 3 nA). Scan speed: 3 lines/sec. No significant light emission is seen corresponding to the styrene lines.

are approximately 100 times higher than in the more gentle conditions used in Figure 4.7.

From these results, we concluded that no light emission can be seen from a styrene or naphthalene molecular line at imaging conditions that preserve the structure of the molecular line. Measurable photon emission seems to only occur when destructive events occurred — presumably, the breaking of bonds in the molecule, or the deposition of "dirt" by the tip. Our experiments cannot determine why light emission was not observed. It is possible that the cross-section of inelastic excitation of a styrene or naphthalene molecule from a tunneling electron is too low at the imaging conditions used. Even if electron excitation does occur, it might be quenched by the Si bulk at a faster rate than the rate of photon emission.

4.8 Possible Improvements

The negative results obtained with out setup, as described in Section 4.7, showed that it was not possible to obtain light emission from a molecular line on Si without destroying it. Since our project to see excitation energy transfer along a line of molecules required good signal to noise so that we might see subtle differences in intensity or color along a single line, it was clear that this goal could not be reached

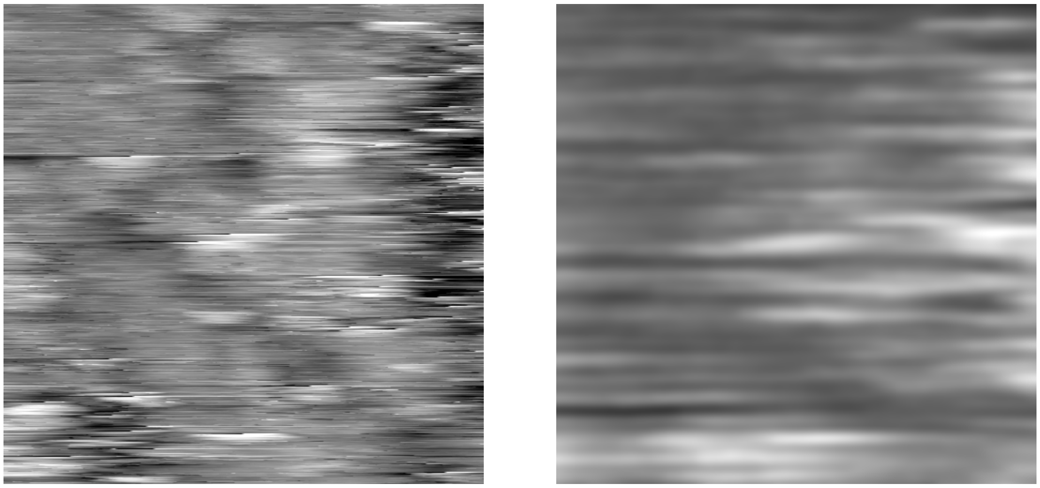

(a) Topography view, 42 nm width.

(b) Photon map (white = 1500 cps) with 5 pixel radius blurring for clarity. Ratemeter time constant of 0.1 sec.

Figure 4.8: STM images and photon map of H-Si(100)-2×1 with vinylnaphthalene lines (+6.5 V, 1 nA). Scan speed: 2 lines/sec. Some of the light emission features seem to correspond to destructive events caused by the harsh imaging conditions.

— we thus chose to abandon the project. From our experience in photon emission from STM, we have determined some improvements that might lead to success:

- Improving the light collection efficiency would directly increase photon counts. For example, the ellipsoidal reflector used in Ref. [66] had a collection angle of nearly 1 sr, which is more than twice what we achieved with lenses. A purpose-built STM could increase this collection angle further. For instance, if the sample were transparent, light could be collected frome *below* the tunneling junction, and one could imagine light collection of a solid angle of up to 2π sr — 14 times more than in our case.

- Aligning the lenses so as to focus perfectly on the tip-sample interface was difficult. A sample that could be lightly touched by the STM tip and produce a large number of photons would have been very useful.

- Larger molecules typically have smaller HOMO-LUMO gaps, meaning that they would be more easily excited by tunneling electrons. If a very large molecule known to fluoresce could be induced to grow lines in an ordered way on Si, this could make the excitation process much more efficient. Unfortunately, it is usually problematic to grow lines of large molecules.

- Reducing the possibility of quenching by the Si surface could be done in a few ways: by depositing a thin insulator layer (such as NaCl) or by using a material with a very wide bandgap (e.g. diamond). In both these cases, STM is difficult (since the sample conductivity is low) and it is unknown if molecular lines would grow on these surfaces.

- Line-growing molecules could be designed such as to space them further from the Si surface, thereby reducing quenching. Allylbenzene, for example, has an extra carbon bond between the terminal carbon and the benzene ring.
- The molecule could be excited in a different way: by placing the tip close to a molecule and using a tuned laser to excite it. Here, we would rely on a local field enhancement effect similar to that which gives surface-enhanced Raman spectroscopy [83] such high signals. However, it is likely that the excitation area would be much larger than a single molecule. Molecular lines would have to be significantly longer than the excitation radius in order to see an excitation energy transfer effect.
- With sufficient photon counts obtained with these improvements, it would then be advantageous to equip the optical system with a grating spectrometer and camera such as that described in [84] to obtain real-time spectral information on the color of emitted light. This would of course require orders of magnitude of improvement in photon counts.

4.9 Conclusions

In this chapter, we presented our idea for a new type of nanoscale information transfer based on excitation energy transfer (EET). We began with a review of EET and showed an example in nature where it is used: light-harvesting antennae in photosynthesis. Next we suggested that the self-assembled molecular lines described in Chapter 3 might be candidate to observe EET. The technology used to detect light emission from a STM was reviewed, along with several results of light-emission from organic molecules detected from a STM. We described the experimental setup we used to attempt to detect photons in our multi-probe STM. The results we obtained showed that we could not observe photon emission from our molecular lines except in feedback conditions that were destructive for our molecular lines. We next presented several ways by which this experiment might be completed.

Chapter 5

Multiprobe STM Hardware

5.1 Introduction

Performing the characterization of nanometer-scale objects requires the technology to probe surfaces with very high accuracy. The scanning tunneling microscope allows atomic imaging of surfaces, but the ways to characterize a material are very limited if only a single tip is available. Therefore, an instrument with several probes, each capable of atom-resolved STM, would be extremely valuable.

Much of my Ph.D. work was related to bringing such an instrument to fruition, our multiprobe STM. This machine was designed and built primarily by Mark Salomons, an engineer in our group. In this chapter we will describe the unique characteristics of the multiprobe hardware. The control software written by the author and used with the machine will be described in Chapter 6.

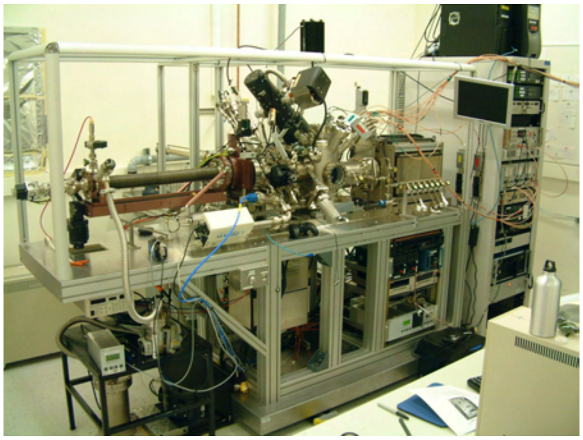

Figure 5.1: Photograph of the multiprobe STM UHV chambers, pumps, frame, and associated hardware.

5.2 STM Tripod Scanner

The main (central) STM in the multiprobe machine uses a tripod scanner, with 3 separate single-crystal piezoelectric elements (see Figure 5.2). This geometry is advantageous because unlike a tube scanner, there is very little cross-talk between channels — changing the voltage on the Z piezo does not significantly change the X or Y positions.

The single-crystal piezos used are said to be less susceptible to piezo "creep" — where after a sudden change in applied voltage, the piezo continues to respond slowly for many seconds or minutes. This creep appears after a sudden change in scan window position, and shows up as a curvature in the image as the creep subsides. In practice, we have indeed found piezo creep to be much less significant with these single crystal piezos as compared with standard tube scanners.

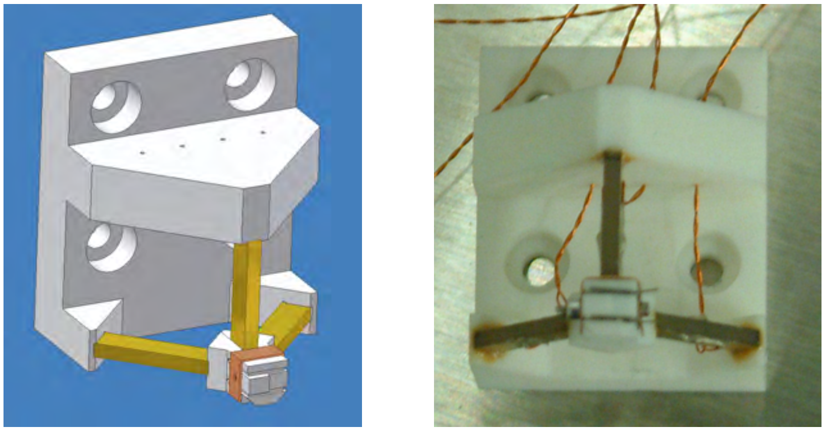

(a) Line drawing of the scanner design.

(b) Photograph of the scanner.

Figure 5.2: The main STM's single-crystal tripod scanner.

5.3 Probe Scanners

Originally, the left and right probe tips were mounted on rigid metal arms incapable of scanning. Our plan was to use the piezos in the coarse motion plates for movement, but this was not successful (see Section 5.4.2).

The rigid arms were therefore replaced with tube scanners, pictured in Figure 5.3. These allow full, 3-dimensional fine scanning with atomic resolution. Because of space limitations, tripod scanners could not be used for the left and right probes so we have had to contend with the larger piezo creep. However, the larger motion of the tube scanners relative to the single-crystal piezos is an advantage for probing without requiring coarse steps.

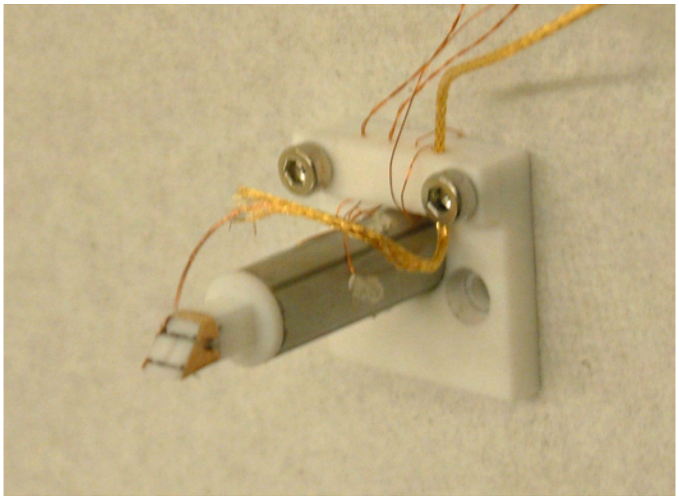

Figure 5.3: Photograph of the tube scanner and tip holder for one of the probes of the multiprobe STM.

Note that the tube scanners are not mounted in the typical vertical configuration, when the Z direction (tip height) is in the same direction as tube extension/contraction. Instead, we must use the tube sideways bending motion as our Z direction — this is a simple matter of switching connections. Tube scanners typically have less sensitivity in the extension direction (normally Z) compared to the sideways (normally X and Y) motion; this means that we have asymmetric piezo sensitivities in our X and Y. This can be reduced by using a larger high-voltage amplifier gain on the tube extension channel, which in our setup is labeled X. Any remaining asymmetry is easily handled by the scanning software, which normally sets the amplitude of the scan voltages used so as to achieve a square scanning area in real space when the piezo sensitivities are known.

5.4 Coarse Motion

5.4.1 Stepping Action

The piezoelectric elements used for STM scanning are only capable of a few microns of travel. For longer-range motion, *coarse movers* are used. These can operate in several different ways; for UHV operation, the stick-slip type mover is commonly used. This consists of two parallel plates mounted with shear piezos (piezoelectric elements where the motion is perpendicular to the applied field) riding on smooth surfaces (such as sapphire rods and plates).

Figure 5.4 shows the steps in a coarse approach using stick-slip movers: a) The mover is at rest, no voltage is applied to the piezos. b) A slow ramp voltage applied to the shear piezos, which move downwards, taking the movable plate along. c) The voltage applied to the piezos is rapidly switched to the opposite polarity. This motion is rapid enough that the movable plate does not stick to the shear piezos, but rather stays in place due to inertia. d) The voltage is slowly ramped back down to zero, with the movable plate following suit. The movable plate has now moved down a certain amount, and another step can be taken.

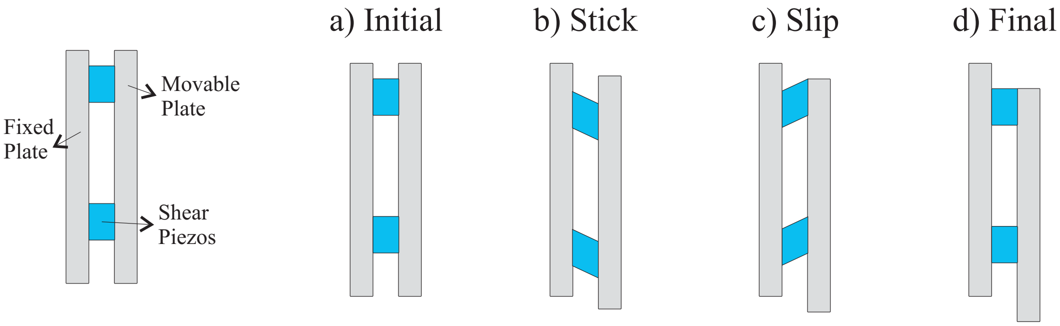

Figure 5.4: Steps in performing a coarse motion step using a stick-slip mover. See text for details.

Early in the use of the coarse motion controller we found them to be unable to reliably move our custom-built coarse movers after a 150 C bake. We went through several iterations of different materials used in the coarse movers before finding that the electronics were not dropping voltage quickly enough in the “slip” step (Figure 5.4 c). Modifications to the electronics fixed this problem.

5.4.2 Fine Scanning With Coarse Movers

Another feature of the Coarse Motion Controller is the ability to apply a constant high-voltage DC output on the shear piezos used for slip stick motion. While this feature significantly increased the complexity of the controller electronics, it allowed us to move the shear piezos in unison with sub-nm precision — giving us 3-dimensional control on the position of the probes. Our intention was to use this capability to perform fine STM scans with both probes, without needing any additional hardware in UHV.

Several issues arose with this strategy. One problem is that the shear piezos have a relatively small sensitivity as measured in nm/V. With the limits to the high-voltage amplifier electronis, this limited the scan range in all 3 axes to approximately 600 nm. This of course gave a maximum scan size of only 600 nm. Shear piezos also have significantly more creep than the more usual tube or tripod scanners.

We also found that performing a tip approach was very challenging. This is due to the fact that the same piezos are used both to perform a coarse step and to probe forward to find a tunneling current. As Figure 5.4 b) shows, one of the steps in the coarse motion involves moving the plate closer to the surface. This step is not performed in feedback control, so if the probe tip is sufficiently close, it will crash into the surface. To circumvent this problem, we added a DC voltage during the entire stepping procedure, so as to ensure that during step b) the tip does not get closer to the surface than in phase a) (essentially making a unipolar ramp rather than a bipolar ramp). After each step, the feedback loop is turned on to allow a slow ramp of the tip towards the surface. This means that we effectively only have half the available scan range for approaching, and that we must take correspondingly small coarse steps.

These problems meant that during a coarse step, the probe tip could come as close as 300 nm from the surface. If all components of the scanner were perfectly rigid, this would not be a problem; however we found that during the violent action of a stick-slip step, the end of the tip would vibrate with an amplitude approaching 1 micron. This “whiplash” effect can be seen in the SEM image in Figure 5.5. The step size is much smaller than one micron, yet the tip vibrates with as much as 1 micron amplitude for a fraction of a second after each coarse step. We believe that this caused probe tip approaches to be unsuccessful, crashing tips repeatedly. Switching to thicker tips (0.5 mm diameter instead of the usual 0.25 mm) seemed to reduce the whiplash amplitude by a factor of $\sim$4, and helped make probe tip approaches more successful. In later implementations, the use of a tube scanner (Section 5.3) provided us with enough Z tunneling range that using thick tips to avoid whiplash was not necessary.

Another problem with the coarse movers is that we found that the electronics caused significant 60 Hz noise pick up in the STM tunneling current. This noise was

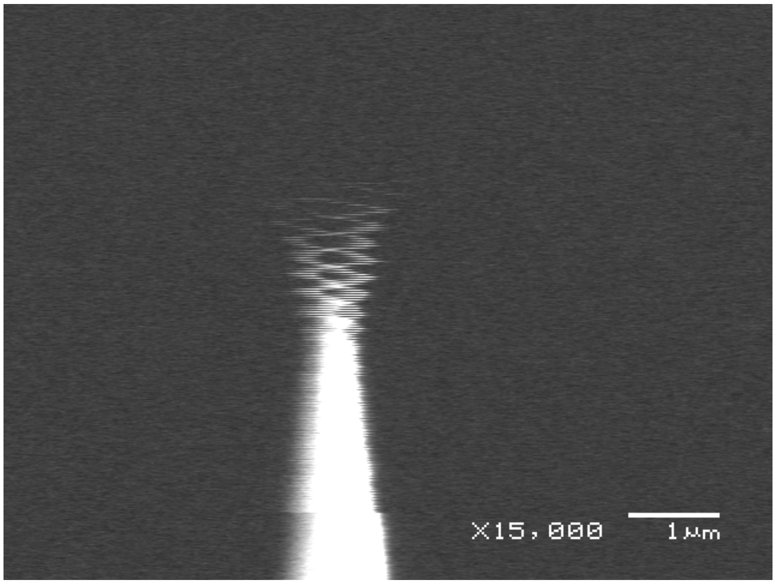

Figure 5.5: SEM image of a tip taken at the instant a coarse step was taken. The oscillations in the image as the SEM beam rasters (from top to bottom) show the $\sim 1\ \mu m$ amplitude of whiplash. 15000× magnification, beam voltage 2 kV.

visible whether or not the tip was in tunneling. Fortunately, the electronics feature adjustable RC filters on the outputs that filtered out nearly all of this noise when turned on. These filters, when on, prevent steps from being taken, so they need to be turned down before coarse steps are to be taken.

5.4.3 Shear Piezo Scanning Results

Figure 5.6(a) shows the best result we achieved when scanning the coarse movers of the sample (for X/Y) and the main STM tip approach (for Z). While the quality is not as high as that obtained with the main STM, Si(100) dimer rows and atomic-scale defects are easily visible. This level of scan quality would be sufficient for most purposes. The results for a shear scan and tip approach on one of the probes are shown in Figure 5.6(b). Atomic resolution was not achieved with the probes — indeed, shear scanning STM images with the probes of surfaces that appeared normal with the main STM regularly appeared as in Figure 5.6(b) — a rough, irregular surface with several nm of topography. We suspect that the whiplash action described previously affects the approach of a probe much more than the main STM, since the probe tip is mounted at a 45 degree angle relative to the sample surface. Any whipping action will be perpendicular to the tip direction; for the main STM's vertically mounted tip, this amounts to very little vertical movement; probe

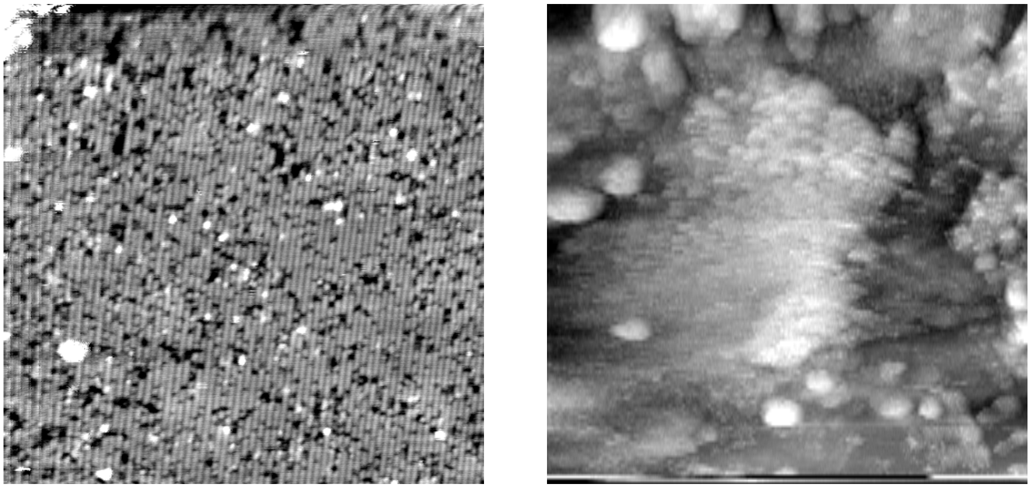

(a) Shear piezo scan STM image using the sample coarse movers for X and Y, and the main STM tip Z coarse mover for Z (~14 nm, −2.6 V, 60 pA).

(b) Shear piezo scan STM image using the left probe coarse mover piezos (~50 nm, −3 V, 100 pA).

Figure 5.6: STM images obtained on Si(100) samples by scanning the coarse movers' shear piezos.

tips might move as much as a micron towards the surface. Thus, it is likely that all the shear approaches using the probes crashed the probe — the subsequent STM images would therefore be unusable.

Because of these difficulties, it was decided that using a conventional tube scanner (see Figure 5.3) rather than the shear piezos would be preferable. This made the in-UHV hardware more complex, especially because of the 10 extra wires required to connect to the X+, X-, Y+, Y- and Z sections of each tube scanner. The custom coarse mover electronics with their DC voltage capability were no longer needed and were later replaced by two commercial Omicron Micro-Slide Control Units.

5.5 Scanning Electron Microscope

The multiprobe machine is equipped with a ultrahigh vacuum field-emission scanning electron microscope (SEM) column from JEOL, model TM-Z040161 — see Figure 5.7. Our multiprobe STM assembly is mounted on a floating table that can be moved up to reach the view of the SEM column, or lowered until springs support the table, providing vibration isolation. While it is possible to perform STM while the table is in the upper position, and therefore in view of the SEM, we do not normally do so because of the much higher vibrations in the machine in that configuration.

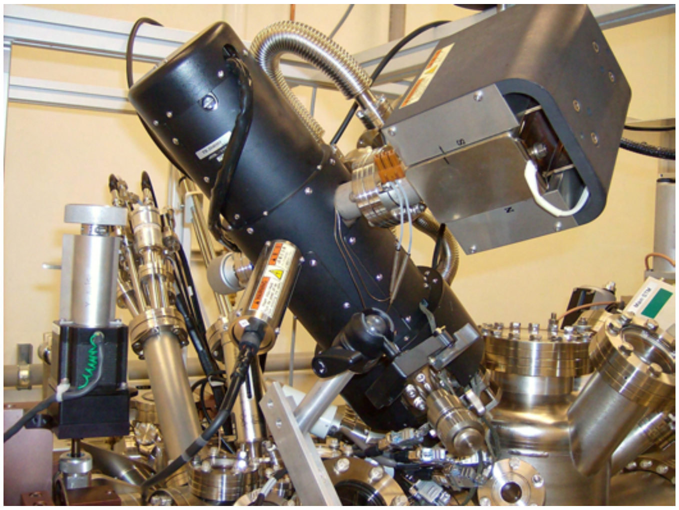

Figure 5.7: Photograph of the JEOL UHV SEM column, mounted on the UHV chamber.

This SEM is specified to be able to reach a resolution of 10 nm (at a 15 mm working distance and 12 kV beam voltage); however in practice a resolution of ≥ 100 nm was all we achieved. The longer working distance required by our geometry reduces the achievable resolution; additionally, the 45 degree mounting angle of the column, relative to Earth's gravity, likely increases the effect of vertical vibrations on the imaging.

The SEM is crucial to performing the fine alignment of tips. To get all 3 probe tips in close proximity to each other, we will typically proceed in this way:

- The STM assembly table is lowered to the STM position (to reduce vibration).
- The main STM tip is approached to the surface under STM control. Since the main STM can only move coarsely in Z, the point where the STM tip meets the sample does not change.

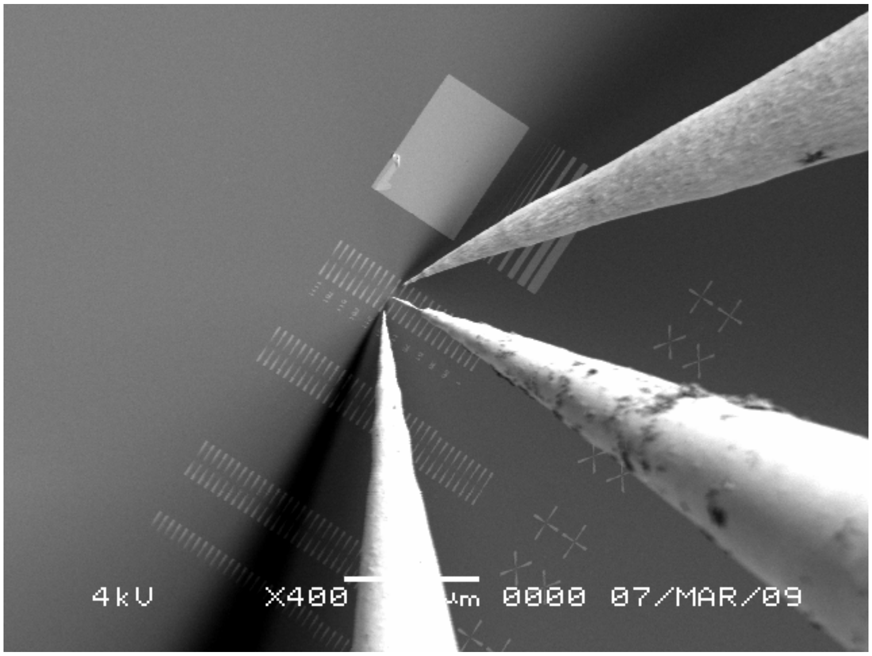

(a) 400× magnification.

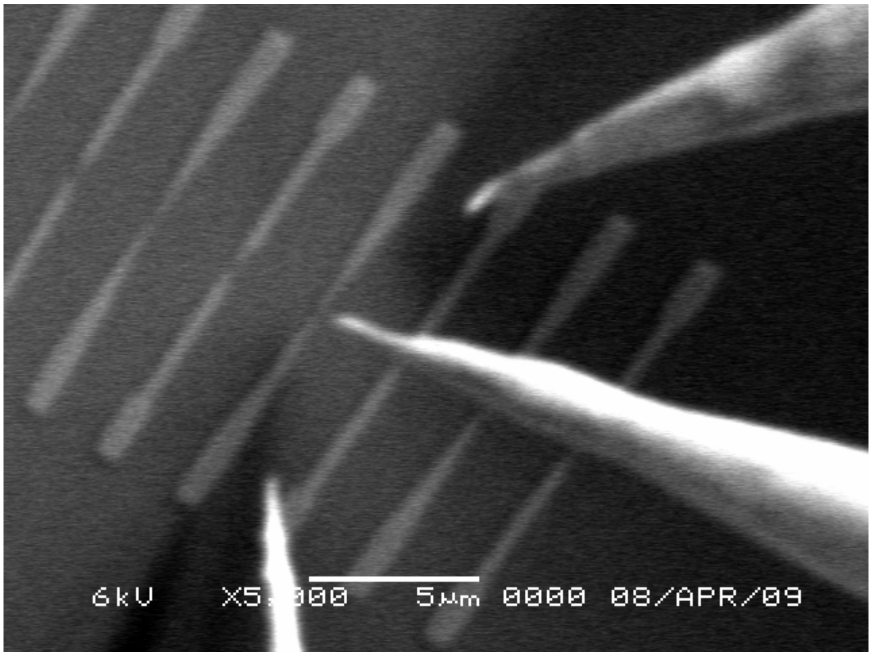

(b) 5000× magnification.

Figure 5.8: SEM images of three STM tips brought in close proximity, over a pattern of metal pads. The spacing between the tips can easily be reduced to below 1 micron.

- The left and right probes are brought close to the main STM tip-sample junction, under magnified camera view.
- Both probes are approached to the surface under STM control. At this point, all 3 probes are close to the surface (known Z), but spaced apart in X/Y.
- All 3 probes are pulled up an equal number of steps (typically 50) to keep them from crashing into the surface.
- The STM assembly table is raised to the SEM view position.
- Under SEM observation, the 3 tips are brought in close proximity. Since the Z coordinate is known from the previous alignment, the X/Y view in the SEM is sufficient to align all 3 probes in 3 dimensions. Figure 5.8 shows the result of such an alignment.

5.5.1 Electron Beam Induced Current Imaging

Electron beam induced current (EBIC) imaging is an alternate way to create an image in a scanning electron microscope [85]. EBIC comes in a few different flavors, which have in common the collection of current using an external, low-noise current-to-voltage amplifier, rather than (or in addition to) collection the secondary electrons emitted from the surface.

An example of the connection diagram for an EBIC experiment observing a pn junction is shown in Figure 5.9(a). The incoming electron beam (with beam current I_b) hits the semiconductor, creating many electron-hole pairs. In the depletion region of the pn junction (of width w), these extra carriers increase the conductivity of the junction. This is observed in the change in the charge collection current I_{cc}. EBIC images can help characterize the pn junction and spatially locate defects.

Our EBIC connection setup is somewhat different, as shown in the schematic in Figure 5.9(b). Rather than have one side of the sample biased and a current continuously flowing, in our setup the sample is floating and the only grounding of the sample is provided by the probe touching the surface. EBIC current is measured via the same preamplifier used for STM, though usually at a lower gain (typically 10^6 V/A). The voltage produced by the preamp is fed back into the electronics instead of the typical voltage from the secondary electron detector. A simple manual switch box allows one to select between the two (though in general it would be possible to set up SEM electronics to record both signals simultaneously, this was not done in this case).

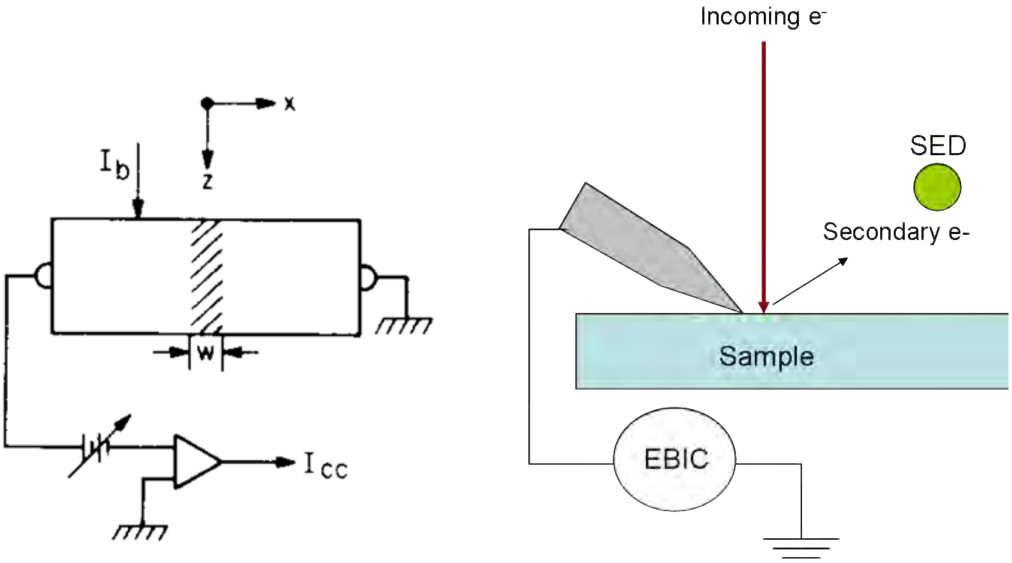

(a) Schematic of a normal EBIC connection diagram for imaging, for example, a pn junction. From Ref. [85]

(b) Schematic of the connections for our EBIC imaging mode.

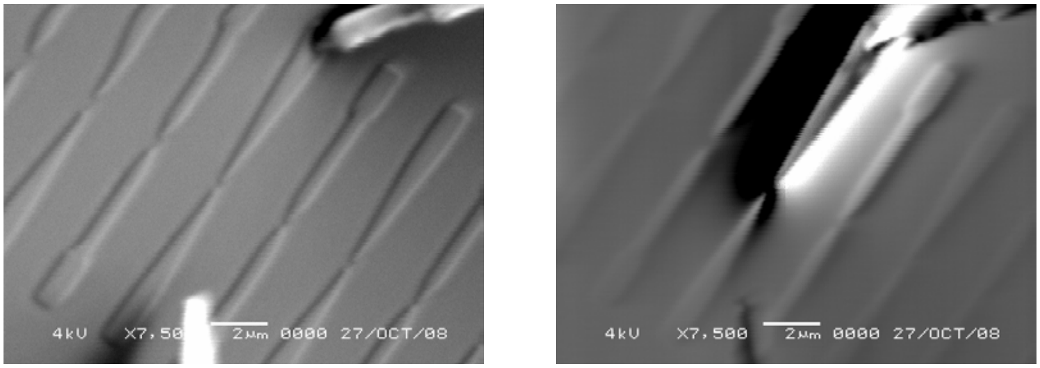

(c) Secondary electron current image of a metal contact structure, with the left probe touching down and grounding one of the contacts (7500× magnification, beam voltage 4 kV). The right probe (bottom) is not touching the surface.

(d) Electron-beam induced current image of the same situation, with 10^6 V/A preamp gain.

Figure 5.9: EBIC schematics and sample images.

A SEM secondary electron image and its corresponding EBIC image are shown in Figures 5.9(c) and 5.9(d). In this sample image, we can see the way our setup creates EBIC contrast: the EBIC image's appearance depends on the speed and direction of the electron beam rastering. The electron beam scans from left to right and from top to bottom. When a metal pad is grounded and the current is collected, as shown, the semiconductor on the left side of the contact appears dark, and the right side appears bright. The exact source of this peculiar contrast is unclear; perhaps the crystal undergoes some charging/discharging near the metal contact, which generates a current that depends on the history of the beam location. The size of the dark/bright regions appears consistent with the scattering volume of high-energy electrons entering a material.

Figure 5.9(d) shows clearly that a break in a metal contact breaks the connection to the preamp and the contact on the lower left does not show the same dark/bright contrast in EBIC mode. Therefore, this EBIC imaging mode can be put to good use to determine whether a metal contact is continuous or not. This will be used in Section 7.6.

5.6 Pliers and Sample/Tip Loading

5.6.1 UHV Pliers

A unique feature of our instrument is the way samples and tips are loaded. Most UHV-STM instruments use a sample holder where the crystal under observation is clamped or epoxied; tips are similarly carrier in tip holders. In the multiprobe STM, only raw (unsupported) crystals and tips are used.

This requires the use of in-vacuum pliers, designed and built by Mark Salomons — see Figure 5.10. These consist of four jaws: two lower fixed jaws, and two upper mobile jaws, which can close to grip a sample or a tip. The size and spacing of the jaws limit the usable sample size to a width of at least 12 and no more than 14 mm. Similarly, STM tips need to be close to 14 mm in length to be usable.

The pliers are mounted on a continuous rotation rotary flange which allows the hardware to be rigidly mounted without flexible wires in vacuum (e.g. for flowing current). The outside pressure is separated from the UHV side by three seals, defining two chambers which are pumped by a small turbomolecular pump and a 2 L/s ion pump.

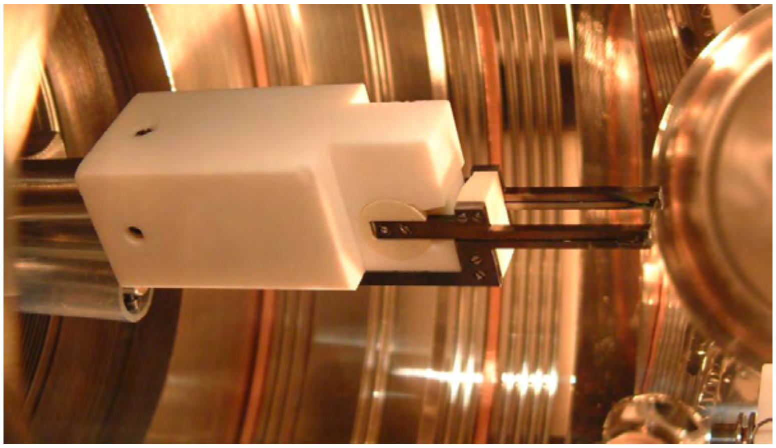

Figure 5.10: Photograph of the pliers used for sample and tip transfer in the multiprobe STM.

5.6.2 Sample and Tip Handling

Samples are typically cleaned by in-vacuum annealing performed by direct current heating through the sample. In traditional machines with sample holders, a lengthy degas period at a lower temperature (typically 600-700 C held overnight) is normally performed. This is primarily to degas the sample *holder*, which sits out of vacuum for extended periods of time. With the raw crystal design, the pliers stay in UHV at all times. For best results, the pliers are degassed with sacrificial crystals — an old or unneeded sample will be heated at 600 C overnight. The crystal is then thrown out, and the pliers will remain clean for a long time. Once the pliers are degassed, samples can be degassed in only a few minutes with minimal contamination. This can increase the throughput of the machine to several samples per day, if needed. It also allows fragile samples to be annealed more gently, by skipping the overnight degassing step.

Samples are held in the STM spot by flexible tantalum foil of 0.05 mm thickness. In the load-lock and in-vacuum storage, the sample simply sit in a groove thanks to gravity.

Similarly, STM tips are handled without tip holders. Raw tungsten wires are picked up and can therefore be heated in the pliers. The pliers typically have to be slightly open so as to avoid draining heat away from the sharp pointed end. This thorough degas of the STM tips and probes similarly helps keep samples as clean as possible. Tips are held into position using small tungsten spring clips.

Another advantage of using raw samples and tips is that when they are no longer needed, they do not need to be load-locked out of the vacuum chamber —

we can simply dispose of them in a small, in-UHV garbage can. The contents of the can are emptied occasionally, when another issue requires breaking vacuum in the preparation chamber.

5.6.3 Pliers Controller

The pliers are mounted on a long flexible bellows; the motion of the pliers is operated by a five-axis stepper motor controller by the Technical Manufacturing Corporation (TMC). Two of the axes control the X and Y motion of the bellows, allowing movement within a 2 inch diameter disk. The Z motion spans most of the length of the machine (approximately 20 inches), which allows the pliers to be moved from the preparation chamber to the STM chamber for tip or sample loading. A fourth axis controls the rotation of the pliers — since they are mounted on a rotary flange, continuous rotation is possible (although wiring can restrict it). The final axis is a push-pull rod, which reaches in UHV up to the pliers to push the jaws closed. Springs are used to open the jaws when the rod is pushing against them.

The TMC stepper controller is equipped with a handheld remote which allows one to move each axis at preset speeds, or to seek known positions. However we quickly found that a finer degree of control was necessary in order to do the precise manipulation needed to load tips and samples. Therefore, we designed an alternate control system which uses the wireless Logitech handheld gaming controller pictured in Figure 5.11.

Figure 5.11: Photograph of the wireless gaming controller used to control the pliers.

This control system operates via a small program written in Visual Basic 6 which monitors the state of the remote and sends commands via RS-232 to the TMC stepper controller box. Compared to the supplied remote, the gaming controller has many advantages. Primarily, the ergonomics are much better, and it can be used without looking at the controller. The joysticks on the controller allow continuous variation of the speed of the Z motor. The speeds are switchable using the triggers, and several motors can be operated at once. In addition, position setpoints can be saved and recalled at anytime, which saves time when performing fine alignment repeatedly. Extra features can be added or keys can be remapped by modifying the program.

5.7 Field Ion Microscope

Invented in 1951, the field-ion microscope (FIM) is the first experimental technique that provided direct imaging of individual atoms [86]. The FIM imaging process is based on the projection of ions away from the field at a very sharp metal tip. A large positive potential is applied on a sharpened metal tip. With the point of the tip having the smallest radius of curvature, it develops the strongest field locally. A gas such as hydrogen or helium is introduced in the vacuum chamber. When an atom is near a critical distance from the tip (~ 0.4 nm for hydrogen), it becomes ionized by the strong field and becomes positively charged. The ionized atom is immediately projected outward, following the electric field lines, until it hits a detector — a microchannel plate — which amplifies it and makes the atom visible. The ionization probability of the gases is very sensitive to the local curvature caused by surface atoms — therefore, more signal is generated near more protruding atoms, giving atomic resolution imaging.

Our multiprobe STM is equipped with a FIM set-up in the preparation chamber. This consists of a tip holder that connects electrically to the outside with a high-voltage feedthrough, and which can be cooled by flowing liquid nitrogen. The assembly is mounted on a linear actuator, which moves it out of the way of the pliers when not needed, and moves the tip a few mm from a microchannel plate (MCP) when in use. The MCP amplified the signal from ions emitted from the tip and projects electrons onto a phosphor screen. A sensitive PixelFly camera records the image on the phosphor screen.

STM tips are typically prepared by electrochemically etch [87, 88]. These tips are then heated in the pliers until they became visible to the naked eye, to a red or dim orange color. This degasses the tips, removing a significant of contaminants, as witnessed by the pressure rise during heating. The tip is then placed in the FIM apparatus and a high voltage is applied while performing FIM imaging. Going to higher fields can help to clean the tip by field-emitting weakly-bound atoms. This tends to round the end of the tip sligthly, but creates a tip point that can be confirmed to be atomically clean. A typical FIM image of tungsten tip prepared in this way is presented in figure 5.12. FIM experiments are often performed at low temperatures, e.g. liquid nitrogen temperature; however we found that we could have images of similar quality by using the camera's electronic image averaging feature. This is advantageous because FIM can be performed much more quickly at room temperature. We do not achieve atomic resolution except in a few points on the image, but the resolution obtained with averaging at room temperature is amply sufficient to determine the cleanliness and crystal structure of the surface. The radius of curvature of the tip can also be determined from a FIM image.

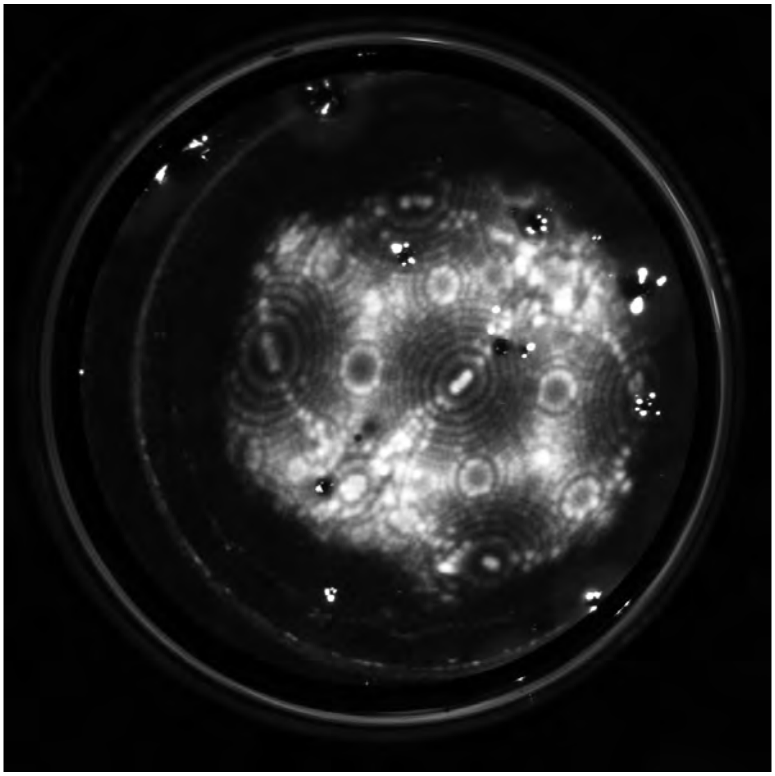

Figure 5.12: Typical FIM image of a sharp tungsten tip. The outer ring is the edge of the window into the UHV chamber. The irregular white spots are defects in the micro-channel plate which are always bright. Voltage 10.4 kV; He pressure 2×10^{-6} Torr.

5.8 Other Equipment

The multiprobe STM machine is also equipped with a residual gas analyzer (RGA) which is used for leak testing, vacuum diagnostics and molecular analysis in the gas phase. Ultra-high vacuum is maintained by two 800 L/s ion pumps (one on the preparation chamber and one on the main STM chamber), each equipped with 3 titanium sublimation filaments.

A side load-lock chamber is pumped with a magnetic levitation turbomolecular pump; it allows loading of up to 4 samples and 4 tips simultaneously and can pump down to an acceptable pressure in less than an hour, giving very high sample/tip loading speed. Four leak valves are placed at different points on the chambers to leak in gases (H_2, He, N_2 or molecules from a manifold). These dosing lines are pumped by a smaller 60 L/s turbomolecular pump.

5.9 Conclusion

The multiprobe STM designed and built by Mark Salomons has a number of attractive and unique features. First and foremost, no other machine in our knowledge combines together 3 probes with routine atomic-imaging capability. The central STM tip in particular is as good a STM scanner as any commercially available unit. The ability to use raw crystals and tips greatly increases experimental throughput; and the combination of a field-ion microscope allows ideal characterization of STM tips. All of these features together make the multiprobe STM an unparalleled instrument.

Chapter 6

Digital Feedback Loop and Software Interface

6.1 Introduction

In the previous chapter we have described the hardware aspects of our multiple probe STM. Of course, no STM is complete without the electronics and software to control the STM and acquire images. We begin by explaining the basics of STM controllers, contrasting analog and digital control systems. We then describe the program written by the author for interfacing with the Createc STM Controllers.

Createc controllers were used for all 3 tips for a certain time; we eventually replaced the main STM controller with a fully digital unit from Nanonis, with its own software. Afterwards, the Createc electronics were still used on both the left and right probes, with the software described in this Chapter.

6.2 STM Controllers

In this section we explore the different technologies that can be used to control a STM.

6.2.1 Analog Feedback Loop

The feedback loop is a crucial electronic component of a STM. To scan in constant-current mode, the feedback loop continually adjusts the voltage on the tip actuator (normally a piezoelectric element) that controls the tip-sample distance, so as to minimize the error between the measured and desired current. The tip-sample current is determined by the rate of electrons tunneling across the vacuum gap;

therefore a perfect feedback loop will maintain the same distance between the end of the tip and the sample at all times. When acquiring a STM image, the tip is scanned in the X and Y directions while recording the voltage applied to the Z piezoelectric element. A topography image is built up from repeated line scans.

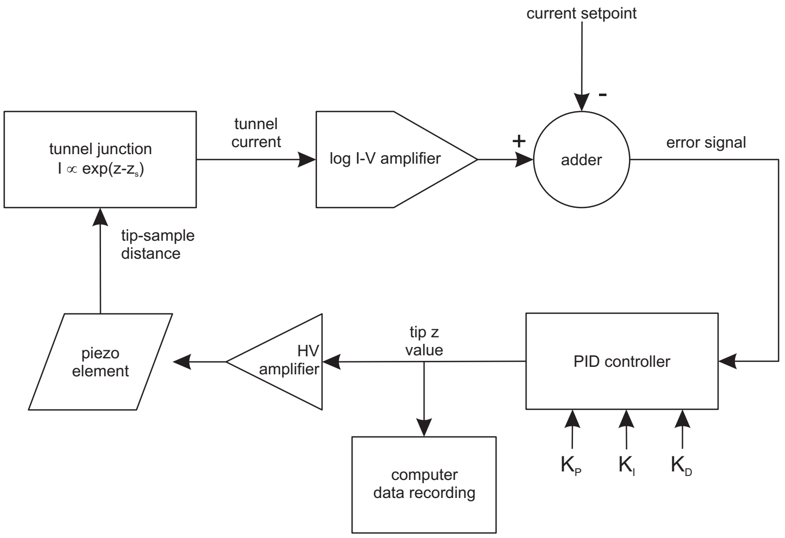

Figure 6.1: Block diagram of a feedback loop.

The first STM controllers as well as many current commercial models use *analog* feedback loops. Figure 6.1 shows a block diagram describing the basic features of a STM feedback loop. A tunnel junction (with an applied bias between the sample and tip) develops a tunneling current $I \propto exp((z - z_s)/d)$, where z is the tip height; z_s is the height of the sample; d is a scaling value - typically tunneling current increases by a factor of 10 if the tip is moved 1 Å closer. A current-to-voltage converter amplifies this current, which is typically in the nA level or smaller. Normally, the amplification is performed by a log amplifier that outputs a voltage proportional to the logarithm of the current — this matches the response of the feedback with the exponential dependance of tunneling current to tip height.

The voltage corresponding to the tunnel current is fed into an adder that subtracts a voltage corresponding to the desired *current setpoint*, producing an *error signal*. This error signal is fed into a PID controller, which outputs a control signal based on the sum of the error signal, its integral, and its derivative, each multiplied by a gain factor K_P, K_I and K_D respectively. This control signal is the height of the STM tip; to actually move the tip, it is amplified to a voltage usable by the Z piezoelectric element. If the tunneling current is higher than the setpoint, the voltage applied to the Z piezo is reduced so as to move the tip away from the sample; and vice-versa, if the current is lower than the setpoint, the tip is moved forward towards the surface. The unamplified control voltage is digitized and fed into a computer for recording images.

Modern STM controllers based on an analog feedback loop normally use computer-driven digital control to determine the feedback loop parameters, e.g. Omicron's SCALA system. The current setpoint, for example, can be set by computer from the output of a digital-to-analog converter (DAC). This makes it much simpler to control and record changes to FB loop parameters, and allows running computer-controlled macros.

6.2.2 Digital Feedback Loop

In a fully digital feedback loop controller, such as that of the Createc, Nanonis and Omicron Matrix systems, there is no analog PID controller system feeding the signal voltage to the Z piezo. Instead, the tunneling current is measured directly using an analog-to-digital converter (ADC) chip; also, the voltage sent to the piezo is produced by a DAC. The proper output voltage is calculated by a digital signal processor (DSP) card, which consists of a computer processor and memory connected with low latency to ADC inputs and DAC outputs. In the diagram in Figure 6.1, the adder and PID controller are both implemented in software; the I-V amplifier and the HV amplifier remain as separate, analog electronic components.

The processor in a DSP is tightly integrated with the analog conversion hardware, allowing it to react quickly enough to run the feedback loop. A significant difference with an analog system is that the digital feedback loop operates in fixed time steps, measuring the error signal and adjusting the output voltage at a fixed frequency. In the Createc system, custom software runs on the DSP card performing the following steps at a rate of 50 kHz:

1. A certain value Z_0 is supplied to a DAC, which produces a proportional voltage to drive the Z piezo.

2. The tunneling current value I is read from the ADC as a digital value. A log operation is done on this value.

3. The difference between I and desired tunneling current I_0 is obtained by calculating the error $e = I - I_0$

4. The voltage sent to the Z-piezo is calculated so as to minimize the current difference: $Z = Z_0 + G_p e - G_d(e - e_{old})$ where G_p is the proportional gain, G_d is the derivative gain, and e_{old} is the error during the previous time step.

5. The new voltage value Z is output to the DAC; The loop then returns to step 1.

6.2.3 Digital Scanning

To scan the STM tip on the surface, voltages are applied to the X and Y piezos. A typical scan pattern is to scan X from left to right, recording the Z, then to backtrack in X back to the left side, move down in Y, and record the next line.

Some STM controllers use analog scanning — in this case, the X signal would be a triangular ramp where the amplitude determines scan size and the DC offset places the scan window on the surface. Similarly, the Y signal would increase stepwise on each X line scan.

In a fully digital STM controller, the X/Y voltages are output by DACs. The same pattern can be used, or can be switched to other patterns through software.

6.2.4 Advantages and Disadvantages of a Fully Digital STM Controller

The main advantage of a fully digital STM controller is in its flexibility. Since all functions of scanning and the feedback loop are controlled through software, they can be extended easily, or changed even during a scan.

For example, a provision to quickly withdraw the tip should an excessive tunneling current be measured can be added to the digital feedback loop software. It is certainly possible to include such a feature in an analog feedback loop, however the circuit would have to be redesigned if it was desired to add this function later.

Another advantage is the ability to lock in the Z piezo voltage to a known value, for example, when performing I-V spectroscopy. Analog feedback loop systems require sample-and-hold circuits to perform this task, but require careful design to avoid drift of the output voltage during use.

An important disadavantage of a fully digital feedback loop that we ran into is related to limitations of the DAC chips used. The first version of the Createc STM controller we purchased, for example, had 16-bit DACs. The smallest measurable change in Z will therefore always be 1/65536 of the full Z-range. The value for a full Z-range depends on the high-voltage amplification gain, and the piezo sensitivity, but for most of our experiments it is desirable for the range to be at least 300 nm, so as to be able to handle sloped samples and unexpected high features. With such a Z-range, at 16-bits the smallest Z step is of 0.05 Å, which is significant compared to the corrugation of Si dimers, for example. In STM images, this digitization limit shows up as an unacceptable speckly “digital noise”.

Similarly, a full X-Y scan range of 2 microns may be desirable, limiting the spacing of pixels to multiples of 0.3 Å in this example. Large, instantaneous steps while scanning could damage the tip, though 0.3 Å is normally small enough to be safe.

A later version of the Createc STM controller used 20-bit DACs, which solved this problem by reducing the smallest Z step by a factor of 16, or only 0.003 Å of “digital noise” in our example above.

6.2.5 Description of DSP Boards

The first version of the Createc STM controllers shipped with a in-computer DSP card called a PC32, based on Texas Instruments’ TMS320C32 processor. It has 4 channels of 16-bit analog inputs, and 4 16-bit analog outputs, as well as 16 digital I/O lines. It uses an ISA slot, which is no longer available on normal modern computers. Fortunately, some industrial motherboard manufacturers do still support ISA slots, even with modern processors, so we were able to procure a modern, high-speed computer that could still use the old PC32 card.

The second version of the Createc STM controller ships with a stand-alone DSP board housed in a separate box, based on the TMS320C6711 but customized by Createc to have 6 20-bit analog outputs as well as 4 18-bit analog inputs. The DSP communicates with the computer through a USB connection, making it much more portable and no longer requiring the use of special industrial motherboards.

The on-board DSP code for both cards was kept very similar by Createc, and I adapted my software to interface to both easily, without recompiling. The main differences are in the way the desktop computer and DSP card communicate to each other. In the PC32 case, the desktop computer directly communicates with the card through the ISA interface, sometimes accessing memory on the DSP card directly. Commands are sent by setting a specific address on the DSP card, and the desktop software waits for acknowledgment by repeatedly polling another memory address.

In the second version, all communication occurs through the USB cable. A commercial software module, QuickUSB, is used to facilitate communication. Commands are stored in a buffer, and then transmitted in one block through the USB connection. Waiting for acknowledgment consists of waiting to receive a data packet from the DSP card with the right information.

Createc engineered the second version of their program to use the same commands, and nearly the same calling structure in the desktop program, basically wrapping the send command/wait for acknowledgment around existing code. I duplicated this in my program, but allowed for a global setting to pick between the first method and the second method, depending on the DSP version used.

Additionally, my software takes into account the different DAC and ADC resolutions of the newer version program, so that the conversion from a DAC unit (the smallest settable bit) to voltage is accurate.

6.2.6 On-Board DSP Software

As mentioned in Section 6.2.5, the two DSP boards were designed to operate very similarly, despite the updated interface and technology of the second version. The following description of the on-board software applies equally to both versions, except where specified.

The DSP software is written in C, and is compiled using Texas Instrument's Code Composer Studio, a compiler specific to the TI processors used on the DSP cards. Before use, the compiled program is loaded onto the card, which is then reset.

Main Program Body

The program's "Main" function — the function that starts when the device is booted and runs forever — consists of some initialization code that sets up a timer interrupt at a frequency of 50 kHz. Once the timer is started, a loop runs continuously to transmit and receive messages through the USB connection (for the second version only).

Timer Loop

Nearly all of the DSP code consists of a tight loop running at 50 kHz — a 20 microsecond clock cycle. The code running within this loop is divided into three sections: the command manager, the feedback loop control and the scanning algorithm. The amount of code that can run within the 20 microseconds allowed is limited, so some steps have to be taken to ensure it runs quickly.

Command Manager

On each clock cycle, the DSP program checks if the desktop program has sent a command request and calls the *cmdmanager* function if it did. The command manager looks at the parameters received from the desktop program, and applies those settings in the DSP program. There are numerous commands available, for example: get ADC value, set DAC output, start/resume a STM scan, change feedback loop parameters, perform a table run (tip macro), perform a lateral manipulation (lateral tip movement).

Feedback Loop Control

The feedback loop code runs on every clock cycle, in the manner described in Section 6.2.2, using feedback loop parameters such as gain and current setpoints received from the desktop software program. If the feedback loop has been turned off (for constant height scanning, for example), the DSP program simply holds the same DAC output on the Z channel to maintain that Z position.

An addition I made to the provided DSP code was the addition of signal averaging. At specific times (when the tip is at a pixel position, during tip macro runs, or during time spectroscopy), the tip Z-position is recorded and added to a total value. Similarly, the tip current, and ADC inputs 1 and 2 are added to total values. After a certain number of clock cycles set by the desktop software, the total of each signal is returned. The desktop software then divides the total by the number of recorded points to obtain the average signal during this time (the number is not divided by the DSP code so as to avoid losing digits to the limits of integer storage). In this way, the noise measured by the program can be significantly reduced by slowing down the scan speed.

Scanning Algorithm

Since there are no continuous analog outputs on the DSP cards used, scanning is performed in digital steps. On every clock cycle, the scanning algorithm determines whether or not it is time to move the tip. To make sure the tip moves at an appropriately slow speed, settings sent by the desktop program determine how many clock cycles to wait between tip movements, and how far to step each time. For maximum safety, the smallest lateral movement would use a single DAC unit change; however with the 20-bit DAC this is such a small movement, only a fraction of a Å, that this would be an extremely slow scan speed. Therefore, many DAC units are stepped at a time.

The DSP has a variable called *scanstatus* which holds an integer describing the current status of the scan. The values are defined as named constants, and the scanning algorithm will typically move the tip in the way that the status indicates. The following *scanstatus* values are handled:

SCANSTART: Begins a new scan by setting the tip in motion to the left until it reaches the start point, where it switches to SCANRUNXFORW.

SCANRUNXFORW: Moves the tip forward in X (to the right). See Figure 6.2. The tip moves in steps of a specific number of DAC units (specified by the desktop program), and waits at each point before moving again. The scanning algorithm can take several steps between pixels (to avoid excessively large movements when scanning large areas) — when it reaches the position of a pixel, it records one data point to a buffer. This data includes the Z tip position, the measured current, and optionally two extra ADC inputs. When it reaches the end of the line, it switches to SCANRUNXBACK.

SCANRUNXBACK: Moves the tip backward in X (to the left). Optionally, it will also record pixel data for the backward scan. When it reaches the beginning of the line again, the scan switches to SCANRUNYFORW.

SCANRUNYFORW: Moves the tip forward in Y (down). This too may occur in several intermediate steps. Once at the start of a new line, the scan switches to SCANRUNXFORW to start scanning that line.

SCANSTOPXBACK and SCANSTOPYBACK: When reaching the last line of a scan, or when manually aborting it, the tip first moves back up in Y and back to center in X, to go back to the hold position.

SCANTABRUN: Runs a table — i.e. a tip macro. A table stores a list of x,y,z positions as well as feedback loop current and voltage setpoints. Not all of these values need to change: it is commonly used to send a short voltage pulse, for example. Current and tip height data is collected at each point.

SCANDESORB: A new scan mode added to perform feedback-controlled lithography (see Section 6.3.10).

SCANSPECTIME: A new scan mode for time spectroscopy (see Section 6.3.9).

SCANRESET: Default value when no scanning or other operation is underway. The tip simply stays at the current position (the feedback loop still runs, if it is turned on).

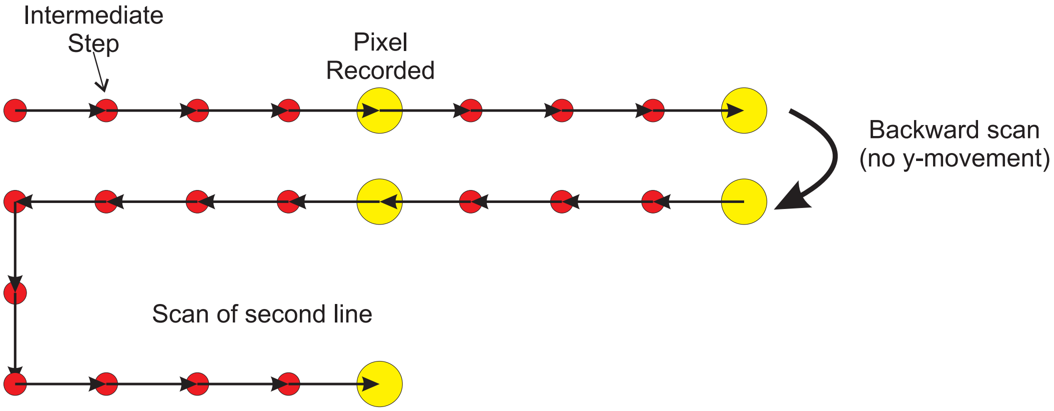

Figure 6.2: Schematic of tip movement during the digital scanning algorithm. The arrows indicate sudden changes in the tip position (from changing the DAC output values). The red circles indicate intermediate points where the tip was help stationary for a certain number of clock cycles. The yellow circles correspond to pixel positions, where the tip z-position and current were recorded and saved to a buffer.

Figure 6.2 shows schematically part of the scanning algorithm described above, and describes how the tip moves in intermediate steps between pixels. Typically, the tip will spend more clock cycles on the pixel position, so as to acquire more data for signal averaging — but this is not required and is changeable in the desktop software.

6.3 Desktop Software Graphical User Interface

The purchased Createc STM controller was supplied with a Delphi-based user interface. The program as written suffered from poor design and limited functionality. For example, it was not possible to offset the scan window in X or Y using the software. This issue, plus the desire to customize the on-board DSP software, led us to develop our own software interface for the Createc DSP board. While the Delphi source code for the Createc software was made available, it was deemed simpler to start over in a different language, using that code as a guide, rather than to try to adapt the existing program.

6.3.1 First Interface Written in Matlab

Our first iteration of the graphical user interface (GUI) was based in Matlab. We chose Matlab for its powerful data acquisition, manipulation and display capabilities. Also, its matrix and vector-based language made code simpler and clearer. Available toolboxes such as the image processing toolbox added plug-in functionality as well.

Communicating with the DSP card required low-level hardware calls, which are not possible in Matlab. Therefore, a “server” program written in Visual Basic 6 was written for this purpose, based on translated Delphi code. The two programs communicated through Windows’ ActiveX server interface. Unfortunately this was not a perfect solution — limitations in both the VB6 and Matlab language required workarounds and caused poor performance. Notably, neither VB6 nor Matlab allow for multi-threaded code; some equivalence of multi-threading was obtained by using the ActiveX server interface scheme.

In addition, we found that building graphical user interfaces in Matlab, while possible, was limited compared to a full Windows programming language. Matlab user interface elements are specific to that language, and are designed to be portable to several operating systems, since Matlab can run on Unix systems. The trade-off is that control of the UI is not as complete as in a native Windows application. Because of these limitations, some functions and features we desired were made impossible.

6.3.2 Second Interface Written in Visual Basic .NET

The second iteration of the Createc GUI used a newer version of Visual Basic, based on the .NET platform: Visual Basic 2005. This modification of the Visual Basic programming language greatly increased its capabilities, while making code development and maintenance easier. The .NET platform contains a plethora of useful functions, such as drawing routines, file input/output, data conversion, and more advanced user interface controls. For our purposes, the most significant improvement versus VB6 is built-in multi-threading support. With this capability, we were able to develop a full STM control GUI based entirely in VB. A few of the windows in the GUI are shown in Figure 6.3.

6.3.3 The Action Queue Thread

During a typical STM scanning session, a user will need to issue many different commands: begin a scan, move the scan window to a new position, change a feedback loop parameter, etc. However, many of these tasks take some time to complete and cannot be performed at the same time. To avoid problems, the commands are not executed immediately, but are instead queued, in the Action Queue, which consists of a list of Actions (commands) that the user has requested be performed. Each new action is added to the end of the queue, and waits to be executed.

A sample of the actions defined in the program, listed by their class name, are

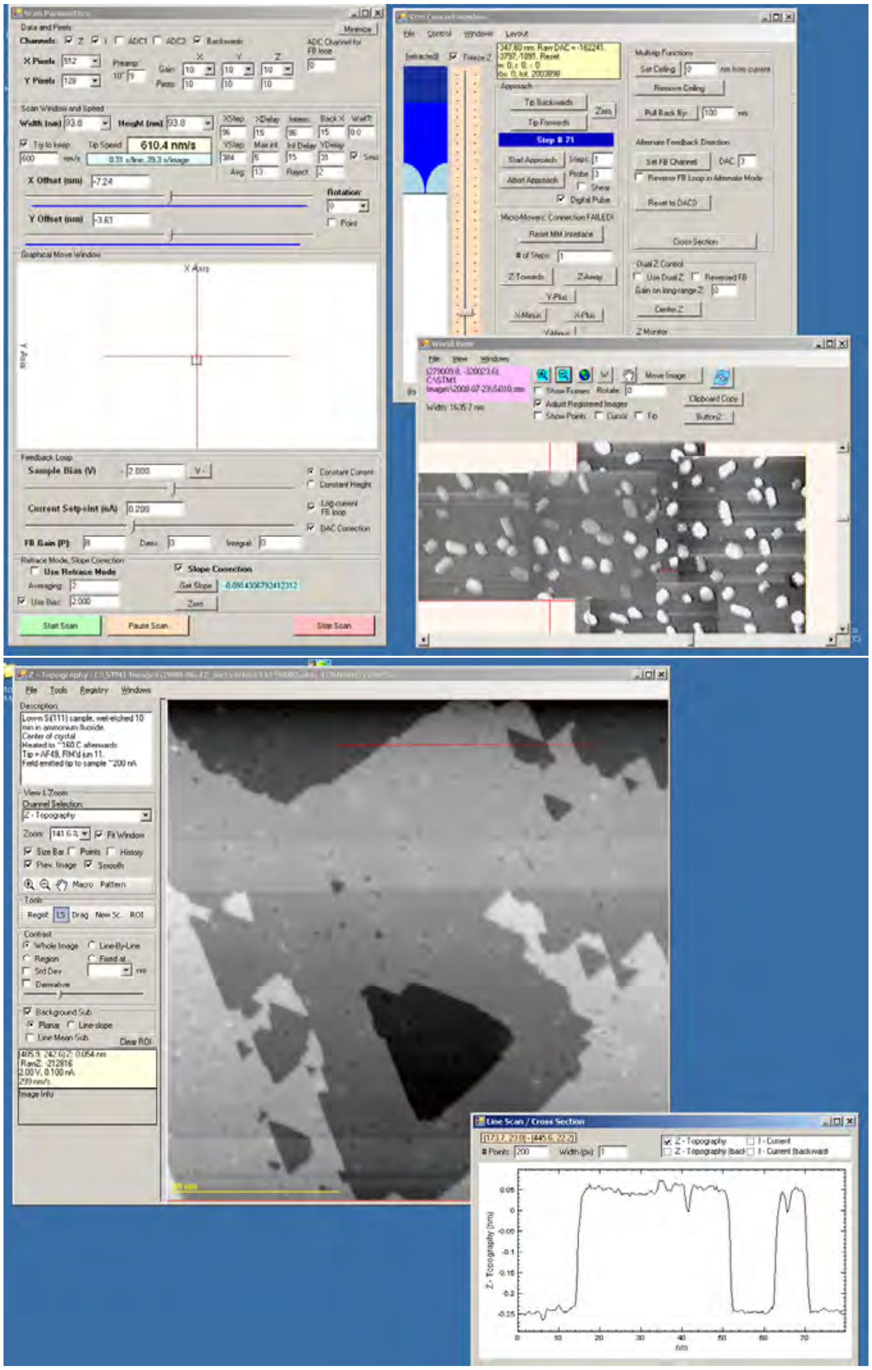

Channels: ☑ Z ☑ I ☐ ADC1 ☐ ADC2 ☑ Backwards

ADC Channel for FB loop: 0

X Pixels: 512

Y Pixels: 128

Preamp: 10^ 9

Gain: X 10, Y 10, Z 10

Piezo: X 10, Y 10, Z 10

Width (nm): 93.8

Height (nm): 93.8

☑ Try to keep 600 nm/s

Tip Speed: 610.4 nm/s

0.31 s/line, 39.3 s/image

XStep: 96

XDelay: 15

Interm: 96

Back X: 15

WaitT: 0.0

YStep: 384

Max int: 5

Int Delay: 15

YDelay: 31

☑ Smo

Avg: 13

Reject: 2

X Offset (nm): -7.24

Y Offset (nm): -3.61

Rotation: 0

☐ Point

Sample Bias (V): - 2.000

● Constant Current

○ Constant Height

Current Setpoint (nA): 0.200

☑ Log current FB loop

☑ DAC Correction

FB Gain (P): 8

Deriv: 0

Integral: 0

☐ Use Retrace Mode

Averaging: 2

☑ Use Bias: 2.000

☑ Slope Correction

-0.0914306792412312

[retracted]

☑ Freeze Z

-347.80 nm. Raw DAC = -182241.
-3797,-1891. Reset
w: 0, r: 0, -: 0
fbs: 0, tot: 2003898

Step # 71

Steps: 1

Probe: 3

☐ Shear

☑ Digital Pulse

Micro-Movers: Connection FAILED!

# of Steps: 1

Set Ceiling: 0 nm from current

Pull Back By: 100 nm

DAC: 3

☐ Reverse FB Loop in Alternate Mode

☐ Use Dual Z

☐ Reversed FB

Gain on long range Z: 0

(279009.8, -320023.6),
C:\STM1
Images\\2008-07-23\5i010.stm

Width: 1635.7 nm

☐ Show Frames

Rotate: 0

☑ Adjust Registered Images

☐ Show Points

☐ Cursor

☐ Tip

Description:
Low-n Si(111) sample, wet-etched 10
min in ammonium fluoride.
Center of crystal
Heated to ~160 C afterwards
Tip = AF49, FIM'd jun 11.
Field emitted tip to sample ~200 nA

Channel Selection: Z - Topography

Zoom: 141.6 %

☑ Fit Window

☑ Size Bar

☐ Points

☐ History

☑ Prev. Image

☑ Smooth

● Whole Image

○ Line-By-Line

○ Region

○ Fixed at

☐ Std Dev

☐ Derivative

☑ Background Sub

● Planar

○ Line-slope

☐ Line Mean Sub

(485.9, 242.6) Z: 0.054 nm
RawZ: -212816
2.00 V, 0.100 nA
299 nm/s

[173.7, 23.0] - [445.6, 22.2]

Points: 200

Width (px): 1

☑ Z - Topography

☐ Z - Topography (back)

☐ I - Current

☐ I - Current (backward)

Figure 6.3: Screenshots showing the most commonly used windows of the Visual Basic .NET desktop graphical user interface program: control, scan parameters, image view, cross-section, world view.

listed below:

WindowChange: Change the scan size or rotation of the window, but without moving the scan window.

MoveScanWindow: Move the scan window to a new position. The tip moves in a straight line to the new hold position at the current tip speed.

MoveTip: Without changing the scan window, move the STM tip to an arbitrary spot on the surface, at the current tip speed.

MoveTipReturn: Returns the tip to the hold position of the current scan. This is used at the end of a series of tip macros.

Point: Execute a tip macro, such as a voltage pulse, at the current tip position. This is commonly preceded with a MoveTip action, to place the tip where desired.

PointDesorption: A special tip macro, used for feedback-controlled tip desorption (see Section 6.3.10).

FeedbackChange: Change one or more settings of the feedback loop.

StartScan: Begin a STM scan.

PauseScan: Pause the current scan and hold the tip at the end of the line.

MicroMover: Send one or more pulses to the coarse movers.

The Action Queue Thread is a process that constantly monitors the entries in the Action Queue. The thread makes sure to wait that the previous action has completed before executing a new one. For example, one might send a command to move the scan window by one micron. If the tip speed is slow, this movement may take several seconds. If the user were to click to another position and have that movement command executed right away, the STM tip would jump to the end of the first move before starting the second, possibly damaging the tip with such an instantaneous movement. However, the Action Queue Thread makes sure that the first move has completed before starting the second.

One exception is the action to start a STM scan, for which the Action Queue does not wait for completion. It is normal to change feedback loop parameters, or move the scan window, or perform a tip macro while scanning. In the original Createc-supplied software, it was not possible to do anything other than change feedback loop parameters without stopping the scan and restarting afterward. I modified the on-board DSP code to allow pausing of a STM scan. Now, to perform a tip movement while scanning, the program seamlessly performs these actions:

1. Send a command to the DSP to pause the current scan.
2. Wait for the tip to reach the end of the line and pause there.
3. Perform all the queued actions, such as tip movements, macros, etc.
4. Return the tip to the previous position
5. Resume the scan.

6.3.4 The Scan Monitor Thread

It is necessary for the program to still be responsive while a scan is active — you cannot wait for a scan to complete before displaying the image. To avoid this, we have a scan monitor thread running in the background.

Once a scan is started, the scan monitor thread repeatedly checks to see if any data have been stored by the DSP card in its buffer. If anything is present, it retrieves those data and stores it in another buffer in the desktop program. The program waits until it has accumulated enough data to display one line of the STM image — the number of bytes to receive depends on how many channels are being acquired.

Once a full line has been stored in the buffer, it is separated into each channel of data. The user can choose to record any of the following data: the tip Z position, the tip current, or the voltage recorded on ADC channels 1 or 2. In addition, the user can choose to record the same data channels on the backward direction scan, in addition (or instead) of the forward direction scan. This gives a maximum of 8 channels of data to record per line. If signal averaging is turned on, it is at this step that the desktop program calculated the average by dividing the total signal reported by the DSP by the expected number of integration cycles.

The scan monitor thread sends notifications to the open current image window that a new line has been recorded, and that the image needs to be updated on screen. The thread also handles pausing and resuming STM scans.

6.3.5 The Tip Monitor Thread

The tip monitor thread requests the current tip position (in 3 dimensions) from the DSP at a certain rate (about 30 Hz, though that setting can be changed by the user). This thread notifies several windows that the tip position has changed, which allows them to update displays of the current tip position or height.

6.3.6 Scan Parameters Window

The Scan Parameters window (see Figure 6.3) is used to choose the scan area and position, as well as to set up the feedback loop parameters.

Recorded Data Settings

The top-most group of controls in the scan parameters window allows you to choose the number of pixels to record (the number of pixels does not need to be equal in both directions). Also, the user can pick to record any of the available data channels: Z, current, ADC1 and ADC2, as well as the backwards scan direction for all of that data.

Scan Window and Scan Speed

The height and width of the scan window are chosen in the next group. The size, in nm, can be typed in, but due to the operation of the all-digital DSP controller, not all sizes are possible. The size chosen needs to be a multiple that is addressable by the digital to analog converters, to the limit of their resolution. In the USB version of the DSP, the resolution is smaller than 1 Å, which does not limit the positioning and size very much — it is more of an issue in the 16-bit DSP version.

There is another consideration when picking a scan window that relates to the scan speed: as described in 6.2.6, the tip movement algorithm moves in smaller steps between pixels. If each pixel is spaced by n DAC units, the only allowed intermediate steps have to be integers divisible into n. The intermediate step is chosen to be the biggest possible value, without exceeding a set distance per step (for example, 2 Å per step). Therefore, some pixel spacings may correspond to prime numbers, and that disallow any intermediate steps. The tip would could then only move directly from pixel to pixel without intermediate steps, or for safety the program moves in a single DAC unit at a time. This can make scan speeds very slow. Pixel spacings that are multiples of many integers are more convenient, since a wide variety of intermediate spacings are possible. Suggested values for scan sizes use such convenient numbers, such as multiples of 32, 64, 128, etc. DAC units.

Feedback Loop Parameters

The feedback loop parameters are also adjusted in the Scan Parameters window: current setpoint; sample bias; proportional and derivative gain values; constant height or constant current mode; scan slope correction; etc.

6.3.7 STM Image Window

The Image Window is where the results of STM scans are displayed. The same window is used both for scans that are in progress, or data loaded from disk from previous scans.

The main part of the Image Window is the image display itself, on the right side. The image is displayed in gray scale, but other elements may be drawn on the image: a scale bar, a circle indicating the current tip position, a yellow rectangle indicating where the next scan will take place.

On the left side of the window are a number of controls that affect the way the image is displayed. A description box can be edited to hold useful details about the image being displayed. A drop-down list allows the user to choose which channel is being displayed — this could be topography, current, or choose the scan direction. The user can also press the number keys from 1 to 8 to quickly switch display channels.

The image can be zoomed by using the zoom in/zoom out mouse cursors, or by typing in a value in the zoom box, or by pressing Ctrl-plus or Ctrl-minus. The image can be panned with a pan cursor or with the scrollbars.

Two sets of controls affect the way the STM image data is drawn on screen. The “Background Sub” section sets how the background slope is subtracted from the data. The user can choose between planar background subtraction, where the average plane of the entire image (or only the region of interest, if selected) is calculated and subtracted from the real topography; or line-slope subtraction, where a simple slope is calculated for each line, and is subtracted from it. The average height of each line can also be subtracted (with or without some averaging), which helps correct for scans with curved appearance.

The “Contrast” section chooses how the data is converted to gray scale. Normally, the highest value in the data is mapped to pure white (255), and the lowest value maps to pure black (0), with the in-between value interpolated from those. It is also possible to use the standard deviation to map between white and black, instead of the maximum and minimum. The calculation of the maxima and minima can be made on the whole image, or only a region defined by the user, or on each line, or directly typed in by the user. The scaling can be adjusted by the user by selecting the image window, and rolling the mouse wheel while holding down the Shift key.

For some images with large variations in height, there is also a derivative mode, where the image is scaled to the x-derivative of topography, instead of to the direct values. A slider bar allows the user to mix the derivative and the real topography together, to form a composite image. This can enhance the apparent sharpness of the image, while avoiding saturating areas that are too high or too low. Image blurring can also be added — each pixel is drawn as the average of a box of surrounding pixels; the width and height of the box is user selectable.

6.3.8 World View Window

The World View window is an interface that allows the user to display many STM images simultaneously. The window consists of a frame the size of the STM's maximum scannable area. STM images can be added to the world view by loading them from disk. Each STM image is displayed in the world view at the same position, angle, and scale as it was scanned. For example, a 20-nm scan window will be rendered at 1/4 the size of an 80-nm scan window, even if both were acquired with the same number of pixels. The images are overlaid on top of each other in the order they were loaded — so if they are loaded in order, the most recent images will be on top.

The world view starts with the full scannable area, but can be zoomed in arbitrarily close to view small scan areas. Dragging with the mouse (in Pan mode, press P on the keyboard) or using the scrollbars allows the user to move the view window.

By right-clicking and choosing a menu option, images can be sent to the front or back of the view. Also, using the mouse wheel, the user can cycle through which STM image is at the front of the view. This feature is especially useful when comparing a sequence of images that were taken on the same spot on the surface, since it allows you to quickly scroll through the progression of images.

The World View window also allows the user to do simple registry of STM image positions. First, the user goes into "move image" mode by pressing M on the keyboard. He can then click and drag any STM image to a new position on the surface. The dragged image becomes semitransparent, making it easy to align with an underlying picture of the same area.

It is also possible to save sets of images (called Quick-Views), which can be recalled by pressing one of the number buttons on the keyboard (0 to 9). A common use for this feature is to load a set of images of a surface before dosing, and after dosing, and register them to each other. Each set is assigned to a different key, and the user can then rapidly switch between the pre-dose and the post-dose images. Differences in the pictures become clearer to the human eye when images are well aligned and can be switched quickly.

The images generated by the World View window can be saved to disk as image files with an arbitrary resolution, creating quick mosaic images. An example of these is shown in Figure 3.17.

6.3.9 Time Spectroscopy

This fairly simple window allows one to use the STM controller to record time-dependent signals. One sets the number of data points to collect, and the time delay between them. The signals to record are checked (available choices are tip Z position, tunneling current, and the two ADC channels ADC1 and ADC2).

6.3.10 Feedback-Controlled Lithography

The STM tip has been frequently used to desorb hydrogen from H-terminated surfaces [89, 90, 91, 92, 93, 94]. Some “recipes” are known to produce patches and lines of desorbed hydrogen reasonably reliably. To remove a single H atom, one will typically apply a current and voltage pulse for a fixed amount of time. Unfortunately, this method is generally a hit-or-miss affair, with either no H being desorbed, or several being removed at the same time [95]. Feedback-controlled tip lithography (FCL) [45] is a way to solve this problem: the feedback loop is left active during the voltage and current pulse. When a hydrogen is desorbed, the resulting change in tip position is detected and the voltages and currents are reduced to a safe value. This way, the removal of a single H is much more likely.

The ease with which the Createc DSP software was modified to include feedback-controlled lithography demonstrates the flexibility of an all-digital STM controller and the usefulness of having custom software. A small routine on the DSP code was added to monitor the tip position during a voltage pulse and to retract the tip as needed. A user interface window allows the experimenter to set parameters, such as the threshold of change for tip retraction. Patterns of desorption routines can be performed, e.g. the line of 10 evenly spaced desorption points in Figure 6.4.

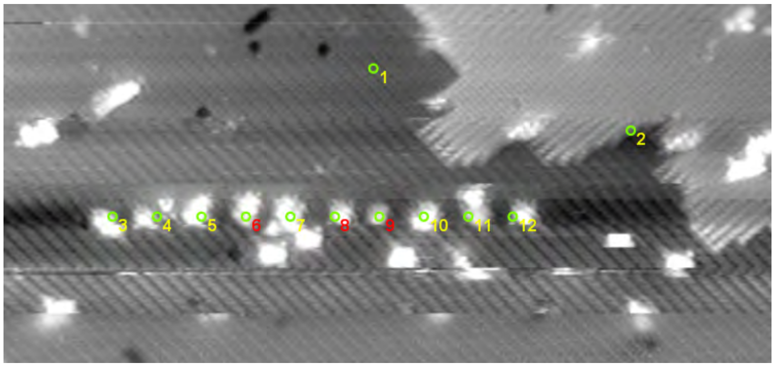

Figure 6.4: STM image (∼45 nm wide, +2 V, 80 pA) showing a row of H by FCL on H-Si(100)-2×1. The green circles indicate where the tip was placed when the FCL routine was executed.

6.4 Coarse Motion Control

For use in our multiprobe STM, we had Lars Holm and others at the University of Alberta Electronics Shop build customized Coarse Mover Controller electronics. This controller powers slip-stick style in-UHV movers, and communicates with the scanning software using a USB interface. This was another area where having our custom STM software was convenient, as it allowed us to customize coarse mover control.

The Coarse Motion Controller is able to move 9 different movers: 3 axes for each of our 2 probes, and 2 axes for the sample position, and one axis for the STM Z motion. Since we need to control up to 3 STMs simultaneously, we need to use up to 3 desktop computers at the same time — however only one can be connected by USB to the Coarse Motion Controller. All 3 computers need to communicate with it, so to solve this problem we set up TCP/IP communication between computers. One computer is set up as the server, and it is the one that is connected via USB to the controller. The other two computers relay requests for motion via TCP/IP, and let the server computer execute them.

As was described in Section 5.4.2, there were several issues with the custom mover electronics and the concept of performing fine scanning with them; eventually we replaced these custom electronics with two commercial Omicron Micro-Slide Control Units (MSCU). Each of these units has 8 channels; since we use a total of 9 channels, we required two units. The left and right probes are connected to one unit, and the main STM to the other, allowing all probes to be controlled without rewiring.

The Omicron MSCU does not allow for full computer control, but can be triggered to take a single step by an external TTL pulse. The control software was thus modified to use the digital IO lines to trigger pulses for tip approach. This requires the user to manually set the Omicron MSCU to accept the pulses in the correct channel and direction. The MSCU connected to both the left and right probes are controlled by a single computer (the right probe computer), as in the case of the custom Coarse Motion Controller. The left probe computer sends a signal via TCP/IP to request that a single step is taken. The main STM, controlled by the Nanonis electronics, is connected directly to its own MSCU.

6.5 Sourcemeter Control

To perform sensitive IV curve measurements, our system is equipped with two Keithley Sourcemeters — models 2400 and 6430 (these models are very similar; model 6430 can use a preamplifier and lacks front inputs). A set of functions were added to the STM software package so as to support controlling these units via the serial port of the computer.

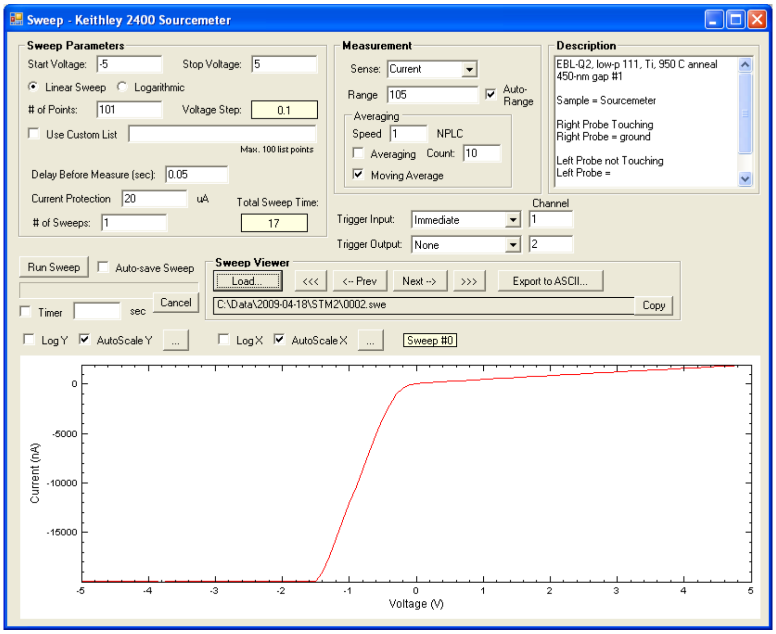
Sweep - Keithley 2400 Sourcemeter

Sweep Parameters
Start Voltage: -5
Stop Voltage: 5
● Linear Sweep ○ Logarithmic
# of Points: 101
Voltage Step: 0.1
☐ Use Custom List
Max. 100 list points
Delay Before Measure (sec): 0.05
Current Protection 20 uA
# of Sweeps: 1
Total Sweep Time: 17

Measurement
Sense: Current
Range 105
☑ Auto-Range
Averaging
Speed 1 NPLC
☐ Averaging Count: 10
☑ Moving Average

Description
EBL-Q2, low-p 111, Ti, 950 C anneal
450-nm gap #1

Sample = Sourcemeter

Right Probe Touching
Right Probe = ground

Left Probe not Touching
Left Probe =

Channel
Trigger Input: Immediate 1
Trigger Output: None 2

☐ Auto-save Sweep
☐ Timer sec

Sweep Viewer
C:\Data\2009-04-18\STM2\0002.swe

☐ Log Y ☑ AutoScale Y ☐ Log X ☑ AutoScale X
Sweep #0

Figure 6.5: Screenshots showing the Sourcemeter Sweep window.

One simple window can take single measurements and output DC voltages. A second window is used to send sweeps to the sourcemeter — see Figure 6.5. Typically, this feature is used to sweep voltage while measuring current, to record an IV curve. Parameters can be set to choose the start and stop voltage as well as the number of points and the time per point. A measurement parameters frame allows the user to pick the averaging and speed of current measurement.

The resulting data is displayed in the plot at the bottom of the window. Data can be displayed in linear or log scales; the limits of the plot can be automatic or manually set. Buttons allow easy navigation between recorded sweep files on the hard drive. There is also a “timer” feature, which repeats sweeps at a fixed time interval.

6.6 Conclusion

This chapter has described the basics of STM feedback loops, both analog and digital; and described the software written by the author for interfacing with two models of Createc fully digital STM controllers. The ability to customize features of the program has proven to be very useful, allowing us to perform experiments and analyze data in ways that would not be possible otherwise. More features can be added as needed, giving a boost to experimental productivity.

Chapter 7

Metal Contacts and Surface Preparation

In this chapter, we describe the technology we developed to obtain a rather unique combination of high-quality Si surfaces while keeping stable, very-high resolution metal contacts. This will allow us to electrically characterize Si surfaces. In the first part, we will describe the technique for growing self-formed titanium silicide islands; next we will describe the use of electron-beam lithography (EBL) to pattern metal contacts directly.

7.1 Usefulness of Metal Contacts

The three-probe STM described in Chapter 5 is a powerful machine that allows 3 tips to be brought to very close distances from each other. However, the ultimate spacing between the ends of the probes is ultimately limited by the radius of the end of the STM tips, as is shown in Figure 7.1.

A typical STM tip has a radius of 20 nm, which would limit the closest tip-to-tip distance to 40 nm. For example, if one of the probes is touching down to the surface to apply a current, the other probe could not come closer than 40 nm to this junction. In practice, it is very difficult to scan so close to a tip without hitting them together and likely damaging them, which means a wider distance would be needed for safety. Also, if one of the tips is damaged from scanning or repeated contacts, its effective radius could be much larger than the typical 20 nm, further increasing the closest approach distance possible.

For these reasons, we started work on developing elongated metal contacts on the Si surface. If a low-profile metallic line could be deposited on the surface, one

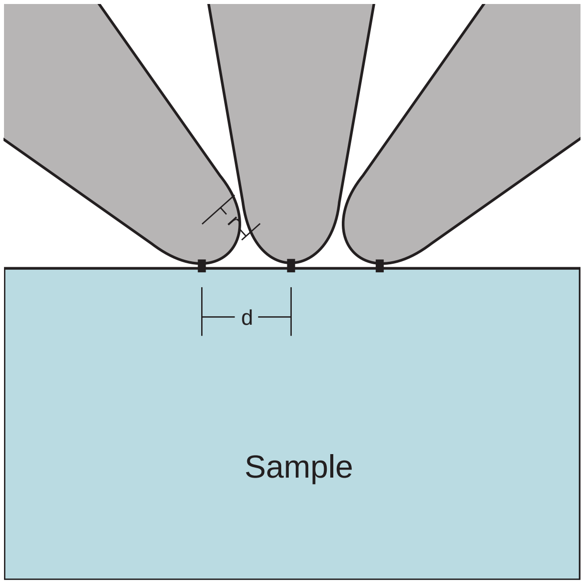

Figure 7.1: Schematic showing the closest approach possible for 3 tips of equal radii r. The closest distance between the tunneling junctions (black bars) is $d \sim 2r$.

tip could touch it while another could reach all the way to its edge, and even image over the metal contact itself.

The experiments planned using metal contacts on Si surfaces included: direct biasing of a dangling bond to controllably charge/discharge it; using an electric field to direct molecular line growth.

7.2 Self-Formed Titanium Silicide Islands

The first method we attempted to use to avoid the tip distance problem described in Section 7.1 was to make self-formed, elongated titanium silicide islands. Such self-formed island growth has been reported several times in the literature, with growth occuring on Si(111) [96, 97, 98, 99, 100, 101] and on Si(100) [102, 103, 104]. While island growth can be obtained via chemical vapor deposition [104], it is typically obtained by evaporating a thin layer of titanium on the sample at an elevated temperature, followed by an annealing phase. The exact temperatures, annealing times, deposition rates and Ti thicknesses used change the morphology of the islands obtained [98, 104, 96].

The $TiSi_2$ islands formed by this process can be of two phases [103]: C49 and C54. The C49 is a base-centered orthorombic structure and it is formed at lower annealing temperatures (lower than 850 C in Ref. [103]). The C54 phase is a face-centered orthorombic structure. C49 islands typically have a flat top, whereas C54 islands appear pyramidal in shape. The resistivity of the C49 phase (of the order of 20 $\mu\Omega\cdot$cm in thin films) is approximately 3 or 4 times that of the C54 phase [105].

7.2.1 $TiSi_2$ Islands on Si(100)

Finding the proper conditions for $TiSi_2$ island growth in our particular setup was an iterative, trial-and-error process. Fortunately, the published data helped guide our progress.

Titanium was evaporated using an e-beam evaporator of brand Tectra. This consists of a replaceable titanium rod that is held at a high voltage, typically of 1.5 kV. The rod is surrounded by a simple tungsten loop filament, which is heated hot enough for it to thermally emit electrons — typically 6.00 Amps of current were sufficient. An electron beam current of a few mA is caused by the electrons hitting the biased titanium rod. The energy of the electrons heats the end of the rod, causing it to start evaporating Ti atoms through an aperture (with a movable shutter to control exposure) and onto a sample. A flux monitor is mounted near the aperture and is used to measure the flux of evaporated ions. This consists of a sleeved, biased at -40 V. Since a fraction of the emitted Ti atoms are positively ionized, they hit the flux monitor and cause a current to be measured (typically a few hundred nA). Since the ionization fraction and other geometrical parameters are not known, this current only gives a relative indication of flux, and cannot be directly converted to a deposition rate in nm/s without external hardware such as a crystal balance. Because our chamber was not equipped with such a balance, we used trial and error to determine the optimal deposition amounts. The flux monitor current can be integrated in time to obtain a measure of the total deposited amount; this integrated amount is measured in nA·s.

Before Ti deposition, the sample was flashed several times to 1200 C. It is also helpful to degas the pliers thoroughly; this can be done by using a sacrificial crystal. During deposition, the sample was held in the pliers, rotated so as to be facing the aperture head-on. Direct current heating was used to maintain an elevated temperature. Since the pyrometer did not have a view of the sample in the deposition position and angle, the deposition temperature was normally calibrated before hand to find the correct current. The pliers were typically rotated so as to be back into view of the pyrometer once deposition was complete to perform the post-deposition annealing step while in view of the pyrometer.

One of the first attempts at $TiSi_2$ island growth is shown in Figure 7.2. A relatively even distribution of islands was obtained, with most islands being square or slightly elongated (Figure 7.2(a)). The islands were typically 30 nm in size,

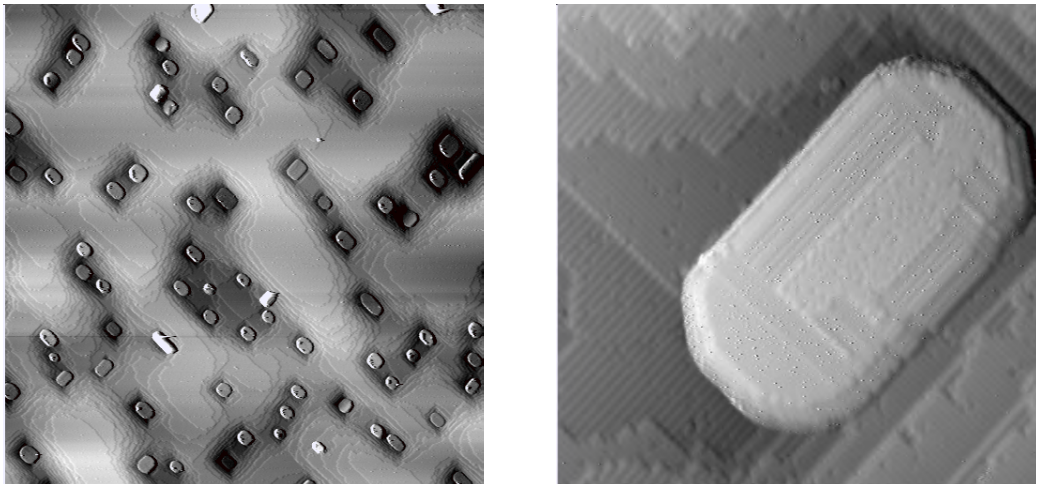

(a) Wide STM image showing a typical distribution of islands (900 nm wide, −2 V, 100 pA).

(b) Close-up image of one of the islands (55 nm wide, −2 V, 100 pA). This island measures $\sim 25 \times 50$ nm.

Figure 7.2: STM images of $TiSi_2$ island growth on Si(100). 12 μA·s of Ti deposited at 650 C (300 nA flux for 40 seconds), followed by a 60 second 900 C anneal. The images are presented as a mix of the height and its derivative for enhanced clarity.

with only a few reaching 80 nm in length. Most islands are flat-topped and formed epitaxially oriented relative to the Si(100) surface, as Figure 7.2(b) shows. The flat top seems to indicate that the phase of $TiSi_2$ obtained is C49 [103], the more resistive phase.

These positive results show that a wide range of annealing parameters will result in high-quality $TiSi_2$ island formation. However the islands shown in Figure 7.2 are too small to be easily used as metal contacts, therefore we refined the annealing parameters so as to obtain larger islands. Figure 7.3 shows the result of depositing more Ti at a higher temperature, followed by a longer anneal. Figure 7.3(a) shows a very long (near 900 nm) single island. The $TiSi_2$ formed is very regular, with a flat top that can be imaged with atomic resolution, as shown in Figure 7.3(b).

One issue with these $TiSi_2$ islands is that the silicide formation process seems to use up the surrounding Si atoms — resulting in the $TiSi_2$ island being formed in a trench of Si. Experiments such as field-directed line growth (see Chapter 8) are more difficult due to the high step density. However, as Figure 7.3(a) shows, for large $TiSi_2$ islands the last terrace closest to the silicide can be up to 20-30 nm in size; this is large enough for many experiments.

A SEM image of the same sample (Figure 7.3(c)) shows the distribution of $TiSi_2$ islands over a larger area. These seem to come in three different types. Some of the

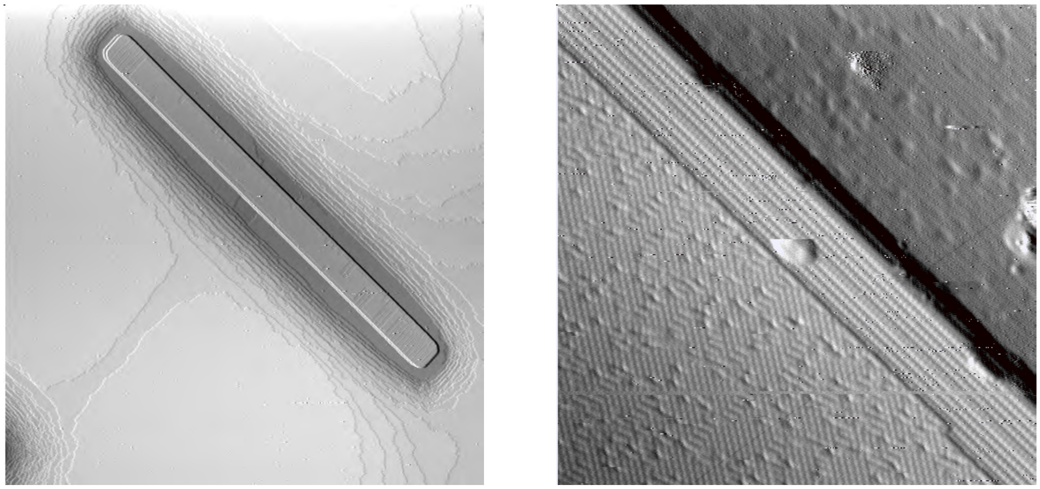

(a) STM image of a single, very elongated $TiSi_2$ island (900 nm wide, −2 V, 100 pA). The island pictured is close to 900 nm in length and 60 nm in width.

(b) STM image of the top of the $TiSi_2$ island (lower left) next to the Si surface (40 nm wide, −2 V, 100 pA, derivative view).

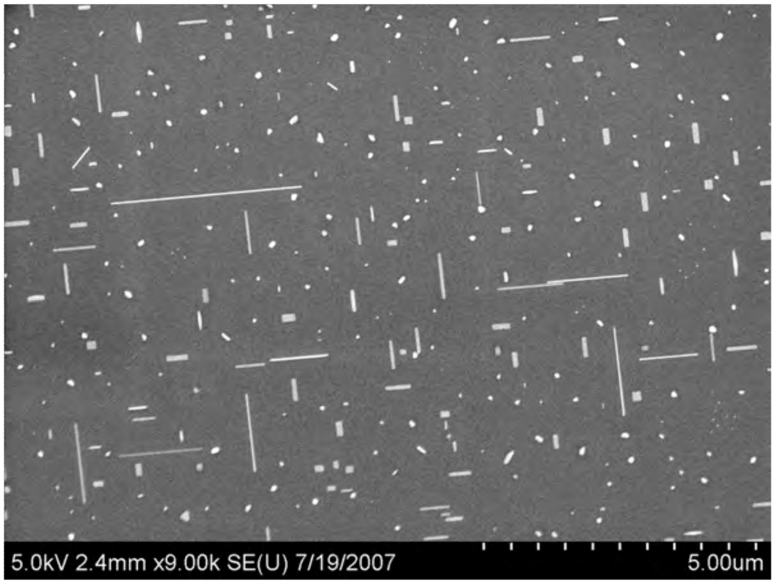

(c) SEM image taken at 5 kV and 9000× magnification.

Figure 7.3: STM and SEM images of $TiSi_2$ island growth on Si(100). 18 μA·s of Ti deposited at 800 C (260 nA flux for 70 seconds), followed by a 10 minute 950 C anneal.

smaller islands are also wider and therefore appear as bars or squares. Many of the islands appear as lines with similar widths, but with varying lengths (ranging from a few hundred nm up to 4 μm). These last two types grow aligned with the crystal structure, and so the lines are perpendicular to each other. However, in some rare cases the islands grow at 45 degrees to the underlying Si lattice.

In the cases shown in Figures 7.2 and 7.3 the resulting Si surface is clean Si(100)-2×1. It is easy, however, to obtain a H-Si(100)-2×1 surface if that is desired. To do this, instead of simply lowering the temperature directly to room temperature after the post-deposition anneal, the temperature is lowered to 300 C. Hydrogen termination then proceeds as described in Section 3.1.1, but without any additional 1200 C flashes. The $TiSi_2$ islands are unaffected by the $\sim$ 300 C temperature used in H-termination, but might be modified by an anneal at a temperature higher than the post-deposition anneal used.

7.2.2 $TiSi_2$ Islands on Si(111)

$TiSi_2$ islands were also grown on Si(111) using the same technique described in Section 7.2.1. One difference was that the Tectra brand e-beam evaporator was replaced by an Omicron brand 3-cell unit with a different controller. The technique is the same, but this particular evaporator uses 800 V on the Ti rod, and requires a filament current of only $\sim$ 2 A to obtain an electron current. The controller is equipped with a built-in flux current integrator, which makes it easier to deposit a known amount of material. The calibration of the flux monitor is different with this unit compared to the Tectra unit, so direct comparisons of total deposition amounts should not be made.

Figure 7.4 shows the result of growth of $TiSi_2$ islands on Si(111). At least three types of islands can be seen to grow with these conditions. First, several irregularly shaped islands are visible. These show a repeated superstructure on different islands, which indicates that the structure on the surface is actually sharper than the tip, and that the STM image is of the shape of the tip.

A second type of islands are flat-topped and are always 1.4 nm high; two of these are visible in Figure 7.4(b). Their dimensions are typically 15-30 nm wide by 80-150 nm long. Unlike the islands on Si(100), there is no trench of missing silicon nearby — making the islands appear to lay flat on the surface. The Si(111) surface has a 6-fold symmetry, and therefore the islands do not form at perpendicular angles as in the case of the Si(100) surface; instead, many more angles seem to occur, but they all seem to be multiples of 30 degrees. A third type of island forms very long and narrow, with a width < 10 nm. These islands are 0.7 nm in height.

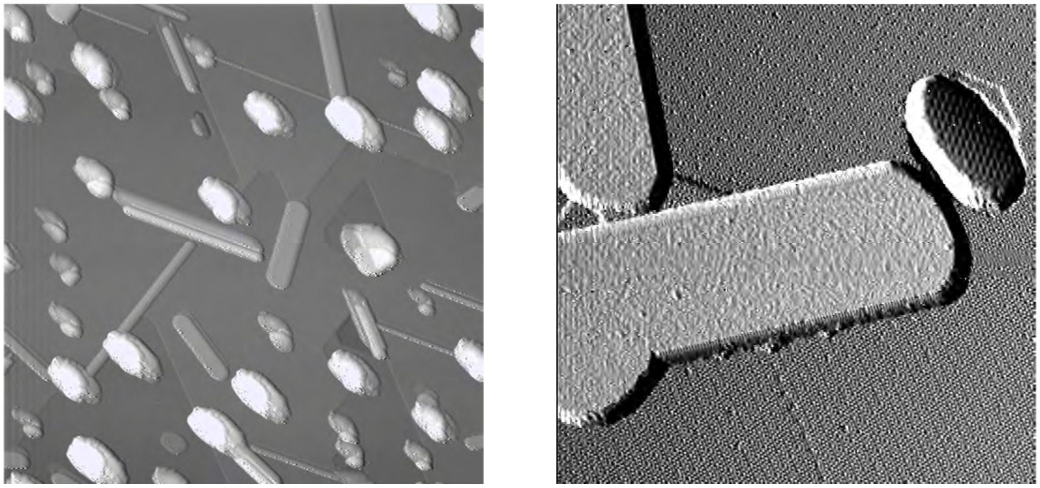

(a) STM image several $TiSi_2$ islands grown in Si(111) (600 nm wide, −2.5 V, 70 pA).

(b) STM image of a few islands and of the 7×7 surface (75 nm wide, −2.5 V, 70 pA, derivative view).

Figure 7.4: STM images of $TiSi_2$ island growth on Si(111). 250 μA·s of Ti deposited at 700 C (200 nA flux for 21 minutes), no post-deposition anneal.

The surface near the $TiSi_2$ islands is high-quality Si(111)-7×7, as can be seen in the derivative view shown in Figure 7.4(b). Therefore, in an experiment requiring contact to this surface, one probe could touch one of the contacts while the other would be able to image the junction perfectly using STM. Refined annealing and deposition parameters (e.g. Ref. [97]) could improve the distribution of $TiSi_2$ islands on Si(111), but this was not attempted on this machine.

7.3 Making Contact to Islands

Once $TiSi_2$ islands of a desirable shape have been produced, the next step in a multiple probe experiment would be to determine the exact location of the two tips relative to each other. The surest way to accomplish this is to scan an area of the surface and recognize the features as unique, and to find the same area with another probe.

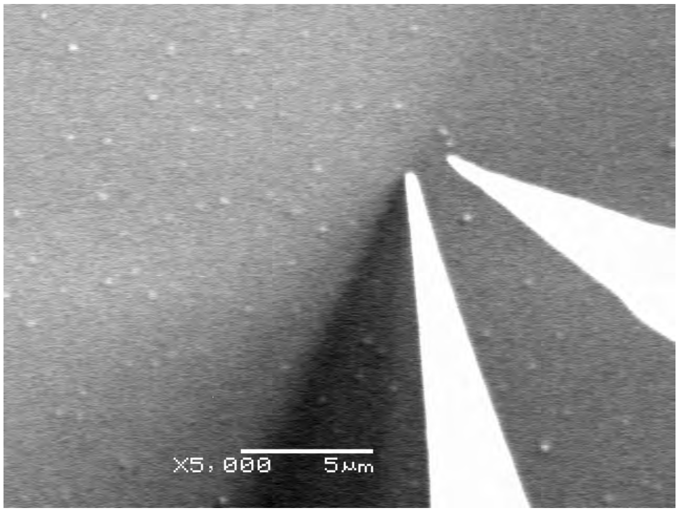

Figure 7.5: SEM image of two STM tips (the right probe and the center STM) brought close to each other over a Si(111) surface with $TiSi_2$ islands. 5000× magnification, 7 kV beam voltage.

The first step in finding the same surface location with two (or more) tips is to bring the probes as close as possible, so that they are within overlapping scan areas. Figure 7.5 shows the SEM view of two probes within one micron of each other. The procedure to reach this tip distance was described in Section 5.5.

Once the probes are close enough, it remains necessary to locate the same area on the surface. The only way to achieve this is to take a large STM image with one probe with enough distinguishing characteristics to give a "fingerprint" of the surface features. Then, a similarly large scan is made with the second probe. This scan may be done at a lower resolution to save time and to avoid damaging the tip needlessly. We then attempt to match the shape of the features in the second scan to those in the first scan.

Before attempting to match the features, it is important to have determined the scan geometries in real space — i.e., the image on the screen must be matched to a known orientation on the sample. I chose the scan directions and polarities so that the "up" direction in the STM images matched the "up" direction in the

SEM image. It is equally crucial to ensure that the horizontal scan direction is not flipped. This calibration of directions is performed by manually moving the tips in X and Y over large distances (with the tip out of tunneling for safety) while imaging the tips with the SEM. The tip movement is easily observed and, if necessary, scan directions can be flipped by reversing wires, for example.

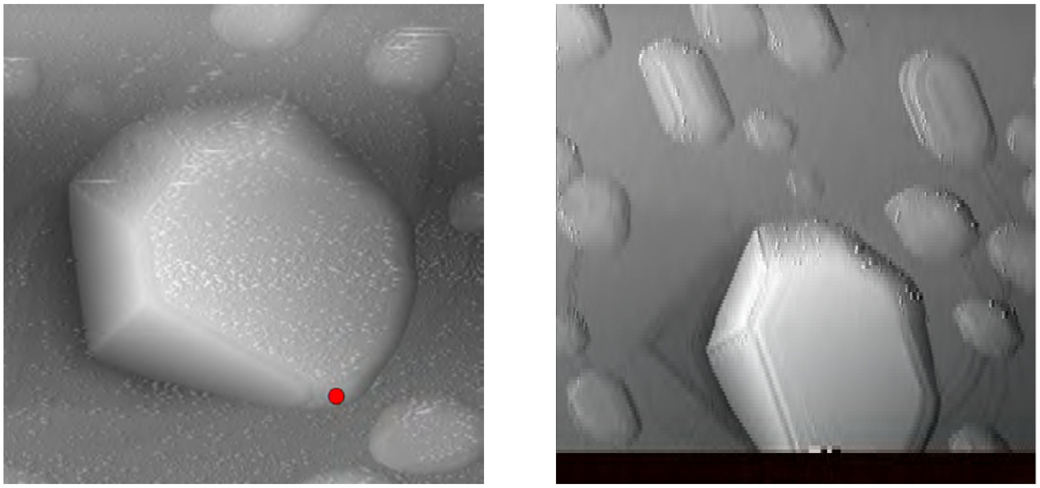

(a) STM image taken with the right probe (~400 nm wide, 2.2 V, 100 pA). The red circle indicates where the probe was touched down.

(b) STM image (500 nm wide, 2.2 V, 100 pA) of the same island taken with the main STM tip. The tip was withdrawn when it hit the right probe (bottom center).

Figure 7.6: STM images of the same $TiSi_2$ island taken by two different probes.

Figure 7.6 shows the same area of the sample imaged by two different probes. Note that the STM image, Figure 7.6(b), is rotated 45 degrees relative to the probe image, Figure 7.6(a). This is because the STM tripod scanner is mounted at 45 degrees to the axis of the probe tube scanners. Taking this rotation into account, it is clear that the images are of the same $TiSi_2$ island.

In this experiment, the right probe STM image was obtained first. The right probe was then touched down onto the corner of the $TiSi_2$ island, at the point indicated by the red circle in Figure 7.6(a). The right probe remained at this point while the STM image of Figure 7.6(b) was obtained. The scan direction was top to bottom — when the STM tip reached the other probe it saw what is effectively a very tall feature as it started to scan the tip. At this point the STM tip was retracted to avoid damaging it by scanning such a tall object. We can estimate that the STM tip reached a distance of ~60 nm before hitting the right probe, which is consistent with normal tip radii.

Finding the same area on the surface with more than one tip is indeed possible, as the preceding figures show. However, it is a very time consuming process. Many large STM images need to be taken in order to find the same area with two tips, and each STM scan takes several minutes. A surface with easily visible features is advantageous — a plain Si surface would be difficult to use since the only recognizable features are defects and step edges, which require much better tips to scan than simple, large $TiSi_2$ islands do. Large areas must be scanned so as to be able to find common features, and to avoid damaging tips, a relatively slow scan speed must be used.

The speed at which the same area might be found depends on the quality of the initial guess position in the SEM — the poor resolution of our SEM made it difficult to bring tips closer than a few hundred nm together. It is possible to spend many hours or even days without finding the same area. As more surface is scanned, the large protrusions of the $TiSi_2$ islands often damage and dull the STM tips, making shapes harder to recognize. Also, care has to be taken in the placement of a first probe when a second one is scanning. It is possible to scan one tip *under* another tip; if the lower tip is then retracted, it will hit the upper tip. Since the feedback loop always assumes that moving *up* breaks the tunneling contact, it will simply try moving further up when it detects the current from the upper tip, damaging both tips. To avoid this, a *ceiling* feature was added to the scanning software, which limits how high the tip could be retracted. It is then a matter of ensuring that the other tip is above this ceiling in order for both tips to be safe.

These issues make finding a tip with another tip very challenging. This was accomplished on only a few occasions with two tips, and it was not attempted to locate all 3 tips on the surface with this method. Because of all these difficulties, we opted to pursue another method of making metal contacts on Si surfaces using electron beam lithography, and this is described in the following sections.

7.4 Electron Beam Lithography

Lithography in electronic circuit manufacturing is a widely used technique where a *resist* is deposited on a substrate, exposed to light which changes its chemical properties. A *mask* is used to define a pattern where light will be exposed. A *positive* photoresist will become soluble to a developer where exposed to light, leaving the substrate exposed. Conversely, a *negative* photoresist is soluble everywhere *except* where light exposure occured, creating a negative of the pattern on the surface.

Electron beam lithography (EBL) works in a similar way as optical lithography, but instead of a mask blocking a broad source of light, it uses a focused electron beam that is scanned across the surface to expose the resist [106]. The main advantage of EBL is that it is not limited by the diffraction limit due to the wavelength of light. The wavelength of an electron is so small that it is the quality of the electron beam focusing and its interaction with the resist that determines the ultimate resolution; modern EBL can define features as small as a few nanometers across. It does not require a mask, but writing a large pattern can take much longer than the short exposure used in optical lithography. It is therefore less suited for mass fabrication of electronics but is commonly used in research and development.

We chose to use EBL to define metal contacts on silicon surfaces. Unlike the self-assembled $TiSi_2$ islands described in Section 7.2, which form randomly, EBL-defined contacts can be reproducibly made to exact specifications. In particular, to attempt field-directed molecular line growth (see Chapter 8), we required a two-contact structure with a small gap. Randomly placed self-grown islands would be exceedingly unlikely to form with the desired gap. Therefore, we defined a pattern (described in Section 7.5.1) that fits our needs. Obtaining high-quality Si(111)-7×7 and H-Si(111)-1×1 surfaces while preserving the EBL-defined contacts was more of a challenge, and is described in sections 7.7 and 7.9.

7.5 Electron Beam Lithography Procedure

Electron beam lithography and metal deposition were performed at the University of Alberta's Nanofab facility by Dr. Stanislav Dogel, post-doc in our group. The procedure he used follows.

- Using a diamond dicing saw, silicon wafers were cut into squares measuring 14×14 mm. This allows 5 samples of 14×2.75 mm to be cut after EBL and metal deposition are completed.
- The wafer was cleaned using a standard Piranha solution (H_2SO_4:H_2O_2, 3:1) for 30 minutes. It was then rinsed in deionized (DI) water and blown dry. To remove residual water, the wafer was baked on a hot plate in air for 5 minutes at 200 C.
- A positive photoresist (PMMA 950 A2) was spun on the silicon wafer at 4000 rpm for 30 seconds. The resulting resist thickness of $\sim$90 nm was confirmed using a profilometer. After spin coating, the resist was baked at 200 C for 2 minutes, in air.
- A Raith 150 EBL instrument was used to design and write the pattern. The pattern described in Section 7.5.1 was written on the resist with an electron

beam current of 0.08 to 0.09 nA, using a line writing speed ranging from 1.8 to 2 mm/s. With these settings, each pattern took about 2.5 minutes to write.

- After the pattern writing was completed, the resist was developed in a 1:3 solution of MIBK:IPA (Methyl isobutyl ketone:isopropyl alchohol) for 45 seconds. The development was then stopped by rinsing in IPA for 15 seconds. The resist was then rinsed in DI water and blown dry.
- The metal was deposited using a sputter deposition system (GATAN Precision Plasma Deposition and Cleaning instrument). A sputtering energy of 10 keV was used, yielding a deposition rate of 0.5 Å/s for titanium.
- After metal deposition, lift-off was performed by dipping the samples in acetone at 60 C in an ultrasonic bath. The samples were typically kept in the acetone for 20 minutes to get a successful lift-off; though the quality of lift-off depends on many parameters, especially the type of metal used.

7.5.1 EBL Pattern

The pattern written by Dr. Dogel by electron-beam lithography is shown in Figure 7.7. The figure shows an earlier version of the pattern with fewer contacts defined. The final version of the pattern includes four columns of two-sided contacts with nominal gaps of ranging from 0 nm (no gap) to 600 nm in steps of 50 nm, continuing to a maximum gap of 1000 nm in steps of 100 nm. The two-contact gap structures consist of a 1×2 μm pad, with a 5 μm long wedge shrinking down to a point. The sharpness of the final point is determined by the tuning of the electron beam, and is typically no better than 20 nm. Along the length of the column, the pads are spaced 4 μm apart, center-to-center. This regular spacing provides an easy way to move to another contact — once one contact is found, moving a fixed number of steps (six steps when using the Omicron MSCU coarse mover controller) will put the next contact over under all three tips, within an error of a few hundred nm. A moderately large STM scan (500-1000 nm) normally makes it easy to find the gap in the contact structure again.

The test lines have widths of 25 nm, 50 nm, 100 nm, 250 nm, 500 nm, and 1 μm to 5 μm in 1 μm steps; they are very useful in finding the patterns and to focus the SEM.

Typically, two copies of this pattern were written on each STM-sized (14×2.75 mm) Si samples. The two patterns were centered width-wise, and spaced 2 mm apart length-wise. This helped increase the sample success rate — if lift-off was

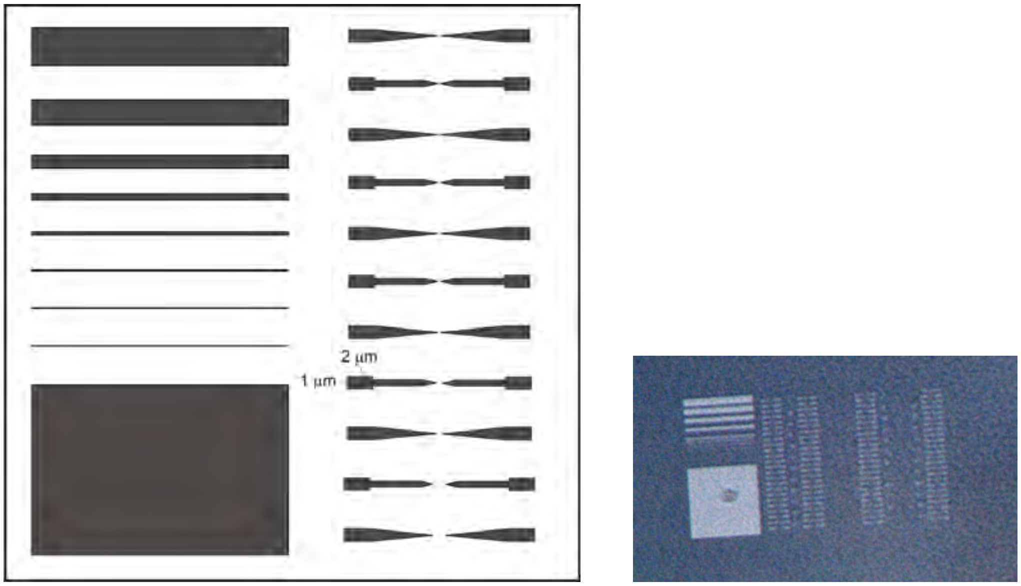

(a) Schematic of a portion of the EBL pattern selected to highlight the important features.

(b) Optical Micrograph of the pattern (100× magnification).

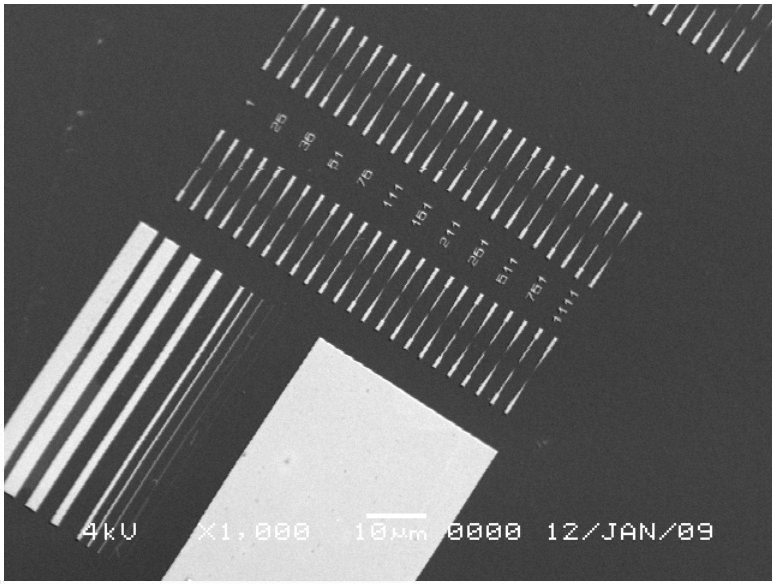

(c) SEM image of the pattern (1000× magnification, 4 kV beam voltage).

Figure 7.7: EBL pattern schematic, optical micrograph and SEM image. The pattern has a large 50 μm × 50 μm square used for pattern finding. Above that is a series of lines of increasing width, from 25 nm to 5 μm. The contacts are arranged in 4 columns on the right side, with increasing spacing towards the bottom of the pattern.

unsuccessful on one pattern, the other was often still usable.

7.6 Annealing Titanium

The first metal we deposited was titanium. As described in the previous section, the metal was deposited on the native Si oxide — indeed, since the silicon crystals need to be moved in air to different machines (from spin coating, to EBL, to sputter deposition), it cannot be avoided. The oxide surface is not of interest to us and cannot be studied by STM, since it is an insulator; it needs to be removed once the sample is placed in vacuum, so that the metal forms a good contact with the underlying Si. Therefore, we proceeded to determine the proper annealing parameters that would result in high-quality Si surfaces on both Si(100) and Si(111).

As we have seen in Section 7.2.1, titanium deposited on Si will form $TiSi_2$ crystals if annealed at the proper temperature. Titanium silicide is often formed in CMOS processes by heating a Ti layer deposited on Si. However, we found that using too high of an anneal temperature resulted in large crystal growth.

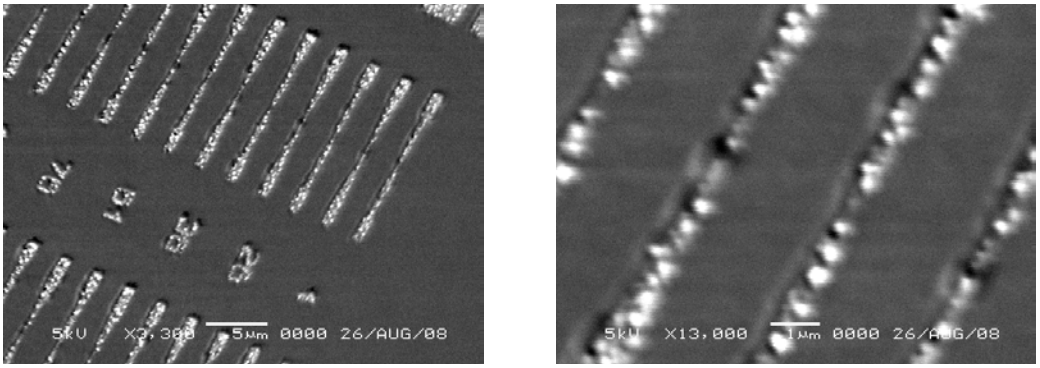

(a) 3300× magnification.

(b) 13000× magnification.

Figure 7.8: SEM images of 15 nm thick Ti contact pads on Si(111) annealed up to 1100 C. 5 kV beam voltage.

Figure 7.8 shows the results of annealing a thin (15 nm) Ti layer on a low-doped n-type Si(111) crystal at temperatures reaching 1100 C. This sample had been annealed for 5 seconds each at progressively higher temperatures: from 900 C to 1100 C in steps of 50 C. The large $TiSi_2$ crystals formed by the annealing procedure can be clearly seen. In addition, a trench of missing silicon can be seen close to the edges of features — this is most visible in Figure 7.8(b). This is presumably a similar effect to the trench forming around self-assembled $TiSi_2$ island experiments, e.g. Figure 7.3(a), caused by diffusion of Si to form titanium silicide.

The large $TiSi_2$ crystals formed with high temperature annealing cause the contacts to break up into segments which are not electrically continuous. This can be seen by taking a SEM image in EBIC mode (see Section 5.5.1) with the probe touching down on a metal line or contact. An example of a broken line can be seen in Figure 7.9. This sample is low-doped n-type Si(111) with 15 nm of Ti deposited, which was annealed a few times up to 1000 C. Figure 7.9(b) shows how the EBIC signal cuts off ∼3 μm from the point of contact, where crystal growth broke the continuity of the line.

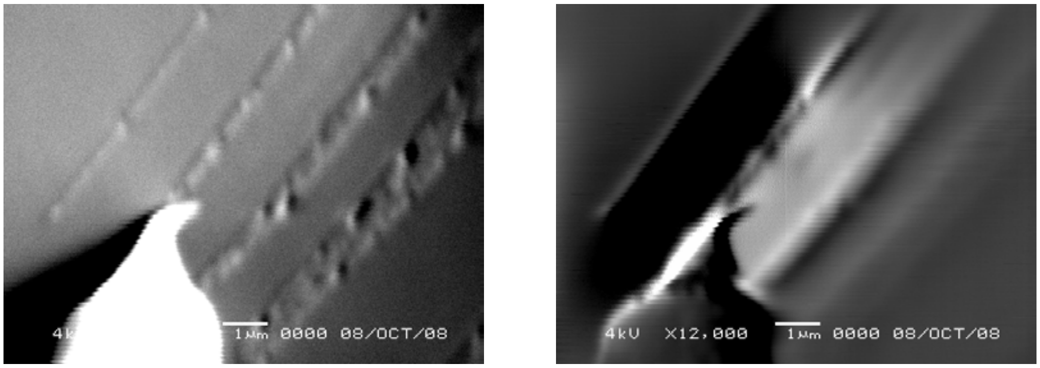

(a) Secondary electron current image.

(b) Electron-beam induced current image, with 10^6 V/A preamp gain.

Figure 7.9: SEM images of a titanium line touched by a STM tip (12000× magnification, beam voltage 4 kV).

7.7 Obtaining the Si(111)-7×7 Surface

One of the surfaces of interest is the Si(111)-7×7 surface. This surface shows interesting conductivity characteristics, which will be discussed in more detail in Chapter 9. For a crystal with no metal contacts, a typical annealing procedure to obtain a Si(111)-7×7 surface is to repeatedly flash the crystal to 1200 C for a few seconds. After the last 1200 C flash, the temperature is dropped in a few seconds down to 850 C, where it is held for 1 minute; the temperature is then lowered to room temperature in approximately 60 seconds. The 1200 C flash is generally helpful in fully cleaning the surface; a crystal subjected to this treatment typically has fewer carbon-contamination islands visible in STM.

To characterize the 7×7 surface, we desire to obtain a high-quality 7×7 reconstruction while preserving the metal contacts made by EBL. The previous section has shown that when annealing EBL-defined Ti patterns, thin Ti layers and excessive temperatures cause $TiSi_2$ crystals to form and break the conductivity of the contacts. However, forming a Si(111)-7×7 surface requires an anneal of sufficient temperature — typically at least 850 C [107, 108]. This is required to remove the native Si oxide and to give sufficient energy for the reconstruction into the complex 7×7 structure, which requires breaking and reforming multiple Si-Si bonds.

After some trial and error, we determined that a thicker Ti layer helped keep the contact pads continuous even after some annealing. We therefore used 30 to 40 nm thick Ti layers for later experiments. A successful annealing procedure we used was to anneal the sample for 5 seconds each at the following temperatures: 900 C, 950 C, 1000 C. A 60 second pause was taken between anneals. Extra anneals could be used when the surface quality was found lacking. After the final 1000 C flash, the temperature was linearly lowered from 950 C to ∼500 C over two minutes, and was then quickly lowered to room temperature. This was found to regularly produce high-quality Si(111)-7×7 surfaces, while preserving the contact pads, as shown in Figure 7.10.

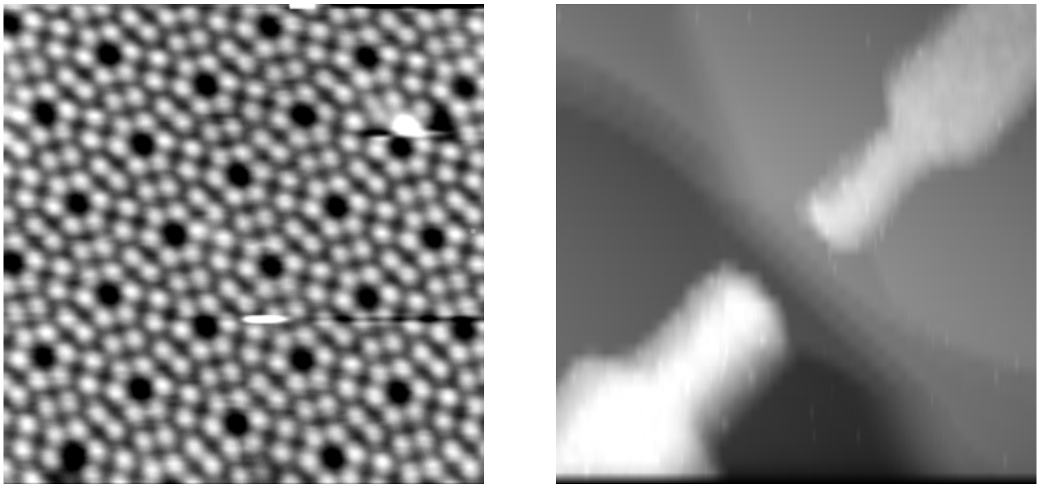

(a) STM image of a high-quality Si(111)-7×7 surface (10-nm wide, +2.0 V, 0.1 nA).

(b) STM image of the gap between the contact pads on low-doped n-type Si(111) (600 nm, -3 V, 100 pA).

Figure 7.10: The Si(111)-7×7 surface and metal contact pads after moderate-temperature annealing.

We found that for low-doped n-type (As-doped) Si(111), the annealing procedure resulted in a large number of steps between the metal contacts, as can be seen in Figure 7.10(b). The height of the silicon next to the metal contact on the lower left of that image is several nm below that of the other metal contact; this orientation was the same for all the contacts observed. The asymmetry of the situation is curious, since nothing in the EBL process should cause a difference on one side of the contact.

The miscut of the Si wafers was below 0.25°. The only process that might give a direction is the annealing, which uses DC current - the direction of the current flow through the crystal was always the same, and might be linked to the direction of the steps. Interestingly, we did not observe this effect after annealing low-doped p-type (B-doped) Si(111), with the other parameters (such as metal thickness and annealing procedure) kept constant. The reason for this is unclear.

7.8 Obtaining the H-Si(100)-2×1 Surface

Obtaining a H-Si(100)-2×1 surface with the metal contacts was straightforward and begins in a similar way as the Si(111)-7×7 surface preparation. First, a few flashes at temperatures up to 1100 C were performed so as to remove the native oxide and other contaminants. The hydrogen termination is then performed in the usual method, as described in Section 3.1.1. This method was found to be successful without excessive $TiSi_2$ crystal formation.

In the gap between the metal contacts, we normally found a fairly high density of steps leading up to each metal contact, with at least one wider, flat terrace halfway between the contacts.

7.9 Obtaining the H-Si(111)-1×1 Surface

Another surface of interest to us is the H-Si(111)-1×1 surface, where each surface Si atom is terminated with a hydrogen atom. This surface was used in our attempts to direct molecular line growth using an electric field described in Chapter 8.

One way we attempted to obtain a H-Si(111)-1×1 surface with metal contacts was to form self-assembled $TiSi_2$ islands on Si(111) (Section 7.2.2) and follow up the silicide island formation, which also removes the native oxide, with an in-UHV hydrogen termination. Unfortunately, unlike the case of Si(100) where a high-quality hydrogen terminated surface can be obtained with UHV-only treatment (see Section 3.1.1), the literature shows that in-UHV H-termination of Si(111) are of fairly low quality, with at least 1% defects [109, 110, 111]. We reproduced the experimental procedure described in these papers and obtained similarly poor results.

7.9.1 Chemical Etching H-Si(111)-1×1 Surface Preparation

The standard method used to hydrogen-terminate Si(111) is wet chemical etching [112, 113, 114, 115]. This procedure is performed in solution and therefore obviously out of the vacuum chamber, but the surface is resilient enough to still be of very high quality after being transported in air to a UHV chamber. A typical Si(111) H-termination procedure we used is as follows:

- The containers and teflon tape (sample holder) that will be used are cleaned with Piranha solution (H_2SO_4:H_2O_2, 3:1) for 30 minutes. Piranha dissolves all organic matter. Because the containers are small and therefore the heat from mixing dissipates quickly, they are kept at 100 C on a hot plate so as to keep the solution effective.
- The Si crystals used are mounted upside-down in slits in a teflon tape. Mounting the samples upside-down is thought to reduce contamination by allowing any dissolved material to fall away from the surface.
- One container is filled with the 40% NH_4F solution that will be used for etching. Argon gas is bubbled through the solution for 30 minutes so as to degas it and remove any dissolved oxygen, which would cause etch pits.
- Another container is filled with ultra pure water (18.2 MΩ, produced by a Milli-Q system). The water is degassed for 30 seconds in the same way as the etching solution.
- One container is filled with Piranha and is used to clean the tweezers used (all-ceramic tweezers) for 30 minutes, maintained at 100 C.
- Another container is filled with Piranha; the teflon tape holding the samples is dipped into it and the samples are cleaned for 30 minutes, maintained at 100 C.
- After the samples are cleaned by Piranha, they are rinsed with ultra-pure water.
- The samples are placed in the NH_4F solution for 8 minutes. The Ar gas bubbling is stopped, but a blanket of Ar is maintained in the container so as to prevent oxygen from dissolving into the solution. Oxygen is thought to cause etch pits in the surface.
- The samples are removed from the NH_4F solution and are rinsed using the degassed ultra-pure water.
- The samples are quickly taken out of the teflon tape and placed into a UHV chamber load-lock, which is pumped down as soon as possible.

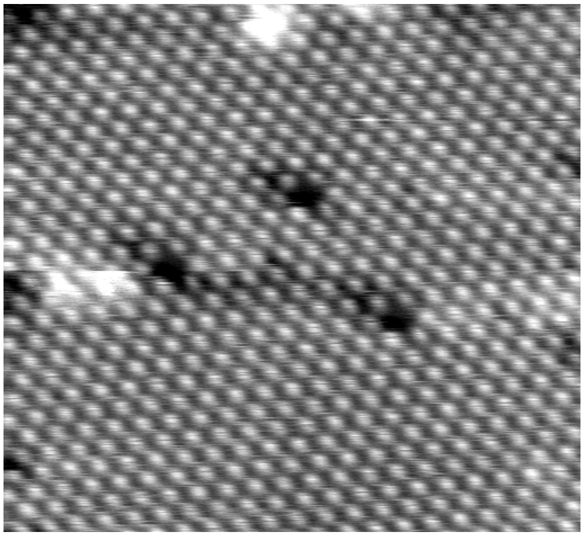

Figure 7.11: Atom-resolved STM image of a low-doped n-type H-Si(111)-1×1 surface obtained by wet chemical etching (6×5 nm, −2 V, 80 pA).

Once the sample is load-locked into the UHV chamber, it is normally annealed for 30 to 60 seconds at 220 to 250 C. This final sample preparation step removes most of the water or other molecules that became physisorbed on the surface during its time in air. It is difficult to obtain atom-resolved STM images on the H-Si(111)-1×1 surface because of low corrugation amplitude; an example is shown in Figure 7.11.

7.9.2 Titanium Contacts on H-Si(111)-1×1

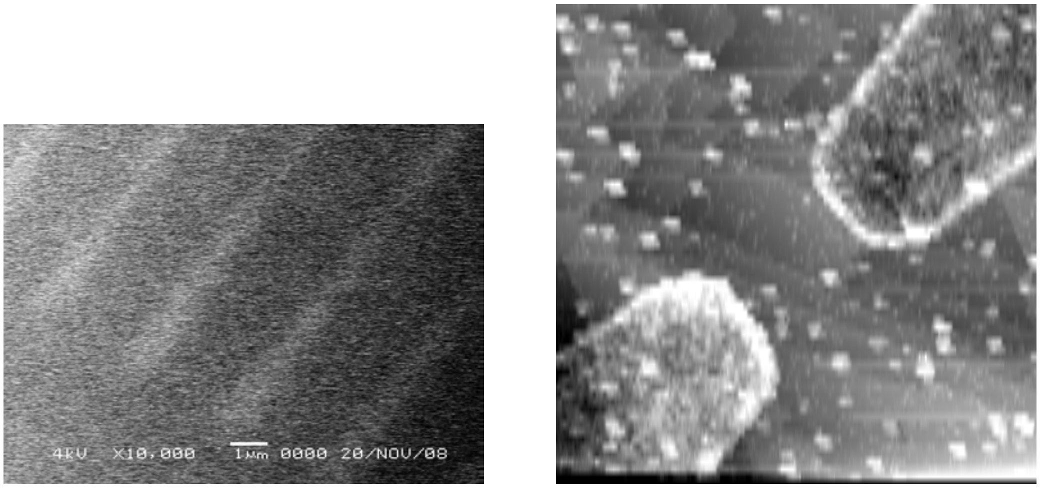

(a) SEM image of the etched Ti contacts on H-Si(111)-1×1 (10000× magnification, 4 kV beam voltage).

(b) STM image of the gap between the contact pads on low-doped n-type H-Si(111)-1×1 (600 nm, −2.8 V, 80 pA).

Figure 7.12: STM and SEM images showing how titanium contacts are etched by Piranha during the Si(111) H-termination procedure.

In our first attempt to obtain a H-Si(111)-1×1 surface with metal contacts, we used a 40-nm thick titanium layer defined by EBL. The H-termination procedure used was as described above, with the only difference being that the samples were cleaned in Piranha for only 4 minutes rather than the usual 30. We unfortunately found that the Piranha step etches away the Ti metal pads in a very short time, as can be witnessed by the images in Figure 7.12. The first indication of etching was that the SEM imaging of the contacts (Figure 7.12(a)) was extremely difficult due to very low contrast. A STM image of the gap (Figure 7.12(b)) shows the clear outline of where the metal was deposited; however there seems to be nothing left of the 40 nm of Ti except for a small (∼1 nm high) ridge around the edge. Another sample prepared with only 1.5 minutes of Piranha cleaning showed the same etching. Because of the short times in Piranha, both these samples showed a less than optimal H-Si(111)-1×1 surface, with more contamination and defects than usual. Only a 30 second Piranha cleaning left any Ti on the surface, but even in that case it etched all but 4 nm; in addition the H-Si(111)-1×1 surface was of very poor quality.

The EBIC-mode SEM images in Figure 7.13 show that the etched Ti lines are not electrically conductive — the EBIC pattern where the tip is touching is the same as if one were touching down on the Si surface with no pattern.

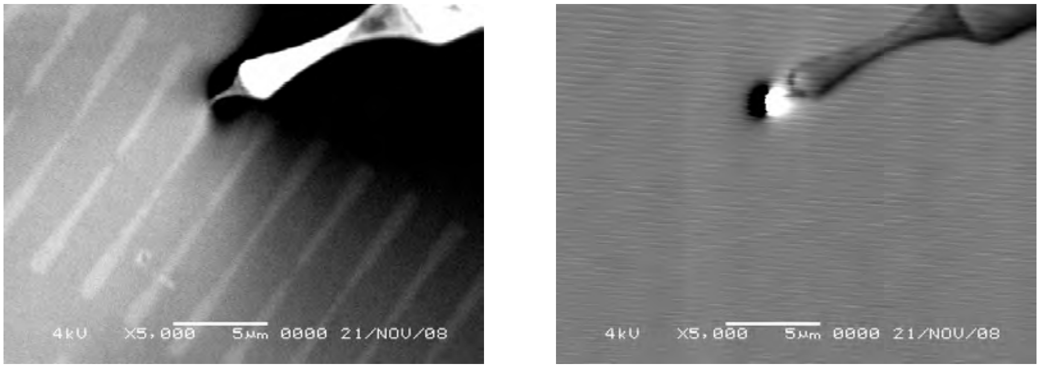

(a) Secondary electron current image.

(b) Electron-beam induced current image, with 10^6 V/A preamp gain.

Figure 7.13: SEM images of an etched titanium line touched by a STM tip (5000× magnification, beam voltage 4 kV). No metal remains after Piranha cleaning, and therefore the line has no electrical conductivity.

7.9.3 Platinum Contacts on H-Si(111)-1×1

These negative results led us to investigate the use of other metals that would resist the etching action of Piranha. Our first attempt was a 40-nm thick platinum film. The first problem was that the film was much more difficult to remove during the lift-off step, as can be seen in Figure 7.14(a). An extra 2 minute dip in Piranha, followed by acetone and methanol ultrasound baths were needed to remove the metal film more completely. The sample was then H-terminated by the usual procedure, with a 2 minute Piranha cleaning. The SEM image in Figure 7.14(b) shows that the metal clearly resisted the total of 4 minutes Piranha cleaning. However, the Pt film did not adhere well to the surface — it can be seen to buckle and peel off the surface. The contacts are therefore unreliable; also, performing a STM scan on them was exceedingly difficult because the tip, when attempting to scan over the thick tip, would touch and stick to the Pt film, which would then peel off.

We next attempted to use a thin layer of 5 nm Pt to protect the Ti film (35 nm) from Piranha etching. It was H-terminated in the usual method, with 15 minutes of Piranha cleaning. As Figure 7.15 shows, it appears that the Ti layer was etched underneath the Pt (presumably from liquid entering from the sides), leaving an extremely thin Pt layer which peeled and folded up on itself. STM scans showed the remaining film to be only 2 nm thick. Pt was thus rejected as a candidate for H-Si(111)-1×1 surfaces with metal contacts.

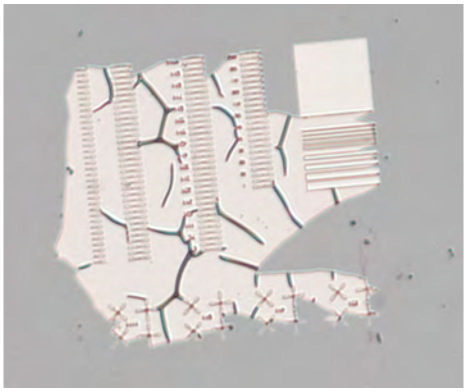

(a) Optical micrograph of the incomplete lift-off of Pt (100× magnification).

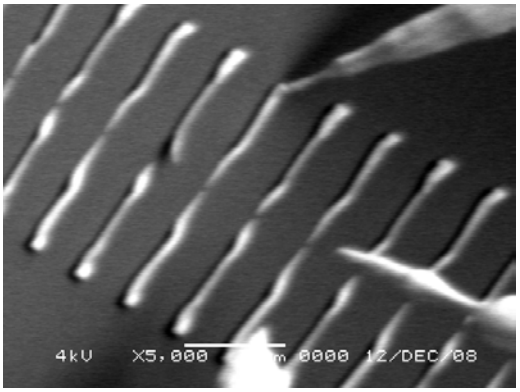

(b) SEM image shown the poor adhesion of Pt contacts on Si(111) (5000× magnification, 4kV beam voltage).

Figure 7.14: Platinum films deposited on Si(111) after wet-chemical H-Si(111)-1×1 termination.

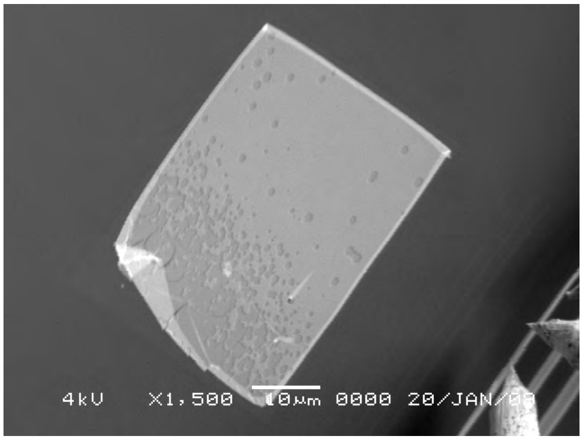

Figure 7.15: SEM image of a 5 nm Pt + 35 nm Ti film peeling off the Si(111) surface (1500× magnification, 4kV beam voltage).

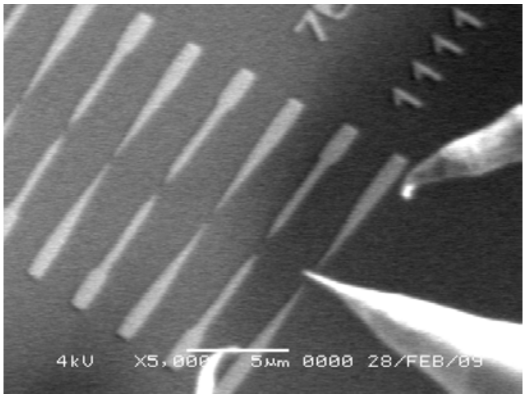

(a) SEM image of the Cr contacts on Si(111) (5000× magnification, 4kV beam voltage).

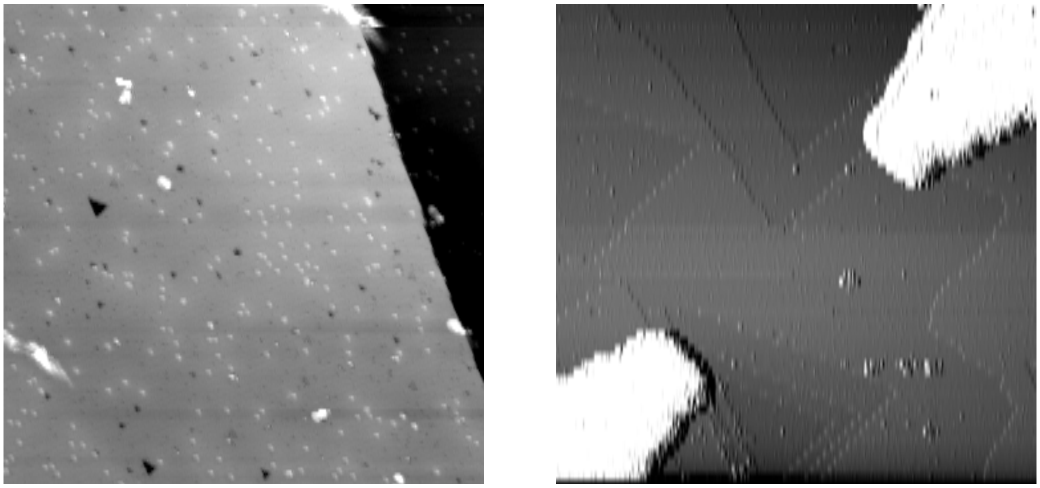

(b) STM image of the resulting H-Si(111)-1×1 surface (70 nm, −2 V, 100 pA).

(c) STM image of the Cr contacts gap area (800 nm, 2 V, 300 pA, mixed height and derivative).

Figure 7.16: Successful preparation of H-Si(111)-1×1 surface with Cr metal contacts.

7.9.4 Chromium Contacts on H-Si(111)-1×1

Our final attempt was to deposit a 20 nm layer of chromium. This metal, which is commonly used as an adhesion layer before depositing other metals, is corrosion-resistant and therefore a good candidate for both adhesion and resistance to Piranha etching. H-termination was performed with a 20 minute Piranha cleaning step. First, the SEM image in Figure 7.16(a) shows that the contacts survived the Piranha cleaning step, and that their adhesion to the surface is much better than that of Pt. The H-Si(111)-1×1 surface obtained was of fairly high quality, as shown in Figure 7.16(b). The STM image of the gap between contacts in Figure 7.16(c) shows that the Cr contacts have sharp edges and a reasonably flat top. It is also clear that the native oxide beneath the Cr metal has been removed by the treatment, since there is an electrical connection between the Cr contacts and the underlying silicon. It seems likely that the oxide underneath the metal is etched by the NH_4F solution penetrating from the sides. The Si surface between the contacts is flat.

7.10 Conclusion

In this chapter we have described our work in producing high-quality metallic contacts by two distinct methods: self-formed $TiSi_2$ islands and electron-beam lithography. By trial and error we have developed techniques to produce high-quality surfaces of H-Si(100)-2×1, Si(111)-7×7 and H-Si(111)-1×1 while preserving the metallic contacts. The electron-beam lithography technique in particular is very flexible, since almost any desired pattern can be written. This technology now gives us the ability to probe surface electrical properties in a way that was not achievable before.

Chapter 8

Field-directed Molecular Line Growth

In Chapter 3 we saw that a wide variety of molecules are able to form lines on Si surfaces, and that the particular chemistry of each type of molecule could have an effect on the pattern of line growth. For example, by combining two species on H-Si(100)-3×1, styrene and trimethylsulfide, we were able to grow lines in "L-shapes" (see Section 3.5). We would have a much more flexible situation if we were able to change the growth direction of single molecular species. With such a system, we would have the ability to grow molecular nanostructures of an arbitrary shape; for example, one could imagine using such structures to make wires to interconnect devices. In this chapter, we describe our attempts to alter the line growth directions not by using chemistry, but by using an external electric field.

8.1 Introduction

During molecular line growth, the intermediate product of the styrene with a carbon-centered radical will remain on the surface for some time — see Figure 3.2, step b. This is because of the presence of a large barrier (18 to 21 kCal/mol) to hydrogen abstraction (Figure 3.2, step c). This intermediate species remains on the surface long enough to perform many rotations, and it possesses an electric dipole moment that will respond to an external static electric field. Therefore, one might expect that the molecule could be "held" in a particular geometry by an external field, keeping it in an orientation that might make it possible to abstract hydrogen from a different site than normal. Line growth would therefore occur in the direction dictated by this external field. By changing the field direction, the growth might be made to occur in arbitrary directions and patterns.

8.1.1 Calculations

To gauge the merit of this idea, Dr. DiLabio performed a density functional theory (DFT) cluster model calculation to find the relative energy of a styrene additon radical on a H-Si(100)-2×1 surface at different orientations in an electric field — see Figure 8.1. In this calculation, the molecule was rotated about the bond highlighted in Figure 8.1(a) and held fixed while an electric field was applied in a direction parallel to the dimer row orientation. The field was set to 0, 0.54 V/nm, 2.7 V/nm and 5.4 V/nm. The calculations show that if a field of 2.7 V/nm or higher is applied, the molecule is most stable at a rotation angle of 0 (which corresponds to the molecule being oriented along the dimer row direction).

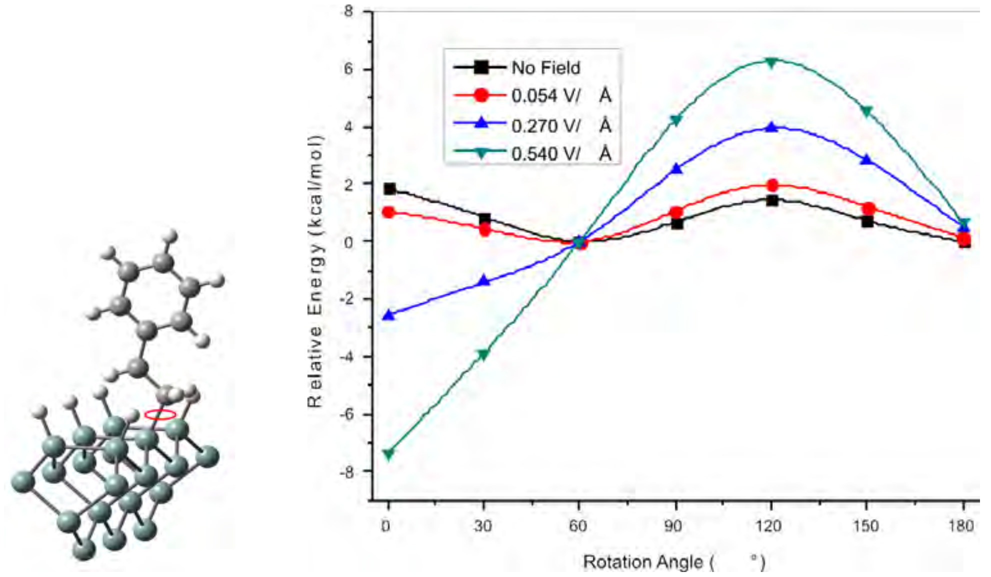

(a) Ball-and-stick representation of the model used in the calculation. The rotation was performed on the bond highlighted with a red oval.

(b) Chart of the results of the calculation, showing that the molecule is most stable at a rotation angle of 0 if a sufficiently strong field is applied. 1 eV = 23 kCal/mol; kT at 300 K = 26 meV = 1.7 kcal/mol.

Figure 8.1: Calculation of the relative energy of a styrene addition radical on a H-Si(100)-2×1 surface in varying orientations at varying electric field strengths. The electric field is applied parallel to the dimer row direction.

8.1.2 Dipole Moments

The response of the molecule to the external electric field will be proportional to its dipole moment. The calculations presented above were for a styrene addition radical with no subtituents. Since it is a fairly symmetrical molecule, the dipole moment of styrene is rather small — 0.12 D according to Ref. [116]; Ref. [117] reports a dipole moment < 0.3 D. However, when the molecule adds to the Si surface dangling bond, it becomes a radical species; its dipole moment then is higher (0.48 D according to calculations performed by Dr. Gino DiLabio).

It is known that in addition to normal styrene, many substituted styrenes grow lines as well [22, 23, 24] — therefore it is of interest to look for a substituted styrene that will have a much stronger dipole moment. Fluorine, with its large electronegativity, is a good candidate substituent. For instance, the dipole moment of meta-fluorostyrene has been reported to range from 1.49 to 1.69 D [118] — already more than 10 times higher than styrene. Another possible molecule is 3-trifluoromethylstyrene, which is easily available from commercial suppliers such as Sigma Aldrich. The presence of 3 fluorine atoms should greatly increase its dipole moment — calculated by Dr. DiLabio to be 2.52 D as a radical species on the H-Si(100)-2×1 surface.

From these results, we expect that 3-trifluoromethylstyrene will be approximately 5 times more susceptible to field-directed molecular line growth than styrene. From the results shown in Figure 8.1(b), we can expect that a field of 0.5 V/nm or higher might have a sufficient effect on the molecule to direct its growth. We therefore chose to use this molecule for the field-directed molecular line growth experiment.

8.1.3 Growth Direction

The calculations presented in Figure 8.1 assumed that the benzene ring of the styrene molecule would be standing perpendicular to the surface, as pictured in the ball-and-stick diagram in Figure 8.1(a). In this situation, the benzene ring would tend to align with the electric field, bringing the carbon-centered radical in line with the field direction. This would cause line growth to occur parallel to the field.

Later calculations showed that due to dispersion interactions the benzene ring of the molecule is actually laying close to flat with the surface — see Figure 8.2. In the case of unsubstituted styrene, Figure 8.2(a), the dipole moment favors growth that is roughly aligned with the row direction. However, the dipole moment of the 3-trifluoromethylstyrene radical is not oriented in the same direction as styrene's.

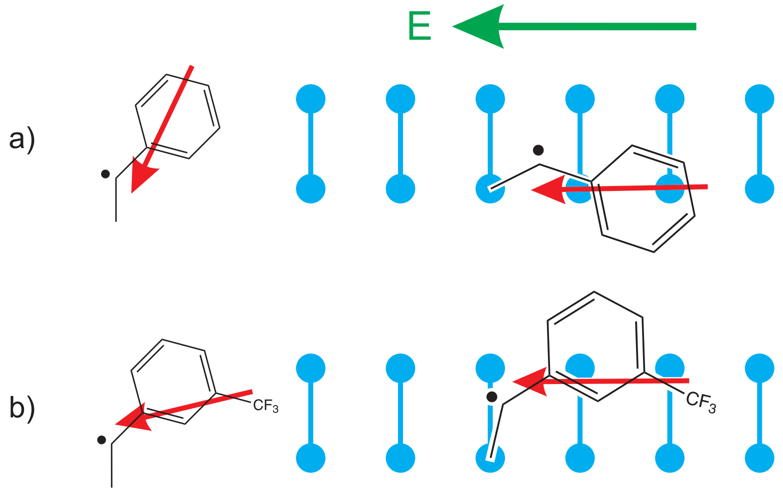

Figure 8.2: Comparison of the dipole moments and growth direction of addition radicals on a H-Si(100)-2×1 surface: (a) styrene, 0.48 D; (b) 3-trifluoromethylstyrene, 2.52 D. The dipole moment orientation of each molecule is indicated by the red arrows. Each dimer of the surface is represented by the underlying blue lines. The electric field *E* is parallel to the dimer row direction. The alignment of styrene promotes growth along the field direction; for 3-trifluoromethylstyrene, perpendicular-to-field growth is promoted.

For that molecule, when the dipole moment of the molecule is aligned with the electric field, the carbon-centered radical is actually better placed to abstract a hydrogen in the direction that is perpendicular to the field, as shown in Figure 8.2(b). Hence, we expect line growth to be perpendicular to the applied electric field for 3-trifluoromethylstyrene.

8.1.4 Surfaces of Interest

The first surface where this experiment might show interesting results is on H-Si(100)-2×1. Styrene and its derivatives grows lines along the dimer row direction with very good reliability, usually forming long straight lines. Therefore, if the use of an external electric field caused the growth pattern to be noticeably changed, e.g. growing across rows or along a diagonal direction, this would be a strong indication of success. Unfortunately, the very small likelihood of cross-dimer styrene growth also means that inducing such growth with the help of an electric-field might be difficult.

Conversely, on the H-Si(111)-1×1 surface there is no built-in directionality to the surface — this is why styrene grows in a random-walk pattern on this surface [20]. Therefore, a modest electric field might be more likely to cause directed growth on this surface than on H-Si(100)-2×1. However, the effect would need to be sufficiently noticeable that it could be clearly distinguished from a random walk. More statistics would be needed, since a single or a few lines growing in the same direction on H-Si(111)-1×1 could be attributed to chance.

8.2 Experimental Method

This experiment requires one to apply an electric field parallel to a Si surface; unfortunately, the charge at the surface of a conductor will always rearrange itself so as to cancel out an external field parallel to its surface. The styrene addition product on Si stands ∼5 Å away from the surface, so there is a possibility to apply a field parallel to the surface at that distance. However, this distance is extremely small, making things very difficult.

8.2.1 Biased Tips Over the Si Surface

One way to apply such a field in our multiple probe STM would be to hold two of the probes close to each other but not in contact with the Si surface, and to apply a voltage between them. To estimate the feasibility of this approach, we performed finite element method (FEM) simulations of the electric field between two tips. Two tips of 20 nm radius were spaced 200 nm apart and 50 nm above the Si surface. These distances are thought to be reasonably easy to achieve in practice. The Si was set to have a resistivity of 5 Ω·cm. Note that this is a 2D model, meaning that it represents, in 3D, long wedges that narrow to a line, not a point as a full 3D tip would; this simplification will make the calculated electric field between the two "tips" higher than it would be in reality.

The results from this model are shown in Figure 8.3. With 1 V between the tips, only 7.7×10^{-4} V/nm are developed 5 Å above the surface, at the midpoint between the tips. Even if the voltage were increased to 100 V, the field would be only 0.08 V/nm — still below the desired field strength. Voltages in this range at such close distances are likely to cause field-induced electron emission, which could damage the hydrogen terminated surface — field emission of electrons to the surface is often used to desorb large patches of H on H-Si(100)-2×1. Considering that this 2D model is likely to overestimate the values, we can see that this approach will not yield the necessary field strengths. This method would also require the precise alignment of all 3 tips, which we have found to be a difficult task in practice (as we described in Section 7.3, page 130). Because of these shortcomings, we opted for a different way to apply the electric field, described in the following section.

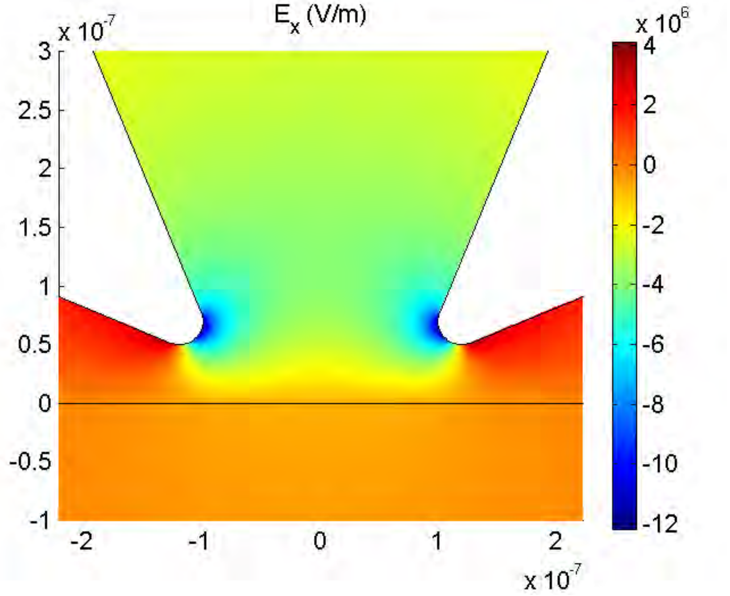

(a) Pseudo-color image of horizontal electric field value.

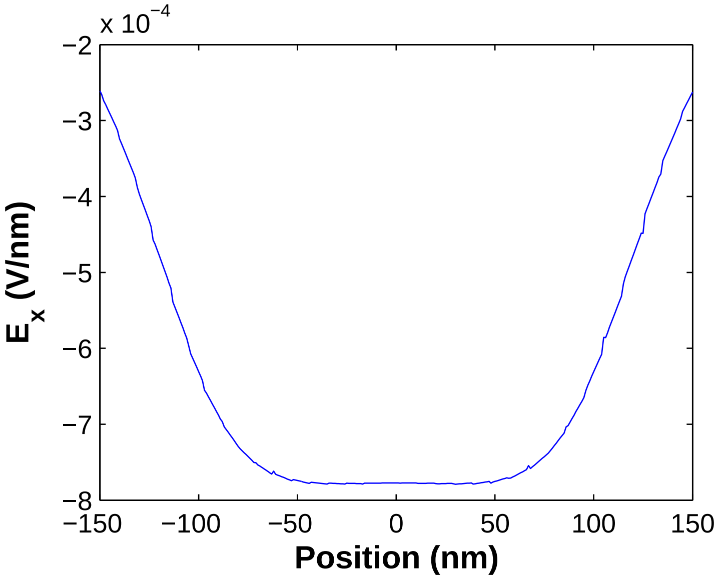

(b) Plot of the horizontal electric field 5 Å above the Si surface.

Figure 8.3: 2D FEM simulation of the electric field between two STM tips spaced 200 nm apart and held 50 nm above a Si surface, with 1 V applied between them.

8.2.2 Metal Contacts on Si

A second way to achieve an electric field parallel to the surface of a conductor is to apply a field within the conductor and to allow current to flow — the horizontal component of the electric field inside the conductor will still be present 5 Å above its surface. The lithographically defined metal contacts we described in Section 7.5 are ideal for this purpose: they are relatively easy to make contact to, and the pattern consists of contacts with increasing gaps, allowing one to choose an appropriate spacing that will generate a strong enough electric field.

For a successful field-directed line growth experiment, we will need to obtain high-quality H-Si(100)-2×1 or H-Si(111)-1×1 surfaces while preserving contacts — the procedure for obtaining these has already been described in Sections 7.8 and 7.9, respectively.

8.2.3 Heating Effect Calculations

As mentioned earlier, by using metal contacts on Si we can successfully apply an electric field at the expense of flowing current through the semiconductor. The material has a certain resistance, which will cause Joule heating of power $P = IV = V^2/R$. We can see from this equation that for a given voltage V, a higher resistance R will yield a smaller heating power P. It is therefore to our advantage to pick the least conductive Si crystal possible. In our case, we used an undoped Si(100) crystal from Virginia Semiconductor, specified to have a resistivity $\geq$ 20 Ω·cm.

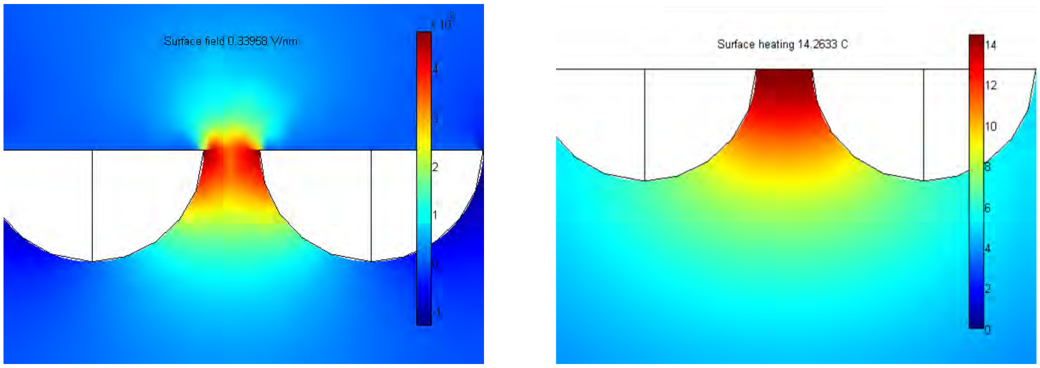

(a) Pseudo-color plot of the electric field between the islands. At the midpoint on the surface, the field is of 0.34 V/nm.

(b) Pseudo-color plot of the heating of the semiconductor. Between the contacts, the temperature is elevated by 14 C.

Figure 8.4: Cross-section view of the FEM simulation of two 50-nm radius islands, spaced 25 nm apart in 20 Ω·cm Si, with 10 V applied between them.

To gauge the level of heating that would occur in a realistic experiment, FEM simulations were performed. The model consisted of a large slab of Si with 20 Ω·cm resistivity and normal bulk Si thermal properties. Two conductive hemispherical islands 50 nm in diameter were placed 25 nm apart in a full 3D model. A voltage difference of 10 V was applied between the islands; the model was solved for both temperature and electric current. Note that this model takes the Si to be a uniform conductor with ohmic contacts, and does not represent the Schottky barriers that are actually present. The results are shown in Figure 8.4. We can see that the field produced in this situation, 0.34 V/nm, might be sufficiently large if using a molecule with a large dipole moment. The increased temperature between the contacts is calculated to be 14 C, which is a manageable amount.

As the distance between the contacts is increased, the voltage required to produce a strong enough field obviously increases. For example, two 25-nm radius islands spaced 100 nm apart would require 50 V between them to produce a field of 0.27 V/nm. The higher voltage and current cause Joule heating to increase to 68 C in this situation according to FEM calculations; this temperature is likely high enough to have negative effects on line growth and stability. At a fixed geometry, temperature scales with the square of the voltage applied, as one would expect from the $P = V^2/R$ relationship.

The temperature dependence of electrical conductivity of Si was not included in this model; since conductivity increases with increasing temperature, there is a possibility of a "run-away" thermal increase. This was observed in a few instances — when an excessive current was used, the Si between the contacts melted explosively, destroying the surface over several microns, and damaging the tips.

With the help of these simulations we can estimate the conditions that are likely to provide a sufficiently strong field without excess heating: a contact gap smaller than 100 nm with a field < 0.3 V/nm; higher fields are possible with smaller gap sizes.

8.2.4 Procedure

A field-directed molecular line growth experiment proceeds thus:

- Under SEM view, the three tips were aligned at a spacing matching the contact pad spacing, as described in Section 5.5.
- The main STM tip is used to find and align to a contact gap of desired size.
- The left and right probes are aligned with their respective metal pads by performing large STM scans.

- Several STM images of the surface between the metal contacts are acquired — these are the “before” pictures.
- The left and right probes are brought into slight contact (overdriven by 10-50 nm).
- The IV curve of each contact is recorded.
- The left contact is grounded while the right is biased using the Keithley Sourcemeter. The sample bias is disconnected.
- IV curves of the current across the gap are recorded. A voltage is chosen that is as high as possible but without excessively large current flowing. This was typically 10 to 20 V, with a current ranging from 50 to 100 μA.
- The gate valve to the ion pump is nearly, but not completely, closed. This helps prevent ion-pump-induced radicals that could damage the H-terminated surface (see Section 3.7).
- The voltage is applied between the contacts, establishing the electric field.
- A leak valve is opened to dose the chosen molecule into the chamber (typically 100 seconds at 10^{-6} Torr of pressure, for a dose of 100 L). The leak valve is then closed.
- The field is kept on for approximately 1 minute, until the chamber pressure returns to a pressure $< 10^{-8}$ Torr. The gate valve to the ion pump is reopened to accelerate pumping.
- The field is turned off and the probes are retracted from the surface.
- More STM images of the gap area are taken and compared with the previous images.
- In a few cases, we performed this experiment without dosing any molecules, to see the effect that the field and current had on the surface.

8.3 Growth of 3-Trifluoromethylstyrene

8.3.1 Growth of 3-Trifluoromethylstyrene on H-Si(100)-2×1

As was mentioned in Section 8.1.2, the dipole moment of 3-trifluoromethylstyrene makes it a good candidate for field-directed line growth. The molecule shown in Figure 8.5(a) was supplied by Sigma-Aldrich with 99% purity and was purified by the freeze-thaw technique. An initial test was made to confirm that the molecule does indeed grow on a H-Si(100)-2×1 surface. In this case, a deuterium-terminated surface was prepared instead, but the results apply to a hydrogen-terminated surface as well. The result of a 60 L dose of 3-trifluoromethylstyrene on undoped D-Si(100)-2×1 is shown in Figure 8.5(b). The molecule grows very well-ordered, straight lines along dimer rows, just as in the case of an unsubstituted styrene molecule. We will be looking for deviations from this behavior when an electric field is applied.

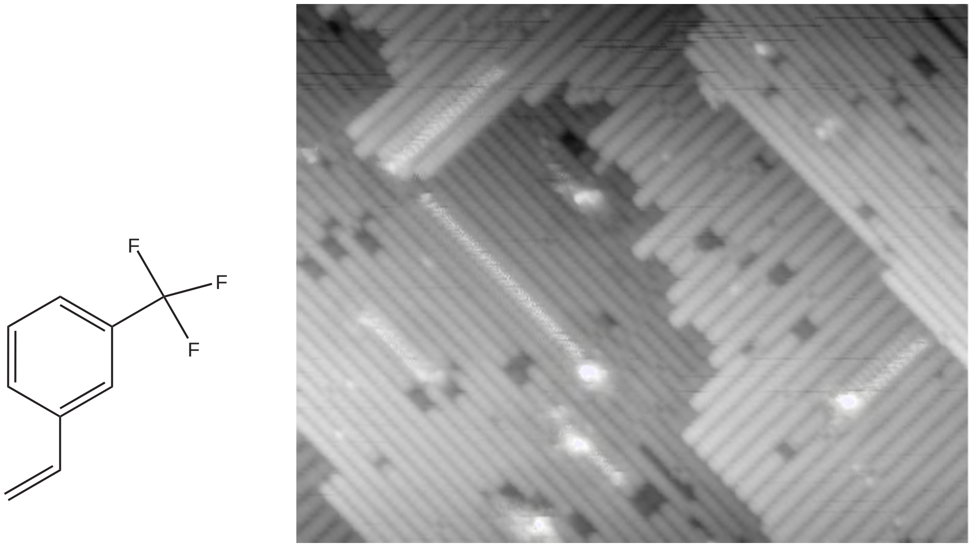

(a) 3-Trifluoromethylstyrene

(b) STM image of lines of 3-trifluoromethylstyrene (60 L dose on undoped D-Si(100)-2×1, 30 nm wide, −3 V, 80 pA).

Figure 8.5: Growth of 3-trifluoromethylstyrene lines on D-Si(100)-2×1.

8.3.2 Growth of 3-Trifluoromethylstyrene on H-Si(111)-1×1

In a later experiment, we attempted field-directed line growth on H-Si(111)-1×1. Although no clear picture emerged of directionality in the gap, STM images were taken a few hundred nm away from the gap to show growth in the absence of a field — see Figure 8.6. These images show that growth seems to occur in a random walk pattern, much in the same way as styrene on H-Si(111)-1×1.

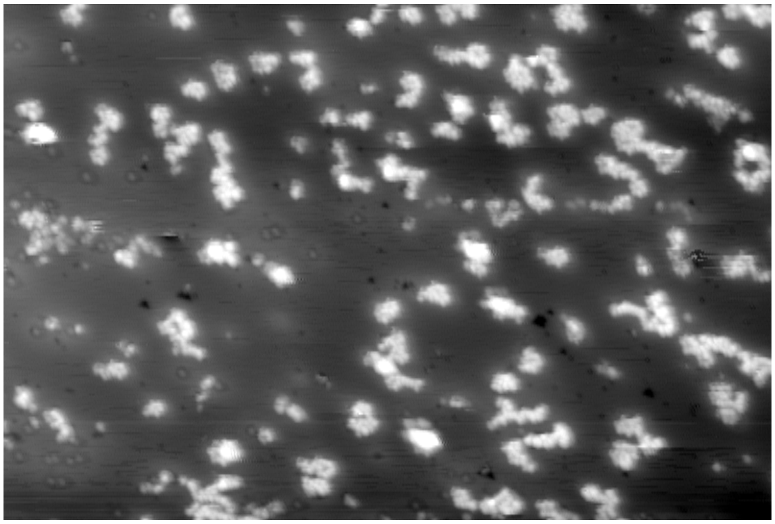

Figure 8.6: STM image of the growth of 3-trifluoromethylstyrene (30 L dose on low-doped n-type H-Si(111)-1×1, 60 nm wide, −2.6 V, 64 pA)

8.4 Heating Effect Observations

As we have seen in Section 8.2.3, when running current across the contact gap we run into the issue of Joule heating. If the temperature rises high enough it can be sufficient to desorb hydrogen from the H-Si(100)-2×1 surface. We looked for this effect in the example shown in Figure 8.7. In this instance, images of the surface across a 90-nm wide gap were taken as the before images. For a period of 2 minutes, 20 V were applied between the contacts — resulting in 100 μA of current. No molecule was dosed during this time, and STM images of the same area were taken afterwards.

We can see in Figure 8.7(b) that the surface was strongly modified. Dimer rows are still visible, but most of the H has been desorbed — the dark patches show where H still remains. These STM images are directly in the gap between the metal contacts; STM images taken ∼150 nm away from the gap show that the surface is still H-terminated, indicating that the heating was extremely local to the gap area. Literature reports that for anneals of comparable time, temperatures near or exceeding 400 C were needed [34, 119, 120, 121] to desorb hydrogen, giving us an indication that the temperature at the surface likely reached this value. This is a larger temperature increase than we would have expected from the FEM simulation results in Section 8.2.3.

We also note that in this and other cases where some desorption due to Joule heating was observed, the largest effect was seen close to the end of the metal

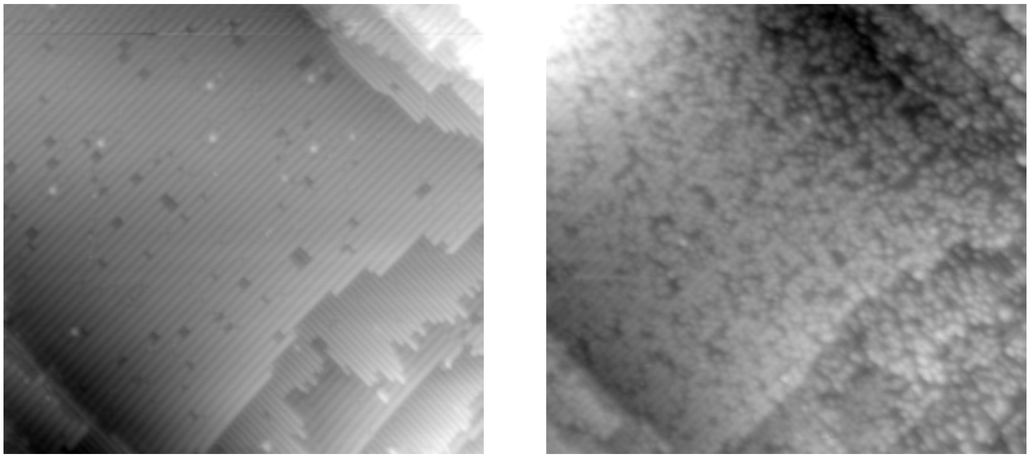

(a) H-Si(100)-2×1 surface before heating.

(b) Desorbed H on the surface after heating.

Figure 8.7: STM images of a H-Si(100)-2×1 surface before and after heating due to current (40 nm wide, −3 V, 80 pA). The metal contacts are to the upper right and lower left of this image.

contacts. FEM simulations showed a similar effect, due to the geometry of the contacts concentrating field lines near their ends. This effect might also be due to the Schottky barrier at the metal contacts, where we would expect a majority of the the voltage to drop.

8.5 Field-Directed Growth Results on H-Si(100)-2×1

An undoped Si(100) sample had 30-nm thick Ti contact pads defined on it by EBL. During sample preparation, the crystal was annealed a few times up to 1100 C, after which the surface was hydrogen-terminated to obtain high-quality H-Si(100)-2×1. A 500-nm nominal gap was used; the actual width of the gap was found by STM imaging to be 300 nm. EBIC images confirmed that the metal contacts were continuous.

8.5.1 Effect of Field on H-Si(100)-2×1

As a first step in the experiment, we investigated the effect on the surface of applying a field without dosing molecules. STM images were taken directly in the gap between the metal contacts; the field was applied from the lower-left to the upper right corner; 21 V was applied producing a current of ∼100 μA; this was held for 2 minutes. Given the 300 nm spacing of the metal contacts, the field strength was ∼0.07 V/nm. Before-and-after STM images are shown in Figure 8.8. Broad desorption of H such as was observed in Section 8.4 was not observed; therefore the local Joule heating did not cause a temperature rise as high as in that case. However, several DBs seem to have disappeared while others have appeared.

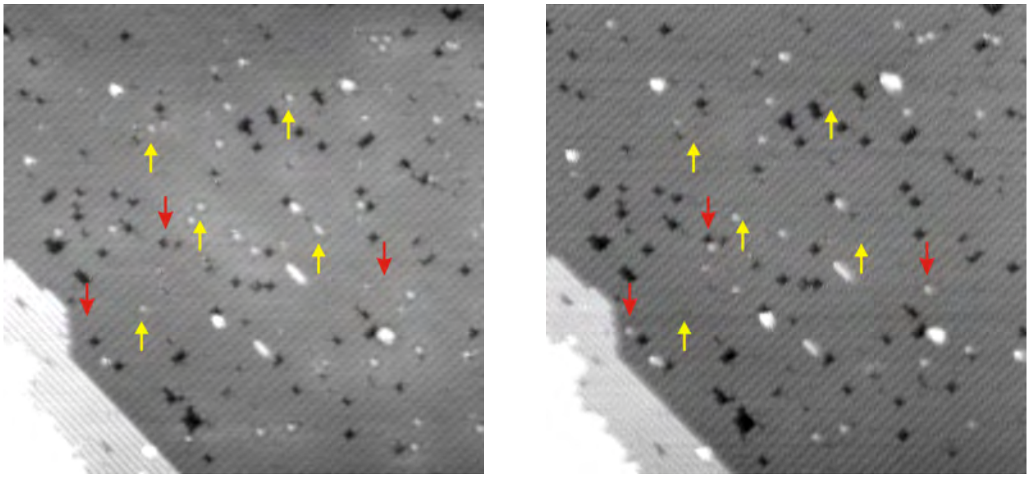

(a) Before applying a field.

(b) After applying the field for 2 minutes.

Figure 8.8: STM images (40 nm wide, −2.7 V, 80 pA) of the effect of applying a field on the H-Si(100)-2×1 surface without dosing any molecules. The yellow arrows point to DBs that seemed to disappear from (a); Red arrows point to DBs that appeared in (b).

Studies of hydrogen diffusion on H-Si(100)-2×1 have been performed by STM at elevated temperatures [122, 123] and with laser-induced heating [124, 125]. It has been found that intradimer diffusion (movement of a H to the other side of dimer) occurs with an attempt frequency $\nu = 10^{10.3}$ s^{-1} and an activation energy $E = 1.01$ eV. Rates of interdimer diffusion (movement of a H to another dimer along the same row) are significantly lower — they have an attempt frequency $\nu = 10^{14.5}$ s^{-1} and an activation energy of $E = 1.75$ eV. The rate of diffusion of a hydrogen to another dimer row has been found to be lower still. In our experiment, the field (and therefore Joule heating) is applied for a few hundred seconds; a hopping rate of 0.01 Hz would therefore be enough to result in visible DB movement. The authors of Ref. [122] found a interdimer hopping rate near 0.01 Hz at a temperature of 260 C.

Unfortunately, it was not possible to locally measure the temperature during the experiment. As mentioned earlier, the absence of H desorption would indicate a temperature below 400 C. It is possible that the sample reached temperatures high enough to thermally induce H diffusion; we also speculate that perhaps the electric field facilitates H diffusion. We note that in order to explain the STM images shown, H diffusion would have to have occured across dimer rows as well as along them.

Another possibility is that some DBs were capped by atomic hydrogen (the source of which is unclear) while others were desorbed, perhaps thermally. Given that the desorption of hydrogen has an activation energy of $E = 2.48$ eV [121], significantly higher than the diffusion activation energies, it seems unlikely that H desorption would be observed without H diffusion, unless an unknown non-thermal process is occuring. Also, we note that the total number of DBs does not significantly change; it seems unlikely that the amount of DB capping would be comparable to that of H desorption — therefore it seems that the diffusion hypothesis is a more viable one.

8.5.2 Field-Directed Molecular Line Growth

After performing this test, we performed the field-directed molecular growth experiment using the same field intensities (21 V applied). A 250 L dose of 3-trifluoromethylstyrene was performed at a pressure of 2×10^{-6} Torr for 2 minutes. The gate valve to the ion pump was partially closed during dosing. After a 1 minute delay, the gate valve was opened and the voltage applied was lowered to 17 V. After another minute the chamber pressure had returned to $\sim 7 \times 10^{-9}$ Torr and the field was turned off. The field was therefore applied for 4 minutes (though at full strength for only 3 minutes) — which is a comparable length of time as that used in the initial step of Figure 8.8.

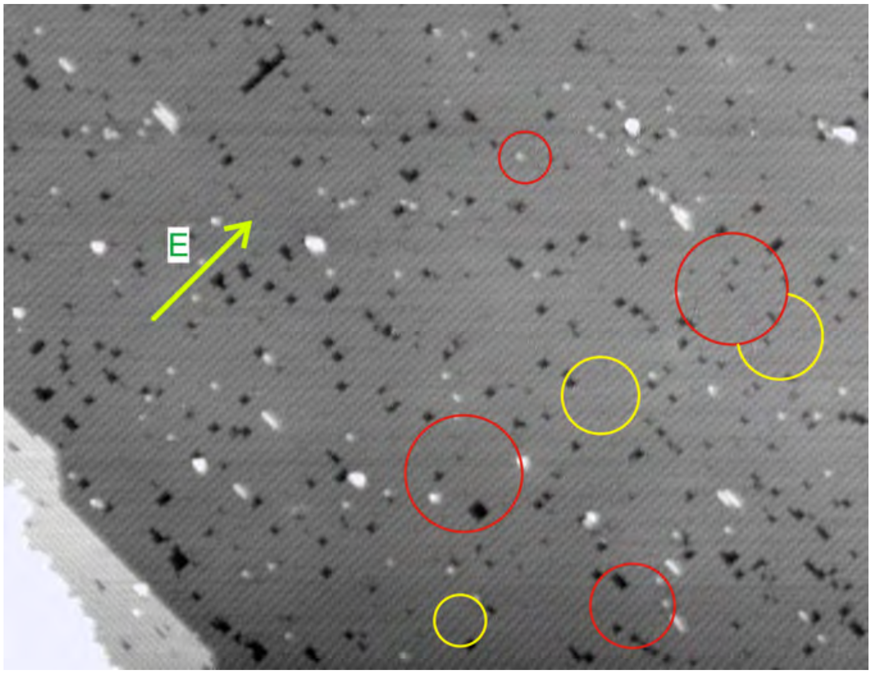

(a) Before dose. The direction of the electric field is indicated by the arrow.

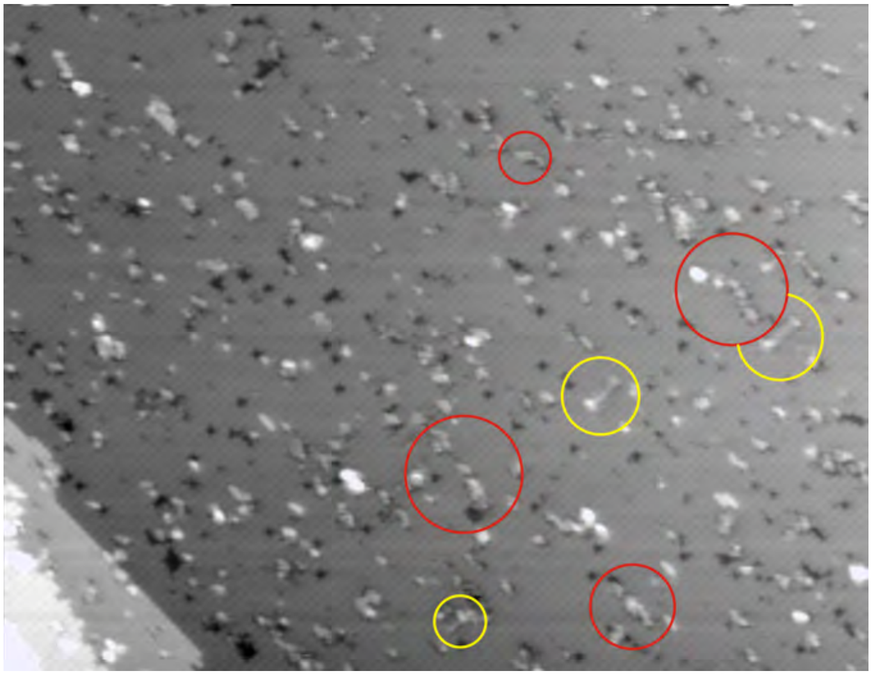

(b) After dosing 250 L with 21 V applied across the metal gap.

Figure 8.9: Before and after STM images of field-directed growth of 3-trifluoromethylstyrene on H-Si(100)-2×1 (70 nm wide, −2.6 V, 80 pA). Red circles highlight examples of cross-dimer-row growth; yellow circles highlight along-dimer-row growth.

The results of this experiment are shown in the STM images in Figure 8.9. We begin by noting that the number of features after dosing exceeds the number of DBs in Figure 8.9(a), and that many of the molecular growth patterns cannot be ascribed to a DB that was previously visible on the surface. Both of these effects could be explained by the DB diffusion we observed in Figure 8.8. First, the starting position of DBs cannot be held to be reliable since DBs would move when the field is applied. Second, it is possible that the DB at the end of molecular line would undergo diffusion before another molecule would bond to it to continue line growth. Therefore, lines might end up broken up in segments as the DB diffuses from point to point during the growth process.

Figure 8.9(b) highlights with yellow circles three molecular lines that appear to have grown parallel with dimer rows — the usual growth direction when no field is applied. These seem to be greatly outnumbered, however, by short lines of a few molecules growing across dimer rows in a more irregular fashion. We note that such growth does not seem to occur at all in normal conditions where no field is applied (see Figure 8.5). As we have seen in Section 8.1.3, we expect line growth to occur perpendicularly to the electric field, which is indicated by the arrow in Figure 8.9(a). Some particularly long examples of cross-dimer-row growth are highlighted with red circles in Figure 8.9(b).

The cross-dimer-row growth induced by the electric field does not produce very well-ordered perpendicular lines such as those of allylmercaptan on H-Si(100)-2×1 [28]. In that situation, the molecule *cannot* abstract hydrogen from the next dimer on the same row, and therefore must grow perpendicularly to rows. In this situation, the electric field increases the odds of cross-row growth at the expense of along-row growth: we therefore expect that each new molecule in a line has a certain probability of either abstracting a H along the same dimer row, or of abstracting a H across to the next row. The resulting lines, therefore, are not perfectly perpendicular to rows but instead show a more irregular, diagonal growth direction.

8.5.3 Line Growth Without Field

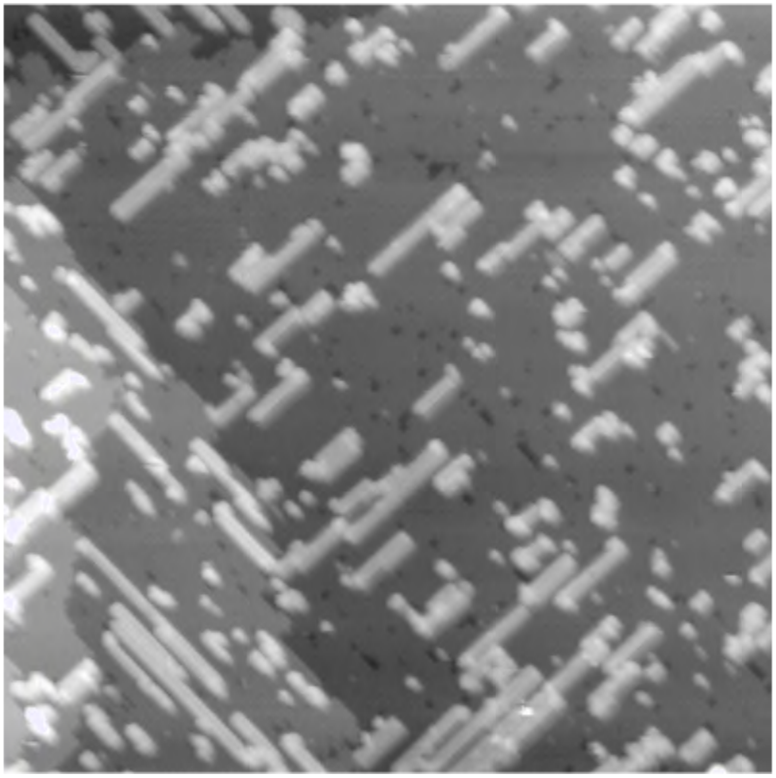

Figure 8.10: STM image of the growth of 3-trifluoromethylstyrene on H-Si(100)-2×1 ∼2 μm away from the area where an electric field was applied (80 nm wide, −2.9 V, 80 pA).

To contrast the line growth of 3-trifluoromethylstyrene with and without an applied electric field, STM images were taken approximately 2 μm away from the gap between the biased metal contacts; at that point no significant electric field was present. As we can see in Figure 8.10, much more line growth occurred away from the gap than in the gap. The molecular lines that formed far from the electric field were predominantly going along dimer rows, as is the normal growth pattern.

Let us first consider the reduced molecular coverage with an applied electric field. It has been shown by Wolkow [126] and later confirmed by Hossain et al. [24] that at elevated temperatures, styrene lines formed at room temperatures could "unzip" — that is, reverse the chain reaction and desorb from the surface, leaving the DB at the original position. For styrene, this unzipping action occurred in a few minutes at 400 K; for 2,4-dimethylstyrene, unzipping was observed at 300 K. The authors conclude that the molecular line growth process has competing forward and reverse components; some molecules such as 1-hexene which do not grow lines at room temperature do grow lines at 180 K thanks to a reduced reverse reaction rate. Since the current flowing between metal contacts increases the temperature of the silicon, we believe that this "unzipping" process explains the reduced molecular coverage we observe in the gap area, as compared to outside the electric field.

Next let us consider the morphology of molecular lines without an electric field. We notice a few small features, of perhaps only a few molecules in size; unfortunately the quality of STM imaging does not allow us to determine if they are short, cross-row lines. No examples of extended cross-row growth are observed, unlike what was shown in Figure 8.8(b). It is clear that the vast majority of the molecular coverage seen is due to normal, along-dimer-row growth. The lines formed are significantly longer than the 3 examples of along-row growth in Figure 8.8(b).

This experiment was repeated on a few occasions, and similar results were obtained. We believe that the STM images indicate that some degree of field-directed line growth occurred, although the effects of higher temperatures caused by Joule heating unfortunately confuse the results.

8.6 Field-Directed Growth Attempt on H-Si(111)-1×1

A low-doped (1-5 Ω·cm) n-type Si(111) crystal with a H-Si(111)-1×1 surface and 20 nm-thick Cr contacts was prepared by the method described in Section 7.9. The surface was obtained was of fairly high quality but suffered from an unusually high DB concentration (see Figure 8.11(a)). It is likely that some hydrogen atoms were desorbed by the annealing step: 200 C for 1 minute followed by 225 C for 1 minute; however such an anneal is necessary to remove physisorbed molecules that are harmful for STM imaging.

Metal contacts with a nominal gap of 250 nm were chosen to perform the experiment; the actual gap was measured by STM to be 100 nm. During dosing, -5 V were applied on the right contact, with the left contact grounded; the field was therefore $\sim$0.05 V/nm. Only 150 nA of current flowed between contacts — therefore Joule heating was likely many times less than in the H-Si(100)-2×1 case.

The result after dosing 10 L of 3-trifluoromethylstyrene is shown in Figure 8.11(c). Unfortunately, the high starting DB density makes the images harder to interpret. The lines formed by the molecule under the applied electric field perhaps seem to be growing diagonally from lower right to upper left more frequently than other directions — this orientation is perpendicular to the applied field. However, without an atomic-resolution STM image of the same area on the surface taken before dosing, showing the position of DBs, we cannot be certain that all growth

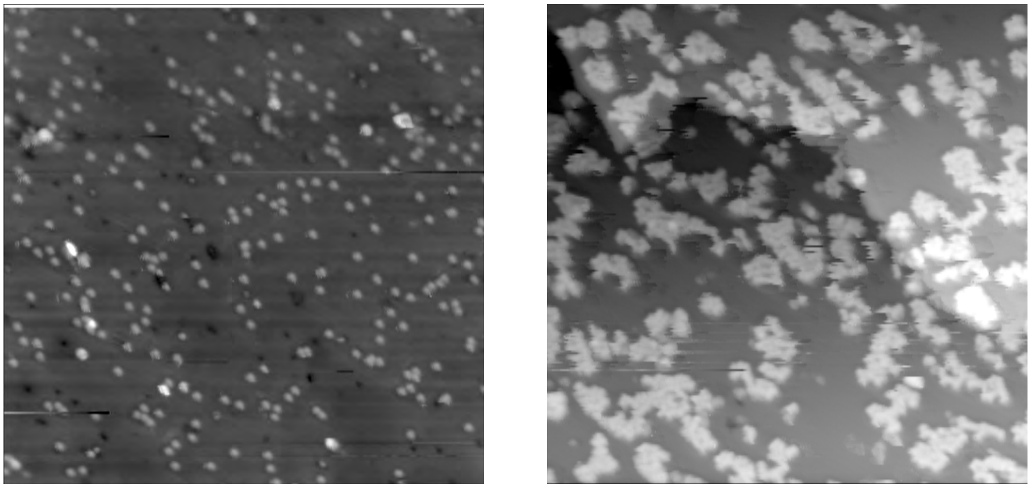

(a) Representative image of the surface before dosing (taken far from the metal contacts).

(b) STM image of line growth ~300 nm away from the gap.

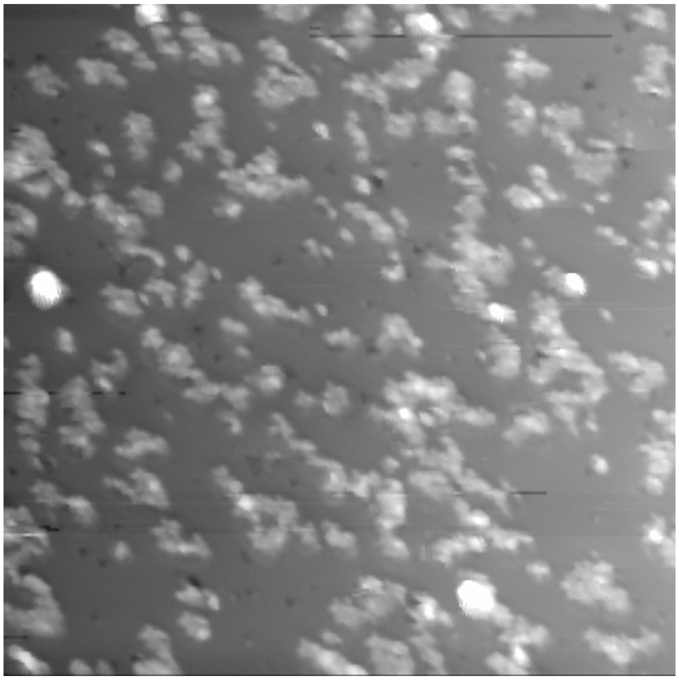

(c) Surface in the applied field region, after a 10 L dose of 3-trifluoromethylstyrene with −5 V applied. The metal contacts are close to the upper right and lower left corners of the image.

Figure 8.11: STM images of a field-directed molecular line growth experiment using 3-trifluoromethylstyrene on H-Si(111)-1×1 (40 nm wide, −2.8 V, 110 pA).

occured in one direction. Unfortunately, we have found that obtaining reliable, high-quality images is typically more difficult on H-Si(111)-1×1 than on H-Si(100)-2×1, and we do not have usable "before" images in this case.

We can compare the line growth in the gap to the line growth 300 nm away from the gap, where the field should be negligeable — Figure 8.11(b). The molecular coverage does not appear significantly different, perhaps indicating that the temperature in the gap was not significantly elevated. However, we cannot conclusively claim that the growth direction was significantly different where the field was applied. Perhaps the field strength, ∼0.05 V/nm, which is a lower value than was used in the H-Si(100)-2×1 case, was insufficient.

To give clearer results, this experiment would need to be repeated with a stronger field, and with high-quality before-and-after STM images. It would also be advantageous to check whether DB diffusion occurs when applying the current through the gap; to the best of our knowledge, there are no published papers on the diffusion of hydrogen on H-Si(111)-1×1. Unfortunately, this surface can only be prepared by a wet chemical process outside of vacuum; therefore one cannot re-use a sample in the vacuum chamber after an attempt. Combined with the difficulty of STM imaging this surface, this makes this experiment significantly more difficult to realize than the H-Si(100)-2×1 experiment described.

8.7 Field-Directed Growth Attempt Using Styrene on H-Si(100)-2×1

The same experiment was attempted on an undoped H-Si(100)-2×1 sample, on a contact with a nominal spacing of 500 nm, measured to be 300 nm by STM. 50 L of unsubstituted styrene were dosed at 10^{-6} Torr while applying +17.5 V on the right contact: this generated a field ∼0.06 V/nm and a current of 65 μA. The before and after STM images of the same area on the crystal, directly between the metal contacts, are shown in Figure 8.12.

Little growth was observed under these conditions — once again, the elevated temperatures due to Joule heating are likely responsible. Before the field-directed growth experiment was attempted, a test of heating was performed by flowing 100 μA through the contacts for 2 minutes (19 V applied). The desorption visible in the upper right corner of Figure 8.12(a) is a sign that near the metal contacts the temperature rose close to 400 C. At the reduced current of 65 μA used during the experiment we would expect the heating power P to be ∼60% of the original power, meaning that the temperature T could still be as high as 250 C (since $T \propto P$).

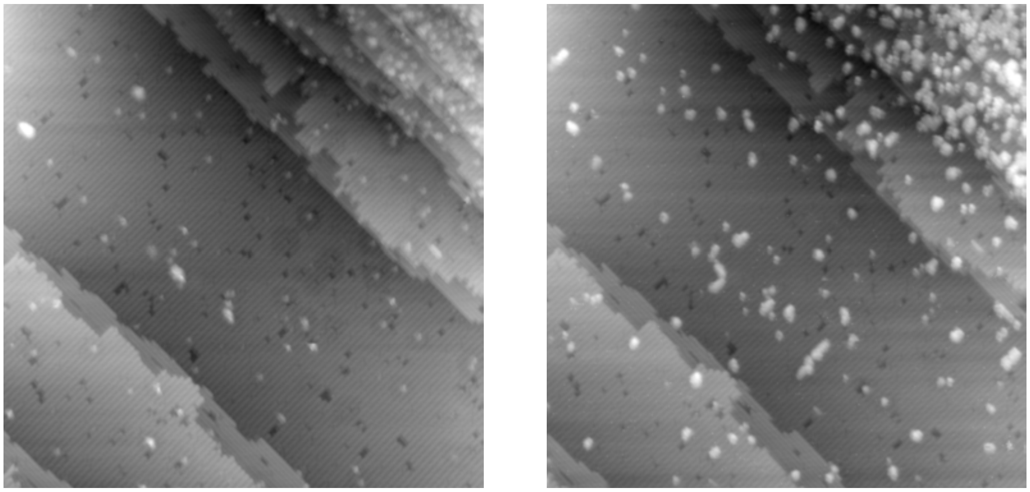

(a) Before dosing. The metal contacts are close to the upper right and lower left corners of the image.

(b) After dosing 50 L of styrene, with 17.5 V across the gap.

Figure 8.12: STM images within the contact gap of a field-directed molecular line growth experiment using styrene on H-Si(100)-2×1(60 nm wide, −2.4 V, 80 pA).

A few lines growing along dimer rows were observed. STM images taken a few microns away from the gap showed denser line growth, with each line significantly longer than the longest ones observed in the gap. Also, several features appeared where no DBs were found initially — this might be due to temperature-induced hydrogen diffusion on the surface, although it appears to have occurred less in this case than in the experiment shown in Figure 8.8.

We expect that styrene will align so as to grow lines in the same direction as the electric field (Figure 8.2); since the largest terraces have dimer rows that are aligned with the field, we would expect along-row growth in those cases, making the field effect indistiguishable from normal growth. Also, styrene has a lower dipole moment than that molecule, so we would expect it not to align as well. We do not observe cross-dimer row growth through more than one row, unlike what was observed in the case of 3-trifluoromethylstyrene; but this experiment is not conclusive.

8.8 Conclusions

We have shown results of field-directed molecular line growth experiments on H-Si(100)-2×1. With an applied electric field during 3-trifluoromethylstyrene dosing, irregular lines growing across dimer rows are observed. This is in stark contrast with the perfectly regular lines growing along dimer rows in the absence of an electric field, and it is consistent with the molecule aligning its dipole with the external electric field. From these results, we believe we have shown some level of field-directed molecular growth on H-Si(100)-2×1. The interpretation of the results is made more difficult by the Joule heating caused by current flowing through the semiconductor during the experiment, increasing the temperature locally. This local heating likely causes DB diffusion, as well as a lower molecular coverage in the region of applied field compared to elsewhere on the surface. Results on the H-Si(111)-1×1 surface were inconclusive and should be repeated.

The resulting lines from field-directed molecular growth are rather irregular and DB diffusion makes their starting points impossible to predict. In an idealized case, a perfectly H-terminated surface could be patterned with isolated DBs as line growth starting points. A prescribed sequence of molecular doses with fields applied in desired directions would cause growth to occur in a known pattern — drawing lines in a similar way as the children's toy "Etch A Sketch" (TM). With several DBs as starting points, complex structures could be formed in parallel. These custom made, arbitrarily-shaped nanometer scale structures might then be used as templates for further functionalization. Unfortunately, the local heating, DB diffusion, and irregular line growth that we have observed in the physical system so far cause our control to be far less than ideal.

Chapter 9

Surface Conductance of Si(111)-7×7

9.1 Introduction

The intricacy and complexity of the 7×7 surface reconstruction of Si(111) has interested scientists for many years. Many experimental and theoretical studies tried to elucidate the exact structure [127, 128, 129]; the invention of the STM allowed scientists to directly image that structure in real space [107].

Each unit cell of the Si(111)-7×7 surface contains 19 dangling bonds [130] which contribute to its interesting electronic character. The Fermi level of the silicon has been found to be pinned at the 7×7 surface at an energy 0.65 eV above the valence band maximum [127]. The presence of a partially filled band in the Si gap [131] would indicate that the surface should be a two-dimensional metallic conductor, although other evidence points to it being close to a Mott-Hubbard metal-insulator transition [132].

Measurements of Si(111)-7×7 surface conductivity have been performed by a wide variety of methods: by monitoring resistance while depositing metals on the surface [133]; with 4 point probes of varying spacing [134, 135, 136, 137]; with macroscopic van der Pauw contacts [138]; with 2 tunneling contacts [139]; with a single STM point contact [140]; by trenches dug with an STM tip into the 7×7 surface [141]. This wide range of methods has yielded values for the surface conductivity of Si(111)-7×7 that range from $10^{-8}\ \Omega^{-1}/\square$ to $2\times10^{-4}\ \Omega^{-1}/\square$; this is well summarized in Ref. [6].

In this chapter we present experimental evidence of the 2D conductivity of Si(111)-7×7 using EBL-defined contacts, conductance measurement and molecular dosing. Our method is advantageous over previously reported results due to extremely small probe separations and STM confirmation of the 7×7 surface reconstruction quality.

9.2 Experimental Method

Our samples consist of titanium metal contact pads, 30-40 nm in thickness, patterned by electron-beam lithography (EBL) on the Si(111) surface. The details of the EBL procedure have been discussed in Section 7.5; a detailed description of the pattern is found in Section 7.5.1; sample preparation has been discussed in Section 7.7. All sample handling (after EBL and metal deposition) was performed in a UHV chamber with pressure $\leq 2 \times 10^{-10}$ Torr.

First, the quality of the Si(111)-7×7 surface was confirmed by performing STM scans on a representative area near the center of the sample (see e.g. Figure 7.10(a)). Next, the three tips were aligned at a spacing matching the contact pad spacing, as described in Section 5.5. Then, the tips were retracted slightly so as to move the sample underneath and position one of the contacts under the tips. All three tips were brought back to within tunneling range of the surface. Large STM scans (typically 2×1 μm) were performed with the left and right probes so as to find the 1 μm wide contact pads. The two probes were then placed at the center of the pads and touched down lightly on the surface — typically overdriving by 10 nm.

A Keithley 2400 Sourcemeter unit was used for IV curve collection. The IV curves of both probe-to-metal pad contacts were measured separately, with the voltage applied to macroscopic clips holding the sample several mm away; the contacting probe was grounded, with the other probe electrically floating. The contact between the tungsten tip and the titanium metal pad was considered to be sufficiently low-resistance and ohmic when overdriving the probe tip a few more nm (and therefore increasing the contact area) did not affect the IV curve of the contact.

Probe-to-probe conductance IV curves were performed by applying the voltage to one probe while grounding the other. The macroscopic clips to the sample were electrically floating. Molecules (styrene, benzene, 1,2,4-trimethylbenzene; supplied by Sigma-Aldrich, purities of 99%, 98.5% and 98% respectively) were purified by several freeze-thaw cycles. The molecules were dosed into the vacuum chamber by a variable-leak valve.

9.3 Metal-Semiconductor Contacts Review

Our contacts are metal directly touching low-doped n- or p-type Si. The workfunction difference between the metal and semiconductor forms a Schottky barrier at the interface (see Figure 9.1). This forms a Schottky diode, the behavior of which is well known. For an n-type semiconductor, with a negative voltage on the Si, current flows easily over or through the barrier — this is the *forward bias* direction. With a positive voltage on the Si, the barrier blocks electrons and current is greatly diminished — this is the *reverse bias* direction. Only electrons tunneling through or hopping over the barrier contribute to the reverse current; the voltages are reversed for a metal on p-type silicon.

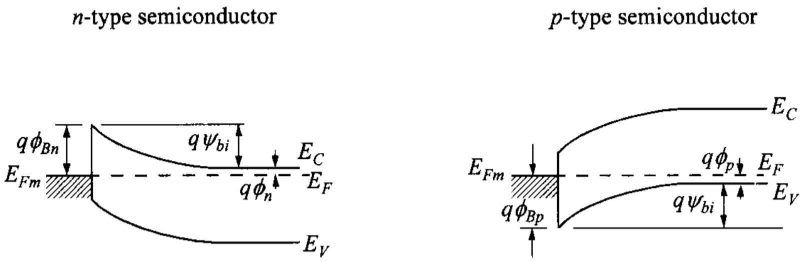

(a)
No Bias

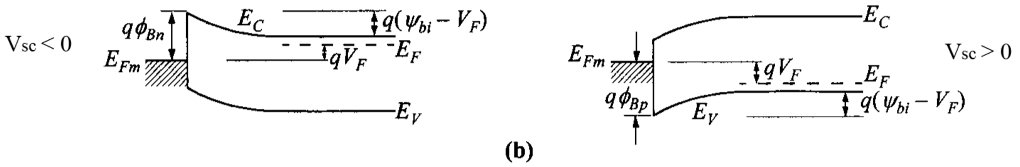

(b)
Forward Bias

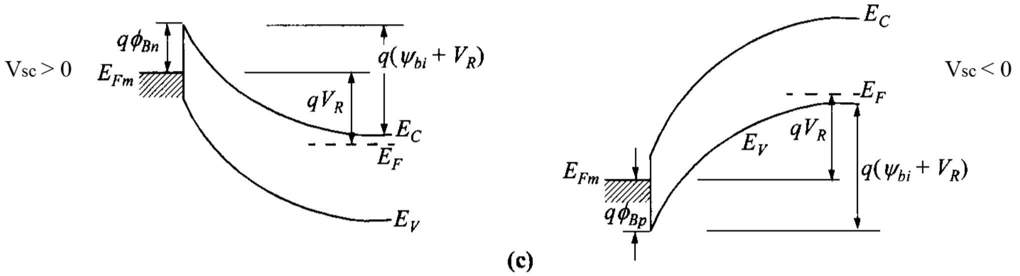

(c)
Reverse Bias

Figure 9.1: Energy-band diagram of the Schottky barrier between a metal and a n-type and p-type semiconductor. (a) No bias applied. (b) Forward bias — the diode conducts well. (c) Reverse bias — the current is reduced. V_{sc} = voltage applied on the semiconductor. From Ref. [11].

9.4 One- and Two-Diode Measurements

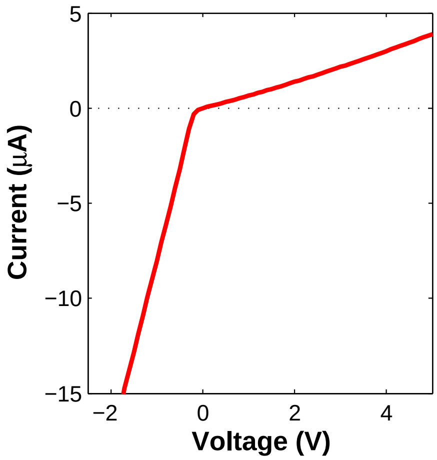

Figure 9.2: Diode-like IV curve for a single metal contact, with a 7×7 silicon surface, on low-doped n-type Si(111). The voltage is applied on the macroscopic clips to the Si, far from the contact.

A typical IV curve for a single contact on a Si(111)-7×7 surface is shown in Figure 9.2. The voltage is applied to the semiconductor, therefore a positive voltage on the Si corresponds to reverse bias. As expected, the contact shows rectifying diode behavior. However, the reversed bias current is quite large, and the rectification ratio of the diode is poor. This indicates that there is a source of significant reverse leakage current, which in Schottky diodes is typically due to thermionic-emission or tunneling through the barrier [142]. It is useful to note that as a Schottky contact shrinks down in size to smaller than a characteristic length scale l_c (described in Ref. [143]), tunneling through the barrier becomes enhanced. The contacts used in this experiment may be approaching this regime.

Figure 9.3 shows the equivalent wiring diagram comparing the connection to a single contact and the connection through both contacts. It is clear that the measurement of the current between the two contacts is equivalent to connecting the two schottky diodes in reverse, irrespective of the polarity applied on one of them. This means that one of the diodes is in forward bias, while the other is in reverse bias; it is the reversed bias diode which limits the current. When the voltage applied changes polarity, the situation is reversed, and the other diode's reverse current is the limiting factor. Therefore, the IV curve measured between the two contacts consists entirely of the leakage current of each diode.

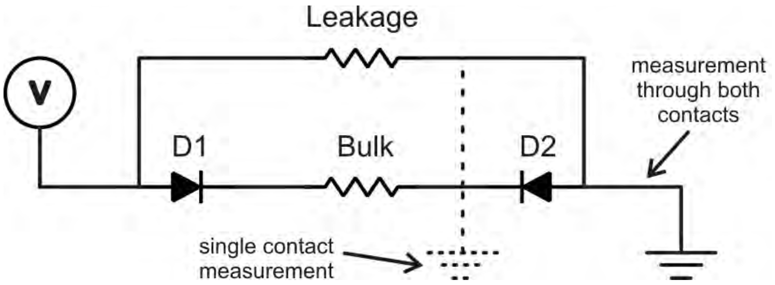

Figure 9.3: Schematic of the equivalent circuit of the two metal contacts. Each metal contact acts as a Schottky diode, indicated D1 and D2. The dashed line indicates the connection when measuring a single contact, which shows diode behavior; when measuring through both contacts one of the two diodes is always in reverse bias, whether the voltage applied is positive or negative.

9.5 Effect of Dosing Molecules

We hypothesized that the large diode leakage current was due primarily to conductance through surface states of Si(111)-7×7. The reaction of a molecule with the dangling bonds on the 7×7 surface disrupts the available surface-states, thereby reducing the surface-state conductance. We performed a 20 L molecular dose while taking repeated IV curves between two contacts spaced ∼300 nm apart. Figure 9.4 shows the very large change in conductance between contacts — up to a 99.8% drop in current at was observed. This indicates that a comparable fraction of the diode leakage current is due to transport through the surface states; the “normal” reverse leakage current due to thermionic emission or tunneling through the Schottky barrier is much smaller.

Indeed, the comparison in Figure 9.5 shows that leakage current observed when measuring the single-contact diode IV curve of a reacted Si(111)-7×7 surface is very close in amplitude to the leakage current of an EBL-defined contact of identical shape, made of Cr, with the surface terminated by hydrogen through chemical etching (as described in Section 7.9). Neither the reacted 7×7 nor the H-Si(111)-1×1 surface has surface states through which to conduct, and therefore show much reduced leakage current as compared to the pristine 7×7 surface (red curve in Figure 9.5).

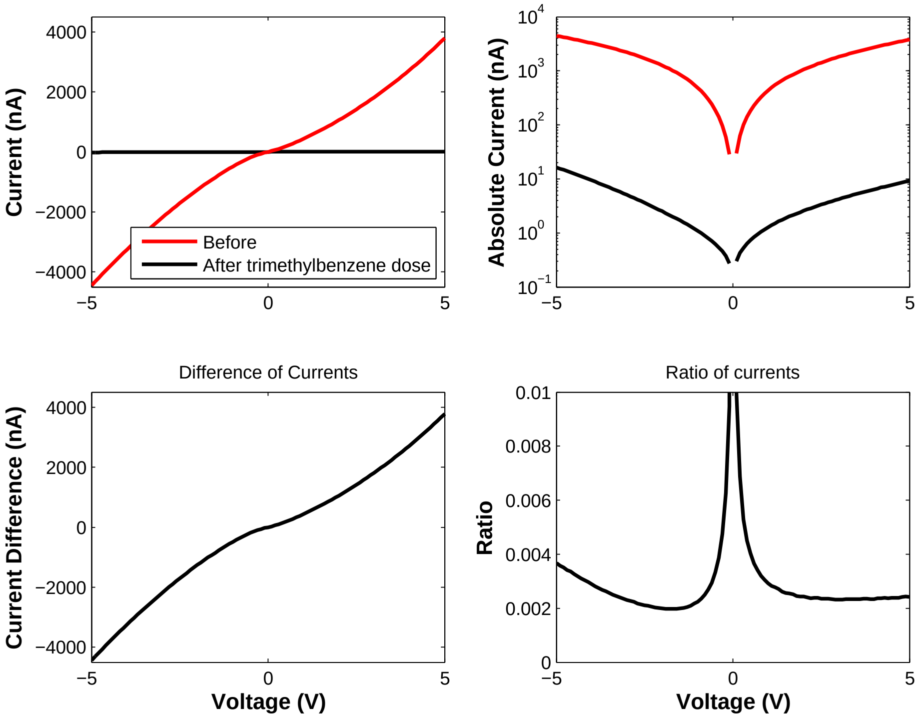

Figure 9.4: IV curves of the current between two contacts spaced ∼300 nm apart, on low-doped n-type Si(111), before and after a 20 L (200 seconds at 10^{-7} Torr) dose of 1,2,4-trimethylbenzene. Above: the currents are plotted on linear and log scales. Below: the difference and ratio of the currents after dosing.

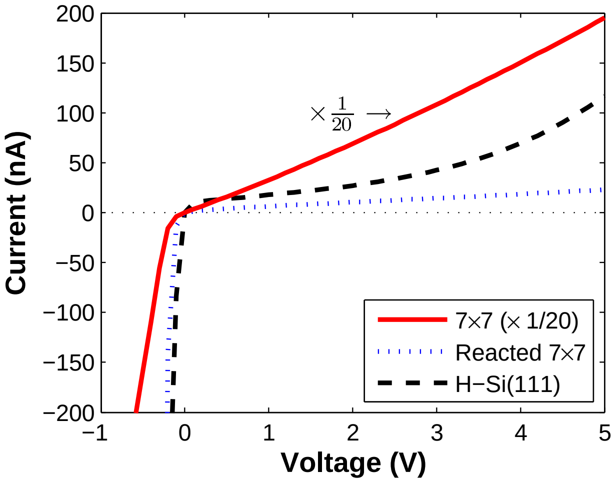

Figure 9.5: Diode-like IV curves in 3 situations, highlighting the reversed bias behavior. Voltage is applied on the sample, far from the contact, which is grounded. All 3 diodes conduct well with a negative voltage on the sample. The reverse current on the 7×7 surface is linear (ohmic) and significantly larger than the other diodes. The reacted 7×7 (20 L of 1,2,4-trimethylbenzene) and a wet-prepared H-terminated Si(111) surface have similar reverse current values.

Figure 9.6 shows the difference in the currents for a single metal contact (with voltage applied on the macroscopic sample clips) before and after dosing 20 L of 1,2,4-trimethylbenzene. The slope of the difference in currents is the same within a factor of ∼2. This indicates that the 7×7 surface conductance pathway is present both in the forward and reverse diode directions; the change in current is not exclusive to the reverse diode behavior. As shown schematically in Figure 9.3, the system behaves as a Schottky diode (which is always present) connected in parallel with a resistive surface (which is extinguished by molecule dosing). The change of current in the forward direction, however, is much less noticeable since it is only a change of a few percent in relative terms. Therefore, observing the reverse bias current change, such as with a probe-to-probe double-diode IV curve, provides a much larger relative current change from molecule dosing.

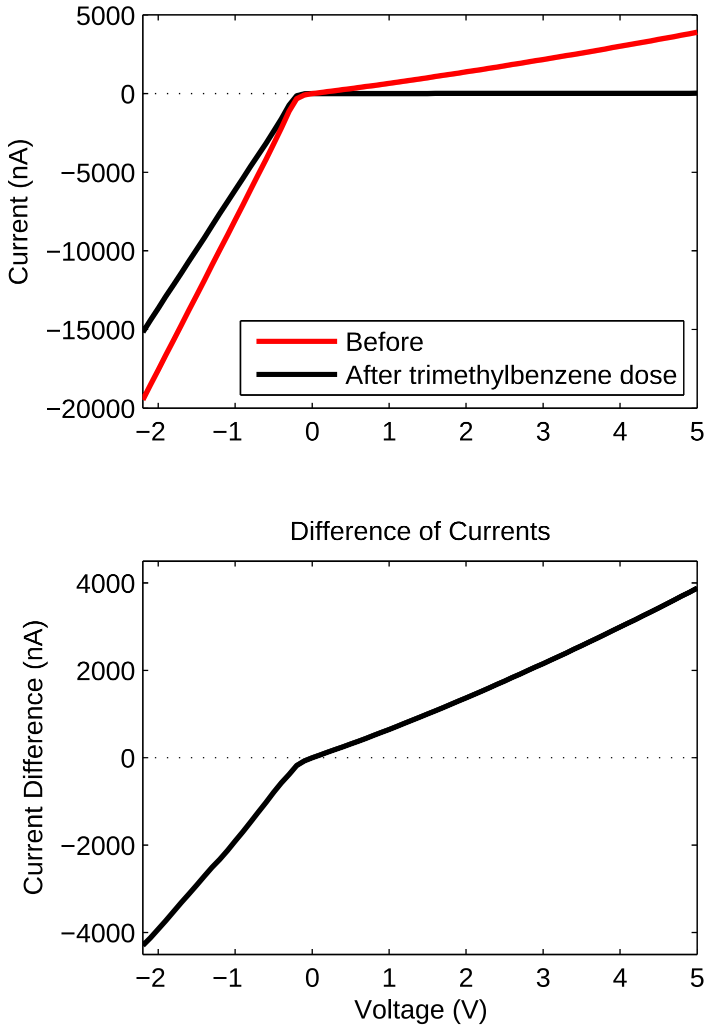

Figure 9.6: Above: diode-like IV curves of a single metal contact on Si(111)-7×7, before and after a 20 L dose of 1,2,4-trimethylbenzene. Below: difference of the current before minus the current after dose.

9.6 Effect of Different Molecules

The change in conductance across the contact gap at saturation (at least 1 L dosed) has been found to vary depending on the molecule dosed. Three different molecules were dosed; typical IV curves before and after dosing are shown in Figure 9.7.

Figure 9.7(a) shows the result when dosing benzene. The current typically drops by 85% — this is the smallest response of the three molecules attempted. This is consistent with our STM experiments that have shown that benzene coverage never reaches 100% — see Figure 9.8. In addition, we have found the current recovers partially (to 30% of its initial value) after a few hours. We have observed in STM images that a large portion (though not all) of the benzene desorbs from the surface in a few hours, which is consistent with the electrical measurement. These observations of benzene desorption are quite consistent with what has been reported in the literature [144].

The result of a saturated (> 10 L) dose of styrene (vinylbenzene) is shown in Figure 9.7(b). For this molecule, the current dropped by 94%; and unlike benzene, the current did not recover with time. STM images confirm that the molecule strongly bonds to the surface — see Figure 9.9(a).

Finally, Figure 9.7(c) shows the result after dosing 20 L of 1,2,4-trimethylbenzene. This molecules gives the largest response — up to a 99.8% drop in current. The current does not recover with time. Out STM images have shown that 1,2,4-trimethylbenzene bonds more strongly than benzene to the Si(111)-7×7 surface (see Figure 9.9(b)), and that it does not desorb at room temperature. The exact way trimethylbenzene bonds to the 7×7 surface is unclear.

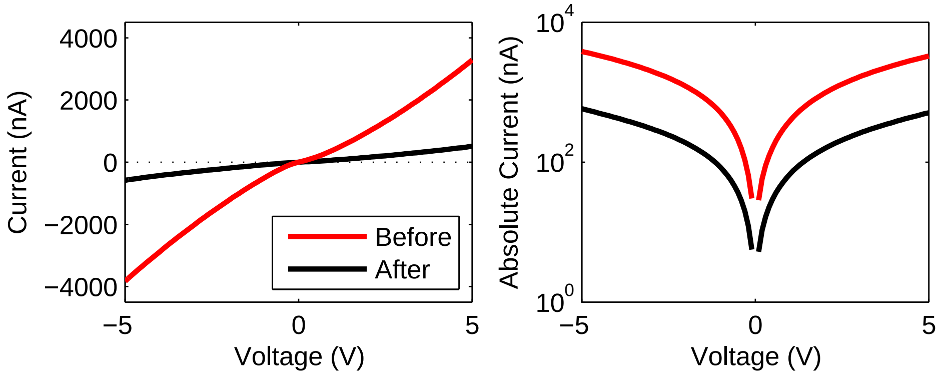

(a) Benzene (12 L dose, 400 nm nominal gap, low-doped n-type Si).

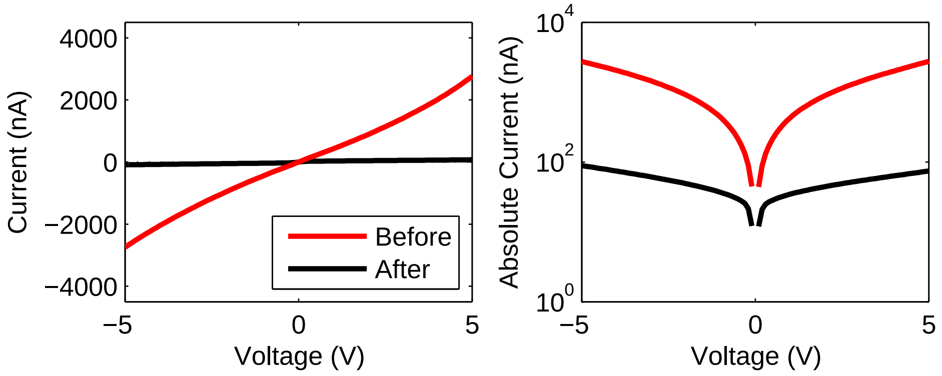

(b) Styrene (>10 L dose, 450 nm nominal gap, low-doped p-type Si).

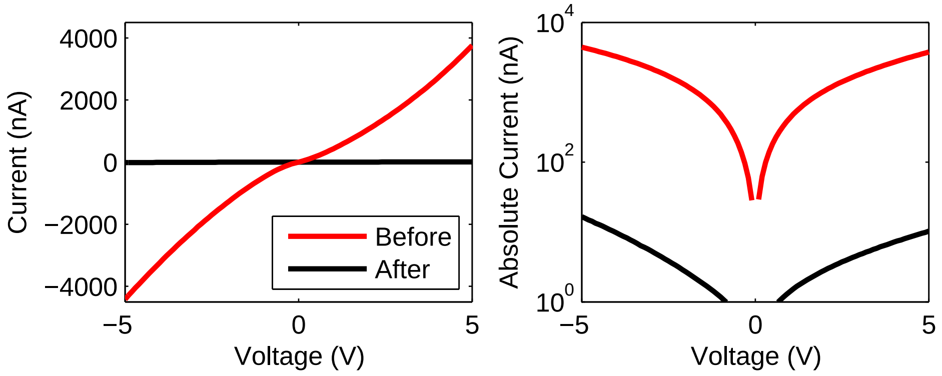

(c) 1,2,4-trimethylbenzene (20 L dose, 550 nm nominal gap, low-doped n-type Si).

Figure 9.7: Effect of dosing three different molecules on the current through EBL-defined gaps. 30 nm thick Ti contacts on Si(111), annealed to 950 C to form 7×7.

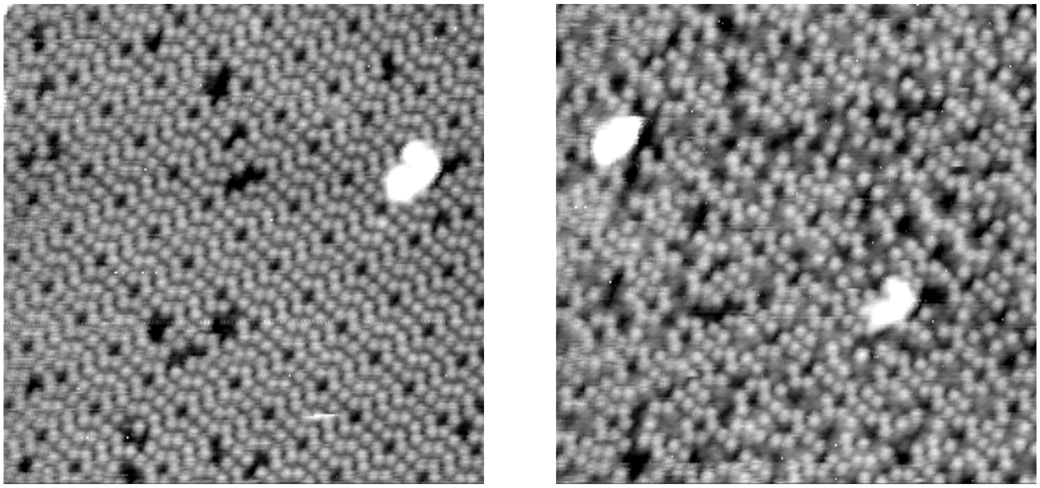

(a) Si(111)-7×7 surface before dosing.

(b) Approximately the same area, after a 15 L dose of benzene.

Figure 9.8: STM images showing a dose of benzene on Si(111)-7×7 — the 7×7 surface structure is still visible; the molecule is easily removed with time or by STM scans. 19 nm, +1.5 V, 100 pA.

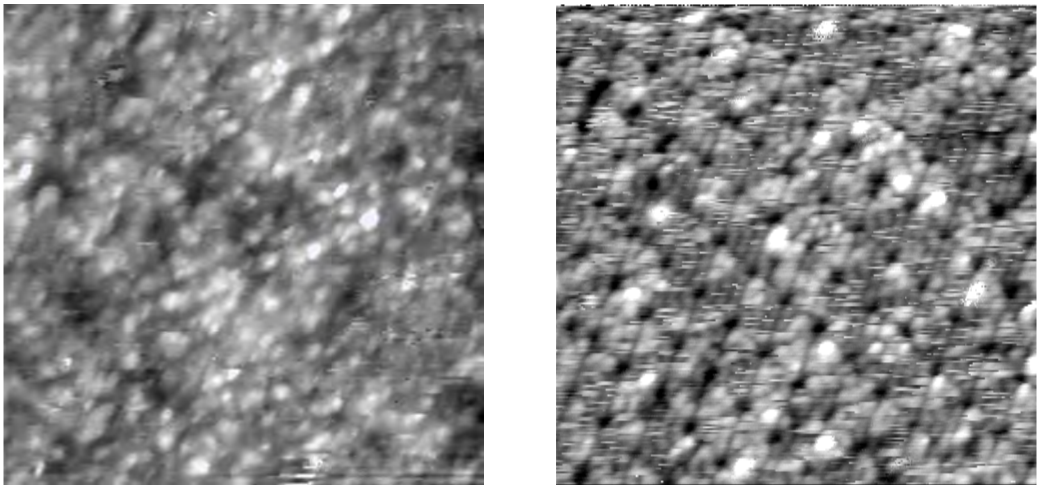

(a) Si(111)-7×7 surface following a 12 L dose of styrene. The molecule has strongly chemisorbed, leaving an irregular appearance on the surface. 19 nm, +2.0 V, 100 pA.

(b) Si(111)-7×7 surface following a 50 L dose of 1,2,4-trimethylbenzene. An outline of the 7×7 structure is still visible. 19 nm, +1.5 V, 100 pA.

Figure 9.9: STM images of the Si(111)-7×7 surface after dosing styrene and 1,2,4-trimethylbenzene.

9.7 Sensitivity of 2D Surface Conductance to Molecular Doses

9.7.1 Styrene Dose

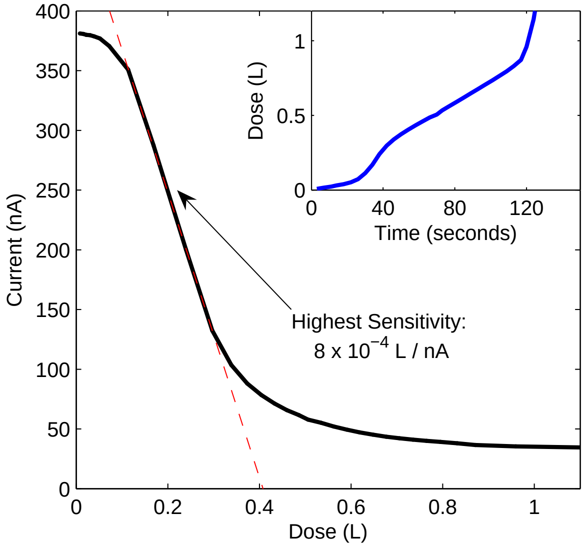

Figure 9.10: Plot of the current between contacts with +1 V applied versus total styrene dose in Langmuirs. The maximum slope corresponds to a sensitivity of 8×10^{-4} L / nA. Inset: Integrated pressure measurement (in L) versus time during the styrene dose. Surface is low-doped p-type Si(111)-7×7; 450 nm gap between Ti contacts.

Figure 9.10 shows the result of dosing a molecule (styrene) while continuously monitoring the probe-to-probe current with 1 V applied. The inset of the figure shows the integrated dose, in L, versus time. The dose began at a low pressure (near 5×10^{-9} Torr); increased around the ∼30 second mark; and went up to 2×10^{-7} Torr after 120 seconds to ensure full coverage.

The current was measured using a Keithley 2400 sourcemeter; using the integrated dose vs time curve, the current vs time data was converted to a current vs integrated dose curve, shown in the the main plot of Figure 9.10. The largest change occurs between 0.1 and 0.3 L; during this part of the dose, the current drops by 1 nA for every 8×10^{-4} L of styrene dosed. Since we can easily resolve changes in current < 0.5 nA, a sensitivity to doses below 4×10^{-4} L is achieved — this is equivalent to detecting a change in molecular coverage of less than 1/2500th of a monolayer.

We can see from the figure that the response saturates near a dose of 1 L — corresponding to a full monolayer coverage, assuming a sticking coefficient of unity. It is reasonable to assume that at this coverage, all of the surface states have been disrupted by bonding to molecules, and that further molecule exposure has no further effect. The current stayed at the same level after the end of the dose.

9.7.2 Benzene Dose

A different behavior can be seen when dosing benzene; this is shown in Figure 9.11. By the end of the 50 L dose, the current has dropped to 15% of its original value; however, as soon as the supply of benzene is turned off, the current begins to recover. As we mentioned previously, benzene desorbs from the surface at room temperature [144], restoring some of the surface's conductivity. The figure indicates three times when the gap area was intentionally heated by passing a relatively high current (typically 100 μA) for a few seconds. The higher temperature in the gap accelerated the desorption of benzene, making the current jump to a higher value in less time. Eventually the current rises to a steady amount near 30% of its original value. STM images show that a fraction of the molecules remain on the surface even after several hours; this is consistent with the current never recovering completely, since the surface never returns to pristine 7×7.

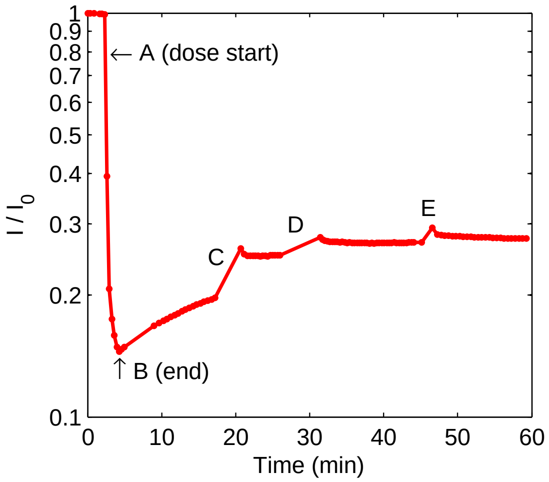

Figure 9.11: Time trace of the relative change in current between contacts (I/I_0) with -2 V applied during a benzene dosing experiment. A) Start of the dose, using a pressure of 5×10^{-7} Torr of benzene. B) End of the dose, total of 50 L. C) Resistive heating performed by applying -20 V, 100 μA for 40 seconds. D) 100 μA for 5 minutes. E) 105 μA for 1 minute.

9.8 Note on the Space-Charge Layer

The Si(111)-7×7 surface states are known to pin the Fermi level of the Si at the surface to 0.65 eV above the valence band maximum (VBM) [127]. The Si just below the surface therefore has a different carrier concentration than the bulk, giving it a different conductivity. This region is called the space-charge layer — see Figure 9.12. When looking at the change in conductance measured, it is important to distinguish between a change in space-charge layer conductance and a change in the 7×7 surface's 2D conductivity.

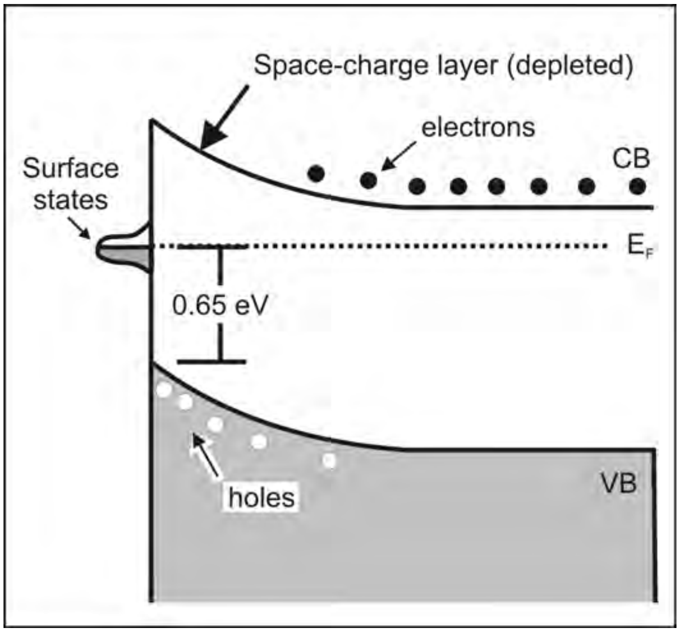

Figure 9.12: Band diagram depicting the pinning of the Fermi level by the 7×7 surface states. For both n-type and p-type Si, the space-charge layer underneath the surface is depleted of majority carriers.

In some cases, a space charge layer can become more conductive than the bulk (e.g. an accumulation layer) providing a pathway for conduction that could be confused with surface-state conductivity. A space-charge layer created by an external electrode is how a field-effect transistor (FET) operates.

In our experiments we used low-doped n-type and p-type Si with 1-5 Ω·cm resistivity. The Fermi level of low-doped n-type Si is 0.87 eV above the VBM; for low-doped p-type Si, the Fermi level is 0.22 eV above the VBM. Therefore, in both these cases, the pinning level at 0.65 eV brings the Fermi level closer to mid-gap (0.56 eV above the VBM), making the layer underneath the surface act more like intrinsic (undoped) silicon and creating a depletion layer.

Using the method described in Ref. [145], we have calculated that for low-doped (2.5 ohm-cm) n-type Si, the space-charge layer underneath the 7×7 surface contains 10^{11} cm^{-2} fewer majority carriers (electrons) than it would in a flat-band situation. Similarly, for low-doped p-type, the hole concentration in the space charge layer is smaller. Therefore, the space-charge layer under 7×7 is much less conductive than the bulk. Since the conductance drops when the surface reacts with molecules, thereby removing pinning, most of the conductance must be due to surface-states.

9.9 Finite Element Modeling

Using commercial finite-element modeling (FEM) software (Comsol Multiphysics), we calculated the sheet conductivity needed to obtain a probe-to-probe current close to what we typically observe experimentally for an unreacted 7×7 surface. The conduction through the bulk was ignored — as we have seen, because of the reverse diode character of the contacts, nearly no current flows to the bulk silicon. It is not possible to model "pure" 2D conduction, therefore we used a 20 nm-thick slab to represent the 7×7 surface. The 2D sheet conductivity of a slab of thickness t with bulk conductivity σ_b is simply $\sigma_s = t\sigma_b$. The 20 nm thickness used is significantly larger than the spatial extent of the Si(111)-7×7 surface states (a reasonable estimate would be 5 Å); however the results of the calculation would be nearly identical. The number of mesh elements for a 5 Å thick sheet would make the calculation unmanageable, therefore a thicker sheet was used instead.

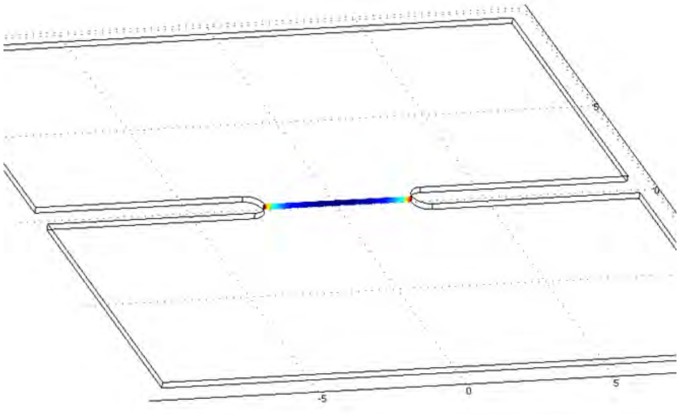

Figure 9.13: Geometry of the model used for FEM. The slice between the contacts shows a color scale of the current density.

The geometry of the model used is shown in Figure 9.13. 100-nm wide wires with 50-nm radius ends were used for both contacts. The edges of one were set to a voltage of +1 V while the other was grounded. The two wires were spaced 500 nm apart. Experimentally, the probe-to-probe current at 1 V was typically of 400 nA. We set the bulk conductivity in the sheet to 12 Ω^{-1}/m, corresponding to a sheet conductivity of $2.4 \times 10^{-7}\ \Omega^{-1}/\square$. With these settings, the probe-to-probe current obtained in the model was of 372 nA, very close to the experimental value.

Note that the calculations assume an ohmic (perfect) contact between the metal pads and the surface-states. Therefore, this is a lower bound to the surface conductivity of Si(111)-7×7. Our value of $\sigma_s \geq 2 \times 10^{-7}\ \Omega^{-1}/\square$ is quite consistent with previously reported values of surface conductivity, which range from $10^{-8}\ \Omega^{-1}/\square$ to $10^{-4}\ \Omega^{-1}/\square$, with several results near $10^{-6}\ \Omega^{-1}/\square$.

9.10 Conclusions

We have measured the surface conductivity of Si(111)-7×7 using EBL-defined contacts and our multiple-probe STM in UHV. Unlike previous experiments, we confirmed the surface quality by STM and used sub-micron contact spacing, giving us a very sensitive measurement of 7×7 surface conductivity. Using experimental results and finite element modeling, we estimate the surface conductivity of 7×7 to be at least $2 \times 10^{-7}\ \Omega^{-1}/\square$. This surface's conductivity is extremely sensitive to reactions with molecules, giving us the ability to electrically detect a change in molecular coverage of 1/2500th of a monolayer.

Chapter 10

Scanning Tunneling Fractional Current Imaging

10.1 Introduction

The electrical conductivity of materials is most commonly measured using the four-point-probe technique, where current is injected in the material at two outer points, and a voltage drop through the material is measured at two inner points. The resistivity of the material can be easily calculated from the current and voltage values if the geometry of the system is known [146, 147, 148]. Four-point-probes can also be used to measure the anisotropy of surface conductance [149, 150, 151], in which case a square geometry must be used.

Our multiple-probe STM (Chapter 5) is equipped with only three probes because of space limitations, preventing us from performing normal four-point-probe measurements. However, we may still be able to achieve similar results with three probes, as Hofmann and Wells state[6]:

> In principle, it should be possible to use an alternative STM approach in which a macroscopic current is passed through the sample and the potential at the surface is mapped. In this way, one performs a three-contact measurement in which one contact (the STM tip) is free to move across the surface. One should thus be able to mimic a four-point probe measurement with all its advantages by mapping the potential at different points.

Such *scanning tunneling potentiometry* (STP), as it is known, was developed in 1985 by Muralt and Pohl [152] - only a few years after the invention of the STM.

We will begin this chapter by describing the STP technique and some published experimental results using STP to characterize silicon surfaces, paying particular attention to the measurement of the resistance of steps on conductive surfaces. Then, we will describe our implementation of scanning tunneling potentiometry, which works by a different principle than standard STP. We will then describe our experimental results on H-Si(111)-1×1 and Si(111)-7×7 surfaces.

10.2 Standard Scanning Tunneling Potentiometry

The goal of scanning tunneling potentiometry (STP) is to measure the local potential at the STM tip position on a sample with a potential gradient applied. A schematic of the circuitry used is shown in Figure 10.1. It works by combining an AC and a DC component to form the tunneling bias. The tunneling current is therefore affected by both the DC and AC components, and is modulated at the same frequency as the AC component of the bias. By using a lock-in amplifier and other circuity, both the AC and DC components of the tunneling current can be measured simultaneously.

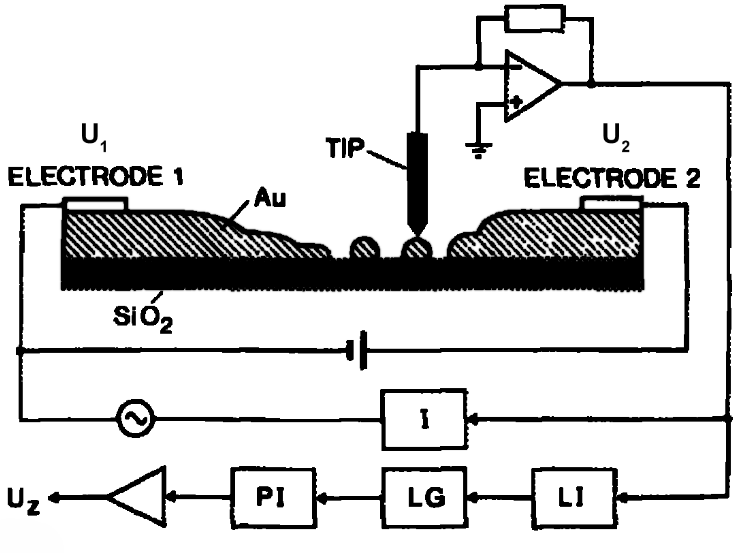

Figure 10.1: Schematic of the scanning tunneling potentiometry circuitry used by Muralt and Pohl. LI: lock-in amplifier; LG: logarithmic amplifier; PI: feedback loop circuit; U_Z: voltage applied to the z piezoelement. From [152].

The AC component of the tunneling current alone is used to regulate the tip-sample distance, by using a normal feedback loop system adjusting the voltage on the z piezoelement. It is in the regulation of the DC component of the tunneling current that the local potential can be measured. As can be seen in Figure 10.1, two DC voltage are applied to two electrodes on a surface: U_1 and U_2. The difference in voltage between the electrodes, $\Delta U = U_2 - U_1$, is kept constant during an experiment. The common component of U_1 and U_2 is called U_{regl}, giving:

$$U_1 = U_{regl} \tag{10.1}$$

$$U_2 = U_{regl} + \Delta U \tag{10.2}$$

At a zero DC tunneling bias, the tunneling current's DC component will be zero. U_{regl} is adjusted using a second feedback loop so as to cause the DC component of the tunneling current to be zero. The value of U_{regl} provided by this second feedback loop directly gives the potential of the surface at the STM tip position.

The STM tip is biased with an AC voltage with a frequency between 0.5 and 3 kHz. Alternatively, the AC voltage can be added to U_1 and U_2 (again keeping ΔU constant). Because the tip-sample distance is regulated by this AC component, which is measured at a smaller bandwidth than the current alone, STM scans have to be performed more slowly — typically by a factor of 3 [153].

Among other applications, scanning tunneling potentiometry has been used to image potential steps at grain boundaries in polycrystalline thin films [154, 155] and to image the electrostatic potential distribution across a semiconductor junction [156].

10.3 Resistance Across Steps as Evaluated by STP and Other Methods

We have shown in Chapter 9 that the Si(111)-7×7 surface is a reasonably good 2D conductor, with a sheet conductivity we estimate to be $> 2 \times 10^{-7}\ \Omega^{-1}/\Box$. However, the surface is not a continuous 7×7 reconstruction, since that surface is interrupted by steps of different silicon height, as was shown in, e.g., Figure 7.10(b). The disruption in the continuous surface states caused by steps likely has an effect on its conductivity; it is therefore of interest to consider their importance on the resistivity of the Si(111)-7×7 surface.

In the many published reports of measurements of the conductivity of Si(111)-7×7 summarized in Section 9.1, to our knowledge only the work of Hasegawa [140] has discussed the effect of steps. They report single-point STM measurements of 7×7 conductance, and find that a small (1000 nm^2) epitaxially grown 7×7 island showed ∼10 times less conductance than the rest of the surface. They attribute the reduced conductance to the surface steps surrounding the island; the steps could scatter electrons [157, 158].

More papers have been found to evaluate the effect of steps of the Si(111)-($\sqrt{3} \times \sqrt{3}$)-Ag surface. This surface is formed by evaporating Ag on a heated Si(111)-7×7 surface; e.g. 12 nm of Ag deposited at 780 K [6]. This surface has the advantage over the 7×7 surface of a much higher sheet conductivity — estimates range from 10^{-5} to 10^{-3} $\Omega^{-1}/\Box$, which puts it several orders of magnitude above most measurements of Si(111)-7×7 conductivity.

Matsuda et al. [159] have measured the electrical resistance of a Si(111)-($\sqrt{3} \times \sqrt{3}$)-Ag monoatomic step by three methods. First, working on a surface with a high density of aligned steps, they used four movable probes in a square geometry to determine the conductivity parallel and perpendicular to the step direction. Second, they used 4 probes in a linear geometry to measure the resistance across a "step bunch" area containing around 300 steps. Third, using STM they imaged the local density of states standing wave (Friedel oscillation) at the step edge. From these results they obtained a value of approximately 5×10^3 $\Omega^{-1}\text{cm}^{-1}$ for the linear conductivity across a monoatomic step.

Bannani et al. [153] performed STP on a stepped Si(111)-($\sqrt{3} \times \sqrt{3}$)-Ag surface and were able to image the potential drop at single steps, as shown in Figure 10.2. The experiment shows that this surface conducts significantly better than the bulk Si — making the potential constant on each terrace. The potential drops in a non-monotonic fashion, consistent with a percolation structure. Because of the high resistivity of the step edges, the potential profile depends on steps around a terrace, rather than on the smooth mesoscopic field distribution one would expect between the two electrodes.

By performing similar STP experiments, Homoth et al. [160] obtained a monoatomic step conductivity value of 3000 $\Omega^{-1}\text{cm}^{-1}$ for current flowing across the Si(111)-($\sqrt{3} \times \sqrt{3}$)-Ag step. This value is in agreement with that of Matsuda et al. The authors find that the voltage drop occurs at a step over a distance smaller than 1 nm. This might lead some to conclude that there would be significant resistive heating at steps, but the authors make an interesting point: "It should be noted that the dissipated power per area is no longer given by $\sigma(\Delta\mu_{ec,STP})^2$ because the voltage drop is due to quantum mechanical reflection and the thermalization of the carriers occurs on a much longer length scale."

The authors were able to calculate the conductivity of a step parallel to current flow, and, interestingly, found it to be much lower: < 300 $\Omega^{-1}\text{cm}^{-1}$. They explain that "[t]his may be explained by the transmission through a tunneling barrier as a

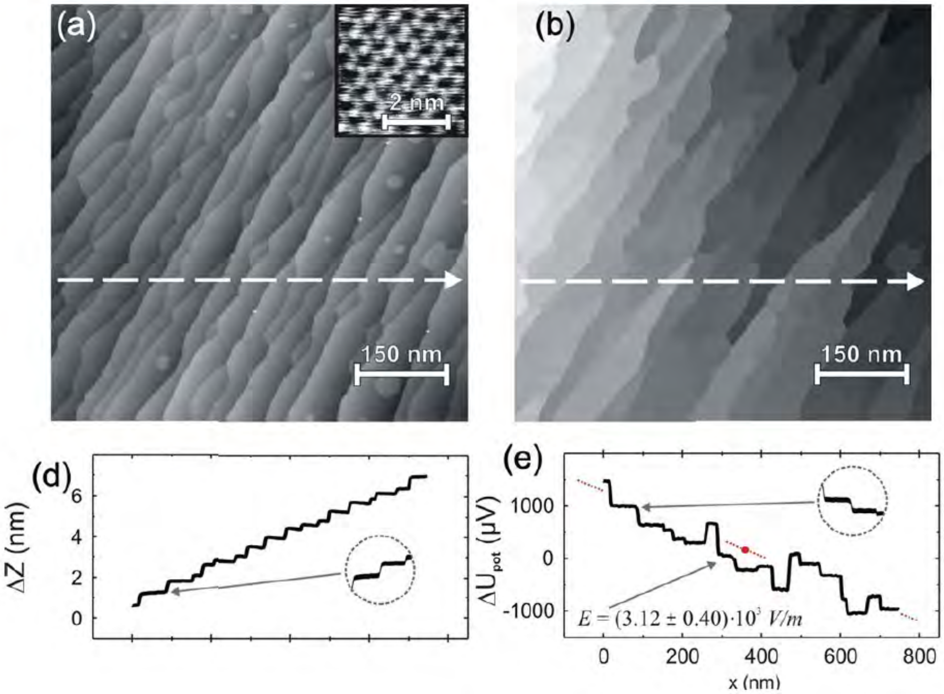

Figure 10.2: STP experiment on Si(111)-($\sqrt{3} \times \sqrt{3}$)-Ag. (a) Topography. (b) Potential map (gray scale range of 4.5 mV). (d) Cross-section plot of the topography along the line indicated in (a). (e) Potential cross-section along the same line, showing the flat regions on each terrace, with potential drops at steps only. Modified from [153].

function of the angle of incidence. The transmission can be calculated analytically for plane waves impinging on a rectangular barrier. It is maximal if the angle of incidence is perpendicular to the step edge ($\theta < 0°$). It remains up to 90% of the maximum for $\theta < 30°$, but it drops to less than 1% for $\theta > 70°$."

10.4 Scanning Tunneling Fractional Current Imaging

The scanning tunneling potentiometry described above typically uses two contacts biased at different voltages. In this section, we describe a variant of STP where there is no bias applied between contacts, which we call scanning tunneling fractional current imaging (STFCI).

10.4.1 STFCI Method

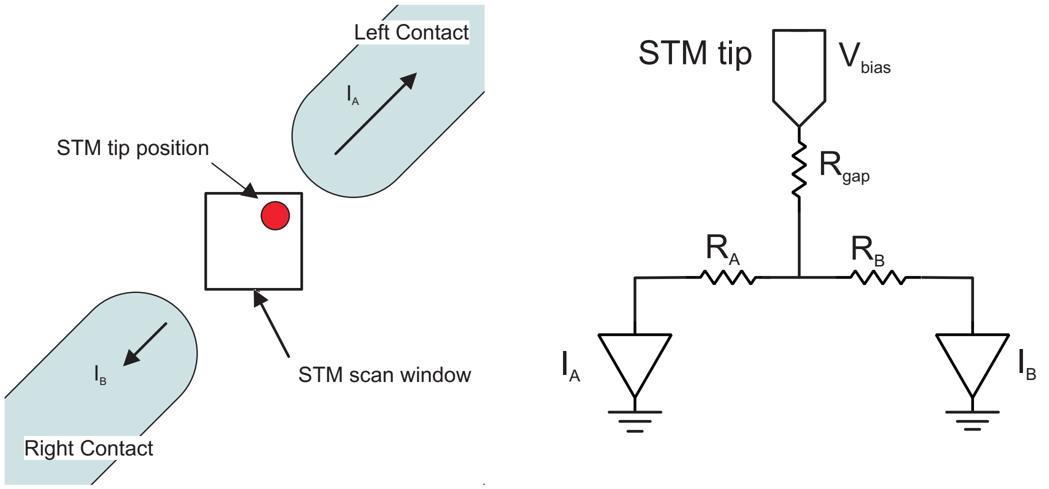

(a) Schematic of the positions of the contacts and tip during a STFCI experiment. The orientation of the left/right contacts corresponds to what is seen in a STM scan.

(b) Schematic of the equivalent electrical connections in STFCI.

Figure 10.3: Schematics of scanning tunneling fractional current imaging.

As in standard STP, STFCI uses two closely spaced contacts on the surface. This can be accomplished using the EBL-defined metal pads described in Section 7.4, or by directly touching down two of the probes to the surface. Our multiple-probe STM, however, allows much smaller distances between the contacts than is typically used; this increases the voltage gradient and makes small variations easier to observe. Both contacts are connected to current-to-voltage amplifiers, which act as two virtual grounds while measuring the current flowing through each contact - see Figure 10.3.

In a STFCI setup, the sample is not biased using the usual macroscopic clips — that connection is left floating. Instead, the sample is grounded via the two probes. The tunneling bias is applied to the STM tip directly, which is not connected to a current-to-voltage amplifier as is usual. As shown in Figure 10.3(a), the STM tip is scanned between the two metal contacts. Each contact collects a current separately, labeled I_A and I_B.

The current value fed to the feedback loop for tip height control is the *sum* of the two currents, $I = I_A + I_B$. Since there are no other connections, this total current correctly reflects the total tunneling current at the tip, and the feedback loop will therefore be able to maintain an equal tip-sample distance no matter how close to one contact it gets. This current addition could performed with a voltage adder circuit, but in our case it was performed using a software setting of our Nanonis controller.

10.4.2 STFCI Data Analysis

When performing a STM scan in STFCI mode, both the left and right probe currents are recorded simultaneously. The clearest way to present the STFCI data is to create an image of the fraction of the current going to one of the probes over the total tunneling current; an example of such data processing is shown in Figure 10.4. Subfigures (a) and (b) show the recorded current flowing to probes A and B. For instance, a large section in the upper part of the image is connected more closely to probe A, and therefore appears bright in the I_A image, but black in the I_B image: most of the current flows directly to probe A, and very little goes to probe B.

The image in Figure 10.4(d) shows the calculated fraction of the current going to probe A, given by $F_A = I_A/(I_A + I_B)$. The image is formed by plotting F_A as a grayscale, where $F_A \leq 0.2$ is black, and $F_A \geq 1.0$ is white; the limits can of course be adjusted to maximize contrast. This image shows the differences in current flow much more clearly than a comparison of either Figure 10.4 (a) or (b). The contrast in the steps in the lower left are clearly visible in the fractional current image, yet hard to distinguish in the current images. Also of note is that the bright lines visible in the current images (where the tunneling current was higher for a short time due to noise or a change of feedback loop settings) are not visible in the fractional current image, since the proportion of current going to probe A or B is unchanged by the change in total current. The resulting F_A image, therefore, suffers much less from transient tip noise. We typically saw some 60 Hz noise in the F_A image (visible as

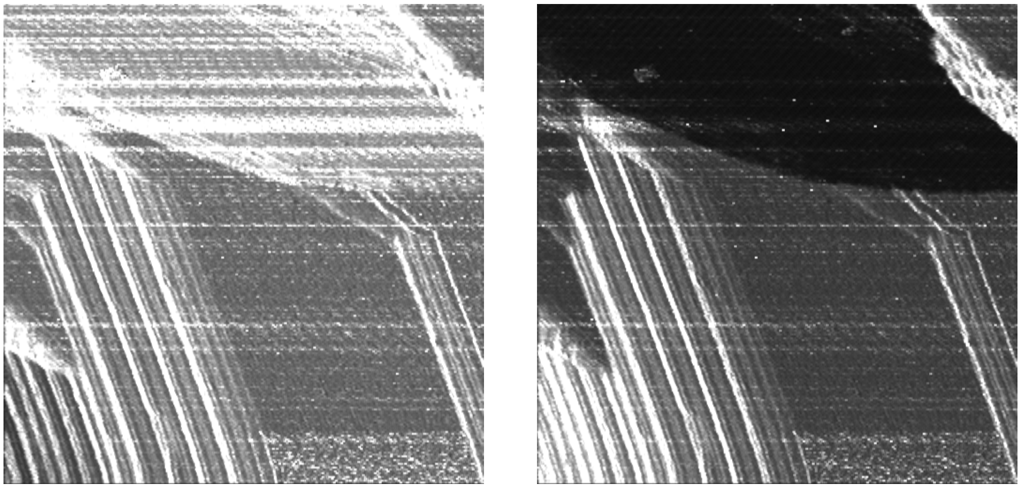

(a) Current from probe A (upper right corner), I_A. 300 pA color scale.

(b) Current from probe B (lower left corner), I_B. 300 pA color scale.

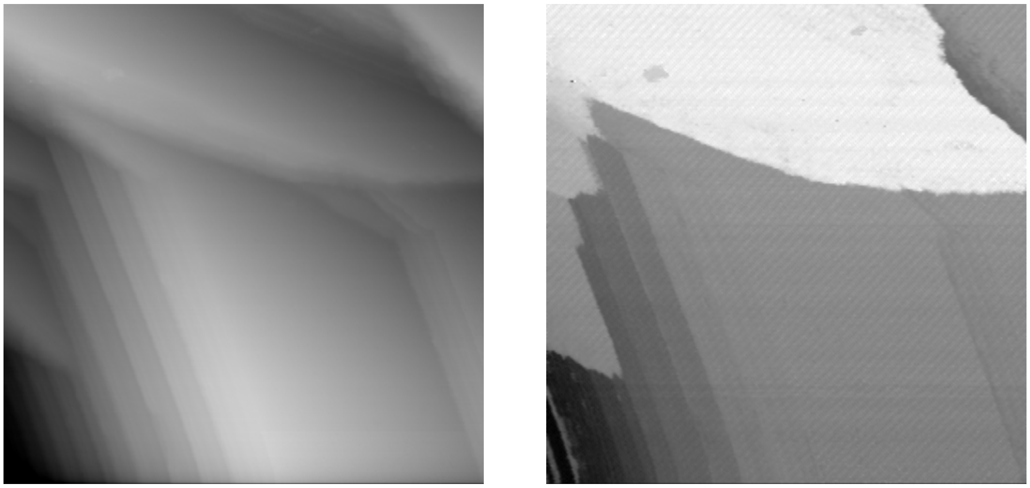

(c) Topography.

(d) Fraction F_A of current going to probe A, $F_A = I_A/(I_A + I_B)$. Color scale: 0.2 to 1.

Figure 10.4: Sample STFCI experiment images. Taken on Si(111)-7×7 between Ti EBL contacts spaced 250 nm apart. 150 nm wide, +2 V tip bias, 150 nA total tunneling current.

diagonal lines in Figure 10.4(d), for example); blurring can be used to reduce its appearance.

10.4.3 Comparison of STFCI to STP

The equivalent circuit of the STFCI setup was shown in Figure 10.3(b). We first note that the tunnel gap resistance, R_{gap}, will be of the order of 1 GΩ or higher ($<$ 1 nA tunneling current at 1 V bias). The gap resistance normally dominates: $R_{gap} \gg R_A$ or R_B. With the feedback loop keeping the tunneling current constant, R_{gap} remains constant during an experiment. We will now compare the results of a STFCI experiment to a similar STP experiment.

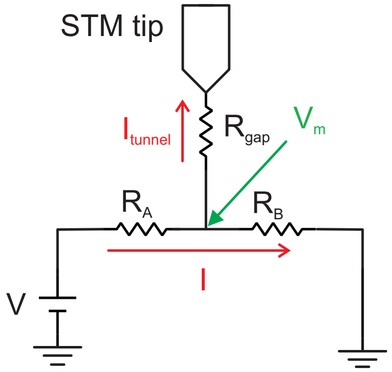

Figure 10.5: Schematic of a STP experiment.

First, we calculate what would be measured in an equivalent STP measurement, shown in Figure 10.5. The geometry of the contacts and tip are the same; only the connections are made differently. Probe A is biased to a voltage V, with probe B grounded. The resistance between A and B is $R = R_A + R_B$, so the current flowing from A to B is $I = \frac{V}{R_A+R_B}$; I_{tunnel} is negligible. At the STM tip position, the tip measures the voltage V_m, which is given by the voltage drop through R_B, $V_m = IR_B$. If we look at the fraction of measured potential V_m over the applied potential V, we get:

$$\frac{V_m}{V} = \frac{R_B}{R_A + R_B} \tag{10.3}$$

Let us now compare the measurement of fractional current, $F = I_A/(I_A + I_B)$, to a STP measurement. In the STFCI experiment, most of the tip bias voltage V_b is dropped through the tunneling gap resistance R_{gap}. The voltage at the surface below the tip is V_t. The currents to probes A and B are simply

$$I_A = V_t/R_A \tag{10.4}$$

$$I_B = V_t/R_B \tag{10.5}$$

and the total tunneling current is:

$$I_{tot} = V_t/R_{tot} \tag{10.6}$$

$$R_{tot} = (1/R_A + 1/R_B)^{-1} \tag{10.7}$$

from which we can calculate the fraction current

$$F_A = \frac{I_A}{I_{tot}} = \frac{V_t/R_A}{V_t(1/R_A + 1/R_B)} = \frac{R_B}{R_A + R_B} \tag{10.8}$$

which is the same value calculated for the fraction of measured voltage V_m/V (Equation 10.3) in the proposed STP experiment. From this result, we find that the fractional current value F_A calculated in a STFCI experiment can be scaled to be equivalent to the measured potential in a STP experiment. This conclusion is independent of the values of R_A and R_B, and of the tip-sample distance. It does, however, assume that the material conductivity is ohmic (does not depend on applied voltage). Also, this derivation is based on a one dimensional model; in Section 10.5.2 we will see FEM calculations showing that STP and STFCI are still equivalent in three dimensional models.

It is worth noting that the voltage developed in the semiconductor at the surface immediately below the tip is quite small. This can be estimated by comparing the tunnel gap resistance (10 GΩ for 100 pA at 1 V bias) to the resistance of the material. From the diode curves in Figure 9.5, on page 176, we can see that for a low-doped crystal with H-Si(111)-1×1 surface, for example, a contact-to-contact resistance of $\sim$100 MΩ is typical. Using these values, we find that approx. 99% of the bias voltage will drop in the vacuum gap, leaving only a few mV at the surface.

10.5 STFCI on H-Si(111)-1×1

10.5.1 Experimental Results

A hydrogen terminated Si(111) surface was prepared by wet chemical etching, with EBL-defined Cr contacts as described in Section 7.9.4. Normal STFCI connections were made to the Cr contacts.

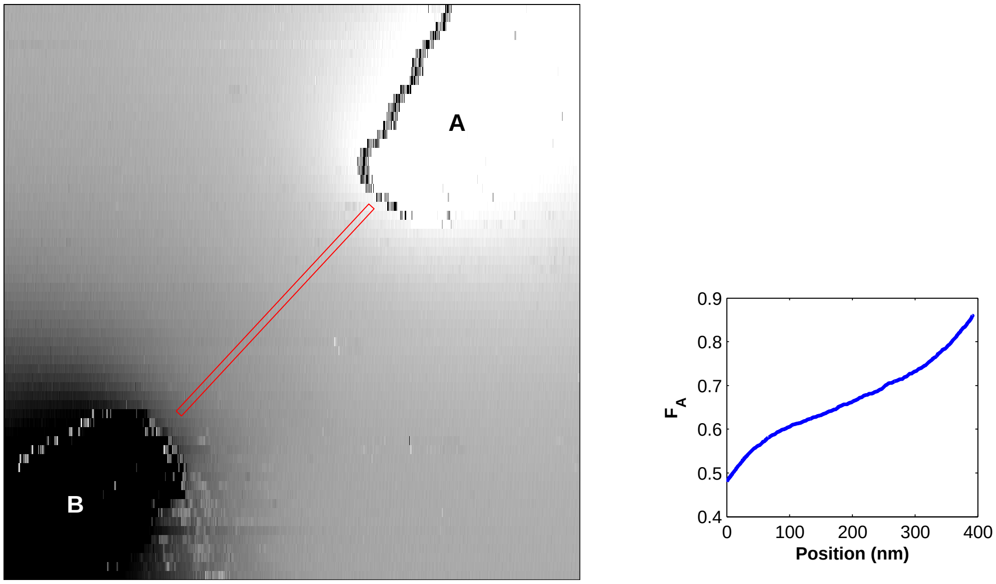

(a) F_A, fraction of current going to contact A (upper right). Color scale: 0.2-0.9.

(b) Cross-section of F_A along the red bar in (a), from lower left to upper right.

Figure 10.6: STFCI image on low-doped, p-type H-Si(111)-1×1. 800 nm, 300 nA, +3.0 V tip bias.

Figure 10.6(a) shows a STFCI experiment performed on the gap between these Cr EBL-defined contacts. The gray scale shows that the surface appears brighter near contact A, indicating that a larger fraction of the current is going to this contact as the STM tip gets nearer to it. A cross-section of F_A taken between the two contacts is shown in Figure 10.6(b); the cross-section was averaged along a width of 10 nm so as to reduce the noise. The shape of the curve is a linear increase in F_A from contact B to contact A, except for a curvature seen near the contacts.

10.5.2 Comparison With FEM Simulation

Finite element method (FEM) calculations were performed to simulate the STFCI images obtained previously. A 3D model was built consisting of a 600 nm cube of material with uniform electrical conductivity corresponding to the low-doped Si used. The surfaces of two quarter spheres on either side of the model were used as grounded metal contacts, spaced 500 nm apart; all other surfaces were insulating. To simulate the STM tip current, a single point was placed on the surface and treated as a 1 nA current injection point. In the calculations, the current flowing out through each of the two grounded contacts was integrated so as to obtain I_A and I_B; $I_A + I_B$ was equal to 1 nA, the injected current. The current injection point was moved along the surface, and the calculation repeated for a matrix of points to find I_A and I_B for each current injection point position — simulating the movement of a STM tip during a STFCI scan. To increase the calculation speed, only one quadrant of the tip positions were calculated, and symmetry was used to fill in the remaining surface. The ratio of $\frac{I_B}{I_A+I_B}$ was calculated at all these points and is plotted in Figure 10.7(a).

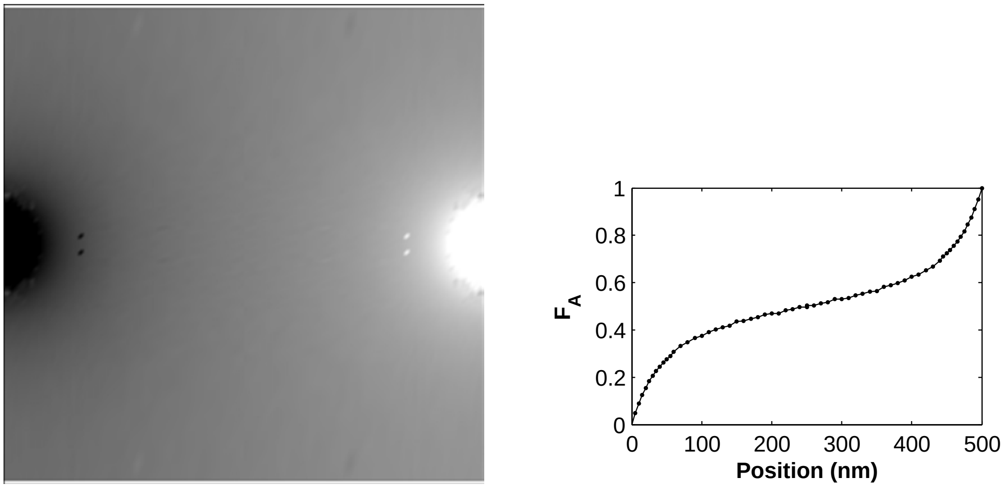

(a) Simulated value of F_A obtained. Color scale: 0.0-1.0.

(b) Cross-section of the simulated F_A along the x-axis, centered in y.

Figure 10.7: FEM simulation of a STFCI experiment on a material with the same conductivity as low-doped p-type Si(111). 50 nm radius contacts were spaced 500 nm apart.

The F_A distribution in Figure 10.7(a) is very similar in appearance to the experimental STFCI image obtained in Figure 10.6(a). The cross-sections of both the experimental data and the simulation also show similar behavior: a curve for ∼50 nm near each contact, with a linear region between the two contacts. There are differences in the quantitative aspects of the curve, however: the experimental curve of F_A varies from approx. 0.45 to 0.9 as it moves from contact A to contact B, whereas the simulation shows a transition from 0 to 1. It is possible that the shape of the STM tip prevents it from accessing the surface immediately next to the metal contacts, due to their high aspect. This could make the closest 10-20 nm of the H-Si(111)-1×1 surface inaccessible, and F_A might reach closer to 0 or 1 close to contacts B and A, respectively. Non-negligible contact resistances would also explain the discrepancy.

A simpler FEM simulation was performed using the same geometry. Instead of injecting current at a point, simulating the STM tip, one of the contacts was biased to +1 V, and the other contact was grounded. The voltage calculated at the surface is equivalent to what would be measured in a STP experiment. A plot of the potential distribution along the surface of the semiconductor matches exactly the simulated F_A image calculated in Figure 10.7(a). We have shown in Section 10.4.3 that the value of F_A is the same as the measured voltage fraction V_m/V in a one-dimensional scenario. This FEM result shows that $F_A = V_m/V$ is true in 3D as well, at least within the limits of this model (ohmic contacts, uniform and constant conductivity).

10.5.3 Dependence on Tip Bias

Figure 10.8 compares STFCI images taken of the same Cr contacts on low-doped n-type H-Si(111)-1×1 at positive and negative tip bias. The behavior of F_A between the contacts is strikingly different: with a positive tip, there is a gradual change from a F_A value of 0.2 to 0.7 as the STM tip moves from near contact B to near contact A (Figure 10.8(b)). However, there is nearly no gradient at all with a negative tip: F_A only changes by 0.04 between the contacts, as shown in Figure 10.8(d). The same effect has been seen on low-doped p-type, with the same polarity — take for example Figure 10.6(a), which shows a gradient of F_A at +3 V tip bias on low-doped p-type H-Si(111)-1×1.

As shown in Figure 2.7(a) on page 23, when a tip is biased at +2 V, this places its Fermi level into the valence band of the semiconductor. This means that the tip injects holes into the semiconductor, and that the motion of holes will determine the currents flowing to contacts A and B. Conversely, a negatively biased tip will inject electrons into the semiconductor conduction band, as in Figure 2.7(b).

The current transport paths in a Schottky contact are shown in Figure 10.9. In the STFCI experiment, the Schottky barrier has effectively no bias across it, since the voltage drop across the semiconductor is actually quite small, as we have seen in Section 10.4.3. With no bias applied, a Schottky barrier persists. Injecting electrons from the semiconductor towards the metal contact requires them to go over the barrier. Conversely, if holes are injected from the valence band into the

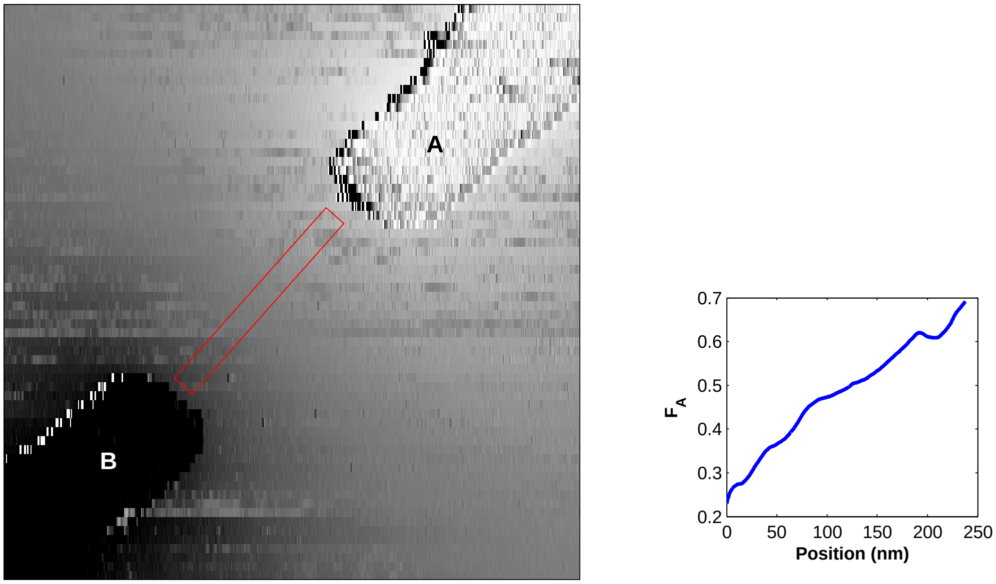

(a) F_A for +2 V tip bias. Color scale: 0.0-1.0.

(b) Cross-section of F_A along the red bar in (a), from lower left to upper right. 25-nm wide averaging.

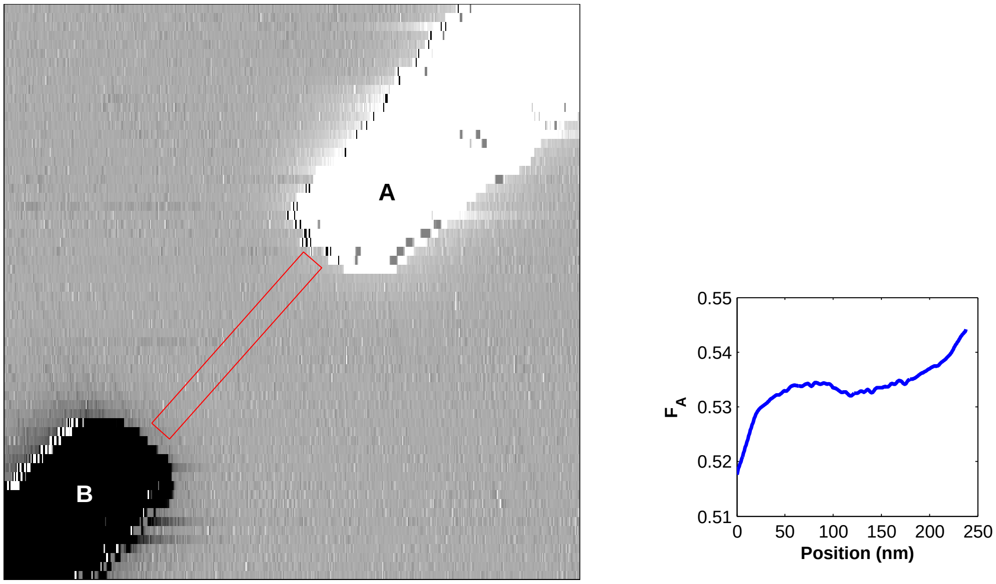

(c) F_A for −2 V tip bias. Color scale: 0.4-0.6.

(d) Cross-section of F_A along the red bar in (c), from lower left to upper right. 25-nm wide averaging.

Figure 10.8: Dependence on tip bias of STFCI images and F_A cross-sections on low-doped, n-type H-Si(111)-1×1. 600 nm, 300 nA; contact A is on the upper right corner.

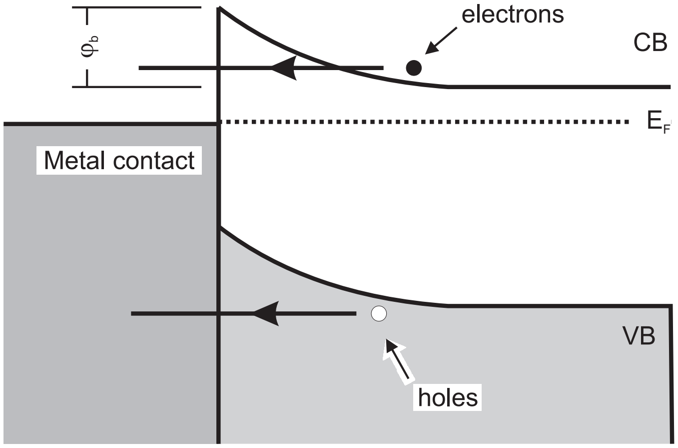

Figure 10.9: Band diagram showing the injection of electrons or holes into a metal in contact with a semiconductor. ϕ_b: Schottky barrier height; E_F: Fermi level in the semiconductor. Electrons need to tunnel through or pass over the Schottky barrier, whereas holes do not see a barrier.

metal, they have no barrier to cross and should flow readily.

Returning to the resistance model described in Section 10.4.3, let us represent the Schottky barriers of both metal contacts as additional resistances for both A and B current paths: $R_{A,barrier}$ and $R_{B,barrier}$. We can add these resistances in Equation 10.8 to obtain:

$$F_A = \frac{R_B + R_{B,barrier}}{R_A + R_B + R_{A,barrier} + R_{B,barrier}} \tag{10.9}$$

In the case of electron transport (corresponding to a negatively biased tip), the barrier is significant. If the barrier resistance dominates the material resistance, then we can represent it by $R_{A,barrier} \gg R_A$ and $R_{B,barrier} \gg R_B$. Equation 10.9 thus becomes:

$$F_A \approx \frac{R_{B,barrier}}{R_{A,barrier} + R_{B,barrier}} \tag{10.10}$$

which is approximately a constant, no matter what the position of the STM tip (which determines R_A and R_B but does not change $R_{A,barrier}$ or $R_{B,barrier}$). Since both Schottky contacts are of very similar geometry, we expect that $R_{A,barrier} \approx R_{B,barrier}$, making $F_A \approx 0.5$. This is very consistent with what was observed experimentally in Figure 10.8(d).

A positively biased tip will be injecting holes into the semiconductor. The Schottky barrier does not restrict hole movement into the metal contacts, so we take $R_{A,barrier} \ll R_A$ and $R_{B,barrier} \ll R_B$, making the fractional current measurement sensitive to R_A and R_B again:

$$F_A \approx \frac{R_B}{R_A + R_B} \tag{10.11}$$

therefore, as the STM tip moves between the contacts, the change in R_A and R_B will be visible in the F_A image, as shown for example in Figure 10.8(a). This explanation for the dependence on tip bias of the fractional current image fits qualitatively with the observed images. In particular, the behavior would be the same on low-doped p-type as on low-doped n-type; and this is what was observed experimentally.

We saw experimentally that F_A typically did not reach exactly 0.0 or 1.0, even when extremely close to contact B or A. Let us consider a case where the tip is very close to contact B, so we would expect $F_A = 0$, since $R_B \approx 0$. In general, $R_{B,barrier}$ might be of the same order as R_A or R_B, so

$$F_A = \frac{R_B + R_{B,barrier}}{R_A + R_B + R_{A,barrier} + R_{B,barrier}} \approx \frac{R_{B,barrier}}{R_A + R_{A,barrier} + R_{B,barrier}} \tag{10.12}$$

which is only close to 0 if $R_A \gg R_{B,barrier}$. This explains the experimental result where F_A varies, for example, from 0.45 to 0.9 as the tip moves from contact B to contact A.

10.6 Desorption of H on H-Si(111)-1×1 to Form Si(111)-7×7

10.6.1 STFCI Results

In Section 8.2.3 on page 154, we presented FEM simulation results showing that significant resistive heating could occur when flowing current between the EBL-defined metal contacts; in Section 8.4, we saw that heating H-Si(100)-2×1 in this way desorbed H from the surface.

If a H-Si(111)-1×1 surface is heated sufficiently, the H will desorb and the surface Si atoms will reconstruct into the 7×7 pattern. Another possible surface is Si(111)-2×1, which is obtained by cleaving in vacuum [161] or by thermally desorbing H at temperatures insufficient to form the 7×7 reconstruction.

A current-induced desorption was performed on a low-doped, p-type H-Si(100)-2×1 surface with Cr contacts. A current source applied a current of 1 mA through the contacts for 60 seconds; a 2.5 MΩ resistor was placed in series to avoid destructive semiconductor thermal run-away. After turning off the heating current, the probes lost contact — this might be due to thermal expansion of the silicon pushing the

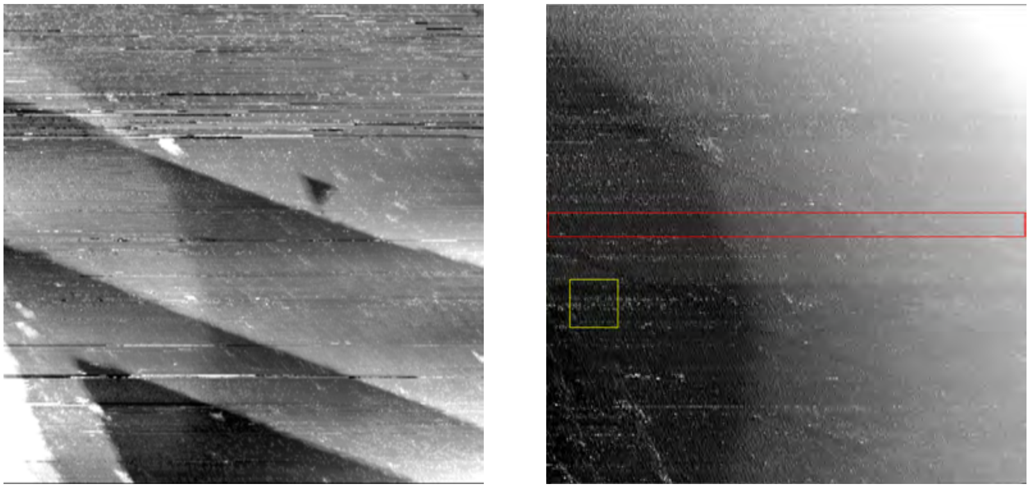

(a) Topography image (200 nm wide). The metal contact is close to the lower left corner. The bright patch is Si(111)-7×7.

(b) F_A image of (a). Color scale: 0.3-0.7. The yellow box indicates the location of the image in (d).

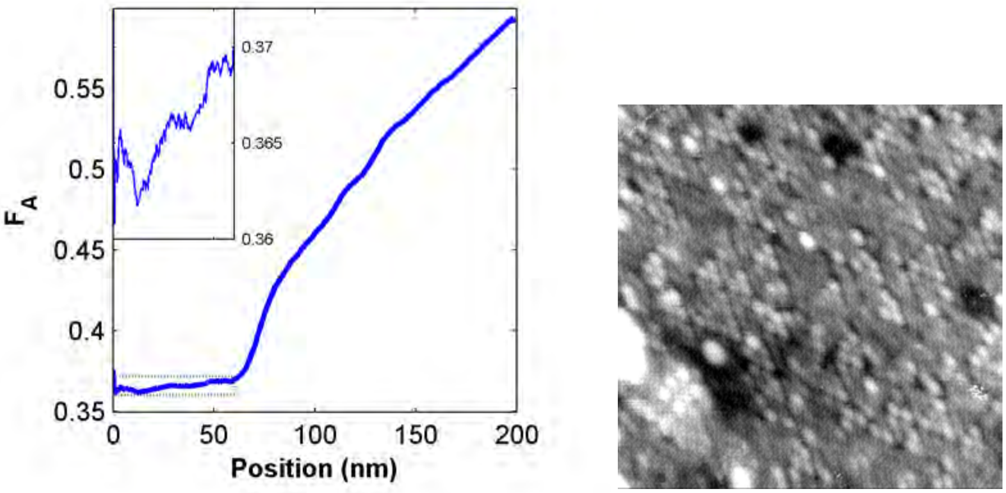

(c) Cross-section F_A along the x-direction indicated by the red box in (b). Inset: F_A in the 7×7 region.

(d) STM image taken in the desorbed region (20 nm wide).

Figure 10.10: STFCI image showing the higher conductivity of a patch of Si(111)-7×7 desorbed on low-doped, p-type H-Si(111)-1×1. 300 nA, +2.0 V tip bias.

probes away, bending them out of contact once the Si had cooled down.

Figure 10.10 shows the result of this heating. The topography image in Figure 10.10(a) still shows the triangular steps that were on the H-Si(111)-1×1 surface before heating. However, a ∼60 nm wide patch of the surface appears brighter than the surrounding H. This patch is located close to the metal contact on the lower left side; a similar patch could also be seen in other STM images close to the other metal contact. A smaller STM image taken in the desorbed patch (Figure 10.10(d)) shows signs of partial 7×7 reconstruction. STM images taken far from the boundary appeared to be H-Si(111)-1×1; unfortunately, STM imaging was too poor to clearly image the boundary between desorbed and intact H.

The fractional current image shown in Figure 10.10(b) shows very different character in the desorbed region. As the cross-section in Figure 10.10(c) shows, there is a strong gradient of F_A in the intact region, whereas the desorbed region is nearly flat. The inset, which scales up the first 60 nm of the cross-section, shows a variation of only 0.007 in F_A in the desorbed region, whereas there is a change of 0.13 in the next 60 nm in the intact region. The small slope in the desorbed region indicates that it is much more conductive than the H-terminated region.

10.6.2 FEM Simulations

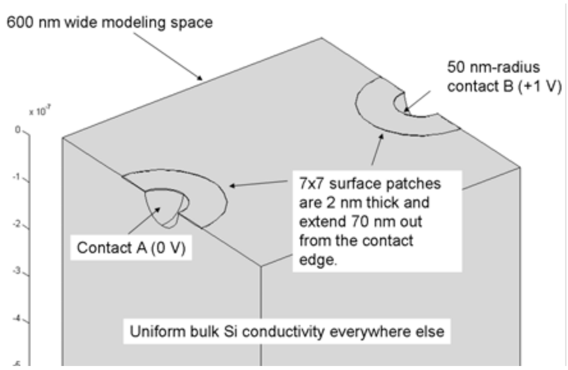

(a) Geometry of the FEM model.

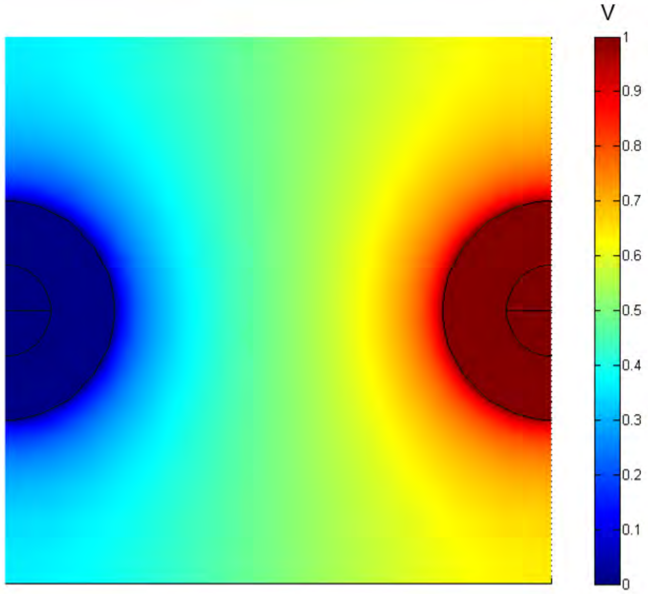

(b) Results of the FEM calculations: pseudo-color plot of the potential at the Si surface.

Figure 10.11: FEM calculations representing a 2D conductive patch around two metallic contacts, biased with 1 V difference.

A FEM simulation was performed that reproduced the observed STFCI results — the geometry of the model is shown in Figure 10.11(a). The two contacts were 50 nm in radius, spaced 500 nm apart. A 600-nm cube of uniformly conductive material represented the bulk silicon. The patch of desorbed hydrogen was represented by 2 nm thick layer with higher conductivity, extending 70 nm past the edge of the contacts.

The bulk conductivity value was set to $\sigma_b = 40\ \Omega^{-1}m^{-1}$; the conductivity value in the desorbed patch was adujsted so as to reproduce the experimental results. A value of 10^5 $\Omega^{-1}m^{-1}$ was used in the 2 nm thick patch, corresponding to a 2D sheet conductivity of $\sigma_s = t\sigma_b = 2 \times 10^{-4}$ $\Omega^{-1}/\Box$. The calculated surface potential is shown in Figure 10.11(b). Within the higher surface conductivity patches, the potential appears nearly flat. A cross-section taken in the area shows a nearly linear 0.006 V change in potential — this corresponds closely to the 0.007 change in F_A seen experimentally. Past the desorbed patch, the behavior of F_A in the simulation is comparable to the experiment, except that it starts from a value of 0 rather than near 0.35.

This model makes several approximations: the metallic contacts are assumed to be ohmic; no tip-induced band bending in the silicon is included. The Si(111)-7×7 surface conductivity value obtained with this model, 2×10^{-4} $\Omega^{-1}/\Box$, is at the high range of conductivities reported in the literature [6]; it is also higher than that estimated by us from molecular dosing experiments in Chapter 9.

10.7 STFCI on the Si(111)-7×7 Surface

Figure 10.12 shows STM images taken in STFCI mode of terraces of Si(111)-7×7 close to one of the EBL-defined metal contacts (contact B). First, we note how the topography image in Figure 10.12(a) shows bunches of several steps; this was repeatedly observed after annealing Ti contacts on low-doped n-type Si(111); see for example Figure 7.10(b). Curiously, much fewer steps between the contacts were observed for annealed low-doped p-type samples, with all other characteristics nearly identical. The reason for this is unknown.

The fractional current image obtained is shown in Figure 10.12(b), and a cross-section of both Z and F_A is shown in Figure 10.12(c). First, we note the stepwise change of F_A on each individual terrace. The large terraces show a small slope (e.g. a change of 0.015 across terrace 1), but the largest part of the gradient taking F_A from 0.4 to 0.8 occurs at the step bunch regions. This tells us that bunches of steps on the Si(111)-7×7 surface are significiantly more resistive than the surface itself.

Let us note that the value of F_A in the step bunch regions (which are highlighted by the gray bars in Figure 10.12(c)) is not reliable because the tunneling current was higher than in flat regions due to slow feedback loop response as the tip moved from left to right. F_A is the same on the flat terraces in both the forward and backward scan directions, but at steps it is different; it should be disregarded in those regions.

Another interesting feature of the image is that the change in F_A is not monotonic as the tip moves from contact B (close to the left edge of the image) closer to contact

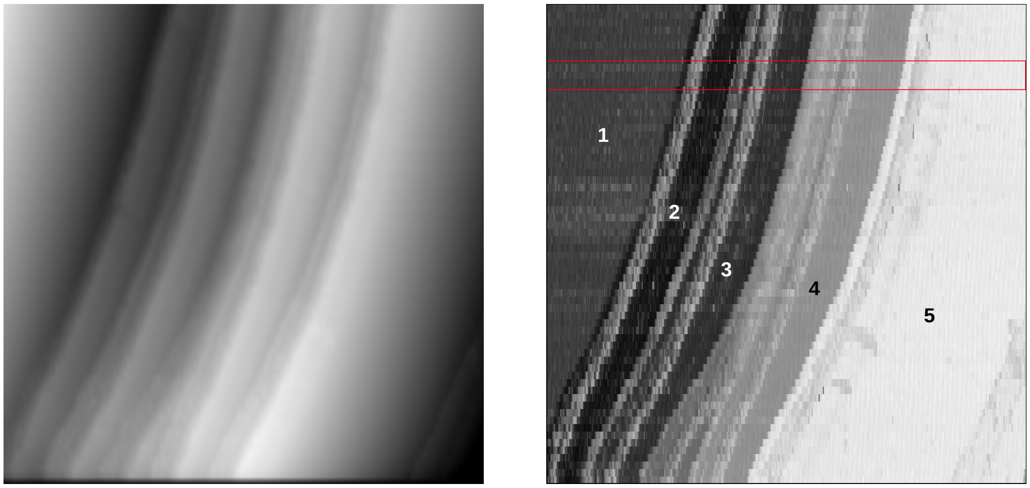

(a) Topography.

(b) F_A, color scale 0.3 to 0.8. Some of the terraces have been labeled 1 through 5.

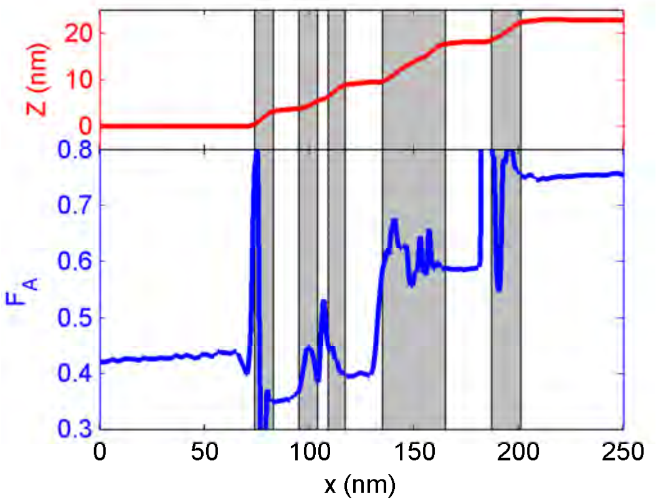

(c) Cross-section of z (above) and F_A (below) along the red bar in (b). 15-nm wide averaging. The gray bars indicate step bunch regions.

Figure 10.12: STFCI images of several terraces of Si(111)-7×7 separated by bunches of several steps. Contact B is close to the left edge of the images; contact A is far (∼1 μm) to the upper right.

A, towards the upper right. Terraces 2 and 3 have F_A values lower than that of terrace 1, which is actually closer to contact B and therefore should have a lower F_A. This effect is similar to that reported in Ref. [153] and reproduced in Figure 10.2 for Si(111)-($\sqrt{3} \times \sqrt{3}$)-Ag terraces: the fractional current at each terrace depends on the percolation network of resistances that reach each contact. Terraces 2 and 3 are smaller and surrounded by large step-bunching regions, which perhaps resistively isolated them from contact A more than terrace 1.

10.8 STFCI of Single Steps on the Si(111)-7×7 Surface

10.8.1 Introduction

We saw in the previous section that terraces with a 7×7 reconstruction were significantly more conductive than step-bunch regions, where we observed large changes in fractional current. In Section 10.3, we reviewed results showing measurements of the resistance of a monoatomic Si step for the Si(111)-($\sqrt{3} \times \sqrt{3}$)-Ag surface; to the best of our knowledge, no measurement of the resistance of a Si(111)-7×7 step has been reported. Since the Si(111)-($\sqrt{3} \times \sqrt{3}$)-Ag surface is more conductive than 7×7 by orders of magnitude, this is perhaps not surprising.

In this section, we will show that STFCI is sufficiently sensitive to resolve the change in fractional current occuring at a single atomic step on Si(111)-7×7.

10.8.2 Measurements

We saw in Section 10.7 that when annealing crystals with EBL-defined Ti contacts, a large number of steps would form between the contacts, usually in “bunches” of several steps. Single monoatomic steps were difficult to find, therefore we used a different technique to perform STFCI experiments on single Si(111) steps. A Si(111)-7×7 surface was prepared in a usual manner, with no EBL-defined contacts. The left and right probe tips were brought into contact with the surface, as shown in Figure 10.13.

The two probes were directly used as current-measuring contacts A and B. The right probe was brought into close proximity to the STM tip, and touched down to the surface, forming contact B. The left probe was placed ∼100 μm away from the STM tip, forming contact A. Electrical connections were made in the same way shown in Figure 10.3(b).

After locating the position of contact B with the STM tip, a large scan in STFCI mode was taken (Figure 10.14). There was significant contamination forming islands

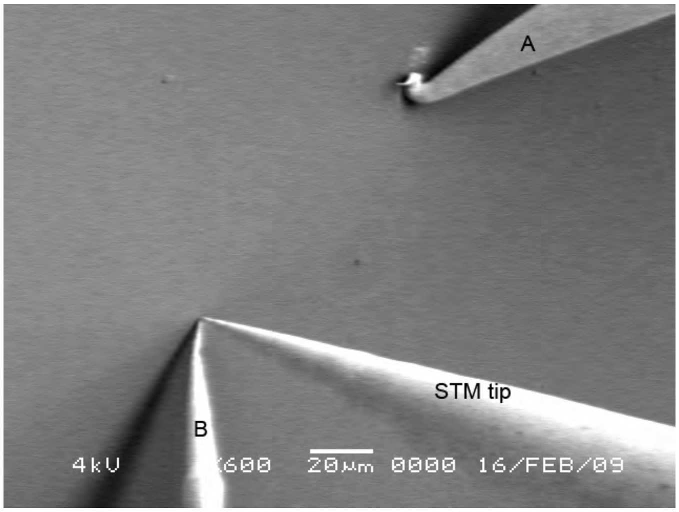

Figure 10.13: SEM image of the positions of the tips in the STFCI experiment. The contacts and STM tip are indicated.

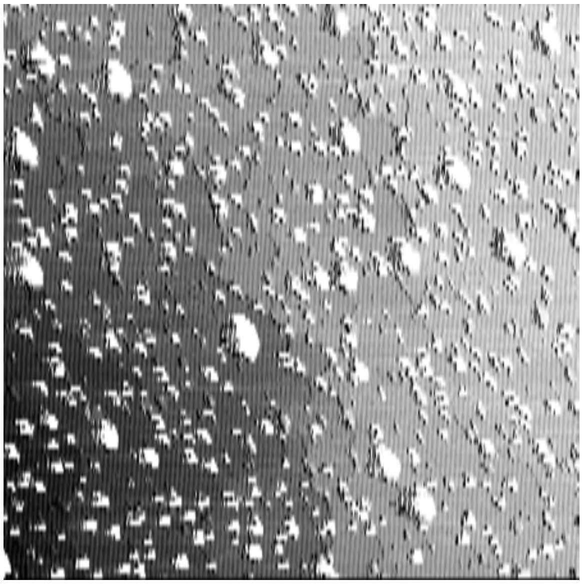

Figure 10.14: F_A image taken with the contacts made by touching down the tips directly on a low-doped, n-type Si(111)-7×7 surface. 1 μm wide, +2 V, 300 pA, color scale 0.02 to 0.22. Contact B is made near the lower left corner.

on the surface; these appear as bright spots in the F_A image and should be ignored. In a way consistent with a spreading resistance model, a F_A value near 0 is observed close to contact B, increasing as the STM tip moves away, up to ∼0.25 some distance away.

10.8.3 Resistance of Steps

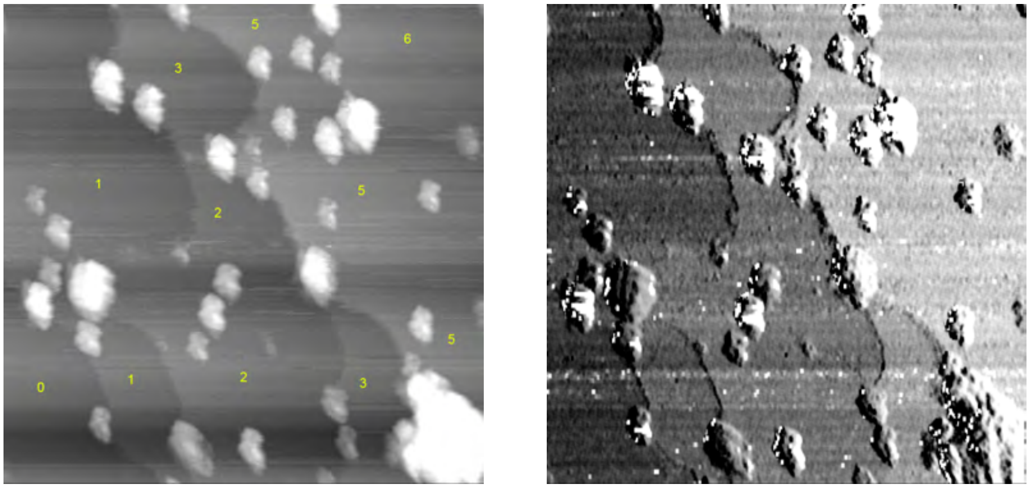

(a) Topography. The numbers indicate the height, in monoatomic Si(111) steps, of each terrace.

(b) F_A image. Color scale: 0.08 to 0.16.

Figure 10.15: STFCI experiment images showing a few steps on Si(111)-7×7. 250 nm, +2 V, 300 pA.

Figure 10.15 shows a close-up view of a region with a few single, double and triple steps. The F_A image clearly shows that most of the change in F_A occurs at the step edges — even for monoatomic steps. Double or triple steps show an even clearer change in F_A. This shows that even monoatomic steps on the Si(111)-7×7 surface are significantly more resistive than the surface itself.

Figure 10.16 shows a STFCI scan taken on a frame with a single monoatomic Si(111) step separating two terraces. The difference in the F_A value between the left and right terraces is easily visible in Figure 10.16(b). The cross-section in Figure 10.16(c) shows that the change in F_A was of 0.015. The slope on the terrace is much smaller, again indicating that a single step is more resistive than the 7×7 terrace.

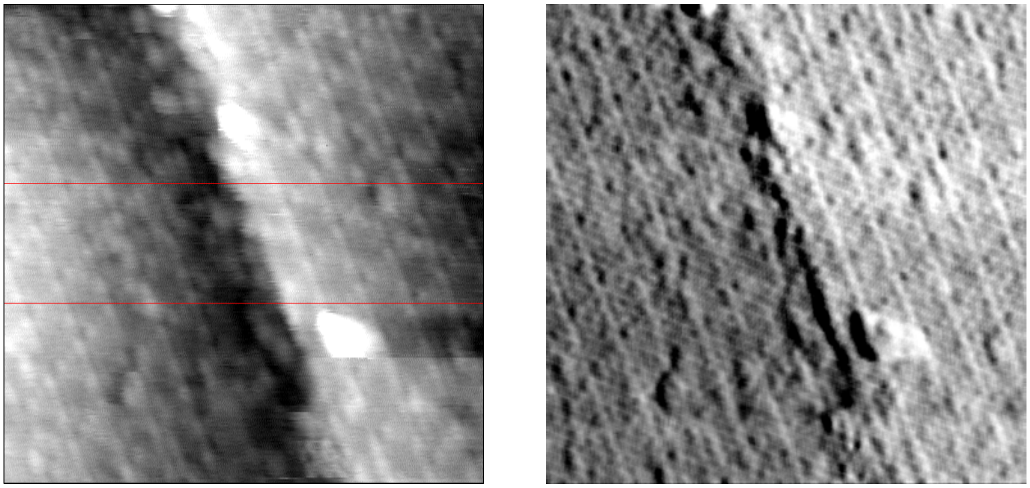

(a) Topography: 20 nm, +2 V, 300 pA.

(b) F_A, color scale 0.06 to 0.11.

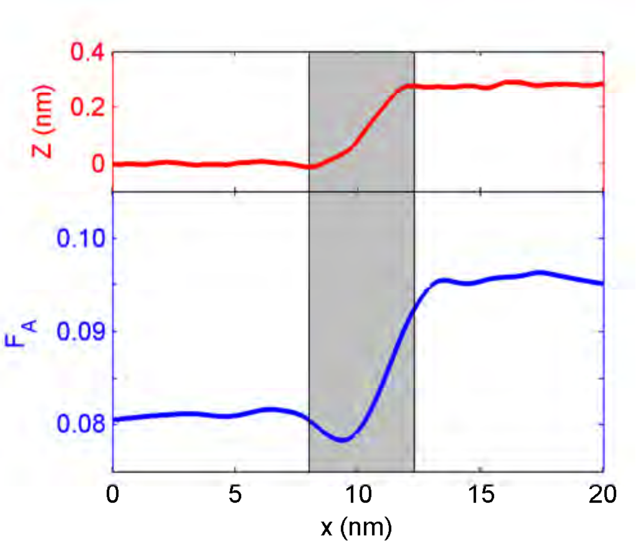

(c) Cross-section of z (above) and F_A (below) along the red bar in (a). 5-nm wide averaging, 5-nm smoothing. The gray bar indicates the region around the step.

Figure 10.16: STFCI images of a single monoatomic step on a Si(111)-7×7 surface.

10.8.4 Effect of Dosing Molecules

We have seen in Section 9.5, page 174, that dosing organic molecules that bond to the Si(111)-7×7 surface disrupts its 2D conductivity. If we quell surface conductance in this way, we would expect to see the importance of the resistivity of steps to be reduced in STFCI images. The result of such an experiment is shown in Figure 10.17. The STFCI images were acquired after a 10 L dose of 1,2,4-trimethylbenzene, a molecule which we previously found to reduce the probe-to-probe conductance by up to 99.8%. Unfortunately, high-quality images were more difficult to obtain than with unreacted 7×7; this may be due to the reduced conductivity of the surface, which would force the tip to be closer to the surface in order to maintain the same tunneling current. A reduced tip-sample distance makes the tip more susceptible to damage.

In the F_A image shown in Figure 10.17(b), the terrace on the upper right does appear significantly brighter (large F_A than the nearby terraces). This terrace is separated by a step bunch region of height of 3 monoatomic steps. However, the cross-section shown in Figure 10.17(c) shows that there is no discontinuity in F_A at a single step; rather, F_A linearly changes by ~ 0.012 over the 80 nm length of the cross-section. However, when the cross-section is extended to cover the nearby triple step, a sudden change in F_A of around 0.03 is seen there. It appears that despite having lower surface conductivity, multiple steps still cause a stepwise change in F_A.

10.8.5 Conclusions

We have seen several experimental STFCI results that show the relative conductivity of atomic steps vs. the Si(111)-7×7 surface. A clear change in F_A at steps was observed, even for single atomic steps; to the best of our knowledge, this is the first measurement that directly shows the resistance of a single monoatomic step on the Si(111)-7×7 surface. Dosing an organic molecule was found to quell the surface states which offer increased surface conductivity, thereby reducing the stepwise change in F_A at single steps. Multiple steps still showed some stepwise change, however.

Unfortunately, it is not possible to directly obtain a value for the resistance of a step using the STFCI method. Only *relative* conductivities can be observed using a map of F_A — specifically, the gradient of F_A will show the resistivity. To model the resistance of a step, an accurate measurement of the conductivity of a Si(111)-7×7 *without* any steps would be required; such a value is not known. There is considerable disagreement in the literature as to the value of Si(111)-7×7 surface

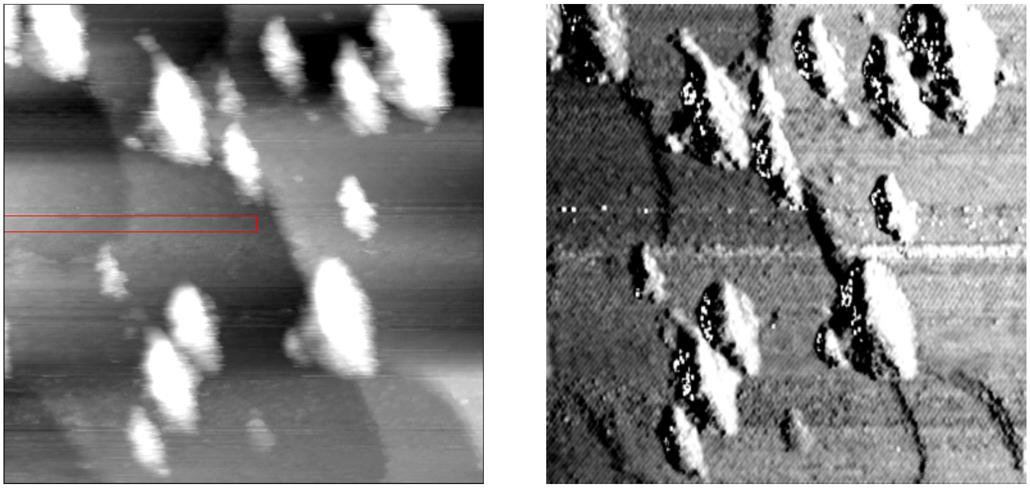

(a) Topography: 150 nm, +2 V, 300 pA.

(b) F_A, color scale 0.10 to 0.18.

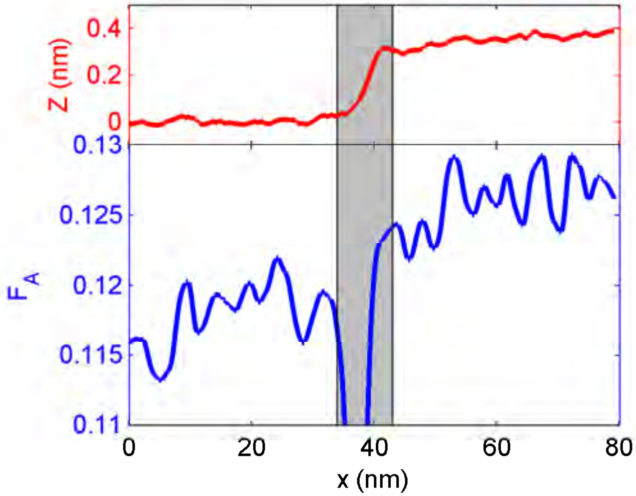

(c) Cross-section of z (above) and F_A (below) along the red bar in (a). 5-nm wide averaging, 5-nm smoothing. The gray bar indicates the region around the step.

Figure 10.17: STFCI images of a few steps on a Si(111)-7×7 surface dosed with 10 L of 1,2,4-trimethylbenzene.

conductivity [149]; given the importance of step resistance, the disagreement may be at least partially due to the fact that step density was not typically measured or even considered in previous Si(111)-7×7 surface conductivity measurements.

10.9 STFCI of Steps on H-Si(111)-1×1

Figure 10.18 shows a STFCI experiment on a H-Si(111)-1×1 surface. The smooth variation of F_A along single terraces shown in Figure 10.18(b) is quite different from the sudden change at steps seen on Si(111)-7×7 surfaces. The z and F_A cross-sections in Figure 10.18(c) highlight how F_A varies smoothly; it has a gentle curve and no step-wise change at steps. This demonstrates that this surface is not conductive; steps do not interrupt conductance since electron transport occurs primarily through the bulk of the material, not along the surface.

An interesting feature emerges if one observes the F_A image in Figure 10.18(b) closely: along the step edges on the left side of the image, dark bands in F_A are visible. The bands are present on the right side of each step — i.e. on the lower terrace. The same bands with the same pattern are visible in both the forward and backward scan directions, therefore they are not artefacts of a slow feedback loop or of tip changes.

The dark bands in F_A indicate that at these spots, less current flows to contact A (towards the upper right) than in the surrounding area. It is interesting to note that the two steps on the right side of the image do not show such bands; these steps are oriented along the axis formed by contacts A and B, whereas the steps with bands are roughly perpendicular to that axis.

The explanation for these dark bands, which show a non-monotonic change in F_A, is elusive. A patch of high-resistance "dirt" at the surface could cause this by effectively increasing the gap resistance and changing the voltage developed at the surface under the tip. It is unclear why such "dirt" would be present only on one side of particular step edges. Perhaps electrons are scattered by the step edges, ballistically directing more of them towards contact B than would otherwise occur. Unfortunately, the image quality was not very high, and no higher-resolution images of those steps were taken; we attempted to reproduce this observation but have not observed it yet. The technical challenges of obtaining a high-quality H-Si(111)-1×1 surface with metal contacts, and of setting up the STFCI experiment make it difficult to reproduce.

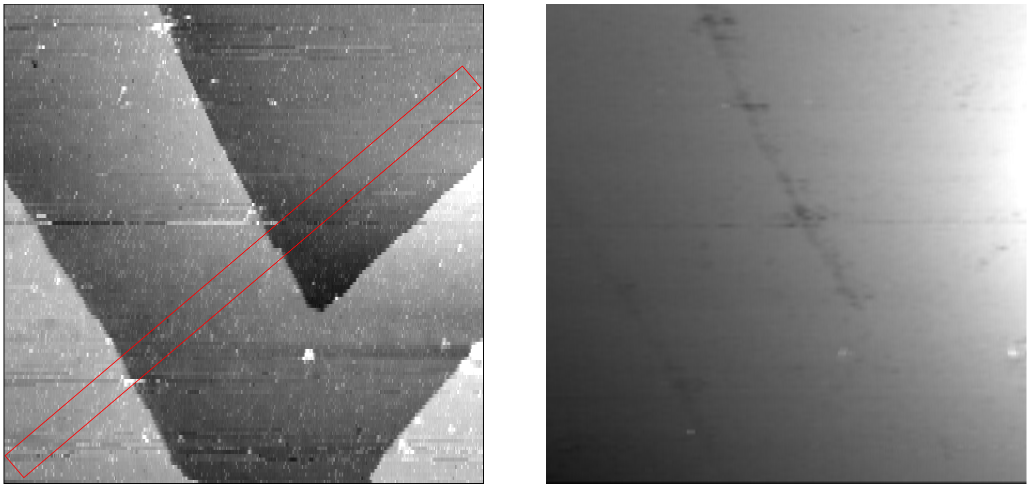

(a) Topography: 250 nm, +2 V, 300 pA.

(b) F_A, color scale 0.55 to 0.85.

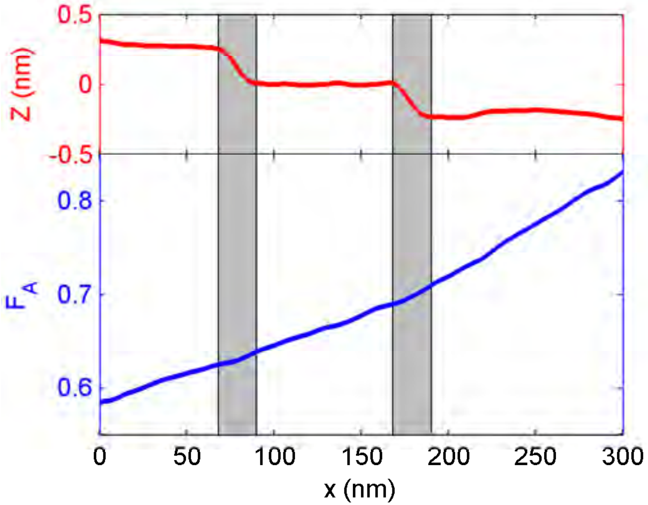

(c) Cross-section of z (above) and F_A (below) along the red bar in (a). 15-nm wide averaging, 10-nm smoothing. The gray bars indicates the region around each step.

Figure 10.18: STFCI images of a few steps on a H-Si(111)-1×1 surface. Contact A is near the upper-right corner; contact B is near the lower-left corner.

10.10 Conclusions

We began this chapter by presenting published results of scanning tunneling potentiometry (STP), which measures the potential under the STM tip with an applied bias between two contacts on a surface. Measurements of the resistance of steps on the Si(111)-($\sqrt{3} \times \sqrt{3}$)-Ag surface, which shows very high surface conductivity, were shown, but no such measurements of the resistance of steps on the Si(111)-7×7 were found in the literature.

We then present a novel technique, scanning tunneling fractional current imaging (STFCI) which is closely related to STP. The experimental technique was described, and the results of STFCI were calculated to be equivalent to STP in some circumstances. STFCI measurements on H-Si(111)-1×1 were shown to be qualitatively similar to FEM simulations. On a Si(111)-7×7 surface with EBL-defined Ti contacts, "bunches" of multiple steps were found to be the location of the largest change in F_A — indicating that step bunches are much more resistive than the 7×7 surface itself. With the probes directly touching the surface, we were able to resolve the change in F_A of single atomic steps of Si(111), and found a change of 0.015; multiple steps showed correspondingly larger changes, confirming that single steps on the Si(111)-7×7 surface are significantly more resistive than the surface itself. Dosing a reactive molecule removed the effect of single steps by removing the surface conductivity; some step change in F_A was still observed, however, at multiple steps. Si(111) terminated by hydrogen through wet chemical means show no higher resistance at steps, since that surface is not conductive.

Chapter 11

Conclusions

The goal of this work was to advance knowledge of nanometer-scale connections to semiconductor surfaces. The work can be divided in two broad parts: self-assembled organic nanostructures on silicon surfaces, and the study of surface conductivity using a new, multiple-probe STM instrument.

The first chapters dealt with molecular lines on silicon. Chapter 2 described FEM simulations useful in characterizing the charge state of dangling bonds on a H-terminated Si surface. Chapter 3 summarized published molecular line growth, and described the growth of several new molecules. When a molecule that grows across dimer rows on H-Si(100)-2×1, allylmercaptan, was found, this motivated us to find other molecules with such a growth direction. We investigated many different molecules and found a few that did not grow lines and many that did. The pattern of line growth depends strongly on the type of molecule dosed. Among the new line-growing molecules we discovered was trimethylene sulfide, which bonds to a silicon surface differently depending on the doping level of the crystal (which controls the charge of DBs). Butadiene and 1,3-dimethylbutadiene showed interesting differences in their growth patterns, which we attributed to steric interactions between the molecule and the surface. Trimethylene sulfide growth following styrene growth on H-Si(100)-3×1 formed the first contiguous, self-formed, “L-shaped” molecular lines. We also presented results on the harmful effects of ion pump-generated radicals on the quality of a hydrogen-terminated Si surface.

Chapter 4 dealt with a project where the aim was to observe excitation energy transfer (EET) along a molecular line on a surface; EET was suggested as a novel way to transmit information on the nanoscale. The experimental apparatus needed to detect photon emission from the STM and some initial results were shown; this project was unsuccessful due to low signal intensities, among other problems.

In chapters 5 and 6, we described a novel instrument: a multiple-probe STM equipped with 3 fully scannable STM tips capable of atomic resolution imaging. A suite of software was written to control the instruments and to allow useful customization and capabilities not available with the supplied commercial control software. To reliably make contacts at sub-micron distances, this machine was combined with the e-beam lithography technology described in chapter 7. A significant feature of the technology we developed was the capability of obtaining continuous metallic pads directly in contact with very high-quality Si(100)-2×1, H-Si(100)-2×1, H-Si(111)-1×1, or Si(111)-7×7 surfaces.

The combination of the multiple-probe STM and the EBL-defined contacts allowed us to perform a difficult experiment known as the "molecular Etch-a-Sketch", described in chapter 8. In the experiment, we used electric fields to direct molecular line growth on Si, by aligning the dipole moment of the addition radical before it abstracts a nearby H atom. A molecule that grows lines exclusively along dimer rows under normal conditions, 3-trifluoromethylstyrene, was found to grow across dimer rows when an electric field was applied on a H-Si(100)-2×1 surface. The Joule heating caused by flowing current through the semiconductor was found to be a significant complication, possibly hindering line growth in general. Results on H-Si(111)-1×1 were not conclusive.

As device sizes shrink, the electron transport properties of surfaces become more significant; therefore we used the exceptional capabilities of our EBL-defined contacts and the multiple-probe STM to investigate the surface conductivity of Si surfaces in the last two chapters. Chapter 9 used IV curve measurements between two EBL-defined contacts to obtain a measure of the surface conductivity of the Si(111)-7×7 surface. Dosing organic molecules to this surface was found to disrupt the surface states responsible for 2D conductivity, reducing the probe-to-probe conductance by up to 99.8%. This was used to "sense" molecular coverage as small as $1/2500^{\text{th}}$ of a monolayer.

Finally, chapter 10 showed results of scanning tunneling fractional current imaging (STFCI), a novel technique analogous to scanning tunneling potentiometry. Experiment and theory were compared and showed good qualitative agreement. Using STFCI on a patch of desorbed hydrogen on a H-Si(111)-1×1 surface, the surface conductivity of Si(111)-7×7 could be imaged directly and shown to be significant larger than that of a terminated Si(111) surface. The effect of atomic steps in the surface conductivity of Si(111)-7×7 was investigated, and it was shown that steps are significantly more resistive than the 7×7 surface alone. Although we could not quantitatively measure the step resistance on 7×7, this is to our knowledge the first direct observation of their resistance.

In conclusion, we used a variety of tools and techniques to investigate how to perform nanometer-scale contacts to silicon surfaces. Self-assembled molecular lines enable one to make nano-scale structures in a massively parallel way on silicon surfaces. Our work extended our knowledge of the type of line growth achievable with several new molecules, made the first contiguous "L-shaped" molecular lines, and used electric fields to direct lines. We also developed a multiple-probe STM, its control software, and a technology to defind metal contacts using EBL while preserving very high quality surfaces. This allowed us to measure the surface conductivity of Si(111)-7×7, and to resolve the effect of steps on this surface using a novel technique, scanning tunneling fractional current imaging.

Bibliography

[1] G. Binnig, H. Rohrer, C. Gerber, and E. Weibel. Tunneling through a controllable vacuum gap. *Applied Physics Letters*, 40(2):178, 1981.

[2] Jack S. Kilby. Miniaturized electronic circuits, U.S. patent 3,138,743, 1959.

[3] G. E. Moore. Cramming more components onto integrated circuits. *Electronics*, 38(8):114–117, 1965.

[4] Peter Perlsoe. Intel CPUs, an overview (http://titancity.com/arti cles/intel.html), July 16th, 2007.

[5] ITRS. International technology roadmap for semiconductors (http://www.itrs.net/home.html), 2007.

[6] P. Hofmann and J. W. Wells. Surface-sensitive conductance measurements. *Journal of Physics-Condensed Matter*, 21(1):013003, 2009.

[7] R. M. Feenstra. Electrostatic potential for a hyperbolic probe tip near a semiconductor. *Journal of Vacuum Science & Technology B*, 21(5):2080–2088, 2003.

[8] R. M. Feenstra, S. Gaan, G. Meyer, and K. H. Rieder. Low-temperature tunneling spectroscopy of Ge(111)-(2x8) surfaces. *Physical Review B*, 71(12):125316, 2005.

[9] R. Seiwatz and M. Green. Space charge calculations for semiconductors. *Journal of Applied Physics*, 29(7):1034–1040, 1958.

[10] J. Shewchun, A. Waxman, and G. Warfield. Tunneling in MIS structures .I. theory. *Solid-State Electronics*, 10(12):1165, 1967.

[11] S. M. Sze. *Physics of semiconductor devices.* Wiley, New York, 2nd edition, 1981.

[12] L Liu, J Yu, and J W Lyding. Scanning tunneling microscopy observation of single dangling bonds on the Si(100)2x1:H surface. *MRS Proceedings*, 705:187, 2002.

[13] J. J. Boland. Role of bond-strain in the chemistry of hydrogen on the Si(100) surface. *Surface Science*, 261(1-3):17–28, 1992.

[14] COMSOL. Comsol multiphysics 3.3 (computer program), comsol inc., 2007.

[15] P. G. Piva, G. A. DiLabio, J. L. Pitters, J. Zikovsky, M. Rezeq, S. Dogel, W. A. Hofer, and R. A. Wolkow. Field regulation of single-molecule conductivity by a charged surface atom. *Nature*, 435(7042):658–661, 2005.

[16] G. P. Lopinski, D. D. M. Wayner, and R. A. Wolkow. Self-directed growth of molecular nanostructures on silicon. *Nature*, 406(6791):48–51, 2000.

[17] D. M. Eigler and E. K. Schweizer. Positioning single atoms with a scanning tunneling microscope. *Nature*, 344(6266):524–526, 1990.

[18] M. R. Linford, P. Fenter, P. M. Eisenberger, and C. E. D. Chidsey. Alkyl monolayers on silicon prepared from 1-alkenes and hydrogen-terminated silicon. *Journal of the American Chemical Society*, 117(11):3145–3155, 1995.

[19] G. A. DiLabio, P. G. Piva, P. Kruse, and R. A. Wolkow. Dispersion interactions enable the self-directed growth of linear alkane nanostructures covalently bound to silicon. *Journal of the American Chemical Society*, 126(49):16048–16050, 2004.

[20] R. L. Cicero, C. E. D. Chidsey, G. P. Lopinski, D. D. M. Wayner, and R. A. Wolkow. Olefin additions on H-Si(111): evidence for a surface chain reaction initiated at isolated dangling bonds. *Langmuir*, 18(2):305–307, 2002.

[21] X. Tong, G. A. DiLabio, and R. A. Wolkow. A self-directed growth process for creating covalently bonded molecular assemblies on the H-Si(100)-3x1 surface. *Nano Letters*, 4(5):979–983, 2004.

[22] G. Kirczenow, P. G. Piva, and R. A. Wolkow. Linear chains of styrene and methylstyrene molecules and their heterojunctions on silicon: theory and experiment. *Physical Review B*, 72(24):245306, 2005.

[23] P. G. Piva, R. A. Wolkow, and G. Kirczenow. Nonlocal conductance modulation by molecules: scanning tunneling microscopy of substituted

styrene heterostructures on H-terminated Si(100). *Physical Review Letters*, 101(10):106801, 2008.

[24] M. Z. Hossain, H. S. Kato, and M. Kawai. Competing forward and reversed chain reactions in one-dimensional molecular line growth on the Si(100)-(2 x 1)-H surface. *Journal of the American Chemical Society*, 129(11):3328–3332, 2007.

[25] J. L. Pitters, I. Dogel, G. A. DiLabio, and R. A. Wolkow. Linear nanostructure formation of aldehydes by self-directed growth on hydrogen-terminated silicon(100). *Journal of Physical Chemistry B*, 110(5):2159–2163, 2006.

[26] X. Tong, G. A. DiLabio, O. J. Clarkin, and R. A. Wolkow. Ring-opening radical clock reactions for hybrid organic-silicon surface nanostructures: a new self-directed growth mechanism and kinetic insights. *Nano Letters*, 4(2):357–360, 2004.

[27] P. Kruse, E. R. Johnson, G. A. DiLabio, and R. A. Wolkow. Patterning of vinylferrocene on H-Si(100) via self-directed growth of molecular lines and STM-induced decomposition. *Nano Letters*, 2(8):807–810, 2002.

[28] Z. Hossain, H. S. Kato, and M. Kawai. Controlled fabrication of 1d molecular lines across the dimer rows on the Si(100)-(2x1)-H surface through the radical chain reaction. *Journal of the American Chemical Society*, 127(43):15030–15031, 2005.

[29] J. Y. Lee and J. H. Cho. Self-directed growth of benzonitrile line on H-terminated Si(001) surface. *Journal of Chemical Physics*, 121(16):8010–8013, 2004.

[30] S. A. Dogel, G. A. DiLabio, J. Zikovsky, J. L. Pitters, and R. A. Wolkow. Experimental and theoretical studies of trimethylene sulfide-derived nanostructures on p- and n-type H-silicon(100)-2 x 1. *Journal of Physical Chemistry C*, 111(32):11965–11969, 2007.

[31] M. Z. Hossain, H. S. Kato, and M. Kawai. Fabrication of interconnected 1d molecular lines along and across the dimer rows on the Si(100)-(2 x 1)-H surface through the radical chain reaction. *Journal of Physical Chemistry B*, 109(49):23129–23133, 2005.

[32] M. J. Frisch, G. W. Trucks, H. B. Schlegel, G. E. Scuseria, M. A. Robb, J. R. Cheeseman, Jr. Montgomery, J. A., T. Vreven, K. N. Kudin, J. C. Burant,

J. M. Millam, S. S. Iyengar, J. Tomasi, V. Barone, B. Mennucci, M. Cossi, G. Scalmani, N. Rega, G. A. Petersson, H. Nakatsuji, M. Hada, M. Ehara, K. Toyota, R. Fukuda, J. Hasegawa, M. Ishida, T. Nakajima, Y. Honda, O. Kitao, H. Nakai, M. Klene, X. Li, J. E. Knox, H. P. Hratchian, J. B. Cross, C. Adamo, J. Jaramillo, R. Gomperts, R. E. Stratmann, O. Yazyev, A. J. Austin, R. Cammi, C. Pomelli, J. W. Ochterski, P. Y. Ayala, K. Morokuma, G. A. Voth, P. Salvador, J. J. Dannenberg, V. G. Zakrzewski, S. Dapprich, A. D. Daniels, M. C. Strain, O. Farkas, D. K. Malick, A. D. Rabuck, K. Raghavachari, J. B. Foresman, J. V. Ortiz, Q. Cui, A. G. Baboul, S. Clifford, J. Cioslowski, B. B. Stefanov, G. Liu, A. Liashenko, P. Piskorz, I. Komaromi, R. L. Martin, D. J. Fox, T. Keith, M. A. Al-Laham, C. Y. Peng, A. Nanayakkara, M. Challacombe, P. M. W. Gill, B. Johnson, W. Chen, M. W. Wong, C. Gonzalez, and J. A. Pople. Gaussian 03, revision C.02 (computer program), gaussian inc., 2003.

[33] J. Zikovsky, S. A. Dogel, M. B. Haider, G. A. DiLabio, and R. A. Wolkow. Self-directed growth of contiguous perpendicular molecular lines on H-Si(100) surfaces. *Journal of Physical Chemistry A*, 111(49):12257–12259, 2007.

[34] J. J. Boland. Scanning-tunneling-microscopy of the interaction of hydrogen with silicon surfaces. *Advances in Physics*, 42(2):129–171, 1993.

[35] J. Zikovsky, S. A. Dogel, S. Sinha, G. A. DiLabio, and R. A. Wolkow. Scanning tunneling microscopy and computational study of the self-directed growth of 1,3-butadiene and 2,3-dimethyl-1,3-butadiene on hydrogen-terminated silicon(100)-2 x 1. *Chemical Physics Letters*, 458(1-3):117–121, 2008.

[36] A. Sato, S. Yamashita, and H. Kawarada. Scanning tunneling microscopy and spectroscopy for studying hydrogen-terminated homoepitaxial diamond surfaces. *Silicon Carbide and Related Materials 1995*, 142:1099–1102, 1996.

[37] E. R. Johnson and G. A. DiLabio. Theoretical study of dispersion binding of hydrocarbon molecules to hydrogen-terminated silicon(100)-2x1. *Journal of Physical Chemistry C*, 113(14):5681–5689, 2009.

[38] J. Zikovsky, S. A. Dogel, A. J. Dickie, J. L. Pitters, and R. A. Wolkow. Reaction of a hydrogen-terminated Si(100) surface in UHV with ion-pump generated radicals. *Journal of Vacuum Science & Technology A: Vacuum, Surfaces, and Films*, 27(2):248–252, 2009.

[39] Varian. Ion pumps catalog (http://www.varianinc.com/image/vimage/docs/products/vacuum/pumps/ion/shared/ion-catalog.pdf), May 1st, 2009.

[40] NIST. Nist chemistry webbook (http://webbook.nist.gov/chemistry/), April 17th, 2008.

[41] M. H. Hablanian. *High-vacuum technology: a practical guide, 2nd edition.* Marcel Dekker, New York, 2nd edition, 1997.

[42] I. A. Dogel, S. A. Dogel, J. L. Pitters, G. A. DiLabio, and R. A. Wolkow. Chemical methods for the hydrogen termination of silicon dangling bonds. *Chemical Physics Letters*, 448(4-6):237–242, 2007.

[43] J. L. Pitters, P. G. Piva, X. Tong, and R. A. Wolkow. Reversible passivation of silicon dangling bonds with the stable radical tempo. *Nano Letters*, 3(10):1431–1435, 2003.

[44] P. Vettiger, M. Despont, U. Drechsler, U. Durig, W. Haberle, M. I. Lutwyche, H. E. Rothuizen, R. Stutz, R. Widmer, and G. K. Binnig. The "millipede" - more than one thousand tips for future afm data storage. *Ibm Journal of Research and Development*, 44(3):323–340, 2000.

[45] M. C. Hersam, N. P. Guisinger, and J. W. Lyding. Isolating, imaging, and electrically characterizing individual organic molecules on the Si(100) surface with the scanning tunneling microscope. *Journal of Vacuum Science & Technology A*, 18(4):1349–1353, 2000.

[46] R. Livingston. Intermolecular transfer of electronic excitation. *Journal of Physical Chemistry*, 61(7):860–864, 1957.

[47] T. Forster. 10th Spiers memorial lecture - transfer mechanisms of electronic excitation. *Discussions of the Faraday Society*, 27:7–17, 1959.

[48] G. D. Scholes. Long-range resonance energy transfer in molecular systems. *Annual Review of Physical Chemistry*, 54:57–87, 2003.

[49] D. L. Dexter. A theory of sensitized luminescence in solids. *Journal of Chemical Physics*, 21(5):836–850, 1953.

[50] X. C. Hu and K. Schulten. How nature harvests sunlight. *Physics Today*, 50(8):28–34, 1997.

[51] X. C. Hu, T. Ritz, A. Damjanovic, and K. Schulten. Pigment organization and transfer of electronic excitation in the photosynthetic unit of purple bacteria. *Journal of Physical Chemistry B*, 101(19):3854–3871, 1997.

[52] T. Hori, N. Aratani, A. Takagi, T. Matsumoto, T. Kawai, M. C. Yoon, Z. S. Yoon, S. Cho, D. Kim, and A. Osuka. Giant porphyrin wheels with large electronic coupling as models of light-harvesting photosynthetic antenna. *Chemistry-a European Journal*, 12(5):1319–1327, 2006.

[53] M. Sykora, K. A. Maxwell, J. M. DeSimone, and T. J. Meyer. Mimicking the antenna-electron transfer properties of photosynthesis. *Proceedings of the National Academy of Sciences of the United States of America*, 97(14):7687–7691, 2000.

[54] S. E. Webber. Photon-harvesting polymers. *Chemical Reviews*, 90(8):1469–1482, 1990.

[55] C. M. Atienza, G. Fernandez, L. Sanchez, N. Martin, I. S. Dantas, M. M. Wienk, R. A. J. Janssen, G. M. A. Rahman, and D. M. Guldi. Light harvesting tetrafullerene nanoarray for organic solar cells. *Chemical Communications*, 5:514–516, 2006.

[56] A. J. Bard and M. A. Fox. Artificial photosynthesis - solar splitting of water to hydrogen and oxygen. *Accounts of Chemical Research*, 28(3):141–145, 1995.

[57] T. J. Meyer. Chemical approaches to artificial photosynthesis. *Accounts of Chemical Research*, 22(5):163–170, 1989.

[58] J. H. Alstrum-Acevedo, M. K. Brennaman, and T. J. Meyer. Chemical approaches to artificial photosynthesis. 2. *Inorganic Chemistry*, 44(20):6802–6827, 2005.

[59] D. Gust, T. A. Moore, and A. L. Moore. Mimicking photosynthetic solar energy transduction. *Accounts of Chemical Research*, 34(1):40–48, 2001.

[60] Y. Kobuke. Artificial light-harvesting systems by use of metal coordination. *European Journal of Inorganic Chemistry*, 12:2333–2351, 2006.

[61] H. Salman, Y. Eichen, and S. Speiser. A molecular scale full adder based on controlled intramolecular electron and energy transfer. *Materials Science & Engineering C-Biomimetic and Supramolecular Systems*, 26(5-7):881–885, 2006.

[62] S. A. Crooker, J. A. Hollingsworth, S. Tretiak, and V. I. Klimov. Spectrally resolved dynamics of energy transfer in quantum-dot assemblies: towards engineered energy flows in artificial materials. *Physical Review Letters*, 89(18):186802, 2002.

[63] T. A. Klar, T. Franzl, A. L. Rogach, and J. Feldmann. Super-efficient exciton funneling in layer-by-layer semiconductor nanocrystal structures. *Advanced Materials*, 17(6):769–773, 2005.

[64] J. K. Gimzewski, B. Reihl, J. H. Coombs, and R. R. Schlittler. Photon-emission with the scanning tunneling microscope. *Zeitschrift Fur Physik B-Condensed Matter*, 72(4):497–501, 1988.

[65] D. L. Abraham, A. Veider, C. Schonenberger, H. P. Meier, D. J. Arent, and S. F. Alvarado. Nanometer resolution in luminescence microscopy of III-V heterostructures. *Applied Physics Letters*, 56(16):1564–1566, 1990.

[66] R. Berndt, R. R. Schlittler, and J. K. Gimzewski. Photon-emission scanning tunneling microscope. *Journal of Vacuum Science & Technology B*, 9(2):573–577, 1991.

[67] R. Berndt, R. Gaisch, J. K. Gimzewski, B. Reihl, R. R. Schlittler, W. D. Schneider, and M. Tschudy. Photon-emission at molecular resolution induced by a scanning tunneling microscope. *Science*, 262(5138):1425–1427, 1993.

[68] L. Samuelson, J. Lindahl, L. Montelius, and M. E. Pistol. STM induced luminescence in semiconductors. *Defect Recognition and Image Processing in Semiconductors and Devices*, 135:51–60, 1994.

[69] R. Berndt. Photon-emission induced by the scanning tunneling microscope. *Scanning Microscopy*, 9(3):687–693, 1995.

[70] L. Montelius, M. E. Pistol, and L. Samuelson. Low-temperature luminescence due to minority-carrier injection from the scanning tunneling microscope tip. *Ultramicroscopy*, 42:210–214, 1992.

[71] L. Samuelson, A. Gustafsson, J. Lindahl, L. Montelius, M. E. Pistol, J. O. Malm, G. Vermeire, and P. Demeester. Scanning tunneling microscope and electron-beam-induced luminescence in quantum wires. *Journal of Vacuum Science & Technology B*, 12(4):2521–2526, 1994.

[72] A. Pohl, P. G. Reinhard, and E. Suraud. Towards single-particle spectroscopy of small metal clusters. *Physical Review Letters*, 84(22):5090–5093, 2000.

[73] C. Thirstrup, M. Sakurai, K. Stokbro, and M. Aono. Visible light emission from atomic scale patterns fabricated by the scanning tunneling microscope. *Physical Review Letters*, 82(6):1241–1244, 1999.

[74] E. Cavar, M. C. Blum, M. Pivetta, F. Patthey, M. Chergui, and W. D. Schneider. Fluorescence and phosphorescence from individual C-60 molecules excited by local electron tunneling. *Physical Review Letters*, 95(19):–, 2005.

[75] Z. C. Dong, X. L. Guo, A. S. Trifonov, P. S. Dorozhkin, K. Miki, K. Kimura, S. Yokoyama, and S. Mashiko. Vibrationally resolved fluorescence from organic molecules near metal surfaces in a scanning tunneling microscope. *Physical Review Letters*, 92(8):086801, 2004.

[76] R. Nishitani, M. Tobaru, A. Kasuya, H. W. Liu, and H. Iwasaki. Topography dependence of tunneling-induced fluorescence from porphyrin film. *Japanese Journal of Applied Physics Part 2-Letters & Express Letters*, 45(24-28):L627–L629, 2006.

[77] H. W. Liu, R. Nishitani, Y. Ie, K. Sudoh, M. Nowicki, T. Yoshinobu, Y. Aso, and H. Wasaki. Molecular fluorescence from H2TBP porphyrin film on Ag substrate excited by tunneling electrons. *Ultramicroscopy*, 106(8-9):785–788, 2006.

[78] J. Buker and G. Kirczenow. Theoretical study of photon emission from molecular wires. *Physical Review B*, 66(24):245306, 2002.

[79] X. H. Qiu, G. V. Nazin, and W. Ho. Vibrationally resolved fluorescence excited with submolecular precision. *Science*, 299(5606):542–546, 2003.

[80] R. R. Chance, A. Prock, and R. Silbey. Comments on classical theory of energy-transfer. *Journal of Chemical Physics*, 62(6):2245–2253, 1975.

[81] A. Adams, R. W. Rendell, W. P. West, H. P. Broida, P. K. Hansma, and H. Metiu. Luminescence and nonradiative energy-transfer to surfaces. *Physical Review B*, 21(12):5565–5571, 1980.

[82] T. Hayashi, T. G. Castner, and R. W. Boyd. Quenching of molecular fluorescence near the surface of a semiconductor. *Chemical Physics Letters*, 94(5):461–466, 1983.

[83] A. Campion and P. Kambhampati. Surface-enhanced Raman scattering. *Chemical Society Reviews*, 27(4):241–250, 1998.

[84] G. Hoffmann, J. Kroger, and R. Berndt. Color imaging with a low temperature scanning tunneling microscope. *Review of Scientific Instruments*, 73(2):305–309, 2002.

[85] H. J. Leamy. Charge collection scanning electron microscopy. *Journal of Applied Physics*, 53(6):R51–R80, 1982.

[86] J. A. Panitz. Field-ion microscopy - a review of basic principles and selected applications. *Journal of Physics E-Scientific Instruments*, 15(12):1281–1294, 1982.

[87] Y. Nakamura, Y. Mera, and K. Maeda. A reproducible method to fabricate atomically sharp tips for scanning tunneling microscopy. *Review of Scientific Instruments*, 70(8):3373–3376, 1999.

[88] P. J. Bryant, H. S. Kim, Y. C. Zheng, and R. Yang. Technique for shaping scanning tunneling microscope tips. *Review of Scientific Instruments*, 58(6):1115–1115, 1987.

[89] P. Avouris, R. E. Walkup, A. R. Rossi, T. C. Shen, G. C. Abeln, J. R. Tucker, and J. W. Lyding. STM-induced H atom desorption from Si(100): isotope effects and site selectivity. *Chemical Physics Letters*, 257(1-2):148–154, 1996.

[90] J. W. Lyding, G. C. Abeln, T. C. Shen, C. Wang, and J. R. Tucker. Nanometer-scale patterning and oxidation of silicon surfaces with an ultrahigh-vacuum scanning tunneling microscope. *Journal of Vacuum Science & Technology B*, 12(6):3735–3740, 1994.

[91] T. Ono, H. Hamanaka, T. Kurabayashi, K. Minami, and M. Esashi. Nanoscale Al patterning on an STM-manipulated Si surface. *Thin Solid Films*, 282(1-2):640–643, 1996.

[92] J. W. Lyding, T. C. Shen, G. C. Abeln, C. Wang, and J. R. Tucker. Nanoscale patterning and selective chemistry of silicon surfaces by ultrahigh-vacuum scanning tunneling microscopy. *Nanotechnology*, 7(2):128–133, 1996.

[93] J. W. Lyding. UHV STM nanofabrication: progress, technology spin-offs, and challenges. *Proceedings of the Ieee*, 85(4):589–600, 1997.

[94] T. Hallam, F. J. Ruess, N. J. Curson, K. E. J. Goh, L. Oberbeck, M. Y. Simmons, and R. G. Clark. Effective removal of hydrogen resists used to pattern devices in silicon using scanning tunneling microscopy. *Applied Physics Letters*, 86(14):–, 2005.

[95] X. Tong and R. A. Wolkow. Electron-induced H atom desorption patterns created with a scanning tunneling microscope: implications for controlled atomic-scale patterning on H-Si(100). *Surface Science*, 600(16):L199–L203, 2006.

[96] I. Goldfarb, S. Grossman, and G. Cohen-Taguri. Evolution of epitaxial titanium silicide nanocrystals as a function of growth method and annealing treatments. *Applied Surface Science*, 252(15):5355–5360, 2006.

[97] H. C. Hsu, W. W. Wu, H. F. Hsu, and L. J. Chen. Growth of high-density titanium silicide nanowires in a single direction on a silicon surface. *Nano Letters*, 7(4):885–889, 2007.

[98] H. C. Hsu, H. F. Hsu, T. F. Chang, K. F. Liao, and L. J. Chen. Effects of substrate temperature on the initial growth of titanium silicides on Si(111). *Japanese Journal of Applied Physics Part 1-Regular Papers Short Notes & Review Papers*, 43(7B):4537–4540, 2004.

[99] P. A. Bennett, B. Ashcroft, Z. He, and R. M. Tromp. Growth dynamics of titanium silicide nanowires observed with low-energy electron microscopy. *Journal of Vacuum Science & Technology B*, 20(6):2500–2504, 2002.

[100] T. Soubiron, R. Stiufiuc, L. Patout, D. Deresmes, B. Grandidier, D. Stievenard, J. Koble, and M. Maier. Transport limitations and schottky barrier height in titanium silicide nanowires grown on the Si(111) surface. *Applied Physics Letters*, 90(10):102112, 2007.

[101] I. Goldfarb, S. Grossman, G. Cohen-Taguri, and M. Levinshtein. Scanning tunneling microscopy of titanium silicide nanoislands. *Applied Surface Science*, 238(1-4):29–35, 2004.

[102] G. A. D. Briggs, D. P. Basile, G. Medeiros-Ribeiro, T. I. Kamins, D. A. A. Ohlberg, and R. S. Williams. The incommensurate nature of epitaxial titanium disilicide islands on Si(001). *Surface Science*, 457(1-2):147–156, 2000.

[103] G. Medeiros-Ribeiro, D. A. A. Ohlberg, D. R. Bowler, R. E. Tanner, G. A. D. Briggs, and R. S. Williams. Titanium disilicide nanostructures: two phases and their surfaces. *Surface Science*, 431(1-3):116–127, 1999.

[104] T. I. Kamins, R. S. Williams, and D. A. A. Ohlberg. Annealing of chemically vapor deposited nanoscale Ti-Si islands on Si. *Applied Physics a-Materials Science & Processing*, 80(6):1279–1286, 2005.

[105] D. Gupta. *Diffusion processes in advanced technological materials.* William Andrew Pub., Norwich, N.Y., 2005.

[106] P Rai-Choudhury. *Handbook of microlithography, micromachining, and microfabrication. volume 1: microlithography.* SPIE Press Monograph Vol. PM39. SPIE Publications, 1997.

[107] G. Binnig, H. Rohrer, C. Gerber, and E. Weibel. 7x7 reconstruction on Si(111) resolved in real space. *Physical Review Letters*, 50(2):120–123, 1983.

[108] L. T. Vinh, M. Eddrief, C. A. Sebenne, P. Dumas, A. Talebibrahimi, R. Gunther, Y. J. Chabal, and J. Derrien. Low-temperature formation of Si(111)7x7 surfaces from chemically prepared H/Si(111)-(1 x-1) surfaces. *Applied Physics Letters*, 64(24):3308–3310, 1994.

[109] F. Owman and P. Martensson. STM study of Si(111)1x1-H surfaces prepared by in-situ hydrogen exposure. *Surface Science*, 303(3):L367–L372, 1994.

[110] F. Owman and P. Martensson. STM study of structural defects on in-situ prepared Si(111)1x1-H surfaces. *Surface Science*, 324(2-3):211–225, 1995.

[111] F. Owman and P. Martensson. STM study of hydrogen exposure of the Si(111)root 3x root 3-in surface. *Surface Science*, 359(1-3):122–134, 1996.

[112] G. S. Higashi, Y. J. Chabal, G. W. Trucks, and K. Raghavachari. Ideal hydrogen termination of the Si-(111) surface. *Applied Physics Letters*, 56(7):656–658, 1990.

[113] H. Angermann, K. Kliefoth, and H. Flietner. Preparation of H-terminated Si surfaces and their characterisation by measuring the surface state density. *Applied Surface Science*, 104:107–112, 1996.

[114] P. Dumas, Y. J. Chabal, and P. Jakob. Vibrational properties of H/Si(111)-(1x1) surfaces - infrared-absorption and electron-energy loss spectroscopic studies. *Applied Surface Science*, 65-6:580–586, 1993.

[115] V. A. Burrows, Y. J. Chabal, G. S. Higashi, K. Raghavachari, and S. B. Christman. Infrared-spectroscopy of Si(111) surfaces after HF treatment - hydrogen termination and surface-morphology. *Applied Physics Letters*, 53(11):998–1000, 1988.

[116] J. W. Smith. *Electric dipole moments.* Butterworths Scientific Publications, New York, 1955.

[117] K. B. Everard, L. Kumar, and L. E. Sutton. Polarisation in conjugated systems .1. the refractions and electric dipole moments of some derivatives of benzene, styrene, diphenyl, stilbene, and 1-4-diphenylbutadiene. *Journal of the Chemical Society*, pages 2807–2815, 1951.

[118] E. Bock and D. Iwacha. Electric dipole moments of ortho-, meta-, para-, and pentafluoro styrene. *Canadian Journal of Chemistry*, 46:2961–2962, 1968.

[119] J. J. Boland. Evidence of pairing and its role in the recombinative desorption of hydrogen from the Si(100)-2x1 surface. *Physical Review Letters*, 67(12):1539–1542, 1991.

[120] K. Sinniah, M. G. Sherman, L. B. Lewis, W. H. Weinberg, J. T. Yates, and K. C. Janda. New mechanism for hydrogen desorption from covalent surfaces - the monohydride phase on Si(100). *Physical Review Letters*, 62(5):567–570, 1989.

[121] U. Hofer, L. P. Li, and T. F. Heinz. Desorption of hydrogen from Si(100)2x1 at low coverages - the influence of pi-bonded dimers on the kinetics. *Physical Review B*, 45(16):9485–9488, 1992.

[122] E. Hill, B. Freelon, and E. Ganz. Diffusion of hydrogen on the Si(001) surface investigated by STM atom tracking. *Physical Review B*, 60(23):15896–15900, 1999.

[123] J. H. G. Owen, D. R. Bowler, C. M. Goringe, K. Miki, and G. A. D. Briggs. Hydrogen diffusion on Si(001). *Physical Review B*, 54(19):14153–14157, 1996.

[124] M. Durr, A. Biedermann, Z. Hu, U. Hofer, and T. F. Heinz. Probing high-barrier pathways of surface reactions by scanning tunneling microscopy. *Science*, 296(5574):1838–1841, 2002.

[125] C. H. Schwalb, M. Lawrenz, M. Durr, and U. Hofer. Real-space investigation of fast diffusion of hydrogen on Si(001) by a combination of nanosecond laser heating and STM. *Physical Review B*, 75(8):085439, 2007.

[126] R. Wolkow. Unpublished results.

[127] F. J. Himpsel, G. Hollinger, and R. A. Pollak. Determination of the fermi-level pinning position at Si(111) surfaces. *Physical Review B*, 28(12):7014–7018, 1983.

[128] D. E. Eastman. Geometrical and electronic-structure of Si(001) and Si(111) surfaces - a status-report. *Journal of Vacuum Science & Technology*, 17(1):492–500, 1980.

[129] K. Takayanagi, Y. Tanishiro, M. Takahashi, and S. Takahashi. Structural-analysis of Si(111)-7x7 by UHV-transmission electron-diffraction and microscopy. *Journal of Vacuum Science & Technology a-Vacuum Surfaces and Films*, 3(3):1502–1506, 1985.

[130] R. Losio, K. N. Altmann, and F. J. Himpsel. Fermi surface of Si(111)7x7. *Physical Review B*, 61(16):10845–10853, 2000.

[131] J. E. Northrup. Origin of surface-states on Si(111)(7x7). *Physical Review Letters*, 57(1):154–157, 1986.

[132] R. Schillinger, C. Bromberger, H. J. Jansch, H. Kleine, O. Kuhlert, C. Weindel, and D. Fick. Metallic Si(111)-(7x7)-reconstruction: a surface close to a mott-hubbard metal-insulator transition. *Physical Review B*, 72(11):–, 2005.

[133] S. Hasegawa and S. Ino. Surface-structures and conductance at epitaxial growths of Ag and Au on the Si(111) surface. *Physical Review Letters*, 68(8):1192–1195, 1992.

[134] J. W. Wells, J. F. Kallehauge, T. M. Hansen, and P. Hofmann. Disentangling surface, bulk, and space-charge-layer conductivity in Si(111)-(7x7). *Physical Review Letters*, 97(20):206803, 2006.

[135] I. Shiraki, F. Tanabe, R. Hobara, T. Nagao, and S. Hasegawa. Independently driven four-tip probes for conductivity measurements in ultrahigh vacuum. *Surface Science*, 493(1-3):633–643, 2001.

[136] S. Hasegawa, I. Shiraki, F. Tanabe, R. Hobara, T. Kanagawa, T. Tanikawa, I. Matsuda, C. L. Petersen, T. M. Hansen, P. Boggild, and F. Grey. Electrical conduction through surface superstructures measured by microscopic four-point probes. *Surface Review and Letters*, 10(6):963–980, 2003.

[137] T. Tanikawa, K. Yoo, I. Matsuda, S. Hasegawa, and Y. Hasegawa. Non-metallic transport property of the Si(111)7x7 surface. *Physical Review B*, 68(11):113303, 2003.

[138] K. Yoo and H. H. Weitering. Electrical conductance of reconstructed silicon surfaces. *Physical Review B*, 65(11):–, 2002.

[139] P. Jaschinsky, J. Wensorra, M. I. Lepsa, J. Myslivecek, and B. Voigtlander. Nanoscale charge transport measurements using a double-tip scanning tunneling microscope. *Journal of Applied Physics*, 104(9):094307, 2008.

[140] Y. Hasegawa, I. W. Lyo, and P. Avouris. Measurement of surface state conductance using STM point contacts. *Surface Science*, 358(1-3):32–37, 1996.

[141] S. Heike, S. Watanabe, Y. Wada, and T. Hashizume. Electron conduction through surface states of the Si(111)-(7 x 7) surface. *Physical Review Letters*, 81(4):890–893, 1998.

[142] E.H. Rhoderick and R. H. Williams. *Metal-semiconductor contacts.* Oxford University Press, Oxford, 2nd edition, 1988.

[143] G. D. J. Smit, S. Rogge, and T. M. Klapwijk. Scaling of nano-schottky-diodes. *Applied Physics Letters*, 81(20):3852–3854, 2002.

[144] R. A. Wolkow and D. J. Moffatt. The frustrated motion of benzene on the surface of Si(111). *Journal of Chemical Physics*, 103(24):10696–10700, 1995.

[145] R. H. Kingston and S. F. Neustadter. Calculation of the space charge, electric field, and free carrier concentration at the surface of a semiconductor. *Journal of Applied Physics*, 26(6):718–720, 1955.

[146] F.M. Smits. Measurement of sheet resistivities with the four point probe. *Bell Syst. Tech. J.*, 37:711, 1958.

[147] L.J. Van der Pauw. Determination of resistivity tensor and hall tensor of anisotropic conductors. *Phillips Res. Repts*, 16:187–195, 1961.

[148] J.D. Wasscher. Note on four-point resistivity measurements on anistropic conductors. *Phillips Res. Repts*, 16:301–306, 1961.

[149] T. Kanagawa, R. Hobara, I. Matsuda, T. Tanikawa, A. Natori, and S. Hasegawa. Anisotropy in conductance of a quasi-one-dimensional metallic surface state measured by a square micro-four-point probe method. *Physical Review Letters*, 91(3):036805, 2003.

[150] H. Okino, R. Hobara, I. Matsuda, T. Kanagawa, S. Hasegawa, J. Okabayashi, S. Toyoda, M. Oshima, and K. Ono. Nonmetallic transport of a quasi-one-dimensional metallic Si(557)-Au surface. *Physical Review B*, 70(11):–, 2004.

[151] H.C. Montgomery. Method for measuring electrical resistivity of anisotropic materials. *Journal of Applied Physics*, 42(7):2971, 1971.

[152] P. Muralt and D. W. Pohl. Scanning tunneling potentiometry. *Applied Physics Letters*, 48(8):514–516, 1986.

[153] A. Bannani, C. A. Bobisch, and R. Moller. Local potentiometry using a multiprobe scanning tunneling microscope. *Review of Scientific Instruments*, 79(8):083704, 2008.

[154] M. A. Schneider, M. Wenderoth, A. J. Heinrich, M. A. Rosentreter, and R. G. Ulbrich. Scanning tunneling potentiometry study of electron reflectivity of a single grain boundary in thin gold films. *Journal of Electronic Materials*, 26(4):383–386, 1997.

[155] J. J. Versluijs, F. Ott, and J. M. D. Coey. Potentiometric imaging of (la0.7sr0.3)mno3 thin films. *Applied Physics Letters*, 75(8):1152–1154, 1999.

[156] Y. Dong, R. M. Feenstra, R. Hey, and K. H. Ploog. Scanning tunneling potentiometry of semiconductor junctions. *Journal of Vacuum Science & Technology B*, 20(4):1677–1681, 2002.

[157] M. Jalochowski and E. Bauer. Quantum size and surface effects in the electrical-resistivity and high-energy electron reflectivity of ultrathin lead films. *Physical Review B*, 38(8):5272–5280, 1988.

[158] Y. Tokura, T. Saku, S. Tarucha, and Y. Horikoshi. Anisotropic roughness scattering at a heterostructure interface. *Physical Review B*, 46(23):15558–15561, 1992.

[159] I. Matsuda, M. Ueno, T. Hirahara, R. Hobara, H. Morikawa, C. H. Liu, and S. Hasegawa. Electrical resistance of a monatomic step on a crystal surface. *Physical Review Letters*, 93(23):236801, 2004.

[160] J. Homoth, M. Wenderoth, T. Druga, L. Winking, R. G. Ulbrich, C. A. Bobisch, B. Weyers, A. Bannani, E. Zubkov, A. M. Bernhart, M. R. Kaspers, and R. Moller. Electronic transport on the nanoscale: ballistic transmission and Ohm's law. *Nano Letters*, 9(4):1588–1592, 2009.

[161] J. A. Stroscio, R. M. Feenstra, and A. P. Fein. Electronic-structure of the Si(111)2x1 surface by scanning-tunneling microscopy. *Physical Review Letters*, 57(20):2579–2582, 1986.